TUFTS UNIVERSITY

DOE/ER/40702–12
Tufts University
December 14, 1995

Study of Atmospheric Neutrino Interactions and Search for Nucleon Decay in Soudan 2

William R. Leeson

(Ph.D. Thesis – Tufts University)

U.S. DEPARTMENT OF ENERGY
GRANT
DE–FG02–92 ER40702

December 14, 1995

Study of Atmospheric Neutrino Interactions and Search for Nucleon Decay in Soudan 2

A dissertation

submitted by

William R. Leeson

In partial fulfillment of the requirements

for the degree of

Doctor of Philosophy

in

Physics

TUFTS UNIVERSITY

December, 1995

Adviser: W. Anthony Mann

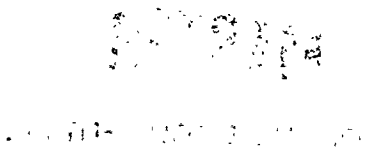

ABSTRACT OF THE DISSERTATION

Study of Atmospheric Neutrino Interactions and Search for Nucleon Decay in Soudan 2

by William R. Leeson, Ph.D.

Dissertation Director: W. Anthony Mann

Contained event samples, including 30 single–track, μ–like events, 35 single–shower, e–like events, and 34 multiprong events, have been obtained from a 1.0 kiloton year exposure of the Soudan 2 detector. A sample of 15 multiprong events which are partially contained has also been isolated. Properties of these events are used to examine the verity of the atmospheric neutrino flavor ratio anomaly as reported by the Kamiokande and IMB–3 water Cherenkov experiments. The compability of Soudan data with each of two 'new physics' explanations for the anomaly, namely proton decay and neutrino oscillations, is investigated.

We examine background processes which have not been explicitly treated by the water Cherenkov detectors. We find that our single track sample and multiprong sample has a neutron–induced background contamination of 5.7 ± 3.5 events and 1.1 ± 2.4 events respectively. The single shower sample contains a residual n/γ background of 2.0 ± 3.7 events. We check the atmospheric neutrino flavor ratio obtained from Soudan 2 data by incorporating visible ionization evaluations by physicists; we obtain $R' = 0.63 \pm 0.22$, where the error is dominated by the uncertainty from

neutron/gamma background subtraction.

We examine whether the anomaly persists with neutrino interactions of $E_\nu > 1$ GeV. We developed two methods for estimating the atmospheric neutrino flavor components of the Soudan 2 contained multiprong sample. The first approach utilizes Soudan's capabilities for distinguishing the various elementary particles (p, $\pi^\pm$, $\mu^\pm$, $e^\pm$ and γ). In this approach, whether or not either of the two charged current leptons ($\mu^\pm, e^\pm$) can be present, is established on an event–by–event basis. In the second approach the number of pion tracks which are tagged by scattering processes, is used to estimate the total number of inclusive charged pions in the entire sample; the remaining tracks are then taken to be muons. The two methods give similar results, with large statistical errors. We do not find an obvious trend which would confirm the Kamiokande report that the atmospheric neutrino anomaly persists in contained event samples from neutrino interactions with E_ν above 1.33 GeV.

The possibility that the Bugaev–Naumov flux is the best approximation to the true atmospheric neutrino flux is investigated. We argue that the rate of single–ring e–like events with lepton momenta of 100 - 600 MeV/c appears to be enhanced; the spectral excess follows three–body $p \rightarrow e^+\nu\nu$ phase space. The e–like event excess from 7.7 kiloton–years exposure of the Kamiokande detector yields $\tau/B \sim 3.0 \times 10^{31}$ years.

We have searched for other nucleon decay modes which are similar to $p \rightarrow e^+\nu\nu$. A 90% confidence level limit of $\tau/B \geq 5.02 \times 10^{31}$ years is established for the mode $n \rightarrow e^+e^-\nu$. Limits on the modes $n \rightarrow \bar{\nu}\eta^0$ and $n \rightarrow \bar{\nu}\pi^0$ are $\tau/B \geq 1.62 \times 10^{31}$ and $\tau/B \geq 3.24 \times 10^{31}$ respectively.

We have isolated single π^0 production by neutral current reactions. After background subtraction we observe 2.67±1.97 neutral current candidates per kiloton–year for the reaction $\nu N\pi^0$.

For contained multiprong and also partially contained event samples, inclusive distributions of track and shower momenta, event visible energy, and event topology

have been compared with simulations using a first-generation Monte Carlo. For the contained multiprong sample, we observe that the number of showers exceeds the number of tracks on average per event; this trend is not reproduced by the Monte Carlo.

Acknowledgements

Once upon a time in a different part of the world, in a city called Valparaíso (CHILE), two students decided against all odds to come to the United States, enroll in a Ph. D. program in physics and see if they could make it. It has been an exciting adventure and a gratifying learning experience. I must thank Juan F. Astorga for taking this odyssey with me and for sharing his friendship since sophmore years.

I am particularly indebted to Sergio Del Campo and his family whose help and moral support when I first arrived in the United States will never be forgotten. I am also deeply thankful for his constant advice through the Ph. D. program. Sincere thanks belong to M. Villanueva for having an apartment in which to live.

I would like to thank all of those within the Tufts University Community who, since I first arrived, in some way affected my life so profoundly, both intellectually and socially.

First and foremost, I will be forever grateful to my adviser, Professor W. Anthony (Tony) Mann for giving me a chance to finish this Ph. D. program after my stormy, but quite profitable learning experience through Astronomy. Also by challenging me, and suggesting a Thesis topic that nobody in the collaboration would pursue. I am very thankful for his ability and willingness to share his knowledge, insight and experience in physics and other related fields with me. Also I am very grateful for his infinite patience. Without his direction and constant support, this thesis dissertation could never have reached completion.

Among others within the Tufts Department of Physics and Astronomy, who deserve special thanks is Professor Tom Kafka for his generous assistance in writing the enormous amount of computer code without which my analysis would have

been impossible. His thorough review of my thesis dissertation was also greatly appreciated.

The Tufts–Soudan group meetings were always enhanced when graced with the presence of Professors R. Milburn, A. Napier, W. Oliver, and J. Schneps. These outstanding professors sacrificed time from their own busy schedules to share their thoughts with me.

I have enjoyed working within the Tufts High Energy Physics group and would like to acknowledge all my fellow graduate students, especially J. Astorga, D. Benjamin, M. Roach–Bellino, B. Ewen, D. Passmore, N. Sundaralingam, S. Willocq and D. Wall for making my life at the STC Building enjoyable, as well as for their enduring friendship. I must thank Larry McMaster, Dennis Dupuis and Bill Page for their technical support in the veto shield shop.

The Physics Department has perfected the art of choosing secretaries, as exemplified by its selection of, among others, Waltye Greene, Pamela Welch (sweet Pam), Dottie DeStefano, Rita Fleisher and Jackie DiMichele. One could not image a more competent, enthusiastic and friendly support staff. Thank you, ladies, very much.

I offer my special thanks to the Tufts University Graduate School of Arts and Sciences and specially to Dean Robert P. Guertin for allowing me the time necessary to perform my research while I cared for my wife.

I sincerely thank the International Center and especially the director Ms. Jane Etish–Andrews for making a foreing student life at Tufts better bearable and even exciting, as well as for her enduring friendship.

I could never forget my fellow workers at Carmichael Dining Hall for their friendship and moral support. There are too many people to thank individually, but all of you have a special place in my heart and in my life. During my stay at Carmichael I learned about cooking and I have made many unforgettable friends. Gracias, amigos, hasta la vista friends.

I want to thank the entire Soudan 2 collaboration for their help with this analysis.

There are too many people to thank individually, but all of my collaborators have had a hand in this thesis.

Tom Fields, Maury Goodman and Peter Litchfield deserve special thanks for sharing their knowledge with me, for providing useful feedback, for teaching me most of what I know about the Soudan 2 detector, particle identification, and neutrino interactions. I would like to give a special acknowledgement to John Alner, Dave Ayres, Geoff Pearce, Earl Peterson, and Don Perkins.

While working at the Soudan underground mine, I was fortunate to be helped by professionals who were always pleasant and cheerful. My special thanks to Bill Miller and the entire mine crew who helped me in a number of ways. Also thanks to my fellow graduate students at the University of Minnesota, especially C. Bode, D. Roback, D. Demuth, and G. Villaume for their help in understanding the Soudan 2 software.

Finally, this thesis which represents the culmination of one step in my life, could never have been possible without the encouragement and constant support of my wife Verónica . Her patience in enduring the spartan lifestyle of a struggling graduate student reflects the deeper bond of love and respect that we have for each other. These acknowledgments could not be complete without adding that my faith in Jesus Christ has sustained me trough all this time.

"For God sent not his Son into the world to condemn the world;
but that the world through Him might be saved."
(John 3:17)
"Jesus saith unto him: I am the way, the truth, and the life:
no man cometh unto the Father, but by me."
(John 14:6)

This dissertation is dedicated to my parents

Rosa Tiffou Ferruzola and William Leeson Rodriguez

for their love and support.

Table of Contents

List of Tables

List of Figures

Chapter 1
Underground Physics

1.1 The Standard Model

At present, nearly all observations pertaining to the known elementary particles and their electromagnetic, weak and strong interactions are encompassed by the so–called "Standard Model". The model has at its foundation three main ingredients. Firstly, it presupposes certain particles to be fundamental; including spin–1/2 fermions and spin–1 gauge bosons. Secondly, it describes interactions between these particles using gauge fields with specific symmetries. And finally, it utilizes a dynamical prescription known as spontaneous symmetry breaking that gives rise to the electroweak and to the strong interactions wherin the unbroken symmetries are "hidden", while providing a mechanism for the $W^{\pm}$ and Z^0 gauge bosons to acquire mass.

The Standard Model contains three families of quarks and leptons. The first family includes the "up" and "down" quarks. These fermions possess fractional electric charge and half–integral spin; they are to be distinguished according to their "handedness" or "chirality", denoted (u_L,d_L) and (u_R,d_R), where L and R stand for left or right–handed projection of spin along the direction of momentum. Each quark comes in three varieties, designated by the strong interaction "color" labels: red, yellow and blue. There are, in addition, three light fermions, the "leptons", (e_L,ν_L) and (e_R). Thus the first family has twelve quarks and three leptons, i.e. fourteen two–component fermions and one massless neutrino ν_L [1, 2].

The second family is a near replica of the first. New quantum number labels,

"charm" and "strangeness", identify the second family quarks, which are to be associated with the muon and its neutrino. As in the first family, there are altogether fifteen fundamental fermions. Similarly, the third family consists of "top" and "bottom" quarks together with the tau lepton and its neutrino. In addition to the $45 = 3 \times 15$ fermions of the three families, there are twelve spin one bosons: the photon γ^0, W^+, W^-, Z^0 and eight gluons. Nine of these bosons, namely the γ and eight gluons, are massless. The twelve bosons are all "exchange messengers" associated with conveying the forces between quarks and leptons. In addition, the Standard Model predicts one additional special particle, the scalar Higgs H^0. All particles except the Higgs have been observed and their masses and spins determined (though the mass of the top quark is under active investigation). Data from CERN, Fermilab, and SLAC have confirmed theoretical expectations for the $W^{\pm}$ and Z^0 masses to within 1% [3, 4].

In field theories of particle physics, the fundamental interactions involving particle multiplets possess certain mathematical symmetries. The symmetries are associated with well–known groups, e.g. U(1), SU(2), and SU(3). In gauge field theories, the gauge symmetries give rise to both a conserved quantity and a bosonic gauge particle that serves as the "carrier" of the force that is associated with the conserved quantity. In gauge field theory for electromagnetism, a U(1) gauge or phase symmetry accounts for electric charge conservation, and also give rise to a spin 1 particle with the properties of the photon as the carrier of the electromagnetic force [2].

In the Standard Model, a product SU(2) x U(1) symmetry describes a new force known as the electroweak interaction, which incorporates both the electromagnetic and weak forces [1]. These two forces, which seem distinct at low energies, are really different manifestations of the single electroweak force. At low energies its SU(2) x U(1) symmetry is spoiled by spontaneous symmetry breaking, leaving the familiar, and apparently distinct, weak force and the electromagnetic force. The energy scale at which the weak and electromagnetic interaction strengths become comparable

and are more obviously a unified electroweak force, is about 100 GeV.

The spontaneous symmetry breaking process endows three of the four electroweak gauge bosons, the $W^{\pm}$ and the Z^0, with masses on the order of the electroweak unification energy scale. The fourth gauge boson, identified with the photon, remains massless. In the Standard Model, even though the electromagnetic and weak forces appear in the Lagrangian with a single coupling strength g, the spontaneous symmetry breaking causes the electroweak force to appear in two different manifestations at low energies: The weak force appears with a coupling strength g as a short range interaction because its gauge bosons are massive; the electromagnetic force appears with comparable coupling strength of $e = g/\sin\theta_w$ (where θ_w is the Weinberg angle; $\sin^2\theta_w = 0.23186 \pm 0.00034$ [4]), but with an infinite range due to the masslessness of the photon [2].

The strong force is described in the Standard Model by an SU(3) gauge group; the conserved quantity is referred to as "color", and the carriers of the strong force are called gluons. Thus, the overall Standard Model has an SU(3) x SU(2) x U(1) gauge symmetry. At low energies, the SU(2) x U(1) symmetry is broken, but the SU(3) symmetry remains intact. The fact that the strong force is associated with the SU(3) gauge group explains many aspects of the behavior of the strong force, including the asymptotic freedom and the suggestion of the confinement of quarks into mesons and baryons. The coupling strength for the strong force, g_s, is taken to be much larger than the coupling g of the electroweak interaction at the electroweak unification scale. This disparity between the strengths of the couplings suggests that the strong force, although incorporated, is not truly unified with the other forces within the Standard Model framework [2]. It would be more desirable to have a single coupling strength for the entire theory.

For many years, neutrinos were considered to have zero rest–mass and to travel at the speed of light, however this is now open to question. Experiments show that, at least for electron and muon–neutrinos, the masses must be small, but need not

be zero. The number of light neutrino species has been estimated from the collider measurements of the Z^0 decay rate to be 3.00 ± 0.04 [4]. Limits on the number of light neutrino species can also be derived from the known cosmological abundances of the elements He^3 and He^4, thought to have been manufactured in the first few minutes of the Big Bang. Cosmologists have suggested that cosmology may be consistent with three or four light neutrinos [5].

In the Standard Model the electrically charged leptons, as well as the quarks, exist in both left and right states of chirality. Neutrinos (anti–neutrinos) however, seem to come only in left–handed (right–handed) form – they spin like left–handed corkscrews along their line of motion [1]. There is at present no evidence for the existence of right–handed neutrinos. Correspondingly, the weak force bosons, W^+ and W^-, couple only with left–handed chiral currents. Is there a fundamental right–left symmetry in nature, spontaneously broken at some higher energy scale? Are there right–handed weak currents; are there right-chiral neutrinos? These are important questions for fundamental theory which may, or may not, be answered with the next generation of accelerators (LEP–2 or the LHC).

1.2 Physics Beyond The Standard Model

Even though no prediction of the Standard Model has yet been contradicted by measurement, few physicists are satisfied with its theoretical structure. Its most unappealing feature is perhaps the multitude of fundamental constants and fields it invokes. The Standard Model contains 18 fundamental parameters: 3 coupling constants ($\alpha, \alpha_s, \sin^2\theta_W$), the neutral Higgs boson mass, the Higgs vacuum expectation value, and 13 Yukawa couplings, corresponding to 4 Kobayashi–Maskawa angles, 3 charged lepton masses, and 6 quark masses. The Model has nothing to say about the values to be assigned to these parameters. The number of fermion generations is arbitrary.

Other questions left unanswered are the following: Why do fermions appear in the representations that they do, namely: left–handed quarks and leptons in SU(2) doublets, right-handed quarks and leptons in SU(2) singlets, all leptons in SU(3) color singlets, and all quarks in SU(3) color triplets? Why do the fundamental fermions have the hypercharges and hence the electric charges that they have? Why are neutrinos massless or at least nearly massless? Where does the form of the Higgs scalar potential come from, and why do the constants describing this potential have the values that they have? Is the Higgs scalar a fundamental particle or is it composite? Are the quarks and leptons composite objects? The repetitions of quark–lepton generations with higher–mass fermions in successive generations suggests such a possibility.

There are two kinds of experimental undertakings which are currently being pursued, which are motivated in part by considerations stemming from new theories which are more comprehensive than the Standard Model. These experiments are *i)* the searches for nucleon decay, and *ii)* searches for neutrino oscillations. The existence of either or both nucleon decay and neutrino oscillations are necessary consequences in many grand unified theories (GUTs), either without or including supersymmetry. Overviews of the existing observations and phenomenology pertaining to these two phenomena are given in Sections 1.3 and 1.4 below. It is the primary goal of this Thesis, to obtain new measurements and insights which have bearing on the existence of nucleon decay and on oscillations involving atmospheric neutrinos.

1.3 Nucleon Decay: An Overview

The stability of the electron is ensured from charge conservation plus the fact that there are no lighter particles for it to decay into. The proton (or neutron) however is a composite object made up of three quarks. There are no gauge fields in the

Standard Model that imply a conservation law for baryon number, moreover there exist ten particles that have masses smaller than that of the proton, such that there is ample phase space for protons to decay into them. In the Standard Model, the stability of the proton is sustained by the fact that it is the lightest configuration of three quarks and that there is no mediating boson in the theory that is capable of converting a quark into lepton(s).

It is possible that there exist mediating bosons which can convert quarks into leptons but which, due to their high masses, have not yet been detected. As a result of fluctuations allowed by the uncertainty principle, these massive bosons could conceivably induce spontaneous proton decay at a very slow rate, in a manner analogous to the spontaneous weak decay of free neutrons. Such quark–lepton conversions can yield lighter mass particles, consequently a number of decay channels are possible. Similarly, phase space considerations would no longer protect bound neutrons from spontaneous decay by the exchange of these heavy particles. Thus, the observation of nucleon decay would provide direct evidence that the Standard Model is incomplete.

Even before the first dedicated nucleon decay search experiment was built, the proton lifetime was known to be very long; theoretical estimates of the lifetime currently span the range of 10^{29} to 10^{37} years [6]. For the experimental detection of nucleon decay it is necessary to gather and monitor a large collection of nucleons. If the average nucleon lifetime is 10^{32} years, and if a collection of 10^{33} nucleons ($\sim$ 2 kilotons) is monitored for one year, then ten nucleons would likely decay. The particles with masses small enough that they may be produced in nucleon decays are $\nu_l, \gamma, e^{\pm}$, $\mu^{\pm}$, $\pi^{\pm}$, π^0, $K^{\pm}$, $K^0/\bar{K}^0$, and the resonance states η, ρ, ω, and K^{0*}. In principle, if the final state particles are imaged with sufficient detail, a nucleon decay event can be reconstructed unambiguously (if the decay products do not include neutrinos).

In searches for nucleon decay, events caused by cosmic ray processes must be eliminated from consideration. A first step is to define a central fiducial volume,

and thus a fiducial mass, within the detector. Events that show activity in detector regions outside the fiducial volume are to be put aside. The remaining "contained events" have no obvious cause from the outside. Assuming that the detector is large and noiseless, only neutrino interactions and nucleon decays should qualify for 'contained events'. In reality, there is another source of contained events which must be dealt with, namely gamma and neutron–induced events where particles produced by cosmic ray muon or neutrino interactions in the surrounding rock enter the detector.

As shown in Fig. 1.1 [7], a number of nucleon decay detectors have been in operation, and nearly two kiloton decades of exposures have been accumulated. No convincing evidence for nucleon decay has been observed to date. Several detectors have reported "candidate" contained events in a number of the anticipated nucleon decay channels, but all have been consistent with expectations from the neutrino background. Table 1.1 shows the lower limits on the nucleon lifetime at 90% CL for Δ(B–L)–violating nucleon decay from the Frejus experiment [8]. For each decay mode, Table 1.1 shows the expected neutrino induced background, the number of observed candidates N_c, together with lower limits on ratios of nucleon lifetime over unknown branching ratio τ_N/BR, into the considered decay mode without background subtraction. A more dramatic visual presentation of nucleon partial lifetimes is Fig. 1.2. Here, the 90% confidence level lower limits for various two body nucleon decay modes are shown, as obtained from the IMB (solid triangles), Kamiokande (open circles), and Frejus (solid squares) experiments.

1.4 Neutrino Masses and Oscillation: An Overview

In the Standard Model, the neutrino is assumed to be massless. However, Grand Unification Theories generally allow the neutrino to have a small rest mass. A small neutrino mass may imply the existence of detectable phenomena such as neutrino

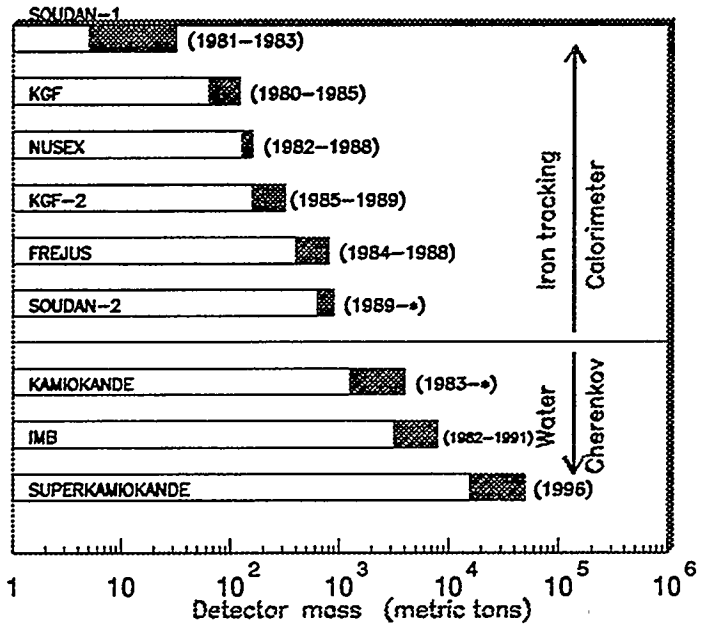

Figure 1.1: Nucleon decay experiments: The open bars represent the fiducial masses, while the shaded extensions indicate the total masses. Turn–on/off dates are indicated for each experiment (excerpted from Ref. 7, page 1674).

Frejus Nucleon Decay Limits (from Ref. 8)				
Δ(B-L)	ΔB=1	bkgrnd	N_c	τ_N/BR (10^{31} yr)
2	$n \to e^- e^+ \nu$	< 0.10	0	7.4
	$n \to e^- \mu^+ \nu$	< 0.10	0	4.7
	$p \to e^+ \nu\nu$	6.08	11	0.7
	$p \to \mu^+ \nu\nu$	11.23	7	0.8
	$p \to e^- \pi^+ \pi^+$	2.50	1	2.3
	$p \to \mu^- \pi^+ \pi^+$	1.72	1	1.4
	$n \to e^- \pi^+ \pi^0$	0.78	1	2.5
	$n \to \mu^- \pi^+ \pi^0$	0.78	0	3.4

Table 1.1: Experimental limits on nucleon decay from the Frejus planar iron tracking calorimeter experiment.

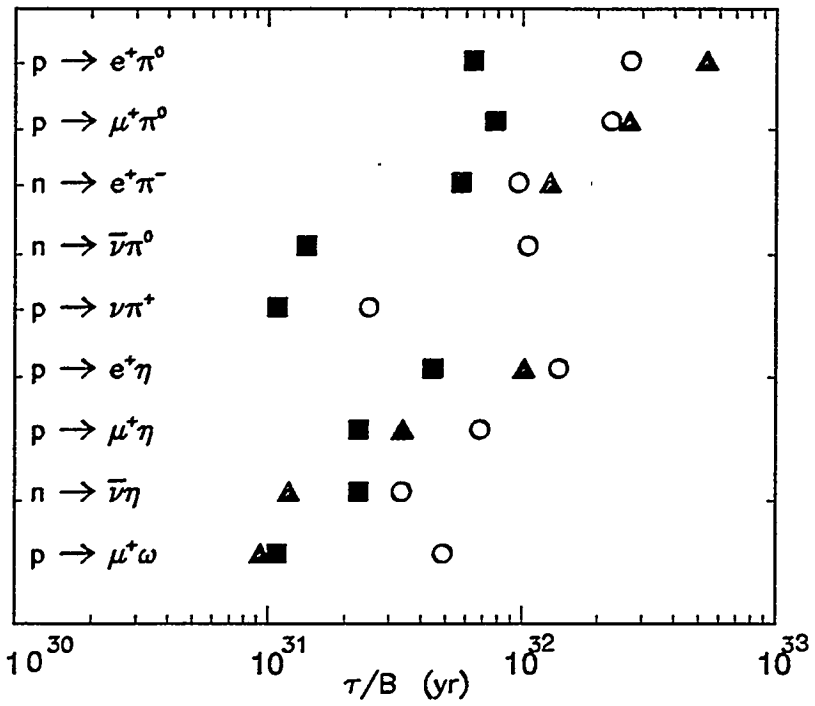

Figure 1.2: The 90%–confidence–level lower limits of the nucleon partial lifetime for various nucleon decay modes into lepton plus meson, obtained by the IMB (triangles), Kamiokande (circles), and Frejus (squares) experiments (Ref. 7).

flavor mixing. Searches for neutrino oscillations can and are being undertaken with the underground detectors originally designed for nucleon decay. In nucleon decay detectors, normal neutrino interactions can mimic the signal from nucleon decay. A major effort in experimental nucleon decay searches is devoted to understanding and accounting for this background to nucleon decay.

Neutrinos have the ability to pass through enormous amounts of ordinary matter. This property follows from the basic nature of neutrinos: they are neutral and are coupled to electrons and nuclei in matter only by the weak–interaction force. This force has both a charged current and a neutral current component, arising from the exchange of the massive $W^{\pm}$ and Z^0 gauge bosons.

Massive neutrinos imply that the neutrino flavor states (e, μ, or τ) are superpositions of the neutrino mass states. Physical implications of this assumption plus the consideration that the lepton number is not conserved are several: neutrinos could decay weakly or radiatively, and so could contribute to the non–luminous mass of the

universe (dark matter); it may be possible to observe double beta decay modes that proceed without neutrino emission; and neutrinos might undergo flavor oscillations [9].

We summarize here phenomenology describing neutrino oscillations between two species, $\nu_\mu \longleftrightarrow \nu_\tau$. A more general treatment can be made for three–flavor mixing; see reference [10] for an excellent review of three–flavor mixing.

If neutrinos have mass, the eigenstates of the weak interaction are mixtures of mass eigenstates. The flavor eigenstates $|\nu_\mu>$ and $|\nu_\tau>$ are expressed by mass eigenstates $|\nu_1>$ with mass m_1 and $|\nu_2>$ with mass m_2 by

$$\begin{pmatrix} |\nu_\mu> \\ |\nu_\tau> \end{pmatrix} = \begin{pmatrix} \cos\theta & \sin\theta \\ -\sin\theta & \cos\theta \end{pmatrix} \begin{pmatrix} |\nu_1> \\ |\nu_2> \end{pmatrix} \tag{1.1}$$

where θ is the mixing angle with $0 \leq \theta \leq \pi/4$. The evolution of a state $|\nu(t)>$ may be written as a superposition of $|\nu_\mu>$ and $|\nu_\tau>$,

$$|\nu(t)>= \nu_\mu(t)|\nu_\mu> + \nu_\tau(t)|\nu_\tau> . \tag{1.2}$$

The propagation in the space–time is determined by the Schrodinger equation;

$$i\frac{d}{dt}\begin{pmatrix} \nu_\mu \\ \nu_\tau \end{pmatrix} = \begin{pmatrix} E_1\cos^2\theta + E_2\sin^2\theta & (E_2-E_1)\sin\theta\cos\theta \\ (E_2-E_1)\sin\theta\cos\theta & E_1\cos^2\theta + E_2\sin^2\theta \end{pmatrix} \begin{pmatrix} \nu_\mu \\ \nu_\tau \end{pmatrix} \tag{1.3}$$

We can subtract any multiple of the unit matrix from Eq. (1.3) because $|\nu_\tau|^2$ and $|\nu_\mu|^2$ are not changed. One can modify (1.3) to be traceless:

$$i\frac{d}{dt}\begin{pmatrix} \nu_\mu \\ \nu_\tau \end{pmatrix} = \begin{pmatrix} -(\delta m^2/4p)\cos 2\theta & (\delta m^2/4p)\sin 2\theta \\ (\delta m^2/4p)\sin 2\theta & (\delta m^2/4p)\cos 2\theta \end{pmatrix} \begin{pmatrix} \nu_\mu \\ \nu_\tau \end{pmatrix} \tag{1.4}$$

where $\delta m^2 = m_2^2 - m_1^2$ and p is the momentum of the neutrino.

The probability that a neutrino born as ν_μ remains ν_μ at a distance L(km) is

$$P(\nu_\mu \to \nu_\mu) = |<\nu_\mu|\nu(t)|\nu_\mu>|^2 = 1 - \sin^2 2\theta \cdot \sin^2(\pi\frac{L}{L_v}), \tag{1.5}$$

$$L_v = 2.48km \times \frac{p}{\delta m^2} \tag{1.6}$$

where p is in GeV and δm^2 in eV. These formulas characterize two–flavor oscillations in vacuum.

Recently Mikheyev and Smirnov showed that, applying the matter oscillation developed by Wolfenstein (MSW) [11], neutrino oscillation is drastically enhanced in some special conditions. In the case of solar neutrino $\nu_e \longleftrightarrow \nu_\mu$ oscillations, the effect of the matter oscillation must also be taken into account. The MSW effect is due to a phase mismatch in scattering amplitudes between ν_e and ν_μ, which is caused by the difference in their forward scattering cross sections.

1.5 Atmospheric Neutrinos

Atmospheric neutrinos are decay products of pions, kaons, and muons produced in cosmic ray showers. These air showers result from the interactions in the upper atmosphere of cosmic ray primaries and atmospheric nuclei. The neutrino flux is peaked just under 1 GeV where most secondary mesons decay. The resultant neutrino flux flavor ratio ν_μ/ν_e is approximately 2. The detected ratio depends strongly on neutrino energy since below the muon mass, no charged current muon events can occur and at high energies, experimental containment criteria may preferentially reject muon–neutrino charged current events. If atmospheric neutrinos undergo flavor oscillations, at least three effects may be detectable. The neutrino flavor ratio will likely be different from the expectation without oscillations. The angular distribution could also be affected since the probability of oscillation is dependent on the distance from the neutrino production point to its interaction point. Similarly, the oscillation probability is dependent on neutrino energy so neutrino oscillations may be detectable by comparing energy distributions of detected data and simulated data.

There are however problems associated with using atmospheric neutrinos to detect neutrino oscillations. The knowledge of the absolute neutrino flux is uncertain

by at least 20% or more [12], the directions of the interaction products and the incident neutrino are not well correlated at low energies; and $\nu_e, \bar{\nu}_e, \nu_\mu$ and $\bar{\nu}_\mu$ are all present simultaneously. Moreover, interaction rates are relatively low, so that event samples accumulate slowly in detectors of mass in the one kiloton range.

1.6 The Underground Non–Accelerator Experiments

A number of large–scale non–accelerator experiments have been deployed underground in order to carry out searches for nucleon decay. A partial decay lifetime lower limit on $p \rightarrow e^+ + \pi^0$ of 2.5×10^{32} years is indicated by current experiments [7]. There are, however, a few candidate events for modes $p \rightarrow e^+ + K^0, N \rightarrow \nu + \eta$ and $N \rightarrow \nu + K^0$. A firm detection of modes involving K–mesons would signal supersymmetry and also explain the longer lifetime. Background due to atmospheric neutrinos might make it difficult, on Earth, to be sure of a real signal for proton decay if its lifetime much exceeds 10^{33} years [13].

To date, proton decay search experiments have been carried out using one or the other of two kinds of detector. KAMIOKANDE and IMB are large tanks of water in which relativistic particles traversing the detector create ring patterns of Cherenkov light on the chamber walls. Photons from the Cherenkov rings are detected by photomultiplier tubes. Water detectors are massive since they are relatively cheap to deploy; they have good directionality determination, and they have excellent electron energy resolution. However these detectors have poor spatial resolution, and have relatively limited pattern recognition capability, since they are unable to detect sub-relativistic particles. The other detector strategy is to use iron tracking calorimeters that detect charged particles by their ionization in gas; NUSEX, Frejus, and Soudan 2 are examples of the latter approach. Calorimeters offer advantages in spatial resolution and in tracking, and the ability to detect subrelativistic particles. They are however, generally less massive since their cost per ton is high. To date,

all five experiments have recorded samples of atmospheric neutrino interactions, and have examined the relative neutrino flavor composition of the atmospheric flux.

KAMIOKANDE: The Kamioka Nucleon Decay Experiment is deployed in the Kamioka metal mine in Japan [14]. The mine is approximately 1 km underground with an overburden of 2700 mwe (meter water equivalent). The detector is a cylinder, 14.4 m in diameter and 13.1 m high, containing 2142 metric tons of water. The cylinder is outfitted with 948 20–inch diameter photomultiplier tubes that cover 20% of the detector surface. The Kamiokande detector is calibrated by lowering a light source into the tank.

The detector has been upgraded three times since data–taking began. The experiment was known as Kamiokande I (KAM I) from July 1983 until November 1985, from November 1985 to September 1990 as Kamiokande II (KAM II), and since that time as Kamiokande III (KAM III). The data from the KAM I period was analyzed in two phases. In phase one, the detector had a fiducial volume mass of 880 metric tons, spatial resolution of 165 cm, angular resolution of 11°, and a trigger threshold of 50% at 30 MeV/c for electrons and 50% at 205 MeV/c for muons. In KAM I phase two, defined by the addition of an anticounter and a better trigger, the trigger threshold was 13.5 MeV/c for electrons and the fiducial mass was 780 fiducial tons. The KAM II period was defined by an electronics upgrade and better water purification. KAM II had a fiducial volume of 1040 metric tons, a trigger threshold of 7.6 MeV/c for electrons and 165 MeV/c for muons, spatial resolution of 60 cm and angular resolution of about 4°. The trigger rate in Kamiokande II is between 0.45 and 1.5 Hz with the cosmic muon flux making up approximately 0.37 Hz of the total rate.

Particle identification in water Cherenkov detectors is based on the patterns of detected rings. The pattern recognition efficiency is reported as high even though the spatial resolution is poor. The "diffuseness" of a ring is studied

to determine if a muon (sharp ring) or an electron (fuzzy ring) created the Cherenkov light pattern. From Monte Carlo simulations, KAM I misidentifies atmospheric neutrinos in $2.2 \pm 0.9\%$ of events, KAM II in $1.4 \pm 0.7\%$ of events, and $1.2 \pm 0.6\%$ is reported for KAM III [15].

The combined results from KAM I, II and III suggest that a muon neutrino deficit exists [16]. To avoid the errors of at least 20% in absolute neutrino fluxes, the ratio of ν_μ/ν_e induced events is generally presented. This ratio is then usually compared to the Monte Carlo prediction,

$$R \equiv \frac{(\nu_\mu/\nu_e)_{Data}}{(\nu_\mu/\nu_e)_{MC}}, \tag{1.7}$$

Experimental results are usually expressed in terms of the "ratio of ratios", R'_ν:

$$R'_\nu \simeq \frac{(track/shower)_{measured}}{(track/shower)_{predicted}} \tag{1.8}$$

The Kamiokande collaboration has presented results from 7.7 fiducial kiloton years of exposure, containing 482 single ring events and 208 multi ring events (a total of 690 fully contained events) [17]. With these data, the ratio of ratios in the Sub–GeV region ($E_{vis} < 1.33$ GeV) is

$$R'_\nu = 0.60^{+0.06}_{-0.05}(stat) \pm 0.05(syst). \tag{1.9}$$

They have also reported results from the Multi–GeV region ($E_{vis} > 1.33$ GeV), using both fully contained and partially contained events. In this new regime, the ratio of ratios is

$$R'_\nu = 0.57^{+0.08}_{-0.07}(stat) \pm 0.06(syst). \tag{1.10}$$

See reference [17] for the raw Kamiokande atmospheric neutrino numbers and their interpretation of the angle dependence of the muon deficit as evidence for neutrino oscillations.

IMB: The IMB detector (an acronym for the original collaborating institutions: Irvine, Michigan, and Brookhaven) was a large water Cherenkov detector located in the Morton-Thiokol Salt Mine near Cleveland, Ohio [18]. This detector consisted of about 8000 tons of water in a rectangular parallelepiped–shaped hole. The mine is 650 meters underground at an equivalent depth of 1570 mwe. At this depth, the cosmic muon rate is 2.7 Hz and the atmospheric neutrino interaction rate in the 3300 ton fiducial mass detector is about 1/day. From September 1982 to June 1984 the experiment was known as IMB–1. For this early data taking with 2048 5" photomultiplier tubes on a 1 m lattice, the trigger threshold was 50 MeV and spatial resolution was 30 cm. From May 1986 until January 1991, the experiment was known as IMB–3. This era was defined by the addition of wave shifters to 8" PMTs to improve the light collection efficiency. The trigger threshold for IMB–3 is 18 MeV and spatial resolution is about 8 cm. Calibration was performed by firing a nitrogen laser into the detector while varying filters and trigger delays. An online event cut is made by rejecting events with a very large number of hit PMTs. This reduces the triggers by 50%. The remaining data are analyzed by two independent groups of physicists with their output later merged to form one sample. The analyses typically use number of hit PMTs and Cherenkov cone geometry to look for contained events.

Once an event is identified as contained, its particle type was determined using three independent algorithms. A "vote" was then taken among the three algorithms to find the most probable particle type. The efficiency for this approach to correctly identify particle type is 87% for showers and 92% for non-showers [19].

IMB has measured the atmospheric neutrino event ratio from 7.7 fiducial kiloton years of exposure. They recorded 753 contained events, of which 507 are single ring, 246 are multiple ring, and 293 have a muon decay associated

with them [19]. The results are presented as the non–showering fraction. From the sample populations presented, the ratio of ratios can be calculated to be

$$R'_\nu = 0.54 \pm 0.07(stat) \pm 0.06(syst). \tag{1.11}$$

The IMB collaboration has made two other measurements relevant to atmospheric neutrino oscillations. Results have been presented for the ratio of upward-going to downward-going atmospheric neutrino interactions [20], and for the absolute flux of upward-going atmospheric neutrinos [21]. Neither measurement is taken to be evidence for neutrino oscillations.

Frejus: The Frejus experiment was located in the Frejus alpine road tunnel connecting Modane in France to Bardonecchia in Italy [22]. The average overburden was 1780 meters or 4800 mwe. The detector was a 6m × 6m × 12.3m, 900 ton fine grained tracking calorimeter of average density 1.95 g/cm^3. The detector granularity was 5mm × 5mm and the angular resolution was 1.0°. The calorimeter was read out by 912 vertical flash chamber plates and 113 Geiger tubes. These elements were arranged in alternate horizontal and vertical cells to give two orthogonal views. The experiment began data taking in February 1984 and shut down in September 1988.

Frejus triggered on hits in the Geiger tubes. In a time window of 300 ns, there must be at least 5 hits in 5 adjacent planes with no more than 3 hits coming from any one plane. In the 2.5 kiloton year exposure of the experiment, $1.2 \cdot 10^6$ triggers were recorded with approximately half coming from cosmic ray muons and the other half produced by radioactive background.

Trigger thresholds for Frejus are 200 MeV/c for single muons and 150 MeV/c for electrons. The trigger efficiency for charged current neutrino interactions reaches 80% for neutrino energies of 1 GeV. The trigger efficiency for neutral current events is not as good, ranging from a few percent at 1 GeV to 80% at 10 GeV.

This experiment has been calibrated by analyzing data from a detector very similar to the Frejus planar calorimeter; the data was obtained in the Aachen–Padova neutrino experiment at CERN [23]. The latter experiment collected a sample of accelerator neutrino interactions equivalent in exposure to 60 kiloton years of atmospheric neutrinos. This exposure was relied upon heavily by the Frejus group for algorithm development. The Frejus data was passed through three analysis stages. In the first stage, a physicist using a graphical display chose the topology that gave the best momentum balance. Then, a pattern recognition program using a maximum likelihood test determined particle type. Finally, graphical image scanning was augmented with a fitting program. Events identified as neutrino–induced were classified as charged–current ν_e, charged current ν_μ, or neutral–current events. The identification efficiency is reported to be 95% for muons and 86% for electrons [24].

Final results from the Frejus detector have been reported [25]. With 1.56 kiloton years of exposure, 188 partially or fully contained events have been collected. From the published sample populations, the ratio of ratios can be calculated to be

$$R'_\nu = 0.87 \pm 0.21(stat), \tag{1.12}$$

from the fully contained events. If partially contained events (PCE) are included, the ratio is

$$R'_\nu = 1.06 \pm 0.23(stat). \tag{1.13}$$

Thus the Frejus experiment did not observe an anomaly in the atmospheric neutrino flavor ratio.

NUSEX: The NUSEX experiment was located in a road tunnel under Monte Blanc [26]. The overburden was greater than 4800 mwe in all directions. The detector is a 150 ton planar tracking calorimeter, 3.5 m on a side with an average density

of 3.5 g/cm^3. It is made from 134 horizontal iron plates (1cm thick) interleaved with plastic streamer tubes 3.5m long and 9cm $\times$ 9cm is cross section. The detector is read out in two orthogonal dimensions.

For data taken between June 1982 and June 1988, with an energy cut of 200 MeV on the final state leptons and an analysis trigger of 5 contiguous plates hit, 50 contained events were selected [27]. Of the 50 events, 49 were unambiguously identified and one event contained both a track and a shower. The ratio of ratios was calculated to be

$$R'_\nu = 0.99 \pm 0.40(stat). \tag{1.14}$$

SOUDAN 2: Soudan 2 is an iron tracking calorimeter of honeycomb geometry which is designed to search for proton decay. A detailed description of this detector is given in Chapter 3. Soudan 2 is able to measure the atmospheric ν_μ/ν_e event ratio; its systematic errors are reduced by using data from charged particle test beam exposures which measure particle identification efficiencies directly. Soudan 2 records approximately 100 contained neutrino interactions per fiducial kiloton year (obtained every two calender years of operation).

Soudan 2 has reported a preliminary result on the atmospheric neutrino flavor ratio, which is

$$R'_\nu = 0.64 \pm 0.17(stat) \pm 0.09(syst). \tag{1.15}$$

based on 1.01 kiloton years [28]. This result is consistent with the anomalous flavor ratios reported by the two big water Cherenkov detectors. It is the first of the iron tracking calorimeters to indicate an anomaly.

Experiment	Exposure kty	R'_ν
Kamiokande Sub–GeV (ring)	7.7	0.60 ± 0.06
Kamiokande Sub–GeV (decay)	7.7	0.69 ± 0.06
Kamiokande Multi–GeV	7.7	0.57 ± 0.07
IMB–3 (ring)	7.7	0.54 ± 0.05
IMB–3 (decay)	7.7	0.64 ± 0.07
Frejus (contained)	1.56	0.87 ± 0.21
Frejus (total)	2.00	1.06 ± 0.17
Nusex	~ 0.40	0.99 ± 0.29
Soudan 2	1.01	$0.64 \pm 0.17 \pm 0.09$

Table 1.2: Ratio of ratios for underground experiments.

1.7 The Atmospheric Neutrino Anomaly

The underground experiments which detect atmospheric neutrinos cover a large neutrino energy range and variation in neutrino path lengths. Consequently the experiments offer interesting possibilities for exploring neutrino oscillation effects. The neutrino interactions are being studied using four different topologies: *i)* Contained events (ν_μ and ν_e with energies $\bar{E}_\nu \sim 0.6$ GeV); *ii)* partially contained events ($\bar{E}_\nu \sim 4$ GeV); *iii)* stopping muons (mostly ν_μ's with $\bar{E}_\nu \sim 5$ GeV); and *iv)* throughgoing muons ($\bar{E}_\nu \sim 100$ GeV). The ratio of ν_μ/ν_e events may be contrary to expectations, given that the water detectors show a discrepancy of order $\sim 4\sigma$ between observation and expectation for the ν_μ/ν_e ratio. A summary of these results is shown in Table 1.2. This result is explainable as due to either a deficit of ν_μ's or an excess of ν_e's.

This thesis will begin with an analysis of the atmospheric neutrino flavor ratio results, starting with a summary of the different atmospheric neutrino flux calculations, followed by examination of published IMB–3 and Kamiokande data. Special emphasis will be placed on interpretations of the atmospheric neutrino anomaly, the

implications of the interpretations, and the contributions that Soudan 2 can make in order to clarify the situation. Then present studies are presented using contained events from a 1.01 kiloton year exposure of Soudan 2. An examination of a new sample of partially contained events is also included. The capability of the Soudan 2 detector to explore new physics phenomena is demostrated by new measurements reported here, pertaining to nucleon decay lower lifetime limits in selected modes, and to event rates for single π^0 production in neutral current reactions initiated by atmospheric neutrinos.

References

[1] K. Grotz and H.V. Klapdor, *"The Weak Interaction in Nuclear, Particle, and Astrophysics"*, IOP Publishing Ltd., Bristol, England 1990.

[2] I.D. Lawrie, *"A Unified Grand Tour of Theoretical Physics"*, IOP Publishing Ltd., Bristol, England 1990.

[3] Frank J. Sciulli, *"Recent Results from H1 and ZEUS at HERA"*, Proceedings of DPF92 Meeting, Fermilab, 10–14 November 1992, p. 37.

[4] Average LEP result from a talk given by: D. Schaile, *"New Results from LEP Experiments"*, 15th Workshop on Weak Interactions and Neutrinos, Talloires, France, 4–8 September 1995.

[5] P. D. B. Collins, A. D. Martin and E. J. Squires, *"Particle Physics and Cosmology"*, John Wiley, New York 1989.

[6] J. Ellis *et al.*, Nucl. Phys. **B 176**, 61 (1980).

[7] Particle Data Book, *"Review of Particle Properties"*, Phys. Rev. **D 50**, 1674 (1994).

[8] Ch. Berger *et al.*, Phys. Lett. **B 269**, 227 (1991).

[9] For a review of neutrino oscillation, see: S. M. Bilenky and B. Pontecorvo, Phys. Rev. **41**, 225 (1978); A. K. Mann and H. Primakoff, Phys. Rev. **D 15**, 655 (1977); D. Ayres *et al.*, Phys. Rev. **D 29**, 902 (1984), and S. M. Bilenky and S. T. Petcov, Rev. Mod. Phys. **59**, 671 (1987).

[10] V. Barger *et al.*, Phys. Rev. **D 22**, 2718 (1980).

[11] L. Wolfenstein, Phys. Rev. **D 17**, 2369 (1978); S. P. Mikheyev and A. Yu. Smirnov, Nuovo Cimento **9C**, 17 (1986).

[12] D. H. Perkins, Astroparticle Phys. **2**, 249 (1994).

[13] P. Davies, *"The New Physics"*, Cambridge University Press, Cambridge, England 1989.

[14] K. Arisaka *et al.* J. Phys. Soc. Jap. **54**, 3213 (1985), and K. S. Hirata *et al.* Phys. Rev. **D 38**, 448 (1988).

[15] T. Kajita, *"Results from Kamiokande on Solar and Atmospheric Neutrinos"*, Proceedings of the 25nd International Conference on High Energy Physics, Singapore 1990.

[16] K.S. Hirata *et al.*, Phys. Lett. **B 280**, 146 (1992).

[17] Y. Fukuda *et al.*, Phys. Lett. **B 335**, 237 (1994).

[18] R. Claus *et al.*, Nucl. Instr. Meth. **A 261**, 540 (1987).

[19] S. Dye, *"IMB–3 Atmospheric Neutrino Anomaly"*, Proceedings of Atmospheric Neutrino Workshop, 6–8 May 1993, Louisiana State University.

[20] R. M. Bionta *et al.*, Phys. Rev. **D 38**, 768 (1988).

[21] R. Becker–Szendy *et al.*, Phys. Rev. Lett. **69**, 1010 (1992), R. Svoboda, *"Upward going Muons in IMB–3"*, Proceedings of Atmospheric Neutrino Workshop, 6–8 May 1993, Louisiana State University.

[22] Ch. Berger *et al.*, Nucl. Instr. Meth. **A 261**, 540 (1987).

[23] Ch. Berger *et al.*, Nucl. Instr. Meth. **A 262**, 463 (1987).

[24] H. Meyer, *"Experimental Results from Frejus Experiment"*, Proceedings of Atmospheric Neutrino Workshop, 6–8 May 1993, Louisiana State University.

[25] O. Perdereau *et al.*, *"Final Results of the Frejus Proton decay Experiment on Atmospheric Neutrinos"*, Proceedings of Tests of Fundamental Laws in Physics, Moriond, France 1991.

[26] B. Battistoni *et al.*, Nucl. Instr. Meth. **A 245**, 277 (1986).

[27] M. Aglietta *et al.*, Europhys. Lett. **8**, 611 (1989).

[28] M. C. Goodman, Nucl. Phys. **B** (Proc. Suppl) **38**, 337 (1995).

Chapter 2

The Atmospheric Neutrino Anomaly and its Interpretation

2.1 Summary and Overview

In 1992 we proposed that, if the absolute fluxes of sub–GeV atmospheric neutrinos are below expectations of most calculations, the observed small atmospheric ν_μ/ν_e ratio could be interpreted as evidence for proton decay $p \rightarrow e^+\nu\nu$ occuring in the water or iron media of underground detectors [1]. In this Chapter we review our initial proposal in light of more recent momentum spectra of contained, single–ring events obtained in 7.7 kiloton–years (kty) exposures of the Kamiokande and IMB–3 detectors. We present an analysis that does not rely upon any particular neutrino flux calculation. We show that the rate of single–ring e–like events with lepton momenta of 100 - 600 MeV/c appears to be enhanced; the spectral excess follows three–body $p \rightarrow e^+\nu\nu$ phase space to a greater degree than was found in our original study of the 4.92 kty exposure. The e–like event excess is compatible with $\tau/B \sim 3 \times 10^{31}$ years.

2.2 Experimental Results

The flux of atmospheric neutrinos, originating with decays of cosmic–ray induced $\pi^\pm$, $K^{\pm,0}$ and $\mu^\pm$ within the Earth's atmosphere, gives rise to contained events in massive underground detectors. An expectation common to all calculations of atmospheric neutrino fluxes based on known physics, is that the flavor ratio R_ν of $(\nu_\mu+\bar{\nu}_\mu)$

to $(\nu_e + \bar{\nu}_e)$ is about 2.0. However, contained event samples accumulated by the Kamiokande [2, 3] and IMB [4] water Cherenkov experiments (7.7 kty exposure for each experiment) indicate R_ν to be anomalously low. The observation is based upon relative rates among subsamples of contained events whose images appear either as single, sharply–defined rings (muon–like), or as single, diffuse rings (electron–like). The majority of single–ring events are supposedly quasi–elastic charged current interactions, of the type

$$\begin{aligned} \nu_\mu + n \rightarrow \mu^- + p\,, \qquad \bar{\nu}_\mu + p \rightarrow \mu^+ + n; \\ \nu_e + n \rightarrow e^- + p\,, \qquad \bar{\nu}_e + p \rightarrow e^+ + n. \end{aligned} \tag{2.1}$$

As described in Section 1.6, experimental results are usually expressed in terms of the ratio–of–ratios R'_ν. The observed ratio of contained ν_μ to ν_e events is about 0.6 of the value expected in the two water Cherenkov detectors (see Table 1.2). That is, after detailed simulations of detector response and acceptance effects, the ratio–of–ratios as observed in Kamiokande is 0.60 ± 0.06 [5] and as observed in IMB–3 is 0.54 ± 0.05 [4]. One sees that the water detectors show an approximate 4σ discrepancy between observation and expectation.

On the other hand, measurements with the iron tracking calorimeters give mixed results (see Fig. 2.1). Their statistical uncertainties are significantly larger than for the water detectors. Results from the two planar iron tracking calorimeters, namely NUSEX [6] and Frejus [7], are consistent with no anomaly at all. In contrast, preliminary findings from the Soudan 2 iron honeycomb tracking calorimeter indicate, with modest statistics (and correspondingly large errors), that the anomaly is being seen [8]. The Soudan value is in agreement with the water Cherenkov experiments and supports the view that R_ν is truly anomalous. However, a major concern in the Soudan 2 collaboration is how to estimate and correct for the background contamination of the contained event sample. We know that radioactive nuclei exist both

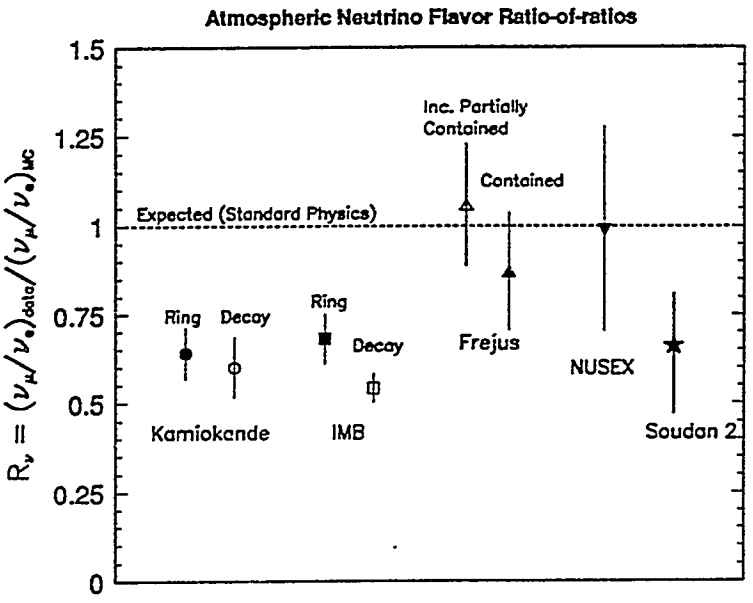

Figure 2.1: Atmospheric neutrino flavor ratio–of–ratios for underground experiments.

in the cavity walls as well as in trace amounts in various components of the detector itself. These unstable nuclei emit photons (in the KeV to MeV) energy range interacting primarily by Compton scattering with atomic electrons. The energy released in the detector from an interaction caused by radioactivity is 0.10 to 1.0% of that released in neutrino interactions or in nucleon decay. An energy cut should in principle eliminate this kind of background. A potentially more serious background arises from particles produced in deep inelastic cosmic ray muon interactions in the rock surrounding the detector. These interactions will occasionally create photons or neutrons or K^0 mesons which can penetrate into the tracking calorimeter. The active shield will only flag such events if the neutrals are accompanied by charged particles. The shield has been mounted immediately adjacent to the cavity walls to maximize the acceptance for these muon reaction products. Contained events with hits in the active shield are due to interactions of neutral particles produced by muon interactions in the surrounding rock. Detailed study of these latter events is needed in order to correct the zero shield hit sample for shield inefficiency, for losses

due to random shield hits, and for remnant neutron–induced and gamma–induced background. In paragraphs below we provisionally assume that the atmospheric neutrino flavor ratio anomaly cannot be ascribed to cosmic–ray induced non–neutrino background processes.

2.3 Anomaly Interpretations and Absolute Neutrino Fluxes

To interpret the low R_ν value, one needs to know whether the μ–like events of the numerator are too few, whether e–like events of the denominator are too numerous, or whether a combination of both circumstances is actually the case. Several different interpretations have been expressed in the literature. A popular view (Refs. [2, 3]) is that there exists an apparent dearth of muon–neutrino events (accompanied perhaps by a mild excess of electron–neutrino events (Refs. [4]), which is interpreted as evidence that neutrino oscillations deplete the muon–neutrino flux over distances of 10 to 10,000 kilometers.

A different view, formulated by us [1, 9, 10], assumes that the expected number of ν_μ events has been detected, and that there is an excess of electron–like events that can be ascribed to predominant nucleon decay via the mode $p \rightarrow e^+\nu\nu$. The situation could be clarified if the absolute fluxes for all neutrino flavors ($\nu_\mu, \bar{\nu}_\mu, \nu_e, \bar{\nu}_e$) were accurately known, which is, however, not the case. The oscillation interpretation is usually formulated using absolute neutrino fluxes calculated by the Bartol group [11, 12] or by Honda *et al.* [13]; these happen to be the highest in the literature. In our original presentation of the proton decay scenario [1], we utilized absolute atmospheric neutrino fluxes calculated by Bugaev and Naumov [14], which are distinctly lower. This interpretation of the low R'_ν has been criticized as depending strongly on a particular atmospheric flux calculation. However the essential argument can be restated in a way which does not rely on any neutrino flux calculation [9, 10], though it does still imply that the absolute neutrino fluxes are relatively low. We assume

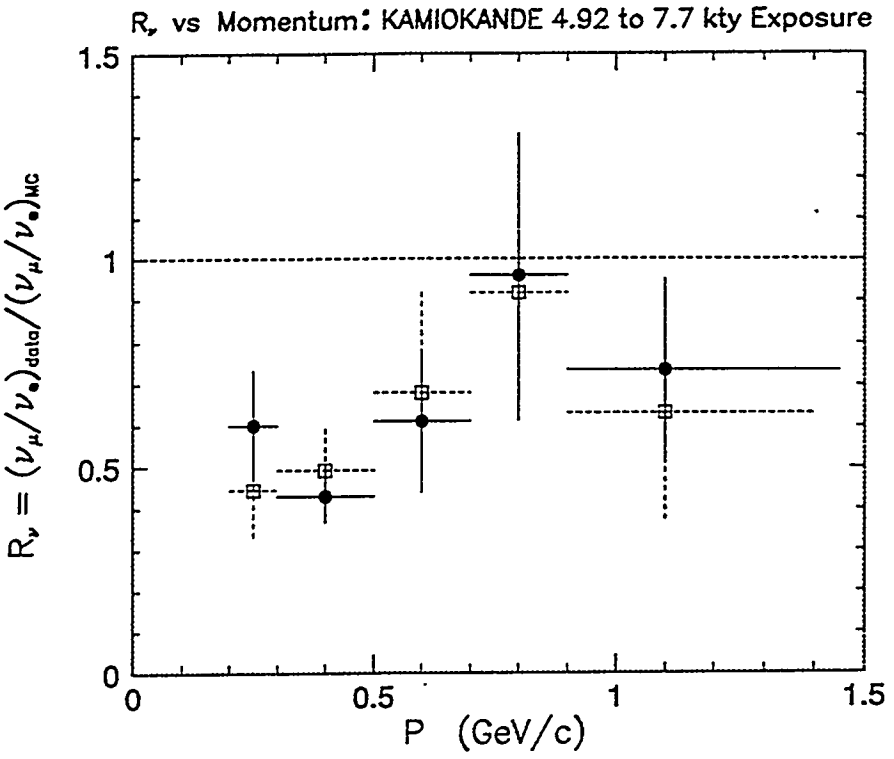

Figure 2.2: Evolution of R'_ν from 4.92 kty (open squares) to 7.7 kty (solid circles) exposure in Kamiokande.

that no atmospheric muon neutrinos are lost due to oscillations or other processes.

2.4 Kamiokande Sub-GeV Sample

In conferences two summers ago (June - Aug., 1994), the Kamiokande collaboration reported an update on their analysis of contained neutrino interactions observed underground [3], which matches the total exposure achieved with the IMB–3 detector. It was necessary for us to review our proton decay scenario in terms of the new data available [10]. The current viability of the $p \rightarrow e^+\nu\nu$ hypothesis is indicated by Fig. 2.2, wherein the R'_ν versus momentum distributions from 4.92 and 7.7 kty exposures [2, 3] of Kamiokande (open squares and solid circles respectively) are shown superposed. We observe that, with the statistical gain in the most recent data, the anomaly is mildly enhanced in the 300 to 700 MeV/c interval while being mildly diminished both below and above this regime. These trends are as expected from $p \rightarrow e^+\nu\nu$ phase space, as will be discussed in paragraphs below.

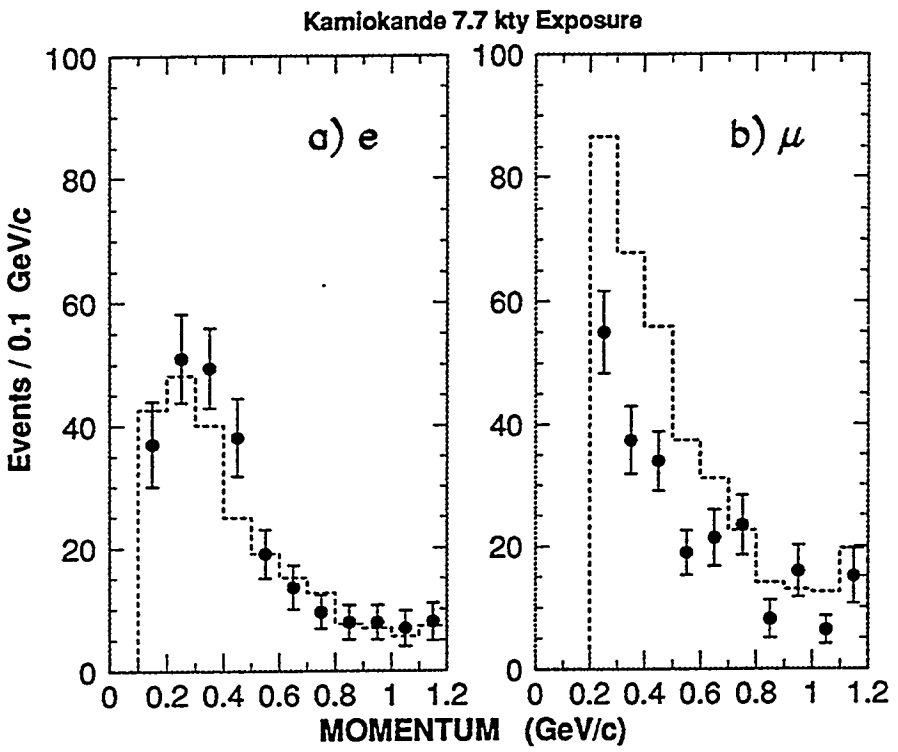

Figure 2.3: The momentum distributions of single–ring a) e–like; b) μ–like events from 7.7 kiloton–year exposure of Kamiokande. The histograms shows the Monte Carlo prediction based on the atmospheric flux calculation of Honda *et al.* (Ref. 12).

The relationship between physics interpretation and a flux calculation is exhibited in the analysis of single–ring samples from Kamiokande's 7.7 kiloton year exposure. The lepton momentum distributions from Ref. [3] are reproduced in Fig. 2.3. The distribution of e–like and μ–like events are shown by solid circles, together with distributions calculated using the Honda *et al.* [13] atmospheric flux spectra (dashed histogram). Fig. 2.3a shows the number of e–like events to be slightly less than the estimate based on the Honda *et al.* flux, with a clear excess in the momentum range of 300 to 500 MeV/c. Contrastingly, Fig. 2.3b shows the number of μ–like events with momenta below 700 MeV/c to be well below the prediction. This latter observation has been heralded as "*The too–few–ν_μ problem*" and is often cited as evidence for ν_μ to ν_τ oscillations occurring in the atmospheric neutrino fluxes.

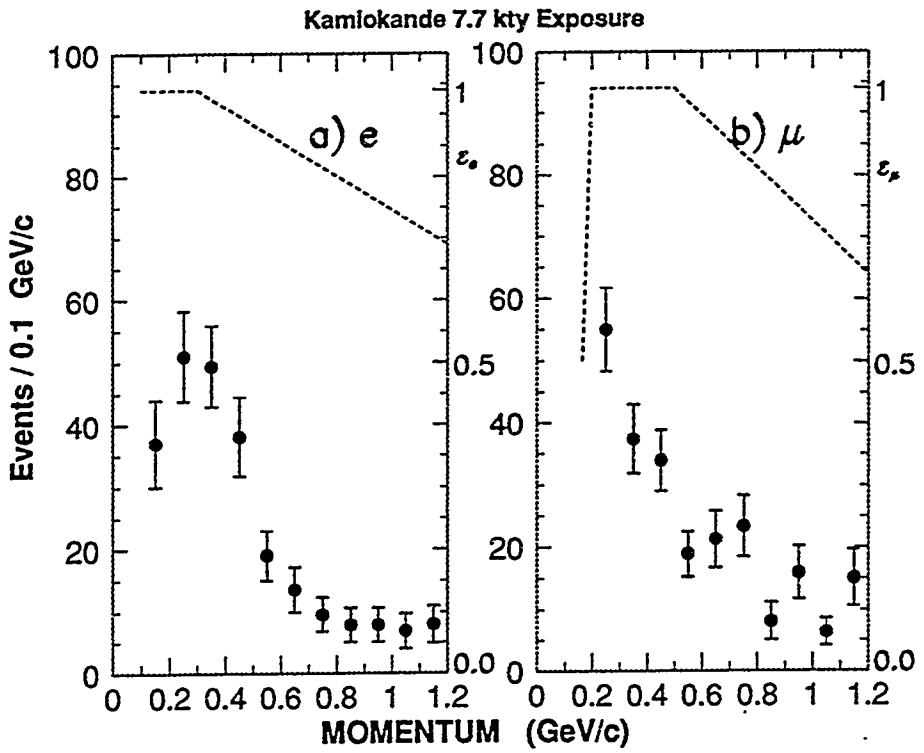

Figure 2.4: The lepton momentum distributions of single–ring a) e–like; b) μ–like events. Detection efficiencies are shown superimposed (dashed line).

2.5 The Case for $p \rightarrow e^+\nu\nu$

Here we start with the premise that no atmospheric muon neutrinos are lost due to oscillations or other processes. In Fig. 2.4a we show the distribution of lepton momentum for all contained, electron–like single ring events in the 7.7 kiloton–year exposure of Kamiokande. The detection efficiency for these events is shown superimposed by the dashed line. The corresponding distribution for muon–like single rings events is shown in Fig. 2.4b.

The Cherenkov threshold for detection of muons in water prevents direct observation of events with muon momenta in the interval 100 - 200 MeV/c. In Fig. 2.5 we show the inferred rate in this unseen bin of 100 to 200 MeV/c. This estimation was calculated using muon quasi–elastic events and then matched to the observed distribution of μ–like events.

We hypothesize that the μ–like event sample is free of any new physics. Also, we assume that neutrino cross–sections are nearly the same for corresponding ν_μ and

ν_e charged current channels. Then we can use the number of μ–like events in each momentum bin, together with the experimental detection efficiencies and the e–like to μ–like event ratio 1:2, to predict the number of e–like events to be observed in the absence of new physics. The expected e–like event rates are depicted by the open triangles in Fig. 2.6. We observe in Fig. 2.6 that there is an excess of e–like events over and above the expectation inferred from the μ–like event distribution and the ν_μ/ν_e ratio obtained in all conventional neutrino fluxes. We note that the statistical excess is only significant ($\geq 2.5\sigma$) in the interval 100 - 500 MeV/c. We now consider nucleon decay processes as candidate sources for this apparent localized excess of single–ring e–like events.

2.6 Nucleon Decay Processes as Origin of the Anomaly

The data restricts the number of viable nucleon decay modes in two ways: (*i*) *Topology constraint:* Single $e^{\pm}$ showers are detected; any accompanying particles leave no signal in a water Cherenkov detector. (*ii*) *Momentum spectrum constraint:* Single $e^{\pm}$ showers are detected with significant rate in the momentum interval from 100 MeV/c to 500 MeV/c.

In our analysis we will first consider the $e^{\pm}$ spectrum constraint (*ii*), and then introduce the visible topology constraint (*i*).

Fig. 2.7 shows the momentum spectra of positrons from four different two–body decay modes with the Fermi momentum of the parent proton in oxygen taken into account [15]. In water Cherenkov detectors, most nucleon decays into ($e^{\pm}$ + meson) yield multi–ring topologies. Current nucleon decay life–time limits on such modes [16, 17], together with the small probability that neither the meson nor its decay products would be detected, preclude a large contribution to the excess of single–ring e–like events. Nevertheless it is informative to consider the spectral shapes. In Fig. 2.7, we see that the channels $e^+\omega^0$, $e^+\rho^0$ yield positron momentum spectra

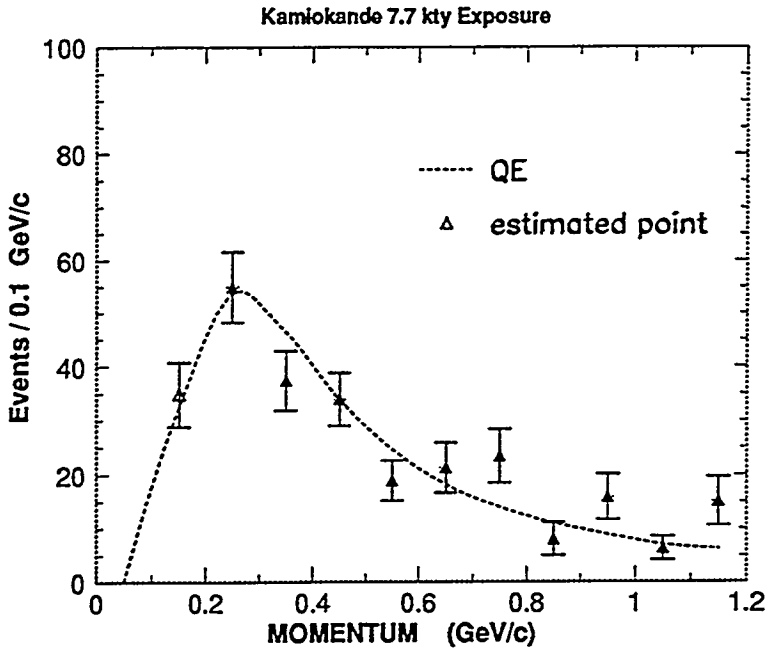

Figure 2.5: Lepton momentum distribution for μ–like events, where the dashed line depicts the distribution shape expected for quasi–elastic events.

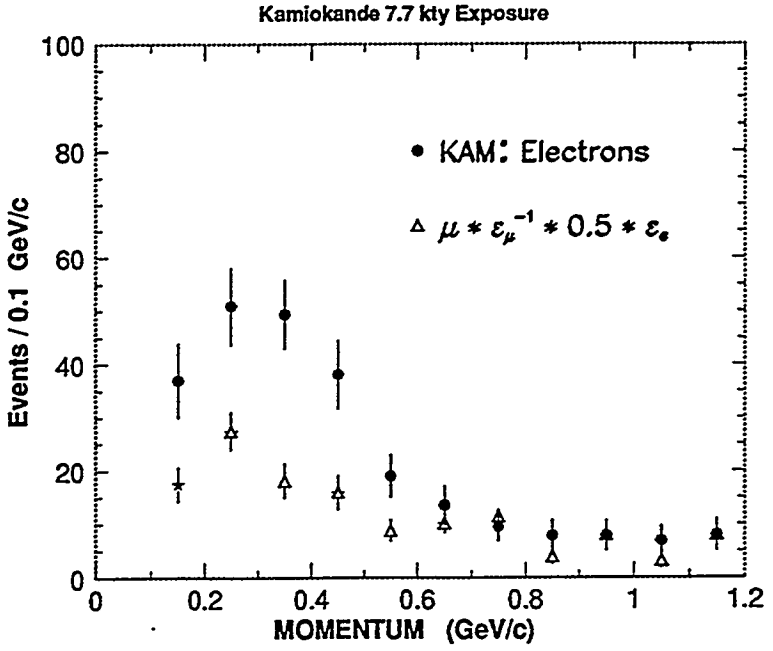

Figure 2.6: Detected lepton momentum distribution for e–like events (solid circles), and the expected e–like event rates calculated from μ–like event data of Fig. 2.5 (open triangles).

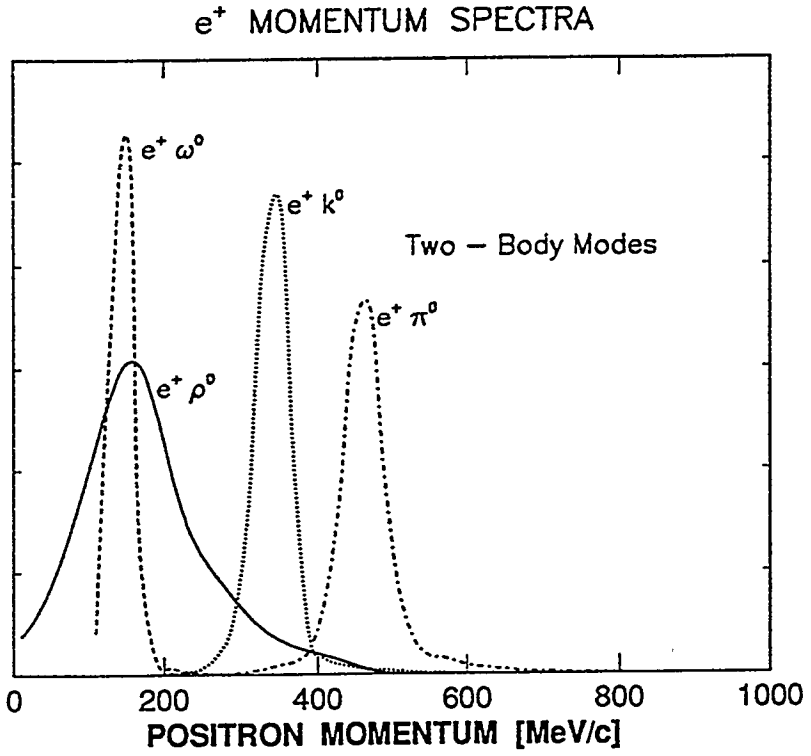

Figure 2.7: Positron momentum spectra from two–body proton decay modes in oxygen nuclei.

below the excess region 200 - 500 MeV/c. $e^{\pm}$ recoiling from a much lighter meson, e.g. $e^{+}\pi$, has a momentum spectrum which is more energetic. The modes $e^{+}K^{0}$ and $e^{+}\pi^{0}$ have e^{+} spectra which peak in the middle of the observed excess region, but their ranges are too narrow. In fact, there is no two–body nucleon decay mode which would alone satisfy the $e^{\pm}$ spectrum constraint.

Fig. 2.8 shows the phase space of three–body nucleon decay modes:

$$p \rightarrow e^{+}(\pi\pi)_{nonresonant}, \tag{2.2}$$

$$p \rightarrow e^{+}\nu\nu. \tag{2.3}$$

It is apparent that the processes $p \rightarrow e^{+}\pi^{+}\pi^{-}$ and $p \rightarrow e^{+}\nu\nu$ yield positron momentum spectra (Fig. 2.8) which are wider than those obtained with two–body modes (Fig. 2.7). Compared to $p \rightarrow e^{+}\nu\nu$, mode $p \rightarrow e^{+}\pi^{+}\pi^{-}$ has a larger rate for positron momenta below 200 MeV/c and falls off more rapidly above 400 MeV/c. On the other hand, mode $p \rightarrow e^{+}\nu\nu$ has the bulk of its positrons within the 200–500 MeV/c region, although non–negligible counting rate below 200 MeV/c is also

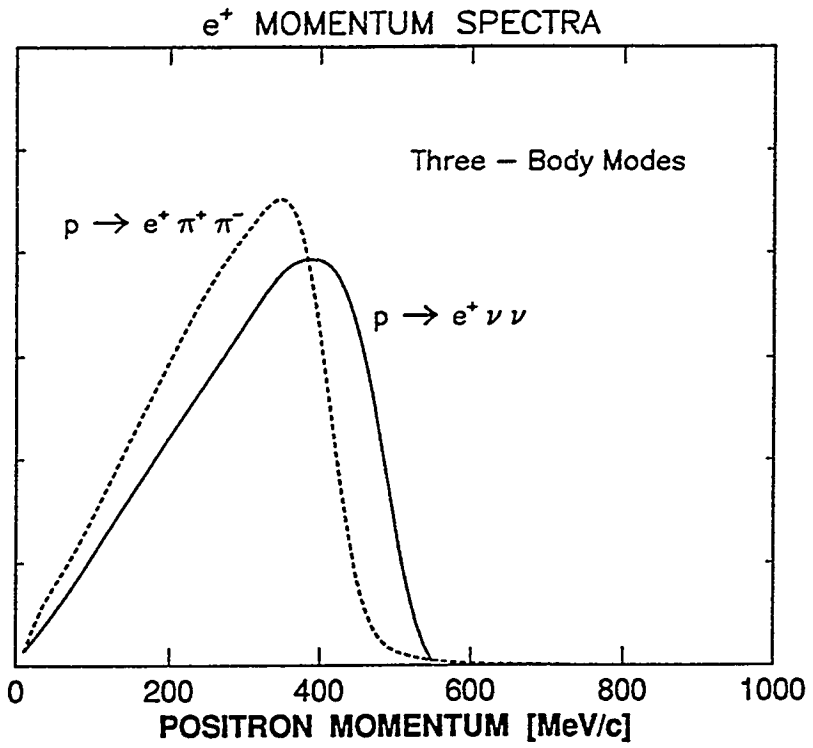

Figure 2.8: Positron momentum spectra from three–body proton decay modes in oxygen nuclei.

implied.

Possibilities with the phase space of four–body nucleon decay are illustrated by the two decay modes shown in Fig. 2.9. The modes $p \rightarrow e^+\pi\pi\pi$ and $p \rightarrow e^+\nu\nu\nu$ differ from the three–body nucleon decay modes, in that they tend to have less energetic single shower spectra (as seen in Fig. 2.9). We observe that the $p \rightarrow e^+\pi\pi\pi$ mode peaks below 200 MeV/c, while the $p \rightarrow e^+\nu\nu\nu$ mode has a larger rate for positron momenta below 300 MeV/c and falls off more quickly above 400 MeV/c. We conclude that only mode (2.3) and possibly (2.2) satisfy the $e^{\pm}$ spectrum constraint.

Concerning mode (2.2), one needs to consider decays wherein the charged pions are not detected. Using three–body phase space, taking the $\pi^{\pm}$ detection threshold to be 200 MeV/c, and assuming the absorption probability per pion to be 0.22 [18], we estimate that 11% of mode (2.2) events will end up as single–ring electron–like events. On the other hand, in about 31% of mode (2.2) decays, neither pion will undergo absorption or charged exchange and the final states will be fully imaged as three–ring

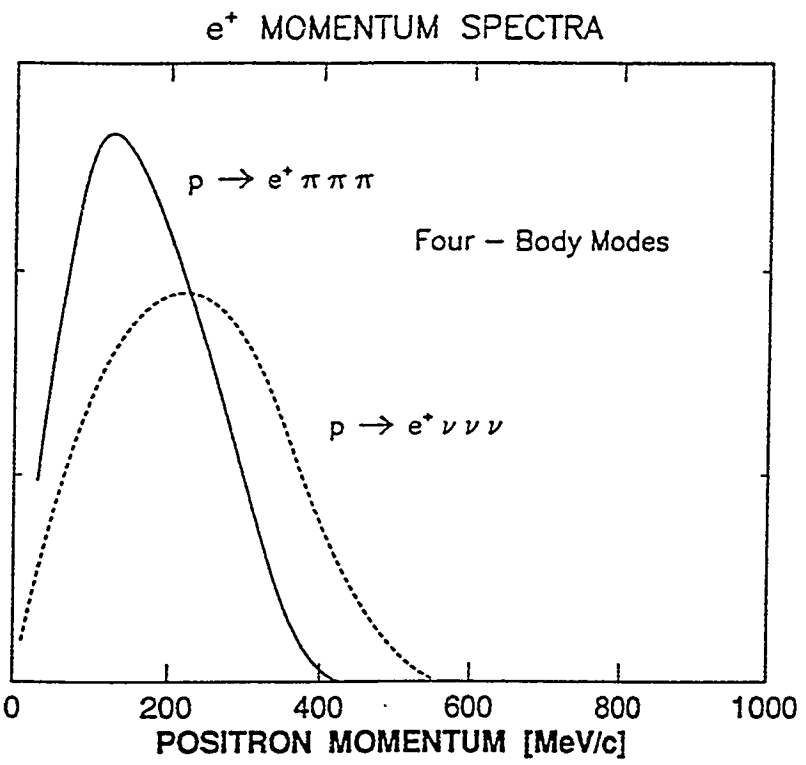

Figure 2.9: Positron momentum spectra from four-body proton decay modes in oxygen nuclei.

events. Thus the excess of e–like single–ring events cannot be predominantly due to mode (2.2), otherwise the existence of proton decay would already be apparent from a fully–imaged subsample of mode (2.2).

We conclude that there is no two–body or four–body nucleon decay mode which, alone, can satisfy the $e^{\pm}$ spectrum constraint [1]. With three–body modes, there is only one which satisfies both the momentum spectrum constraint and the topology constraint and that is mode (2.3). To examine the extent to which mode (2.3) satisfies the positron spectrum constraint (*ii*), we subtract bin–by–bin the rate expectation for the e–like events which is based on the observed distribution of single–ring μ–like events. The excess of e–like events thus obtained is plotted in Fig. 2.10. Superposed on the histogrammed data is the phase space momentum distribution for positrons originating with decay (2.3) in a water medium (dashed line). The shape of the positron momentum spectrum of proton decay mode (2.3) is observed to describe the excess event distribution rather well.

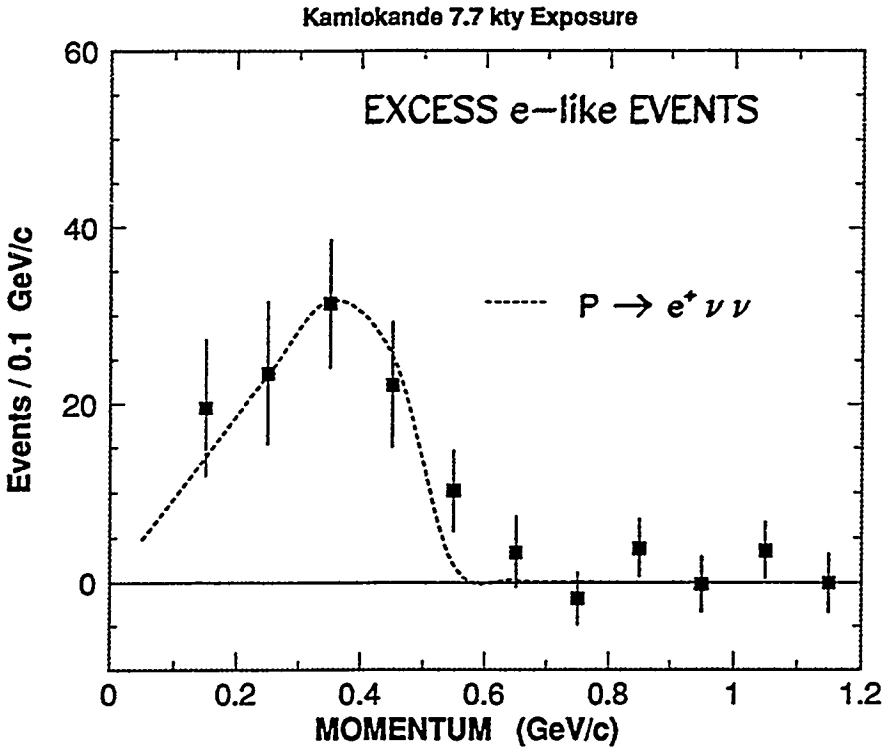

Figure 2.10: Excess e–like events in the 7.7 kty exposure of Kamiokande (solid squares). Superimposed is the phase space momentum distribution for positrons originating from $p \rightarrow e^{+}\nu\nu$ in water medium (dashed line).

2.7 IMB Sub-GeV Neutrino Event Sample

In 1991 the IMB–3 water detector ceased data taking, having accumulated a total exposure of 7.7 kiloton years. This is a water Cherenkov detector similar to Kamiokande, but at a different geomagnetic latitude, with different photomultipliers, resolutions, efficiencies, etc. In Fig. 2.11, the distribution of e–like and μ–like are shown by the open circles and open triangles respectively, together with predicted atmospheric flux spectra (solid line) of Lee and Koh [19]. Fig. 2.11a shows the number of e–like events to be well above expectation for all momenta, plus a low contamination due to the muon decay content of the sample ($\mu \rightarrow e$). On the other hand, Fig. 2.11b shows the number of μ–like events to undershoot the Lee Monte Carlo flux calculation, with a substantial fraction of these events being accompanied by observed muon decays.

In Ref. [4], the IMB–3 estimates that their deficit of muon neutrino events to be less then two standard deviations. They conclude that "*the magnitude of the*

deviation is not sufficient to require neutrino oscillations to explain our data". In our view, the experimental situation remains unsettled, due to the fact that the atmospheric neutrino fluxes are not well understood and are far from being precise [20]. An analysis which is more nearly independent of the atmospheric neutrino flux calculations is highly desirable. In Ref. [4] it is pointed out that the lowest bins of momentum in each plot of Fig. 2.11 should be viewed with some caution. Due to reconstruction and identification efficiencies, we should remove any showering (e–like) events with p < 100 MeV/c and non showering (μ–like) events with p < 300 MeV/c from further analysis.

There are problems with carrying through an analysis of the IMB–3 data using the same method with which we treated Kamiokande data. One is that there are no efficiencies versus momentum given in the literature. Secondly, the first two bins in the μ–like plot are inefficient, namely the 100 - 200 MeV/c bin and the 200 - 300 MeV/c bin. To deal with the second problem, we use the Kamiokande data for those bins; using Fig. 1b of reference [21] we can correct for the geomagnetic effect to go from the Kamiokande to the IMB–3 data sample. In Fig. 2.12a, we show the two inferred points from the Kamiokande data (solid squares) with the IMB–3 μ–like events (open triangles). As a crude check on this procedure we show a quasi–elastic distribution superposed (solid line); the curve suggests that our two estimated points for the 100 - 300 MeV/c region may be on the high side; this caveat should be kept in mind in contemplating the analysis presented below.

Proceeding similarly as in Section 2.5, here we regard the μ–like event sample to be free of any new physics, and we assume that neutrino cross–sections are nearly the same for corresponding ν_μ, ν_e charged current channels. Then we can use the number of μ–like events in each momentum bin, together with the e–like to μ–like ratio 1:2, to predict the number of e–like events to be observed in the absence of new physics. Note that we are not correcting for detection efficiencies, because they are not available. The expected e–like event rates are depicted by solid triangles in Fig.

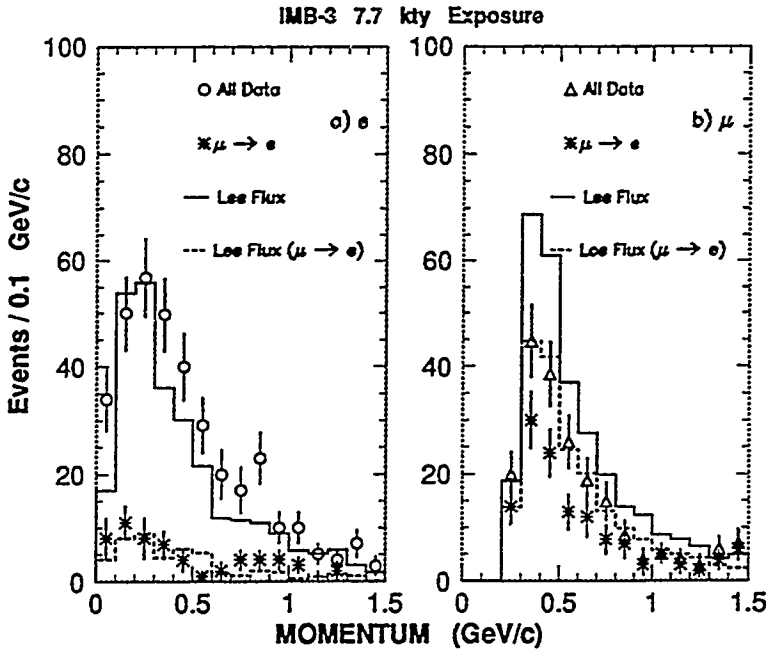

Figure 2.11: The momentum distributions of single–ring a) e–like; b) μ–like events and those with muon decay from IMB–3. The histograms show the Monte Carlo prediction based on Ref. 14.

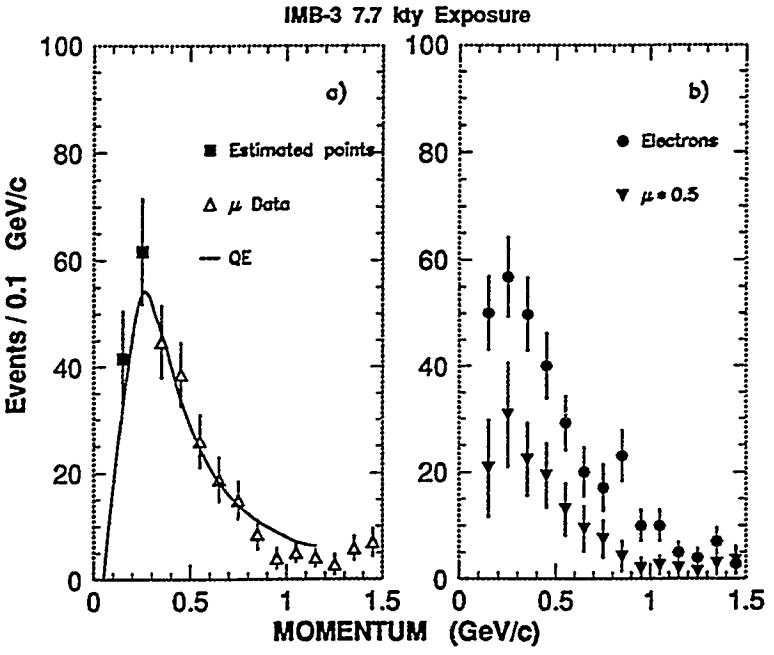

Figure 2.12: a) Expected quasi–elastic distribution for μ–like events. b) Detected e–like events (solid circles); superimposed is the e–like event rate expected from the detected μ–like events (solid triangles).

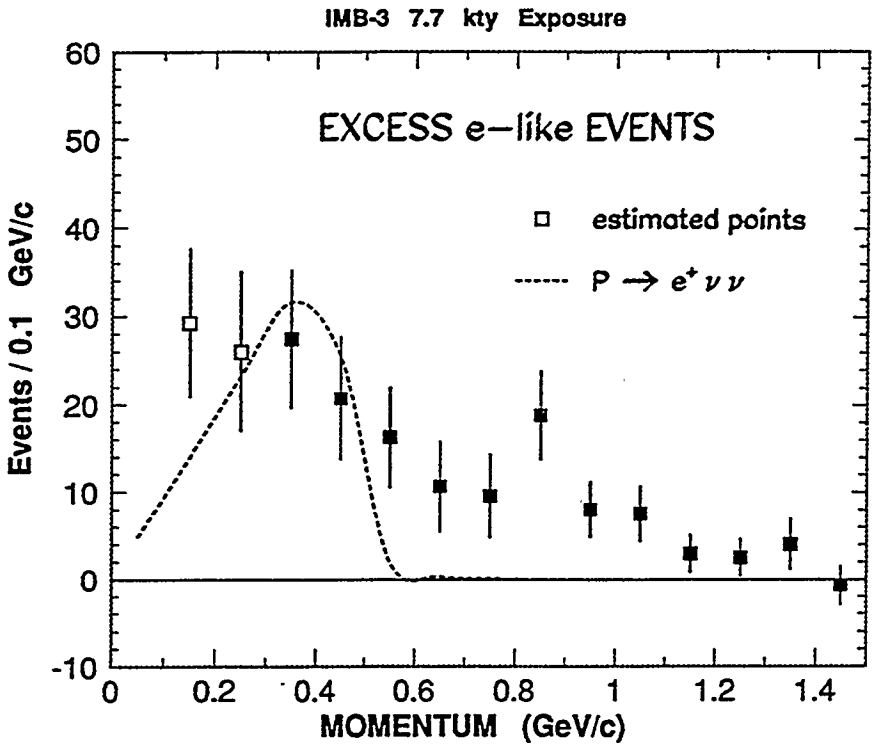

Figure 2.13: Excess e–like events in the 7.7 kty exposure of IMB–3 (close squares). The lowest two bins were inferred from the Kamiokande data sample (open triangles). Superimposed is the phase space momentum distribution for positrons originating from $p \rightarrow e^+\nu\nu$ in water medium (dashed line).

2.12b. We observe in Fig. 2.12b that there is an excess of e–like events above the expectation inferred from the μ–like event distribution. We subtract bin–by–bin the rate expectation for the e–like events which is based on the observed distribution of single ring μ–like events. The excess obtained is then plotted in Fig. 2.13. Superimposed on the histogrammed data is the phase space momentum distribution for positrons originating with decay mode (2.3) in a water medium (dashed line).

In this analysis the IMB–3 data exhibits a trend that is rather different than the one we extracted from the Kamiokande data. Firstly, the excess in Fig. 2.13 is in all momentum intervals. The excess is particularly significant in the momentum interval 200 to 500 MeV/c. However, above 700 MeV/c there also exists an excess. As lepton momentum increases, the excess slowly decreases to a minimum around 1100 MeV/c. In this case (which is different from Section 2.5), the shape of the positron momentum spectrum of proton decay mode (2.3) is observed to describe

Type of event	Kam 7.7 Kty	IMB–3 7.7 Kty
μ–like	234	232
e–like	248	378
Single–ring	482	610
Multi–ring	208	325
Total No. events	690	935
IMB–3 + Kam	**1625**	

Table 2.1: Kamiokande and IMB–3 data sample with a 7.7 kty exposure, where the KAM data has $100 < E_{vis} < 1.33$ MeV and the IMB–3 data has $50 < E_{vis} < 1.5$ MeV.

the excess event distribution only in the 200 to 500 MeV/c, leaving the excess above 700 MeV/c unexplained.

2.8 Event Samples of the Water Cherenkov Experiments

The large water Cherenkov detectors (IMB–3 and Kamiokande) have accumulated 1625 contained atmospheric neutrino interactions. As shown in Table 2.1, 1092 of these events are classified as electron–like (e–like) or muon–like (μ–like). Taken at face value, the comparison between any simulation and observations shows a discrepancy of more than four standard deviations. On the one hand, if the higher neutrino flux calculations [11, 12] prove to be correct, then the discrepancy would imply a deficit of muon neutrino interactions in the detectors; the observed number of electron neutrinos roughly agreeing with expectations. The explanation in terms of neutrino oscillations $\nu_\mu \rightarrow \nu_\tau$, seems to be a plausible explanation for the anomaly. On the other hand, if a lower neutrino flux calculation [14] is the correct one, then we have an excess of electron neutrino events, and the deficit of muon neutrino is

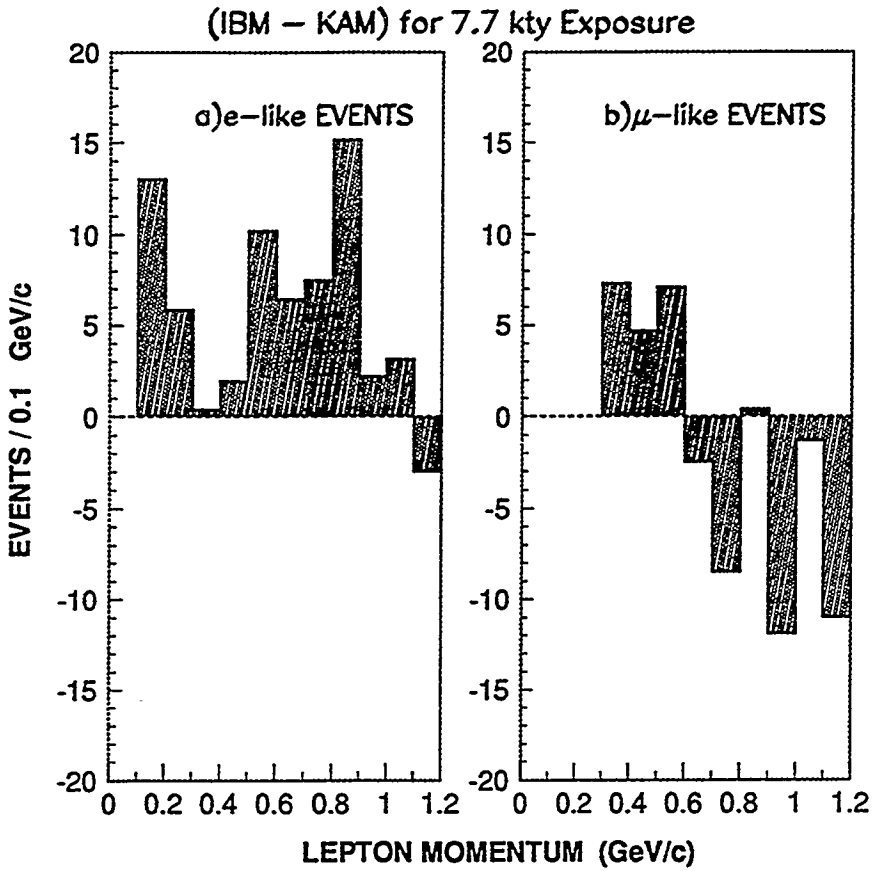

Figure 2.14: Subtracted lepton momentum distribution (IMB3 - Kamiokande); a) e–like events b) μ–like events.

marginal. There are several possible explanations for this scenario. One can still have an oscillation solution, $\nu_\mu \rightarrow \nu_e$, creating an excess of electron neutrino events in the detector. The interpretation in terms of nucleon decay via mode (2.3) remains a viable option.

The proton decay interpretation of the two water Cherenkov data is an intriguing choice. It appears that the Kamiokande data is more compatible with this interpretation than is the IMB–3 data. Using our proton decay scenario we find an excess in the IMB–3 sample over the complete momentum interval 100 - 1200 MeV/c. Such an excess throughout the momentum range can be understood if IMB–3 data suffers from event mis–identification due to the fact that the phototubes they use have poorer resolution then the Kamiokande ones. Indeed the pattern recognition problems must be more difficult in IMB–3 then Kamiokande.

Fig. 2.14a shows the differences between e–like event momentum distributions

of IMB–3 versus Kamiokande data samples. Fig. 2.14b shows the corresponding differences for the μ–like samples. If the water Cherenkov detectors are equivalent, then their data samples should be in rough agreement in all momenta intervals, after allowing for geomagnetic effects. But Figures 2.14a and 2.14b suggest a different story. It seems that the IMB–3 sample in the momenta interval 600 - 1200 MeV/c has a depletion of μ–like events; these events may be mis–classified as e–like events. In any case, there is a level of disagreement between the IMB–3 and Kamiokande contained single–ring samples which affects the kind of analysis presented here.

One may hope that with an exposure of 12 to 16 kiloton years, the trends observed in Fig. 2.2 will continue. Above 700 MeV/c the value of R_ν may tend to unity, meaning no anomaly at all in that momentum range. Additionally if the value of R_ν continues to drop in the interval 300 to 500 MeV/c, an excess of e–like events would be indicated, for which the interpretation could be due to proton decay via mode (2.3). An oscillation solution for this scenario would be hard to sustain, because oscillations should occur at all momenta and not in a particular momentum interval.

Despite our reservations about the IMB–3 data, we combined results from IMB–3 and Kamiokande, by adding the excess of electron like events from each detector. Fig. 2.15 shows the combined e–like events excess, superimposed on the data is the phase space momentum distribution for positrons originating from $p \rightarrow e^+\nu\nu$ (dashed line). We then infer from Fig. 2.15 that 176 ± 26.7 instances of proton decay have occurred in the 15.4 kty combine exposure of IMB–3 and Kamiokande. The lifetime over branching ratio thus implied, $\tau/B \sim 2.8 \times 10^{31}$ years, is compatible with the value which we have obtained using the Kam 7.7 kty data only. This latter lifetime measurement is $\tau/B \sim 3.0 \times 10^{31}$ years.

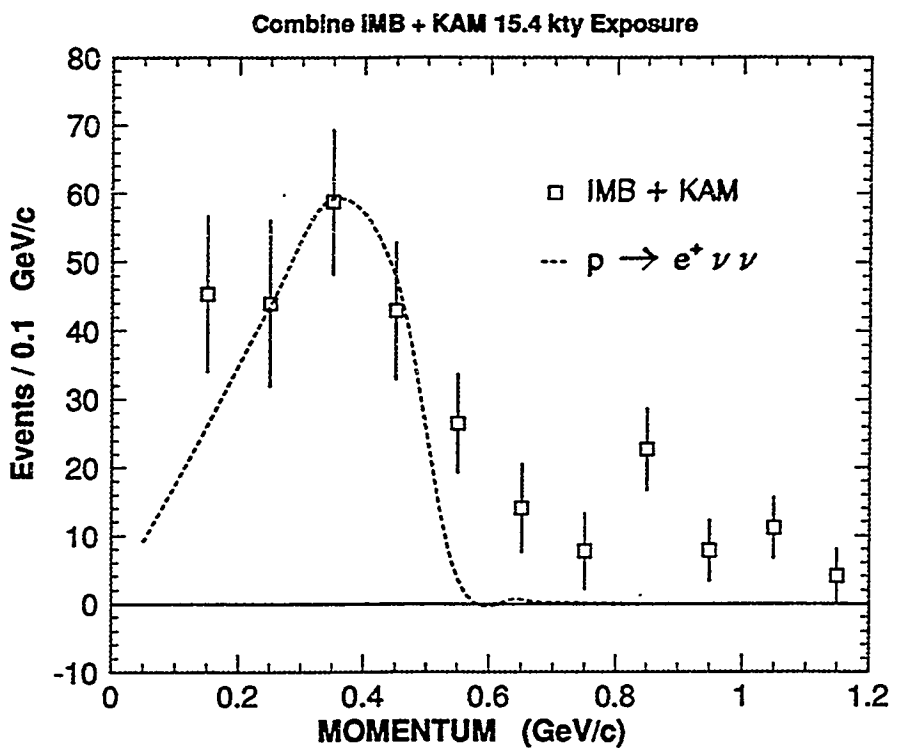

Figure 2.15: Shows the combined e–like excess of the 15.4 kty exposure of IMB–3 plus Kamiokande. Superimposed is the phase space momentum distribution for positrons originating from $p \rightarrow e^+\nu\nu$ in water medium (dashed line).

2.9 Other Observations Pertaining to the Anomaly

There are additional observations and developments which have bearing on the plausibility of proton decay as the origin of the atmospheric neutrino flavor ratio anomaly:

i) In our $p \rightarrow e^+\nu\nu$ scenario, one expects the atmospheric ν flavor ratio anomaly to be difficult to discern in experiments for which event triggering is inefficient for single shower momenta below 500 MeV/c. Thus the relatively high R'_ν values from the planar iron tracking calorimeter experiments NUSEX [6] and Frejus [7] are understandable; they do not constitute evidence against the existence of an anomaly.

ii) The Soudan contained single–track (muon–like) and single–shower (e–like) events contain more information than is presently used for the neutrino flavor ratio.

Most of these events are quasi–elastic reactions:

$$\nu_\ell + \mathrm{N} \rightarrow \ell^- + \mathrm{p} \tag{2.4}$$

and

$$\bar{\nu}_\ell + \mathrm{N} \rightarrow \ell^+ + \mathrm{n}. \tag{2.5}$$

Due to the presence of reaction (2.4), a fraction of each sample can be expected to contain visible recoil protons. Consequently, in the proton decay scenario one expects there to be a dearth of proton recoils observed to accompany single showers in a calorimeter relative to the number observed with single tracks. In the 1.0 kty data of Soudan 2, 22% of single shower events have visible recoil protons whereas 29% of single track events have protons; at present the difference is not statistically significant [8]. This data is discussed in Chapter 6.

iii) For any detector operating at constant fiducial mass, proton decay would generate contained events at a time–independent rate. This is in contrast to interaction rates for atmospheric neutrinos, which may reflect time variations in the fluxes. A modulation of the latter rates is expected to follow the eleven year solar cycle. Since Kamiokande is at low geomagnetic latitude, modulation of the neutrino event rate at this site is small, and so R'_ν will be time–independent in either the proton decay or ν oscillation scenario for the anomaly. Indeed, the Kamiokande R'_ν measurements have shown little deviation from ~ 0.60 even though the data collection spans the solar minimum of 1985–86 and the solar maximum of 1990–91. For sites at high geomagnetic latitude such as IMB–3 and Soudan–2, however, neutrino–induced event rates may vary by 20–30% from solar maximum to minimum [11]. For the proton decay scenario, regular modulation of R'_ν with the solar cycle should occur. With data from a solar minimum to a maximum, (i.e. maximum to minimum in ν flux), an R'_ν

decrease of 8% might be experienced. R'_ν results from IMB–3 (1986–88 versus 1988–91) show this trend, although the magnitude of the decrease is rather large. Results from Soudan–2 exhibit the appropriate reverse trend. The experiment's data taking has run through and away from a solar maximum, and succesive R'_ν values (1989–91 versus 1991–92) have increased [8].

iv) The proton decay scenario requires atmospheric neutrino fluxes which are distinctly lower than the Bartol fluxes [11]. During the past year a reasonable case has been made that, in the regime $0.2 < E_\nu < 1.0$ GeV, the high fluxes of the Bartol calculation are obtained from a more realistic treatment of inclusive pion production than was used in the Bugaev–Naumov calculation [22]. Neutrino fluxes at the Earth's surface necessarily correlate with muon fluxes at high altitude, and it may soon be possible to check the ν flux calculations using precision muon flux measurements. Initial measurements of the muon energy spectrum at altitudes 10–20 km were reported last summer by a Canadian–Italian team [23]. A new calculation of atmospheric ν fluxes has been prepared by D.H. Perkins, which proceeds directly from these most recent measurements of the muon momentum spectra in the stratosphere. The absolute ν fluxes from his calculation agree with the Bartol fluxes to within 15% [24].

v) A new analysis by the Kamiokande collaboration using contained and partially contained multi–GeV events, suggests that R_ν remains anomalously low at high energies [5]. This result, if correct, implies that the ν_μ/ν_e anomaly cannot be predominantly due to a sub–GeV process such as proton decay. We note that with the Kamiokande sub–GeV events, low R'_ν coincides with a distinct dearth of muon–like events as gauged by the Bartol flux. With multi–GeV events of the new analysis, the situation is a bit different. Here, low R'_ν is achieved with a mild dearth of muon–like events together with a more pronounced

excess of e–like events as gauged by interpolation of Bartol [11, 12] to Volkova [25] fluxes. Multi–GeV ν event samples, especially ones which include events partially contained in an underground detector, have not - to date - received the intense experimental scrutiny to which fully–contained, sub–GeV events have been subjected. Systematic uncertainties may involve effects heretofore not fully considered. Given the potential significance of the new Kamiokande results, corroboration is highly desirable.

vi) On the theoretical side, a general class of operators has been proposed which can accomodate a predominant proton decay into the mode $e^+\nu\nu$ [26].

The atmospheric neutrino flavor ratio anomaly continues to tantalize as a plausible harbinger of new physics. We are hopeful that new data from the underground experiments, including Soudan 2, will distinguish among the interpretations in the near future. See Chapter 6 for our revised atmospheric neutrino flavor ratio.

References

[1] W.A. Mann, T. Kafka and W. Leeson, Phys. Lett. **B 291**, 200 (1992).

[2] K.S. Hirata *et al.* (Kamiokande Collaboration), Phys. Lett. **B 205**, 416 (1988); K.S. Hirata *et al.*, Phys. Lett. **B 280**, 146 (1992).

[3] K. Nishikawa (Kamiokande Collaboration), talk presented at the 16^{th} International Conference on Neutrino Physics and Astrophysics, Eilat, Israel, 29 May - 4 June, 1994.

[4] D. Casper *et al.* (IMB Collaboration), Phys. Rev. Lett. **66**, 2561 (1991); R. Becker–Szendy *et al.*, Phys. Rev. **D 46**, 3720 (1992).

[5] Y. Fukuda *et al.* (Kamiokande Collaboration), Phys. Lett. **B 335**, 237 (1994).

[6] M. Aglietta *et al.* (NUSEX), Europhys. Lett. **8**, 293 (1989).

[7] Ch. Berger *et al.* (FREJUS), Phys. Lett. **B 245**, 305 (1990), and **B 227**, 489 (1989).

[8] M. C. Goodman, Nucl. Phys. **B** (Proc. Suppl) **38**, 337 (1995).

[9] W.A. Mann, T. Kafka and W. Leeson, *in*: Proceeding of the DPF92 Meeting, Fermilab, 10–14 November 1992; p. 1330.

[10] W.A. Mann, T. Kafka and W. Leeson, submitted to the DPF94 Meeting, University of New Mexico, Alburquerque, NM, 2–6 August 1994; Soudan 2 Report PDK–590, July 1994.

[11] T. K. Gaisser, T. Stanev, G. Barr, Phys. Rev. **D 38**, 85 (1988).

[12] G. Barr, T. K. Gaisser, T. Stanev, Phys. Rev. **D 39**, 3532 (1989).

[13] M. Honda, K. Kasahara, K. Hidaka and S. Midorikawa, Phys. Lett. **B 248**, 193 (1990).

[14] E. V. Bugaev and V. A. Naumov, Phys. Lett. **B 232**, 391 (1989).

[15] A. Bodek and J. L. Ritchie, Phys. Rev. **D 23**, 1070 (1981).

[16] S. Seidel *et al.*, Phys. Rev. Lett. **61**, 2522 (1988).

[17] R. S. Hirata *et al.*, Phys. Lett. **B 220**, 308 (1989).

[18] R. Merenyi *et al.*, Phys. Rev. **D 45**, 743 (1992).

[19] H. Lee and Y. S. Koh, Nuovo Cim. **105 B**, 883 (1990).

[20] D. H. Perkins, Nucl. Phys. **B 393**, 3 (1993).

[21] E. W. Beier et. al. (IMB Collaboration), Phys. Lett. **B 283**, 446 (1992).

[22] T. K. Gaisser,"*Fluxes of ν_μ and ν_e in the atmosphere: Is there an anomaly?*", Proceedings of the 3rd Int. Workshop on Theoretical and Phenomenological Aspects of Underground Physics TAUP93, Gran Sasso, Italy, Sept. 1993, Nucl. Phys. **B 35**, 209 (1994).

[23] M. Circella *et al.*, *in*: Proceedings of the 23rd International Cosmic Ray Conference, Calgary, July 1993; Vol. 4, p. 503.

[24] D. H. Perkins, "*A new calculation of atmospheric neutrino fluxes*", preprint OUNP–93–32, Oxford Univ. (1993); D. H. Perkins, Astropart. Phys. **2**, 249 (1994).

[25] L. V. Volkova, Sov. J. Nucl. Phys. **31**, 784 (1980).

[26] U. Sarkar and P. O'Donnell, Phys. Lett. **B 316**, 721 (1993).

Chapter 3

The Soudan 2 Detector and Event Selection

3.1 Overview

The heart of the Soudan 2 detector system is a massive tracking calorimeter designed to search for nucleon decay. This Central Detector (see Fig. 3.1) is complemented by the Tufts–designed and –built active cavern–liner proportional–tube Veto Shield. The detector is also being used for studies pertaining to the origin and composition of cosmic rays using single and multiple muons, the neutrino flavor content of the atmospheric neutrino flux, and the existence of magnetic monopoles and other slow, heavily ionizing particles. The detector is located in an inactive iron mine at the Soudan Underground Mine State Park in Soudan, Minnesota. Soudan 2 is a second generation experiment at this location – the 35–ton Soudan 1 was operated at a depth of 1800 m of water equivalent (or 600 m from the surface) between 1981 and 1983. Soudan 2 is located at the depth of 2100 meters–water–equivalent (700 meters from the surface) on the 27^{th} level of the mine.

The purpose of going deep underground is of course to minimize the cosmic ray background to the experiment; at this depth the vertical cosmic ray muon flux is attenuated by a factor of $\sim 10^5$. Construction of a dedicated cavern of size $14 \times 72 \times 11$ m^3 began in 1985. Assembly of the detector started in 1986; the first half of the Central Detector was completed in the summer of 1990 and the detector was operated at the full 963 metric tons in early November 1993. Since that time the experiment has undergone a number of upgrades for both the Central Detector and for the Veto Shield.

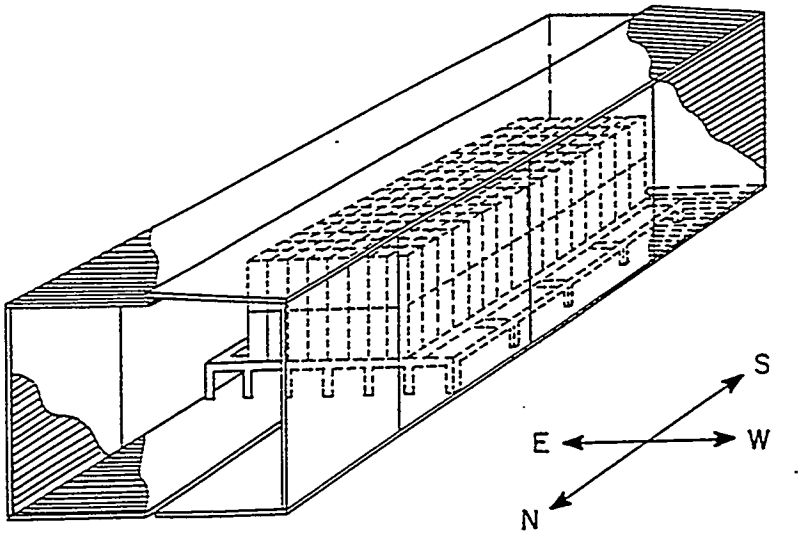

Figure 3.1: Plane view of the Soudan 2 detector.

The Soudan 2 collaboration consists of approximately 70 scientists and 20 technicians (see Appendix A). Teams from each of five major institutions have worked continually on the experiment since its inception. Each of the institutions took on specific responsibilities for the construction and for operation of the detector. The University of Minnesota was responsible for preparation of the mine site, for on-line software, and for fabrication of the drift tube "bandolier" component of the calorimeter modules; Argonne National Laboratory with Rutherford Appleton Laboratory were responsible for module construction; Tufts University was responsible for construction and deployment of the active shield; and Oxford University was responsible for calorimeter components, the detector gas system, and for the experiment's database. The experiment is funded by the United States Department of Energy, the University of Minnesota and the Science and Engineering Research Council in the United Kingdom.

The Soudan 2 Central Detector has superior capabilities in event imaging compared to earlier proton decay search detectors. It is designed to have excellent

background rejection capabilities in complex nucleon decay modes. In particular, it has a good chance of improving and confirming the measurement of atmospheric neutrino interactions. With the excellent spatial resolution and measurement of dE/dx in Soudan 2, particle identification is possible based upon ionization, directionality, topology and muon decay signatures. Soudan 2 can also detect charged particles that are travelling below the Cherenkov threshold in water detectors, such as final state protons produced in neutrino interactions.

The Sections below give information on the Soudan 2 detector design and performance. The Central Detector and Veto Shield are described in Sections 3.2 and 3.3, respectively. Section 3.4 deals with Soudan 2 triggering, Section 3.5 details the offline software, Section 3.6 depicts the time correlation between the Veto Shield and the Central Detector, and basic data processing is described in Sections 3.7 and 3.8. Finally, a brief description of the Soudan 2 Monte Carlo simulation is given in Section 3.9.

3.2 The Central Detector

A brief description of the Central Detector is given here. Details of its design and performance can be found in references [1, 2, 3]. The Soudan 2 calorimeter is a fine grained tracking calorimeter which is modular in design. The modular design of the Soudan 2 Central Detector offers important advantages; it allows the detector to be operated as it is being assembled and permits malfunctioning modules to be replaced with minimal disruption (see Fig. 3.1). Each module has dimensions of 1.0 m $\times$ 1.1 m $\times$ 2.7 m, determined by the size of the Soudan mine elevator cage. The calorimeter modules consist of corrugated iron sheets instrumented with drift tubes, filled with gas and read out by proportional wireplanes. The iron plates provide the source of protons and bound neutrons being monitored for spontaneous decays and also constitute the calorimeter absorber. The main detector consists of 224 modules

arranged into a rectangular block; 8 modules are arranged into structures called "half–walls" which are four modules across and stacked two modules high. Each module weighs 4.3 tons; the detector's 224 modules constitute a total effective mass of 963 tons.

A disadvantage of this design is the presence of inactive regions between modules. One can distinguish four different types of such regions, generally referred to as "cracks". There are cracks between adjacent modules in the same half–wall ($\sim$ 10 cm wide). Secondly, there are cracks between top and bottom modules ($\sim$ 12 cm wide). Thirdly, there are cracks between east and west side adjacent modules ($\sim$ 10 cm wide). Finally, there are cracks between adjacent modules in different half–walls on the same side of the calorimeter ($\sim$ 13 cm wide). The total area of the surface cracks constitute $\sim$ 10% of the total calorimeter surface area [4, 2]. Particles entering through these cracks are sometimes hard to identify.

A schematic drawing of a calorimeter module is shown in Fig. 3.2. A module contains 241 layers of 1.6 millimeter thick corrugated steel sheets of size 1 meter $\times$ 1 meter. The corrugations support 1.5 centimeter diameter Hytrel drift tubes. The drift tubes are sandwiched between mylar sheets, which carry copper high voltage electrodes spaced so as to yield a uniform electric field along the axes of the Hytrel tubes. Additional polystyrene insulation is placed between the mylar and the steel to prevent high voltage breakdown. All drift tubes are filled with a 85% argon and 15% carbon dioxide gas mixture.

When a charged particle traverses the detector (see Fig. 3.3), it ionizes gas molecules within the individual drift tubes. The liberated electrons drift towards a wire plane consisting of vertical anode wires with high voltage ($\sim$ 2150 volts) and horizontal cathode pads held at ground potential (see Fig. 3.4). Each module has two wire planes on opposite sides facing the ends of the drift tube stack. The drift ionization exits the tubes whereupon it is collected on the anode wires and imaged on the cathode pads. The signals on the anodes and cathodes can be matched

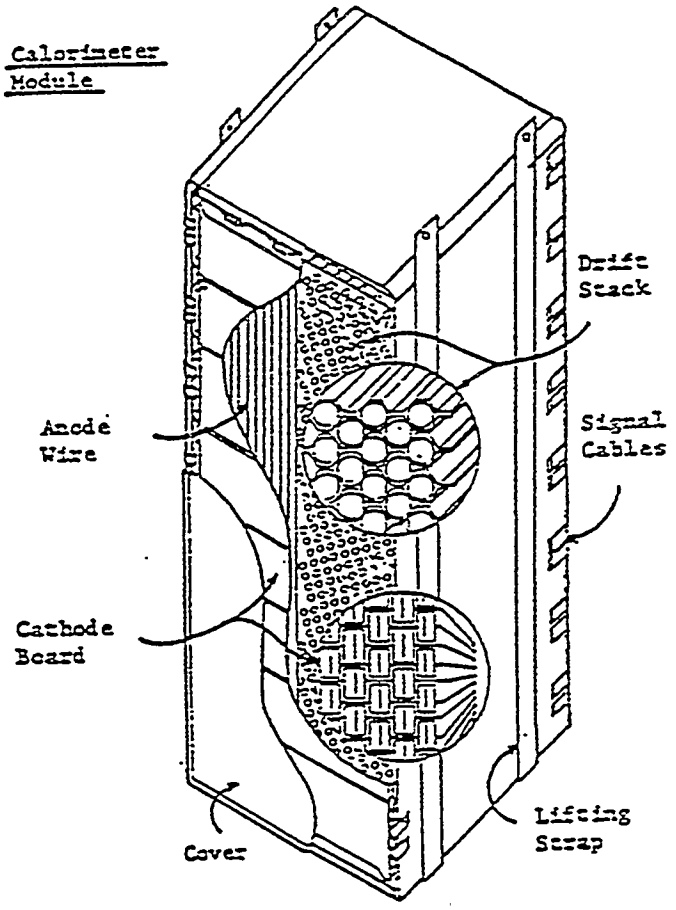

Figure 3.2: A view of a tracking calorimeter module.

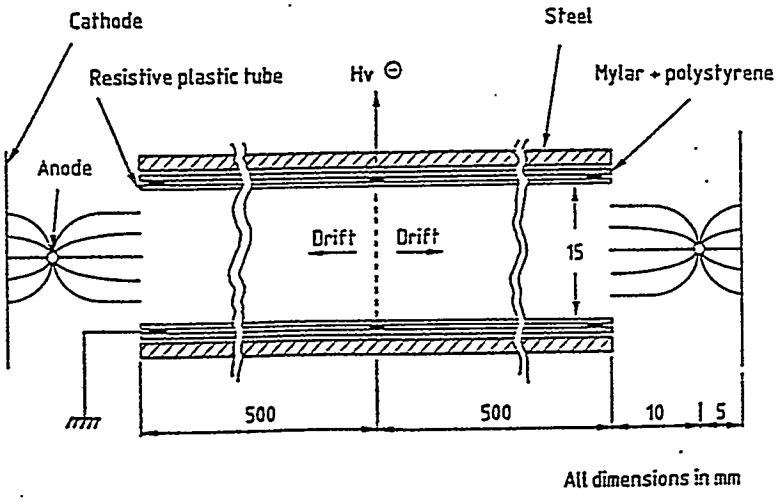

Figure 3.3: Cutaway longitudinal view of a drift tube.

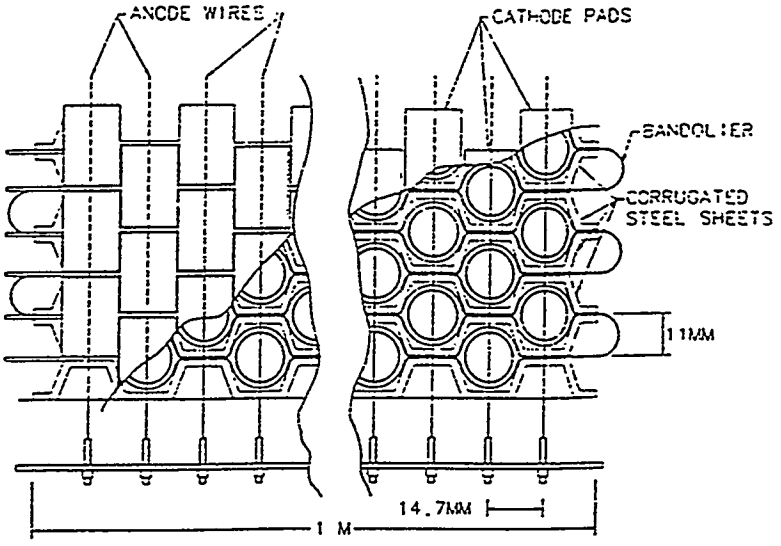

Figure 3.4: A wire plane of the Soudan 2 tracking calorimeter module.

up to determine which tube the ionization occurred in, providing the X and Y coordinates of the hit tube. Furthermore, the data acquisition electronics records the arrival times of the signals, so that the drift time can be used to obtain the Z coordinate of the hit within the drift tube. The maximum drift distance along the Z direction is 50 centimeters. The drift velocity of the electrons is typically 0.6 cm/μs. The calorimeter's spatial resolution is $\sim$ 1 centimeter for each of the three spatial coordinates. The Central Detector provides the trigger for occurrence of charged particles.

3.3 The Veto Shield

The walls, floor, and ceiling of the cavern are completely covered by the Veto Shield. The active Veto Shield is an array of more than 1600 proportional tube manifolds. These manifolds are arranged to cover all of the 4π solid angle (an area of $\sim$ 1700 m^2) of the detector, the necessary exception being the area of the Central Detector support columns. The active Veto Shield is designed to indicate the

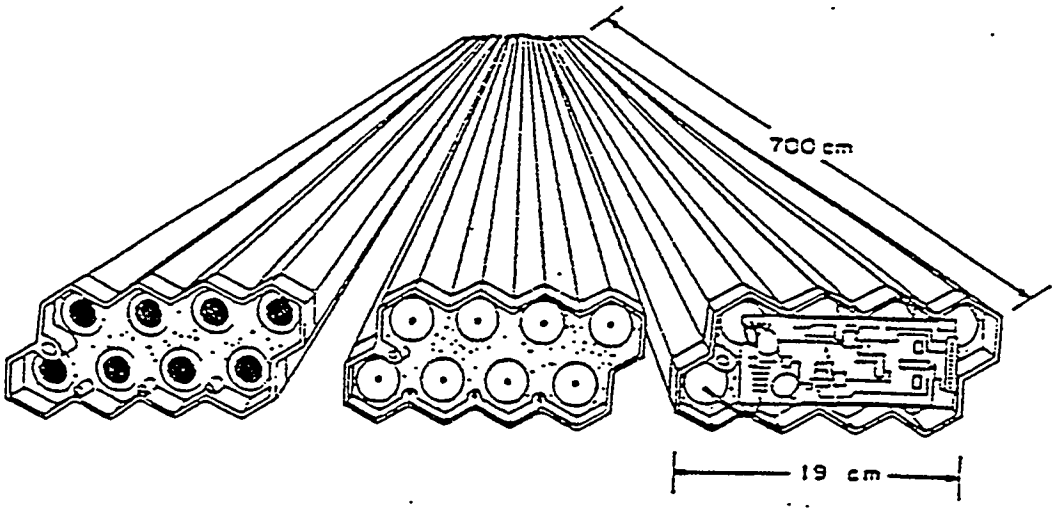

Figure 3.5: View of Veto Shield proportional tube manifolds.

presence of through–going muons in or near the calorimeter and to detect charged products from muon interactions behind the cavern walls which may send only neutral particles into the main detector.

Each manifold consists of eight hexagonal proportional chamber cells arranged in two four–cell layers (see Fig. 3.5). The cell size and shape were chosen to minimize drift times and to provide time resolution comparable to the drift time resolution of the main detector. A sense wire of 60 μm diameter resistive nichrome is strung along the axis of each cell. For more details on construction, operation, and quality control of this manifold, see Ref. [5].

All four top sense wires of the manifold are connected in parallel to be read out on a single channel of electronics, as are the four bottom cell wires. All wires are kept at positive 2300 volts and all the manifolds are filled with a mixture of 95% Ar and 5% CO_2. Output signals from the manifold are fed into preamplifiers mounted on the ends of each manifold and then into the readout electronics. The readout system of the Veto Shield is separate from the Central Detector readout system (see

Ref. [6] for description of the Digital Readout Modules (DRM) designed by Prof. W. Oliver of Tufts). The pulses from each preamplifier are fed into a discriminator, and the discriminator output for each channel is saved in a 128 by 1–bit RAM every 1 μs. When the Veto Shield readout system receives a trigger from the Central Detector, a 128 μs history of the activity on each channel of the shield is available for readout. For each Central Detector trigger, a VAX computer reads out and stores the data from both the Central Detector and the Veto Shield. Although the capability for using the Veto Shield in the trigger exists, it is not being utilized.

The whole Veto Shield is read out by five CAMAC crates, each with a capacity of 15 slots for our single width Digital Readout Modules. Each DRM provides 64 channels to service 32 Veto Shield manifolds. In this form, a Crate/Slot/Channel identifies a Veto Shield hit.

A long–term goal for the Veto Shield is the deployment of more proportional chambers in a criss–cross pattern in the ceiling and floor (and eventually on all the cavern walls). The objective is to obtain a Veto Shield that can stand alone as a muon detector. For this purpose, proportional tubes which were acquired from the defunct Harvard–Purdue–Wisconsin (HPW) proton decay experiment have been deployed in the ceiling and the floor of the cavern. The idea is to measure all three spatial coordinates for through–going muons, thereby improving our angular resolution for muon astronomy, while also enabling muon bundle multiplicity to be determined more easily. Additional information on HPW performance can be found in references [7] and [8].

Candidate contained events are sorted according to hit patterns observed in the Veto Shield. Veto Shield signals are available in four forms for the contained event analysis. Each Veto Shield proportional tube has two layers. Sets of adjacent manifolds of the same length constitute Veto Shield "panels", each with a given number. Within a panel, each manifold is assigned a "tube number". Of the two layers, the layer which is facing the Central Detector is called the "in–layer", while

the other one is the "out–layer". In order to maintain simplicity in programming for data processing and analysis, every shield panel was assigned to a "superpanel", the six superpanels being the ceiling, the floor, and each of the four walls. If ionization lights up any one of the four sense wires within one layer and all neighboring layers are quiescent, the pattern is called a "single hit" (*Single*). On the other hand, if cells from two neighboring layers (in the same tube or in neighboring tubes) light up and the cells form an in–out combination, the configuration is called a "coincident two–layer hit" (*CTL hit*). If a configuration of two or more overlapping hits occurs in adjacent tube–layers, having no spatial gaps, the configuration is called a coincident "adjacent–hit group" (*ADJ hit*). Finally, a configuration of any number of hits (Single or ADJ) which occur in any pair of overlapping panels within a specified time window [1] is called an "overlap" (*OVERLAP*). The singles are generally not used in the analysis of this thesis. The ADJ and OVERLAP hit configurations are used by the contained event software filters and the physicist scanners to discard events in the calorimeter that are associated with cosmic ray interactions occurring within the cavern walls.

3.4 The Triggering

Full details of the trigger system can be found in references [2] and [9]. A brief description of the triggering of an event is given below. As described previously, traversal of charged particles through drift tubes of the Central Detector results in ionization segments whose drift electrons create analog signals on anode wires and cathode strips. The analog signals are amplified and digitized. The leading edge of a pulse above the Central Detector threshold is called an "edge". The trigger system requires a minimum number of edges to trigger an event. Specifically, seven edges from any sixteen adjacent anodes OR eight edges from any sixteen adjacent

[1] –1 μs to +1 μs for Tufts/Tufts overlaps, –1 μs to +4 μs for HPW/Tufts overlaps.

cathodes (denoted as 7 A OR 8 C) within a 72 μs time window are required to trigger an event for subsequent readout. All edges are separated by at least 0.6 μs [10].

The hardware trigger circuit reduces to a manageable level the amount of data read out by the data acquisition computer. The hardware trigger rejects most of the low energy ionization clusters from local radioactivity, which give a random rate $\sim$ 5–50 pulses/anode/second. Ionization from radioactivity is believed to be predominantly Compton electrons scattered by photons from the cavern rock and its concrete cover, and also from calorimeter material, such as the G–10 boards on which some of the wireplanes were fabricated. The recoiling electrons move through the gas of the calorimeter wireplane producing small, localized regions of ionization called "blobs". Compton electrons created near the wireplane have a travel time to the nearest anode wire or cathode strip of less than 200 ns. The pulses which compose the blobs traverse only a few centimeters in the drift direction, and all start at nearly the same sampling time. On the other hand, data from particle tracks of interest consist of pulse patterns which are spread out in sampling time due to their spread along the drift tubes. The hardware trigger was designed to reject blobs by exploiting their time–coincident nature. The trigger demands not only minimum pulse multiplicities but also that the individual pulses occur at different times. Usually a blob will give only one edge.

3.5 Offline Software

Every event that satisfies the Central Detector triggering requirements is written to disk for further processing. A collection of events representing a pre–determined amount of data is called a 'run' and is assigned a five–digit identification number. All of the basic off–line data processing is performed by the Soudan Off–line Analysis Program (SOAP) at the Soudan site. As configured for this purpose, SOAP

reconstructs each event and identifies candidate muon tracks (stopping or through–going, single or multiple), candidate contained and partially–contained events, and candidate magnetic monopole tracks. Events of different types are separated into different data files.

In SOAP, Soudan data is stored in a one–dimensional array organized into data 'banks' by the BOS dynamic memory management system. SOAP represents an overall framework within which individual tasks are performed by software modules called 'processors'. Processors performing basic functions include PGMINI to initialize the program, and PGMEND which is called at the end of the computer job. The calorimeter data is handled by CREPLR which unpacks the raw data, SOFTPL which generates clean 'software' pulses, PMT which matches anode and cathode pulses to find the XY projection of a Central Detector hit, RUFTØ which estimates TØ, and SEARCH which finds straight lines in the XZ and YZ projections.

The PMT processor matches anode and cathode pulses to make a 3–D pulse, based on pulse start times and pulse shapes. This process is done automatically by the online software, however a physicist scanner has the option to modify the pulse matches if he so decides.

SPLASH handles the veto shield data, unpacks the raw shield data, provides information on hardware performance to identify malfunctioning shield elements during data acquisition, translates the Veto Shield information from 'Crate–Slot–Channel' into 'Panel–Tube–Layer', and performs pattern recognition to identify groups of hits that occur within a narrow time window and are contiguous in space. SPLASH also carries out geometric reconstruction, finding the position in space for all identified adjacent groups, or for any shield hits needed for the analysis.

Every SOAP execution can be tailored, using commands in an ASCII text input stream, to select processors to specify input and output files, and to select events. The SOAP routines are organized into libraries, updated and released to the collaboration about twice a year. Release–13 through Release–18 SOAP was used for

processing our 1991–1993 data sample.

3.6 Veto Shields vs. Central Detector Time Correlation

The Central Detector vs. Veto Shield correlation in time can be described as follows: A charged particle deposits ionization in a Veto Shield proportional tube; a digital pulse results which is immediately inserted into a 128 μs long FIFO (First In, First Out) buffer. Next, the particle, as it passes through the Central Detector, deposits ionization that drifts for up to 80 μs to a wire plane. When the subsequent voltage drop is recognized, a trigger signal is formed, transmitted to all Veto Shield CAMAC crates, and the information on the shield activity within the last 128 μs is read out along with information on the Central Detector [2]. The Veto Shield 1 μs 'time slots' are numbered from 1 to 128, with 128 μs being closest to the trigger time. The task is now to find the time of passage of the track through the Central Detector, T_0, in terms of Veto Shield time slots, T_{CD}. In the Central Detector, T_0 is measured in 'clock ticks', with 1 tick equal to 200 ns. If T_{trig} (= 512 ticks) is the time when the trigger is sent to the shield, we find [6]:

$$T_{CD} = (T_0 - T_{trig}) \times 0.2 + t_w + t_d \tag{3.1}$$

where t_w (=128 μs) is the length of the shield time window, and t_d (=1.5 μs) is the delay time between the sending of the Central Detector trigger to the Veto Shield and the onset of readout of the shield data. The latter offset constant has been determined empirically by scanning muon events. The Central Detector T_0 is obtained by taking the average of the anode time T_0^A and the cathode time T_0^C under the following two constraints: (1) the difference between T_0^A and T_0^C should not exceed 100 ticks (20 μs), and (2) the errors on the T_0^A and T_0^C must be less than 30 ticks (6 μs) [11].

Fig. 3.6 shows the distribution of the time difference, $T_{CD} - T_{VS}$, in 1 μs bins. The distribution peaks at about 1 μs and is 3 μs wide.

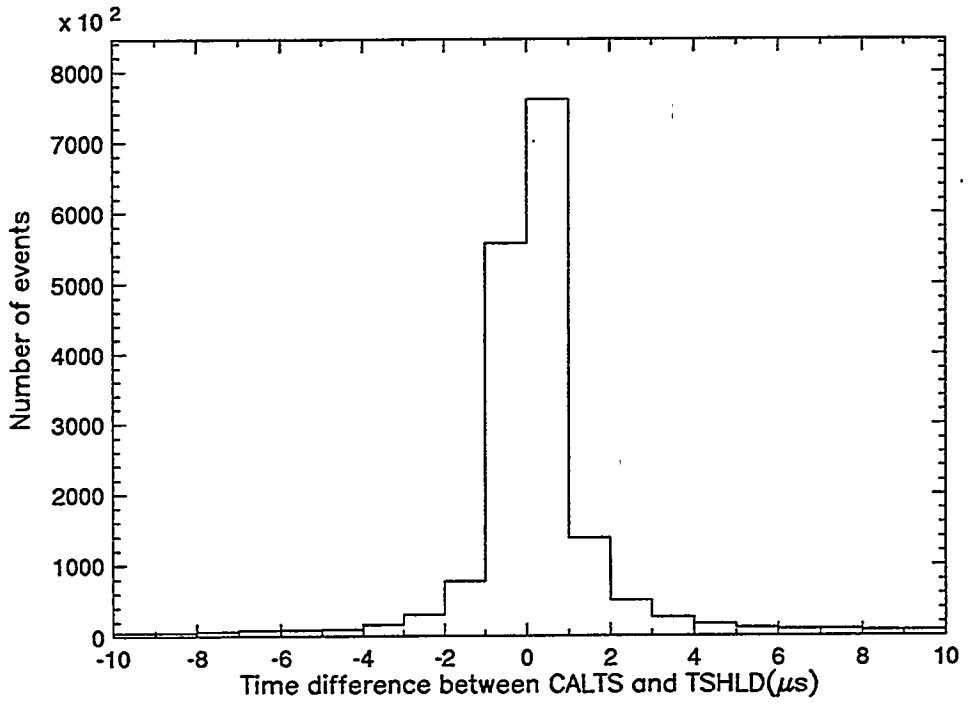

Figure 3.6: The distribution of the time difference between calculated time slot (CALTS) and shield time slot (TSHLD) ($T_{CD} - T_{VS}$).

3.7 Extraction of Contained Events from Raw Trigger Data

In order to isolate contained neutrino events and nucleon decay events from background in the Soudan 2 detector, a sequence of hardware and software filters followed by physicist scans is applied to the raw data. There are five general reduction steps in the Soudan 2 data [9]: *i)* the detector hardware trigger, *ii)* the "PASS1" software filter, *iii)* the "PASS3" software filter (actually two stages, using two different filter codes), *iv)* the physicist FILTER scan, and *v)* the physicist BRONZE scan.

Following the hardware trigger, a succession of three software filters is applied to the data offline, using the computer cluster at the Soudan mine. The contained event filtering is performed within the general software SOAP (Soudan Offline Analysis Program); it is designed to be conservative in order to have the highest possible efficiency for detecting neutrino interactions and nucleon decay events. SOAP consists of a sequence of separate self–contained processors that the user can select or de–select for any particular job. This program enables preliminary event classification

to be made, such as single cosmic ray muons, multiple cosmic ray muons, monopole candidates, stopping muons, and contained events. A first pass software event filter called "PASS1" is applied to all data which satisfy the hardware trigger. Its primary goal is to reject events that are not contained. It actually consists of two independent filters, named the HIT and TRACK filter, respectively. The first filter operates on clusters of pulses, whereas the second operates on tracks. Most events that are cut at this "PASS1" reduction stage are through–going cosmic ray muons, small events made up of random ionization, and events originating outside of the containment volume. The number of events passing the "PASS1" filter is too large to be scanned, and so data are processed by a "PASS3" filter with tighter triggering and containment rules, further reducing the number of events. Approximately 30,000 events per half–kiloton–year of detector live–time survive the software selections. The event output from the software filters is then scanned by Soudan 2 physicists, in order to reject any remaining non–contained events and other backgrounds to the neutrino and proton decay events.

The Soudan 2 tracking calorimeter provides event images whose level of detail is heretofore unprecedented in underground experiments. Physicists need to "train their eye" for these images. This is done by using Monte Carlo simulations of atmospheric neutrino interactions within Soudan modules, and by interactions recorded using a standard calorimeter module exposed to a charged particle test beam at Rutherford Laboratory (ISIS test beam). This training enables bubble chamber style particle discrimination, wherein a physicist can readily discern *tracks* (of charged pions, muons and protons) from *showers* (induced by electrons, positrons and photons).

The first stage of physicist scanning is the so–called "Filter Scan". Here scanning rejection rules are applied to eliminate noise–initiated events, such as wireplane breakdowns (snakes), discharges in a high gain region of a wireplane with non–uniform response (breakdown), and Compton electrons from behind the wireplane

which are attracted to the anode wires and which pass through small gaps existing between cathode boards of some modules (zens). Also eliminated are events which originate along surfaces between modules (crack events), and incoming tracks. All events that are not rejected by the scanners due to the Filter Scan rules are transferred to a new file for further analysis. The event sample which survives the Filter Scan typically contains 2000 events per half–kiloton year; the latter events are then scanned–by a "contained event committee" with a new set of rules. This committee is composed of two independent groups of physicists (one group in the past). In this so called "Bronze Scan", the detector performance is checked on an event–by–event basis. Events are examined for proximity to dead or inefficient regions which could cause events to appear contained to scanners.

Events that pass the Bronze Scan are contained (having no hits closer than 20 centimeters to the outside of the main detector), however most are accompanied by coincident hits in the Veto Shield. Then, based upon the number of Veto Shield hits (actually, ADJ hit groups), the committee classifies the data into three groups, called Bronze, Silver and Gold files. In the Gold file are all contained events with no time–coincident hits in the Veto Shield. Similarly, all events with only one hit in the shield that is in time with the main detector trigger time $T\emptyset$, independently of whether or not the energy flow of the event is aligned with the shield hit, are catalogued as Silver events. The remainder of the contained events with two or more hits in the shield in time with $T\emptyset$ are classified as Bronze events.

3.8 Extraction of Partially Contained Events from Raw Trigger Data

In this Section we review the process of extracting partially contained events (PCE) from the Soudan 2 data. In order to isolate PCE events, a sequence of hardware and software filters followed by physicist scans are applied to the raw

data, in a procedure that is completely different from the procedure used to select CEVs and described in the previous Section.

3.8.1 Data Processing for PCE Candidates

All event selections for our initial data sample were based on the number of adjacent–hit groups in the Veto Shield. For each Soudan 2 event, a 'Veto Shield Type', VS–type, is determined. First, every 1 μs time slot is considered separately. Events with no adjacent–hit groups have a VS–type of 0 (zero) in that time slot. The VS–type is 1 if all adjacent–hit groups occur in the same superpanel, a topology that is regarded to be a 'candidate partially contained event'. If an event has exactly two adjacent–hit groups in different superpanels, the event is considered a 'candidate single through–going muon'. If both of these superpanels are vertical, it is 'candidate horizontal muon' and its VS–type is set to 2. A VS–type of 3 flags a hit topology with three or more adjacent–hit groups located in at least two super panels, considered to be 'candidate multiple muon events'. After the veto–shield type is determined for every time slot, the largest of all VS–types for the individual time slots is assigned to be the VS–type of the event.

The actual event selection is done by the SEARCH and SMU (Stopping MUon) processors incorporating several contained event algorithms. We developed software and scanning procedures which identify candidate neutrino–induced interactions which are partially contained within the fiducial volume of the Central Detector. Our approach is based on the Veto Shield, but also relies upon track reconstruction within the Central Detector (for this software trigger level). Within the SMU processor we require that candidate partially contained events have a VS–type of 0 or 1. The SMU processor generates a logical OR of all the algorithms to select the candidate partially contained events for inclusion in an 'SMU file'.

A data set obtained from April 24 of 1991 to June 3 of 1993, has been used for the analysis of PCE events presented here. Since 1991 the output of the SMU

Event Selection	
Total number of triggers	22,470,616
SMU software trigger	166,957
Total Number of Runs	12,896
Run #'s (bgn-end)	26978–44725
Time period	4/24/91 to 6/3/93
Total running time (hrs)	14,472.6
Total live time (hrs)	13,770.0
Exposure in kty	1.0

Table 3.1: Run statistics for the PCE data sample.

processor has been created during the routine processing at the Soudan 2 site, and no further selection outside the SMU files was needed at Tufts. The total live time for the 1991–1993 data sample of this study is 13,770 hours. A total of 166,957 SMU events were obtained from our data sample, corresponding to 12,896 runs. The event counts are summarized in Table 3.1.

Information essential for further analysis is stored in a Data Summary Tape (DST) binary format. Our DST record is a one–dimensional vector array, in which the data for each event is organized into "blocks" which store the information indicated below:

1. Run information such as run number, event number, date and time for each event.
2. Selected output from the SEARCH processor, including the direction of each track in the Central Detector and the coordinates of exiting points in the Central Detector as well as in the shield.
3. Veto Shield information concerning adjacent hit groups such as the number of groups, the time slot, and the spatial coordinates for each group.

4. Veto Shield information summarizing the single hits.

5. Information about the track extracted from the 'SFIL' bank.

The DST format is described in Appendix B.

3.8.2 PCE Data Selection

In order to reduce the SMU file (161,168 events) to a manageable level, a succession of data selections were imposed on the data sample. All candidate PCE events selected by the Veto Shield software trigger were scrutinized for the presence of through–going muon tracks in the central detector as determined by the SEARCH processor.

Our first selection ("Cut1") eliminated all shield VSTYPE = 2 or 3 events, which correspond for the most part to multiple muons and to wall–to–wall muons. This cut reduced our data sample by ~37%. The remaining events (105,421) were then scrutinized for the presence of single track events. We removed all single track events which had the SFIL bank track classification "downward–going–stopping muon". The survival rate through this second data cut ('Cut2') was only 10.3%. Thus the data sample was reduced to 17,152 events. Table 3.2 summarizes all the computer cuts implemented for this analysis.

The next cut is designed to eliminate all events which have in–time shield hits in the ceiling, presumed to be downgoing muons. The Veto Shield data were examined for correlation with Central Detector tracks, both in time and in space. In our analysis, we consider a Central Detector track to be correlated in time with a Veto Shield hit configuration, if the time difference between the leading–edge time slot for any adjacent–hit group and T_{CD} (Eq. (3.1)) is less than 10 μs. Events having a Central Detector track with ADJ hits in the ceiling occurring within 10 μs of T_{CD} are eliminated. This constitutes our third data selection ('Cut3') and it reduces our data sample to 14,788 events.

Data Selections						
	Phase I		**Phase II**		**Total**	
Data in time	4/91 to 7/92		7/92 to 6/93		4/91 to 6/93	
Exposure (ton–year)	579		472		1000	
SMU software trigger	101,879		65,078		161,168	
Total Number of Runs	6,730		6,166		12,896	
Run #'s (bgn-end)	26978–37009		36900–44725		26978–44725	
	Data	Surv.	Data	Surv.	Data	Surv.
Computer cuts:						
Cut1	64,096	62.9%	41,325	63.5%	105,421	63.1%
Cut2	6,721	6.6%	10,431	16.0%	17,152	10.3%
Cut3	6,003	5.9%	8,785	13.5%	14,788	8.9%
Cut4	5,439	5.3%	7,987	12.3%	13,426	8.0%
Events to be scanned:	5,439		7,987		13,426	

Table 3.2: Data through–put statistics for the PCE data sample.

In our final data selection ('Cut4'), we eliminated events having ADJ groups within 3 μs of T_{CD}, provided these occurred in two or more different wall or floor panels. This final cut reduced our data to 13,426 events, corresponding to 8% of the initial sample.

3.8.3 PCE Scanning

The event sample which survived the computer cuts contained 13,426 events in one kiloton year. The latter events were then scanned by a "committee" composed of T. Mann, T. Kafka and W. Leeson. In this so–called "PCE scan" the selected data sample was divided into two different data sets, indicated in Table 3.2 as Phase I and Phase II respectively. These two data sets were scanned independently by the author and by Prof. Mann to reject non–partially contained events and noise

events. Two other physicists (T. Kafka and D. Wall) also scanned portions of these data sets to familiarize themselves with the operation of the software filters and the detector.

Phase I was a learning stage; the scan rules used to reject events evolved significantly as scanners became more experienced. For Phase II scanning, the rejection rules were applied consistently; each event was either rejected because it belonged in a well defined background category or was retained as a partially contained event candidate. The background categories were as follows:

1. Through–going muons: These are wall–to–wall single muons for which shield hits in one or both walls were absent.
2. Down–stopping muons: Usually these are single muons which enter through the side of the main detector through a crack and have no shield hit associated with the event.
3. Noise–initiated events: Snakes, Breakdowns, Zens (see Section 3.7).
4. Rock events: These events typically have one exiting track but with many associated shield hits.

Most events rejected at this stage ($\sim$ 79%) were events that appeared to be contained but belonged to a noise background category. The second most commonly rejected events were single muons which the Veto Shield did not pick up. Such single muons are, typically, penetrating the Central Detector through the sides or occasionally through a crack. Approximately 98% of the single through–going muons (1592 events) were only picked up at the exit point by shield manifolds located in the floor. The remaining 2% of rejected events represent single muons (33 events) which had no associated shield activity in the walls or the floor. These numbers reflect the inefficiency of the active Veto Shield surrounding the Central Detector. The down–stopping muons represent only 7.8% of the rejected events. These correspond to single muons that enter through the sides of the main detector for which no shield

Rejection Rates		
Total number of events	13,426	100.0%
Noise Events	10,583	78.8%
Through–going muons	1,625	12.1%
Down–stopping muons	1,050	7.8%
Rock events	80	0.6%
Selection Rates		
PCE	15	0.1%
Up–stopping events (raw)	70	0.5%

Table 3.3: Event rejection and selection statistics for the PCE scan.

hit is associated. The Rock events represent a small fraction of the eliminated data. Event rejection rates for the PCE scan are summarized in Table 3.3.

3.9 The Monte Carlo Simulation

Only a brief description of the Monte Carlo operation and output is given here. Details of design and performance can be found in references [1], [2] and [9]. The Monte Carlo starts with the selection of neutrino (ν and $\bar{\nu}$) energy in the range between 50 MeV and 20 GeV, using an atmospheric neutrino flux created by Gaisser [12] which includes muon polarization. A neutrino interaction is then generated in a simulated Soudan 2 calorimeter. Next, the nuclear re–interactions of the outgoing pions are simulated using Tufts own software package 'INTRANUKE' [13]. Finally, all final state particles are propagated through the Soudan material, the ionization is drifted down halftubes, the drifted electrons are avalanched at the wireplanes, the electronic signals from the wireplanes to the ADCs are simulated, and the pulses arriving at the ADCs are digitized, compacted, and converted to the same format as

real data. Calorimeter and active Veto Shield noise collected from random triggers is overlayed on top of the Monte Carlo data. The Monte Carlo trigger time is adjusted to RAM address 512, and a compactor threshold of 3 ADC counts is required.

The Monte Carlo simulation used in this analysis is the first–generation Soudan software. For future analysis, a second–generation of simulation software is now available. Despite some inaccuracies in the older program, ISIS test beam calibration data has been described by the first–generation simulation without major discrepancies [3].

For calculating the hardware, software, and scanning effiencies of the data reduction sequence, a sample of neutrino interactions has been generated to approximately simulate the data. A sample of 3000 Monte Carlo events – 2381 of which left ionization in the calorimeter – were generated. Events originating inside the appropiate fiducial volume were extracted. A fiducial volume is defined as the volume containing the collection of calorimeter nucleons considered for nucleon decay or neutrino interactions. The fiducial volume contains those nucleons located more than 20 cm from the calorimeter steel stack edges in the anode and cathode directions and more than 50 cm from the calorimeter stack edges in the drift direction. After rejecting events outside the fiducial volume, the Monte Carlo data set consists of 1122 simulated atmospheric neutrino interactions, 923 of which left ionization in the calorimeter (corresponding to 3.45 kiloton years of exposure).

See Table 3.4 for a summary of the most prevalent neutrino interactions occurring in the Soudan 2 Monte Carlo simulation. Table 3.4 shows that 87.4% (3.7%) of the showers (tracks) are coming from electron neutrino quasi–elastic (QE) plus non–quasi–elastic ($\overline{QE}$) interactions, 2.8% (69.9%) showers (tracks) are produced from muon neutrino quasi–elastic plus non–quasi–elastic interactions, and 7.3% (15.9%) of the showers (tracks) are produced by neutral currents. This first–generation Monte Carlo predicts that 34.6% of multiprongs are muon–neutrino charged current reactions, while 42.2% are electron–neutrino charged curent reactions, and 23.2%

Soudan 2 Monte Carlo Truth Table				
	Shower	Track	MP	Total
ν_e QE	74.8%	3.7%	9.5%	28.0%
ν_μ QE	2.8%	69.0%	4.6%	28.3%
ν_e $\overline{QE}$	12.6%	0.0%	32.7%	14.0%
ν_μ $\overline{QE}$	2.5%	4.4%	30.0%	14.3%
ν NC	7.3%	15.9%	23.2%	15.4%
Total	100%	100%	100%	100%

Table 3.4: Percentage of shower/track/multiprong events being produced by the Soudan 2 Monte Carlo.

are neutral current. The overall composition of the Soudan 2 Monte Carlo is made of 42.0% ν_e events, 42.6% ν_μ events and 15.4% neutral current events. On the other hand, Table 3.5 summarizes how the events from the Monte Carlo are classified – the so called "confusion table": an electron (muon) neutrino QE reaction are being classified 84.6% (3.2%) as a shower, 5% (91.9%) as a track and 10.4% (4.9%) as a multiprong event.

We have also studied tracks and showers produced in exclusive charged current single pion production events. We have analyzed the following channels using Monte Carlo samples:

$$\nu_\mu + n \rightarrow \mu^- + p + \pi^0, \tag{3.2}$$

$$\nu_e + n \rightarrow e^- + p + \pi^0, \tag{3.3}$$

and

$$\nu + n \rightarrow \nu + n + \pi^0. \tag{3.4}$$

Soudan 2 Monte Carlo Classification Table				
	Shower	Track	MP	Total
ν_e QE	84.6%	5.0%	10.4%	100%
ν_μ QE	3.2%	91.9%	4.9%	100%
ν_e $\overline{QE}$	28.6%	0.0%	71.4%	100%
ν_μ $\overline{QE}$	5.6%	30.0%	64.4%	100%
ν NC	14.9%	39.0%	46.1%	100%
Total	31.7%	37.7%	30.6%	100%

Table 3.5: Classification of events from the Soudan 2 Monte Carlo.

We generated 100 events for each channel, and applied the same procedures used in the contained event sample as described in Chapter 4. We utilized the online software STING to scan, digitize, and reduce the events to a DST format (see Appendix C). Unless otherwise specified, this procedure was repeated with all data and Monte Carlo samples.

For the partially contained (PCE) scenario, a sample of 6000 Monte Carlo events were generated, using the Bartol neutrino flux. As done with the data, all of the events were then passed through SOAP analysis at the mine, where the SMU processor selected 1671 events. The latter events where scanned in order to extract multiprong PCE events originating inside the fiducial volume. The fiducial volume criterion used here is the same as that applied for the contained event sample. In the scanning process we eliminated all events with their vertex out of the fiducial volume, all fully contained events, all partially contained events with fewer than 3 prongs, and all partially contained events where the exiting prong (either track or shower) points to the ceiling. After scanning, 117 simulated atmospheric neutrino interactions remain, representing a Soudan 2 exposure of 17 kiloton–years. This

PCE Monte Carlo simulation, predicts that 83.2% of the events are muon–neutrino charged current reactions, while 15.1% are electron–neutrino charged current events, and 3.2% are neutral current.

References

[1] Steven Werkema, Ph.D. Thesis, University of Minnesota, 1989, unpublished.

[2] David Schmid, Ph.D. Thesis, University of Minnesota, 1992, unpublished.

[3] Carmen Garcia–Garcia, Ph. D. Thesis, Universidad de Valencia, 1990, unpublished.

[4] P. Litchfield, N. West, *"A description of the Soudan 2 detector block geometry for the software"*, Soudan 2 Report PDK–290, June 1986.

[5] W. P. Oliver *et al.*, Nucl. Instr. Meth. **A 276**, 371 (1989).

[6] W. P. Oliver, *"Veto Shield Readout Module"*, Soudan 2 Report PDK–289, September 1986.

[7] L. McMaster, W.A. Mann, *"Inventory for the HPW aquisition"*, Soudan 2 Report PDK–348, Nov. 1987.

[8] B. Ewen et. al., *"The HPW enhancement of the active shield"*, Soudan 2 Report PDK–525, Sept. 1992.

[9] Donald M. Roback, Ph.D. Thesis, University of Minnesota, August 1992, unpublished.

[10] M. A. Thomson *et al.*, Phys. Lett. **B 269**, 220 (1991).

[11] For a more detailed description, see N. Sundaralingam, Ph. D. Thesis, Tufts University, June 1993, unpublished.

[12] T. K. Gaisser, T. Stanev, G. Barr, Phys. Rev. **D 38**, 85 (1988). G. Barr, T. K. Gaisser, T. Stanev, Phys. Rev. **D 39**, 3532 (1989).

[13] W. A. Mann *et al.*, *"INTRANUKE: A Phenomenological Code"*, Soudan 2 Report PDK–377, 1988.

Chapter 4
Reconstruction of Neutrino Events

4.1 The Neutrino Event Samples

In the "Golden" sample, the topology of each contained event is classified as being a single track event (a candidate muon–neutrino quasi–elastic or "ν_μ–QE"), or a single shower event (a candidate electron–neutrino quasi–elastic or "ν_e–QE"), or not being a quasi–elastic interaction (non–QE or multiprong). In principle we are referring to the extraction of the following neutrino reactions:

i)"ν_e **Quasi-Elastic" events (single showers):**

$$\nu_e\, n \;\rightarrow\; e^-\, p, \tag{4.1}$$

$$\bar{\nu}_e\, p \;\rightarrow\; e^+\, n. \tag{4.2}$$

ii)"ν_μ **Quasi-Elastic" events (single tracks):**

$$\nu_\mu\, n \;\rightarrow\; \mu^-\, p, \tag{4.3}$$

$$\bar{\nu}_\mu\, p \;\rightarrow\; \mu^+\, n. \tag{4.4}$$

iii)"ν**-Elastic" neutral current events (single proton tracks):**

$$\nu\, p \;\rightarrow\; \nu\, p. \tag{4.5}$$

iv)"ν**-Inelastic" events (multiprongs):**

$$\nu_l\, N \;\rightarrow\; (l^\pm/\nu_l) + X(hadrons). \tag{4.6}$$

A single shower "e–like" event is displayed in Fig. 4.1 where we see a straight track (recoil proton) and e^- shower emerging from a common point (the vertex). Similarly,

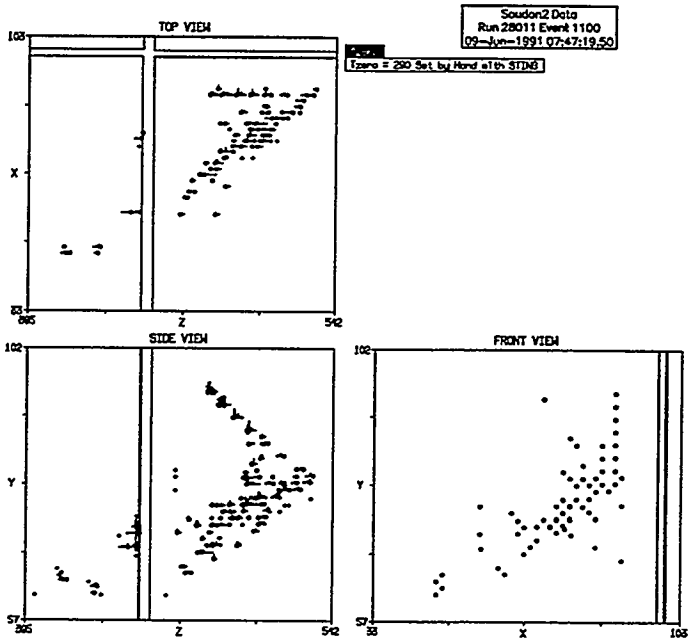

Figure 4.1: Contained single shower event: shower plus recoil proton.

Fig. 4.2 illustrates a single–track or "μ–like" event. Here a two–hit shower is seen at the lower left endpoint. This μ^+ decay signal is characterized by a displacement in the z–direction between the μ^+ track endpoint and the origin of the e^+ shower. Finally, Fig. 4.3 represents a multiprong event, in which we infer a track and two showers emerging from a common vertex.

For the topological classification of "single showers" and "single tracks", recoil protons from primary vertices and muon decays on tracks are ignored. We note that the multiprong events (sometimes referred to as "non–QE" by the collaboration) include both charged current and neutral current inelastic neutrino reactions.

Nearly all of the contained events with time–coincident shield hits (Silver and Bronze events) are believed to be due to interactions of neutral particles produced by high energy cosmic ray muon interactions in the surrounding rock. A study of such events [1] indicates that the probability of detecting at least one accompanying charged particle passing through the active shield is high. The shield efficiency and singles rate are continuously monitored using the 0.2 Hz flux of through–going cosmic ray muons. Our final sample of contained events includes 99 events having

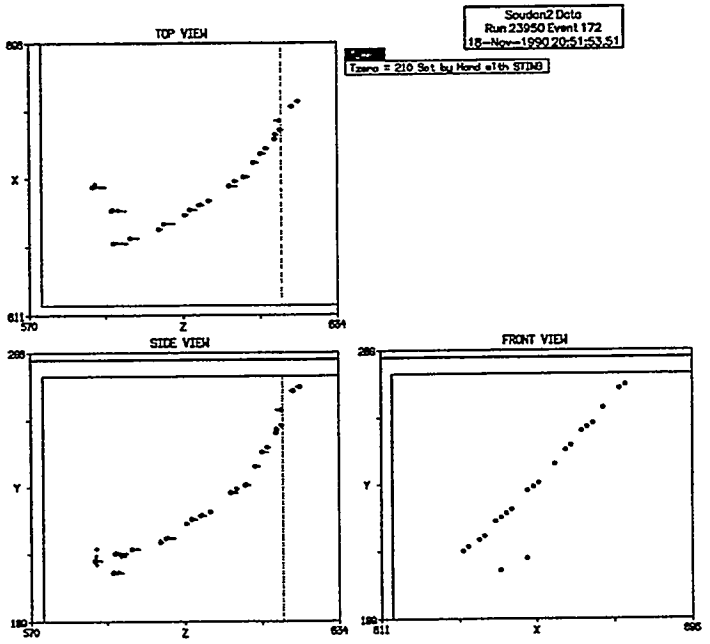

Figure 4.2: Contained single track event: track with a decay in one of its endpoints.

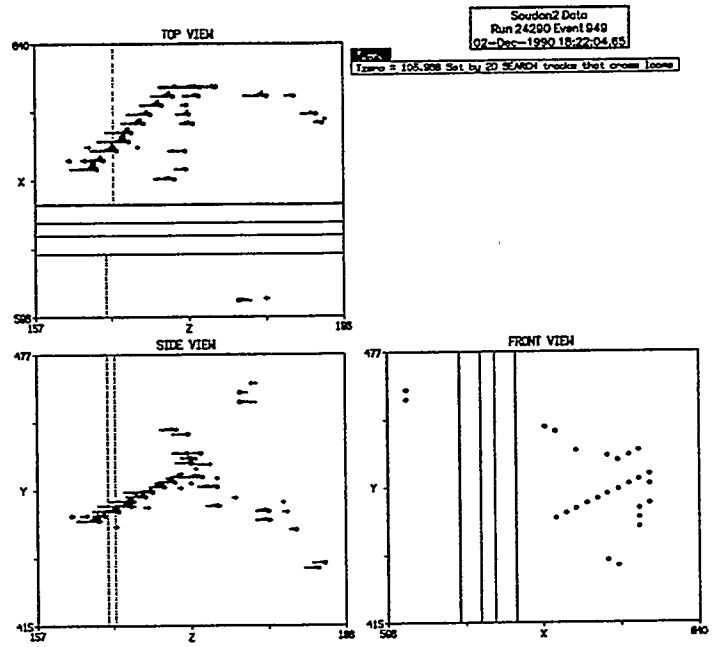

Figure 4.3: Contained multiprong event: a track plus two showers emerging from a common vertex.

Soudan–2 Contained Event Sample			
1.0 Kiloton–year Exposure			
	Gold Sample	Silver Sample	Gold Events with Recoil Protons
Tracks	30	20	9
Showers	35	16	6
Multiprongs	34	7	
Total	99	43	15

Table 4.1: Contained Event Sample

zero Veto Shield hits[1] (Golden events) and 43 events having but one shield hit within the event time window (Silver events). Table 4.1 summarizes the composition of our contained samples [2].

In one kiloton–year of exposure, the Soudan experiment has isolated 30 single track events, 35 single shower events and 34 multiprong events which have attributes compatible with being contained neutrino interactions. A list of these events, with observational details for each, is given in Appendix D. The majority of these events are supposedly quasi–elastic charged current interactions. Since the Soudan 2 experiment has a fine–grained iron calorimeter, we are able to see recoil nucleons from reactions 4.1 and 4.3. Also we are able to differentiate between reactions 4.3 and 4.4 by observing the end–point–decay μ^+ particles, since μ^- decays are largely suppressed by weak nuclear absorption, the inverse of reaction (4.3), in the detector's iron plates.

[1]ADJ hits only are considered here and in all subsequent analysis unless specified otherwise.

All of the events pertaining to the "Golden" sample were scanned by the author and Prof. Mann using the online software STING (Soudan Two INteractive Graphics). Each event image after digitization was reduced to a Data Save Tape (DST) image. For this purpose, we utilized software written by T. Kafka, in which the information obtained by scanning and measuring of STING images is entered on an event–by–event basis into ASCII card images. The format for our DST is given in Appendix E.

4.2 Event Digitization

Each event image was digitized – using the online software STING – for the purpose of reconstructing the reaction's kinematics. The set of rules described below were applied consistently to the single track, single shower and multiprong events. The latter events are the most difficult to digitize.

In repeated scanning passes, tracks are differentiated from showers and an attempt is made to get a global picture of the event. Here it is important to check for the following: *i)* The event T$\emptyset$ needs to be established, *ii)* unmatched hits need to be matched or disregarded, and *iii)* the primary vertex needs to be identified. In a typical multiprong event, the tracks and showers emerge from a common vertex, however in some events there appear track(s) and/or showers(s) which are not connected to the main vertex. Fig. 4.4 schematically depicts the most frequent topological features. Here T1 and T2 are two tracks connected to a main vertex region which is depicted by the solid rectangular box. Showers S1 and S3 are also connected to the primary vertex region, whereas S2 and S4 are 'remote showers' and T3 is a 'remote track'. In Fig. 4.4, the solid and open circles depict matched hits belonging to the various tracks and showers. The event contains 7 prongs which can be enumerated as three tracks (2 connected and 1 remote) and four showers (2 connected and 2 remote).

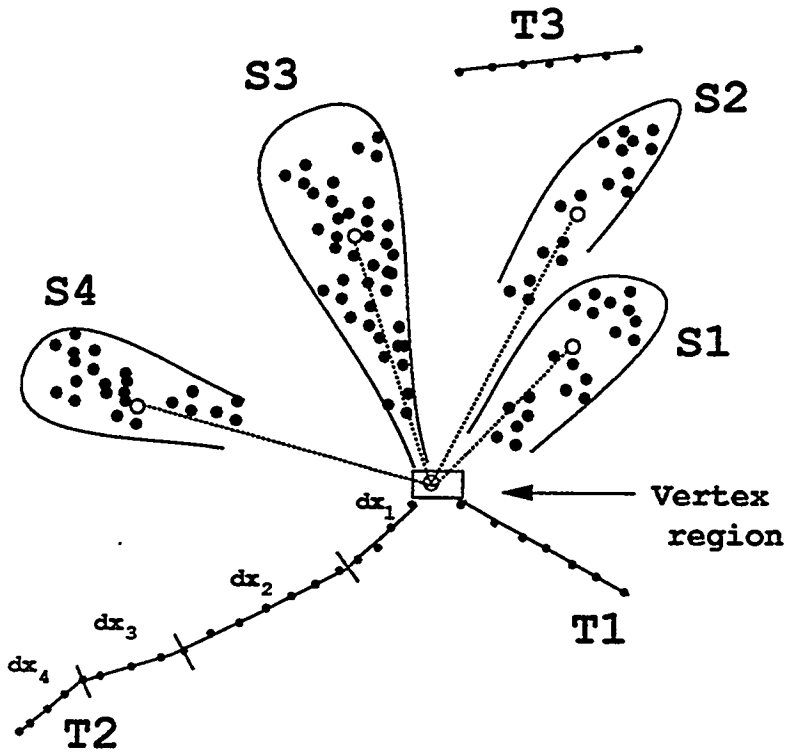

Figure 4.4: Event image digitization: Event contains three tracks (T1, T2 and T3), four showers (S1, S2, S3 and S4), and a vertex region depicted by the solid rectangular box.

The momentum of stopping tracks can be measured by using the observed range, and so we digitize the tracks as follows: *i)* For straight tracks we record the first and last matched hit of the track. Tracks T1 and T3 would be handled in this way. *ii)* For longer straggling tracks, we divide each track into small straight segments as illustrated for track T2 (see segments dx_i in Fig. 4.4). For each segment we record the beginning and end point. The total track length is then taken to be the sum of the segment lengths. The total range is decreased to account for distances across cracks between modules. For all tracks, also the second matched hit is recorded. We determine the track direction at the production vertex, using the first matched hit and the vertex if their distance is ≥ 0.5 centimeters, otherwise the second matched hit and the vertex are used.

Showers generally start in a localized region and then spread out along a particular direction. The vicinity of the shower vertex is usually easy to locate; a second point is chosen to give the direction of shower development. As shown in Fig. 4.4 for

four showers, the direction of each is determined by visually estimating the center of gravity of the shower points and then selecting a matched hit (open circle) which lies along this direction. Additionally, the first matched hit closest to the vertex of the shower is always recorded. Finally, we count all matched hits belonging to each shower, as indicated by the solid lines enclosing matched hits for each shower in Fig. 4.4.

We assign a vertex location by locating a point where the projection of all tracks and showers directions intersect. This is denoted by the symbol $\otimes$ inside the vertex region of Fig. 4.4. There are, of course, a number of plausible assigments. For example, if the track T1 is a recoil proton, then one may prefer a vertex location which is closer to track T2.

4.3 Shower Reconstruction

Several methods have been considered for estimating shower energy in the Soudan tracking calorimeter. From the ISIS test beam and from Monte Carlo studies, it has been determined that the shower energy is most accurately measured by using the number of matched shower hits (pulses) [3].

In our calorimeter, electrons and photons deposit ionization via electromagnetic cascades in the form of showers. As described in Section 4.2, for the analysis of this thesis, the direction of a shower was determined by visually estimating the center of gravity of the shower points and then selecting a matched hit which lies along this direction. Once the vertex and direction points have been assigned, the azimuth angle ϕ and zenith angle β for the shower can be calculated (see Fig. 4.5). Recall that in the coordinate system of the Soudan 2 detector, the x–direction corresponds to increasing anode number on the east side of the calorimeter, the y–direction (vertically upward) corresponds to increasing cathode number, and the z–direction corresponds to increasing halfwall number (even numbers in the East, odd numbered

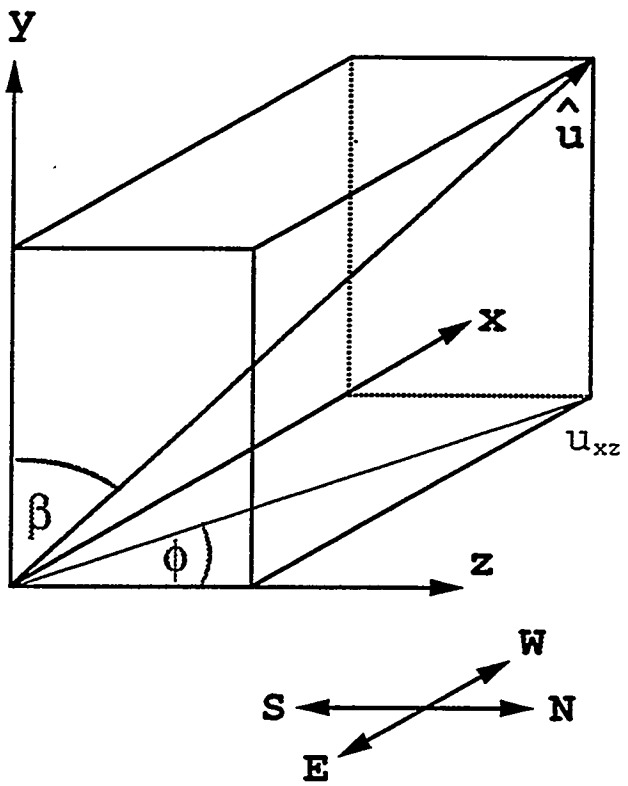

Figure 4.5: Coordinate system for the Soudan–2 cavern: β is the zenith angle and ϕ is the azimuthal angle.

halfwalls in the West).

A polar angle correction must be applied to all electromagnetic showers. The Z axis of the detector is special, because the steel corrugations and the drift tubes are aligned in that direction. A shower with a well–defined trajectory that makes an angle θ_z (Fig. 4.6) with the Z axis can expect to encounter an amount of steel that is approximately proportional to $1/\sin\theta_z$ along this path, relative to a shower that is incident normal to the tubes. Showering particles that traverse the calorimeter at a small angle relative to horizontal drift tubes will leave fewer pulses than those that traverse the calorimeter at larger angles with trajectories more orthogonal to the tube. This correction (see Fig. 4.7) normalizes all showering events to hit sampling in a direction orthogonal to the tube [4].

After the polar angle correction (see Fig. 4.7) is made to showers, the kinetic energy (KE) can be determined. The collaboration bases its KE estimate for showers on two previous independent studies, one done by Garcia–Garcia using ISIS test beam data [3] and one by Schmid using Monte Carlo data [4]. These analyses have

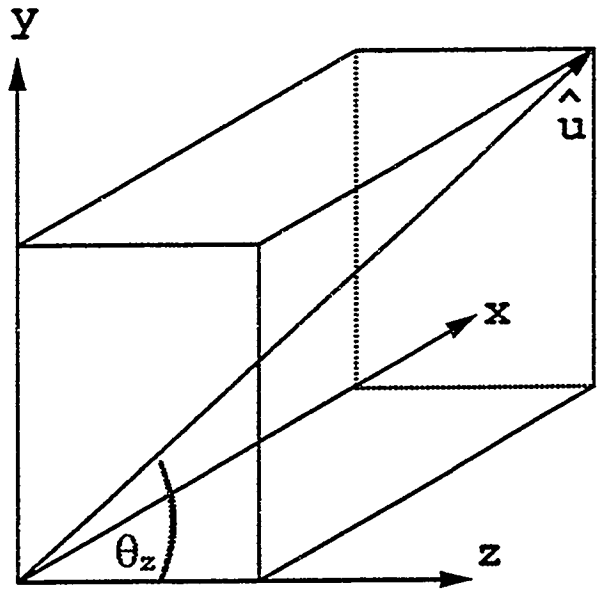

Figure 4.6: θ_z definition.

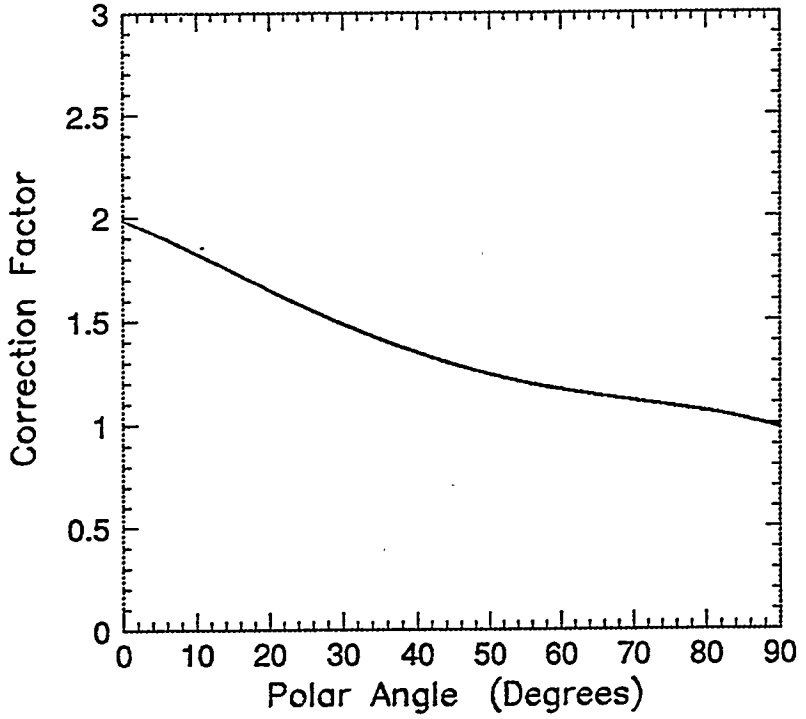

Figure 4.7: Polar angle correction factor for electrons.

given rather different formulas for the kinetic energy of a shower. On the one hand, Garcia–Garcia proposed a quadratic expression (Eq. (4.7)) for the kinetic energy which she used without a polar angle correction:

$$KE_{Garcia} = 11.4 \times Nhits + 0.296 \times Nhits^2 \tag{4.7}$$

On the other hand, Schmid's expression is a linear formula (Eq. (4.8)) which uses hit counts corrected for shower polar angle:

$$KE_{Schmid} = 12.9 \times Nhits_{cor} + 33.4. \tag{4.8}$$

Fig. 4.8 and 4.9 show the differences between the Garcia–Garcia and Schmid algorithms at low and high kinetic energies respectively. Since the polar–angle correction is based upon the detector geometry, it seems to us necessary for the shower reconstruction. Consequently we have introduced this correction to Garcia–Garcia's formula, and have then compared with Schmid's equation. When the corrected number of hits is less then thirty (low shower KE), the Garcia–Garcia formula fits the ISIS test beam data well (shown in Ref. [3]). Schmid's formula however does not represent the ISIS data. The latter formula is an interpolation from a Monte Carlo study with showers which have a high number of corrected hits (high shower KE; see Ref. [4]). Fig. 4.9 shows this higher portion of the shower energy spectrum. Here, as the corrected number of hits increases, the discrepancy between equations 4.7 and 4.8 is clearly seen. In this higher KE regime, the study by Garcia–Garcia may be less accurate, since above 34 hits the ISIS data runs out, and so her fit may be less reliable then Schmid's approach in this regime. From reference [4] we infer that Schmid's work was done with simulated showers having twenty or more corrected hits.

Our conclusion is that more research on the shower energy reconstruction algorithm at higher energies needs to be done, now that a new Monte Carlo is available for the Soudan experiment. However, for showers with number of hits less than fifteen, Garcia–Garcia's formula provides a reasonable energy estimation. Above this

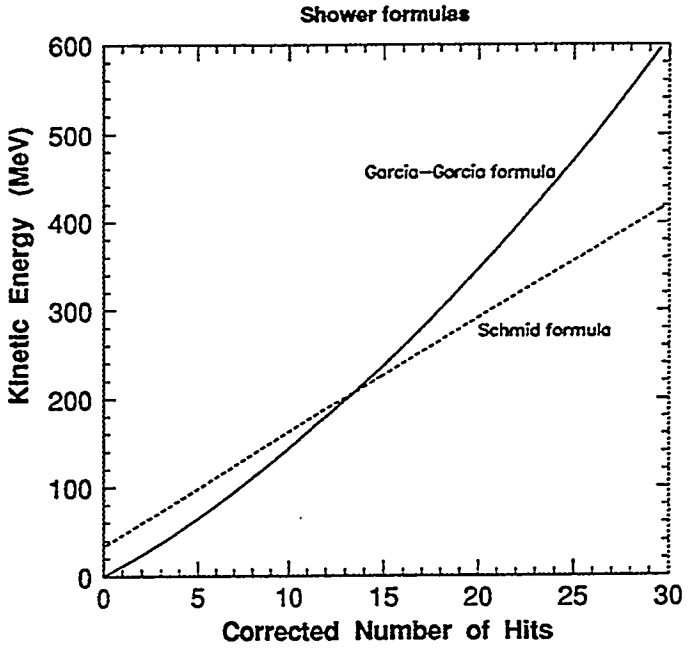

Figure 4.8: Kinetic energy for showers at low energies. The solid line represents Garcia–Garcia's algorithm, while the dashed line is the formula by Schmid.

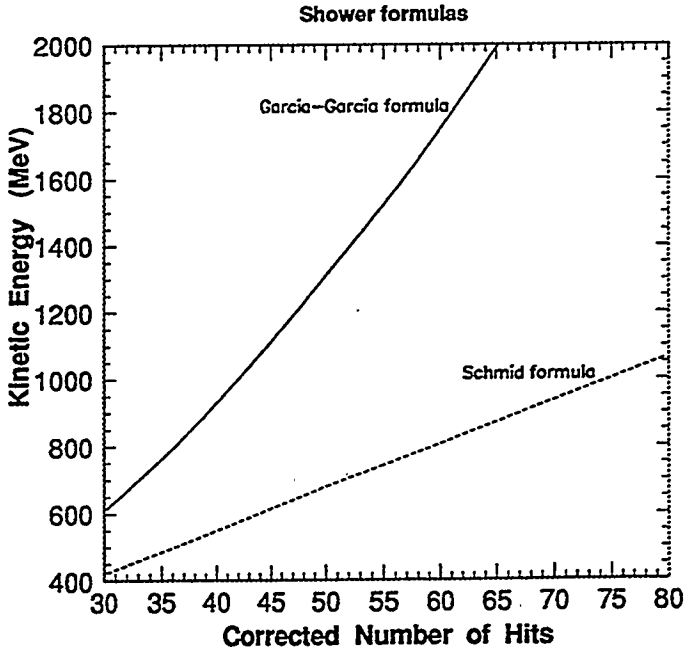

Figure 4.9: Kinetic energy for showers at high energies. The solid line depicts Garcia–Garcia's algorithm; the dashed line is from the work by Schmid.

region (when the number of hits exceeds fifteen), then Schmid's formula may be a better approach. For the purpose of this thesis, we have used the Garcia–Garcia formula augmented with a polar angle correction. Energy estimation for showers with number of hits bigger than fifty are not reliable with this algorithm. Our preference for the Garcia–Garcia formula at low energies is motivated in part by our observation that it provides reasonable estimates for muon endpoint decay showers, in contrast to the Schmid formula (see Fig. 4.10 on p. 89).

4.4 Track Momentum from Range

The momentum of a stopping track can be measured by using the observed range. Muons and charged hadrons leave ionization via dE/dx loss in the form of tracks. The energy liberated by a relativistic charged particle traversing a medium as a function of distance is given by the Bethe–Bloch formula:

$$-dE/dx = 4\pi N_A r_e^2 m_e c^2 z^2 \frac{Z}{A}\frac{1}{\beta^2} \times [\ln(\frac{2m_e^2 c^2 \gamma^2 \beta^2}{I}) - \beta^2 - \frac{\delta}{2}] \qquad (4.9)$$

where $4\pi N_A r_e^2 m_e c^2 = 0.3071\ MeV\ cm^2\ g^{-1}$, $\beta = v/c$, $\gamma = 1/\sqrt{1-\beta^2}$, the ionization constant $I = 16Z^{0.9}$ eV; δ characterizes the relativistic rise and goes as $(\ln\gamma)$ for very high energy. For a given kinetic energy, a heavy particle moves more slowly than does a light particle. Ionization can in principle be used to determine charged particle direction since the particle will ionize more heavily per unit distance as it slows and stops. (However, in Soudan 2 the measurement of particle ionization is affected by many variables [4].)

Although track range can now be calculated using software, for this thesis we have performed a less sophisticated integration by hand as described in Section 4.2.

Our track momentum measurements have been checked using the latest version of TRAJEC, a SOAP processor which fits polynomials to the space points of tracks to obtain trajectories in three dimensions. The fitting has been carried out interactively by a scanner using STING. For short tracks (e.g. < 80 cm) the agreement between

both methods is good. For long, straggling tracks (e.g. > 100 cm) the discrepancy is typically 5% in the reconstructed range.

To calculate the momentum from range for a particular track, we use software used by the collaboration in its magnetic monopole research. Specifically, we use the subroutines RTOMOM, ILOSSR, BBLOCH, and the functions DEDX–FAST, BETHE–BLOCH, and PINTEGRATE. For a given track one specifies the range, the mass assignment, and the mean density of the Soudan detector to these routines, whereupon the codes return the track momentum.

4.5 Track Identification by Ionization

To identify tracks according to the amount of ionization deposited, the relevant quantity to examine is the average dE/dx of the particle when it is propagating in gas. Discrimination between different types of tracks ($\mu^{\pm}, \pi^{\pm}, p$) can also be made based upon the fact that pions and protons will scatter – due to the strong interaction – while muons will not. Our calorimeter is unique among underground experiments in its ability to distinguish protons from muons and charged pions using ionization information (pulse height). At low momenta it is hard to differentiate between pions and muons because they have similar masses and consequently ionize similarly, and because the probability for a pion interaction over modest range is low.

An initial classification of tracks was made according to information available upon scanning. We studied the contained single track and single shower data and then formulated our selection criteria; our main goal is to differentiate protons from charged muons and pions. We identify any track as a proton if the track is observed to have both of the following properties:

i) The track is heavily ionizing, typically having a couple of hits with saturated pulse height;

ii) The track is straight, typically having one hit per tube, with little scatter of

the hits from a straight trajectory.

Using these criteria, we found 11 (12) tracks in the contained single track file and 6 tracks in the contained single shower file to be proton tracks. We note here that, event 22950 – 1034 has been retained as a muon, due to the fact that the last two hits are in the wire plane, which have saturated pulse height (property *i)*). This track has some likelihood – based upon our scanning experience – of being a proton. From those 11 (12) protons, 2 (3) are lone recoil protons and are candidates for our neutron–induced sample (the so–called Rock events, see Ch. 5) or for reactions 4.5 (see Appendix D).

We conclude that in a 1.0 kiloton–year exposure of Soudan–2, we have accumulated 30 contained single track events where 9 of them possess a visible recoil proton at the vertex. In the same exposure we have accumulated 35 contained single shower events, 6 with a visible recoil proton. Also, we have recorded 2 (3) contained, isolated recoil protons.

4.6 Muon Charge Determination

Another feature of the Soudan 2 detector, due to the fact that it is a fine–grained iron calorimeter, is its capability for distinguishing μ^+ from μ^- to some degree. In our calorimeter, charged muons will be observed to range to a stop. Subsequently, positively charged muons and negatively charged muons can interact with the detector medium in different ways. This charge–dependent difference in muon track endpoint behavior can be exploited to distinguish (statistically) muons from anti–muons.

A positively charged muon at rest will be repelled by the positive nuclear charges of the atoms of the detector media. It will never reach a nucleus, therefore it will decay as in vacuum via its weak decay mode $\mu^+ \rightarrow e^+\nu_e\bar{\nu}_\mu$. The μ^+ lifetime is 2.19 μs. This relatively long decay time gives rise to a characteristic signature in Soudan

2. The time delay appears as a displacement in the z–direction between the μ^+ track endpoint and the origin of the e^+ shower. The average displacement due to the μ^+ decay time is about 1.3 centimeters.

In a relatively high Z medium such as iron, a negatively charged muon will be attracted and captured by a nucleus. Once captured, there is a sizeable probability per second, determined by the μ^- wave function density inside the nucleus, that the μ^- will be absorbed by the weak process $\mu^- \; p \rightarrow \nu_\mu \; n$. One concludes that in a dense detector such as Soudan 2, many stopping μ^- tracks will not exhibit the decay shower that is characteristic of a μ^+ decay. However, if a μ^- manages to decay before undergoing nuclear absorption, its decay time will – on average – be shorter than that of a μ^+. According to calculations, roughly 91% of μ^- that stop in iron will not give a decay e^- due to nuclear capture of the μ^-. A Monte Carlo study (see ref. [4]) indicates a slightly larger percentage for the μ^- capture ($\sim$ 95%).

To date, the collaboration has not confirmed these Monte Carlo numbers with ISIS test beam data. The measurements are not easily carried out, because of the problem of determining whether the last hit(s) along the track are associated with the stopping μ^- or with a decay $e^\pm$ signal. Also, a nucleus that absorbs a μ^- may emit deexcitation photons that can mimic a decay $e^\pm$ signal. The best determinations available are those of Garcia–Garcia using the ISIS stopping muon test data [3]. She reports that *"if no hits were observed within 15 centimeters of the end of a muon track, the odds are 3:1 that the track was produced by a μ^-. However, if two or more hits are observed, the odds are 6:1 that it is a μ^+ track"*.

At Tufts, we examined the end–point ionization of candidate muons in the single–track event sample. On an event–by–event basis we estimated whether the last hit(s) in a track belong to a stopping muon track or to a decay signal. As seen in Appendix D, we propose 9 tracks to have muon endpoint decays, where the number of hits associated with the decay $e^\pm$ shower varies from two to four hits. In other words, out of 30 (29) possible muon tracks we recognize 9 of them as having endpoint decays;

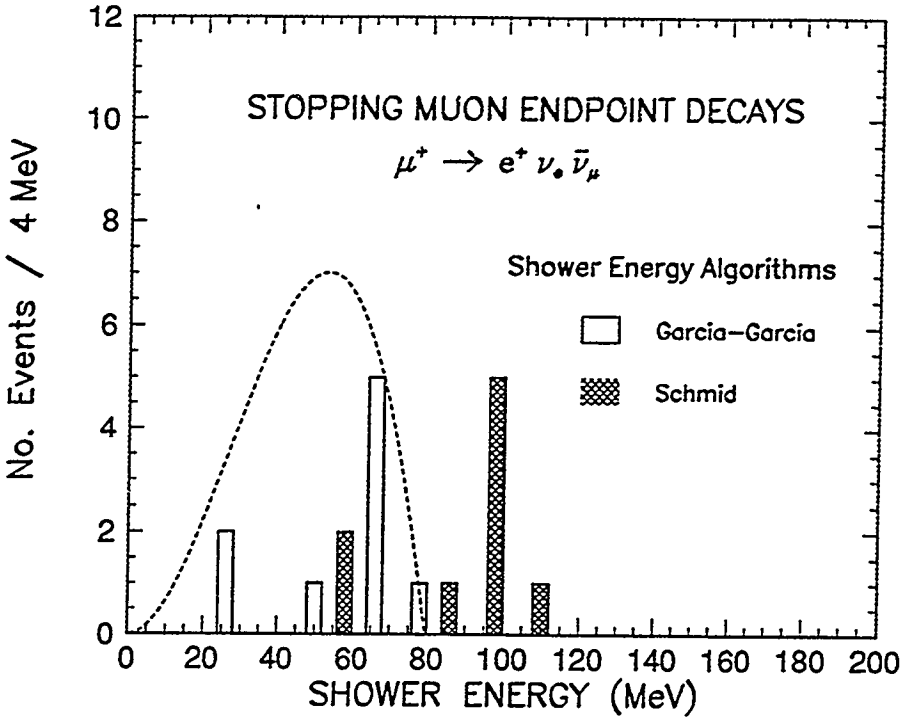

Figure 4.10: Soudan shower spectrum from observed muon endpoint decays. The dashed line is the theoretical spectrum (Ref. [5]) smeared according to detector resolution.

presumably most of these 9 muons are μ^+ particles.

A rough indication that most of the nine endpoint decays arise from μ^+ tracks is indicated in Fig. 4.10. Fig. 4.10 also shows that the Garcia–Garcia algorithm for small showers (with low number of hits, e.g. < 15) yields a more plausible shower energy distribution than does the Schmid formula. Using the Garcia–Garcia algorithm, the low statistics μ decay sample (histogram) plausibly follows the theoretical prediction for decays in vacuum (dashed line).

4.7 Concluding Remarks

With the detailed event images obtained with the Soudan tracking calorimeter we can discern tracks from showers. The energy estimation of tracks from range is straightforward. However, better algorithms for determining shower energies, particularly energies of large showers (e.g. total number of matched hits bigger then fifty) are clearly needed. The experiment's capability to differentiate protons

from charged muons and pions, and to partially distinguish μ^+ from μ^- final states, is providing information which has not been available previously in underground experiments.

Among single track events, we observe 9 to have endpoint decay showers ($\mu^+ \rightarrow e^+\nu\bar{\nu}$). In the iron medium of the Soudan 2 detector, μ^- tracks almost always undergo nuclear absorption before they decay, whereas μ^+ tracks always decay. As a result, observation of track endpoint decay allows discrimination between quasi-elastic ν_μ versus $\bar{\nu}_\mu$ reactions. If the detector efficiencies for the observations can be reliably ascertained, then a measurement of the atmospheric neutrino to antineutrino ratio $\nu_\mu/\bar{\nu}_\mu$ is feasible. A measurement of this quantity would be significant for atmospheric ν flux calculations and for certain neutrino oscillation proposals; to date no experiment has been able to do it.

References

[1] For a more detailed description, see D. M. Roback, Ph. D. Thesis, University of Minnesota, August 1992, unpublished.

[2] M. Goodman in Proc. Calgary Workshop on Atmospheric ν's, 21 July 1993, p. 1.

[3] C. Garcia–Garcia, Ph. D. Thesis, Universidad de Valencia, Sept. 1990, unpublished.

[4] D. J. Schmid, Ph. D. Thesis, University of Minnesota, May 1992, unpublished.

[5] M. Bardon *et al.*, Phys. Rev. Lett. **14**, 449 (1965).

Chapter 5

Rock Event Contamination in Soudan "Quasi-Elastic" Samples

5.1 Introduction

Prior to evaluation of relative contributions from neutrino reactions and/or from nucleon decay to our contained e–like and μ–like samples, it is necessary to estimate contamination arising from fluxes of non–neutrino neutral particles into the Soudan Central Detector. There is a flux of energetic neutrons and of energetic photons within the Soudan cavern originating from cosmic ray muon interactions in the rock surrounding the cavern walls. These particles can interact or convert inside the detector creating undesirable contained events. These non–neutrino cosmic–ray–induced neutral particle interactions are often accompanied by coincident shield hits and therefore can be removed from our contained event sample. However, some of the neutron and gamma induced events need not be accompanied by shield hits, either because of shield inefficiency, or because there is in fact no accompanying charged particle flux from the cavern rock. Among the neutron/photon–induced events which are tagged by the active shield, approximately 28% (4%) are judged to be single (double) proton tracks. Such events can (and should) be excluded from Soudan CEV physics samples. Potentially more dangerous are neutron/photon–induced events whose topology and ionizations match the ones which define our quasi–elastic neutrino (e–like and μ–like) samples [1]. Among the shield–tagged contained events, hereafter referred to as "Rock events", we find that 27% appear as single–shower (e–like) events and 24% appear as single–track (μ–like) events. In this Section

we describe an initial study of neutron–induced and gamma–induced background events using Soudan data. A phenomenological treatment, which identified neutron production processes and estimated their relative contributions, was carried out five years ago by D.H. Perkins [2].

To accomplish our objective, we analyze the penetration depth associated with various event topologies in the Soudan detector. Our goal is to distinguish among processes which have different characteristic penetration depths. Neutrino interactions, because of their small cross sections, will distribute uniformly with increasing penetration depth. Neutral hadrons and photons on the other hand, are expected to exhibit a fall–off in the number of events versus increasing penetration depth, reflecting the relatively short absorption or conversion lengths for these particles in the Soudan medium. Gamma conversions will have an especially short penetration depth, whereas the neutron–induced reactions will penetrate deeper. Neutron penetration receives augmentation from cascading, wherein a high energy neutron interacts to produce secondary neutron(s) which travel further into the detector medium [3].

No detailed investigation of Rock event backgrounds has been reported by other underground experiments. Very recently however, the Frejus collaboration has shown the distribution of penetration depth for their neutrino events (that is, the distance between an event vertex and its entrance point into the detector, along the event visible momentum). Agreement between this distribution and the absolute prediction from their atmospheric neutrino Monte Carlo is cited as evidence for the absence of photon and neutral hadron contamination [4].

5.2 Penetration Depth of Shower and Track Rock Events

For each event we use the visible momentum together with its apparent interaction vertex as the basis for a straight–line extrapolation to the outer wall of the

calorimeter. The extrapolated distance through the detector is taken to be the n or γ penetration depth to the interaction point. The calculation of this distance is carried out using a version of the TRAJEC subroutine TRTRAK which has been modified by T. Kafka and included in the interactive program GMCM2. The routine is run as part of SOAP, which provides the link to the Soudan–2 database. For a particular event, one can extract a complete description of the calorimeter geometry as it existed at that time. Consequently one can determine the amount of material traversed along any specific flight path, accounting for all gaps which are present along the straight–line trajectory through the detector. For each event, one calculates the final state visible net momentum; GMCM2 accepts vertex coordinates and a vector parallel or antiparallel to the event three–momentum as input and then returns the calorimeter exit point, together with the amount of material traversed. Thus one can roughly ascertain the neutral particle penetration depth in grams per square centimeter for each contained event. The penetration–depth distributions obtained for the Rock (shield–tagged) single shower and track events respectively are given in Figs. 5.1 and 5.2.

An important property of the majority of Rock events is their alignment with in time shield hit(s). After scanning Rock event images, we find – as illustrated in Figs. 5.1 and 5.2 – that $65 \pm 8\%$ of the rock single shower events are aligned in three projections with a Veto Shield ADJ hit in time with the Central Detector event. Approximately $27 \pm 5\%$ of the same sample are judged to be nearly aligned, and only about $8 \pm 3\%$ are judged to be not aligned with any in time shield hit. In Fig. 5.1 the dark shaded area depicts the $92 \pm 10\%$ of the Rock single shower events which are aligned or nearly aligned; the lightly shaded area depicts the $8 \pm 3\%$ of the Rock single shower events which are not aligned. Similarly, Fig. 5.2 shows the $76 \pm 9\%$ ($20 \pm 4\%$ aligned plus $56 \pm 7\%$ nearly aligned) of the Rock single track events which are aligned (dark shaded area) and the other $24 \pm 5\%$ which are not aligned (light shaded area). We infer from these observations that the visible momentum in

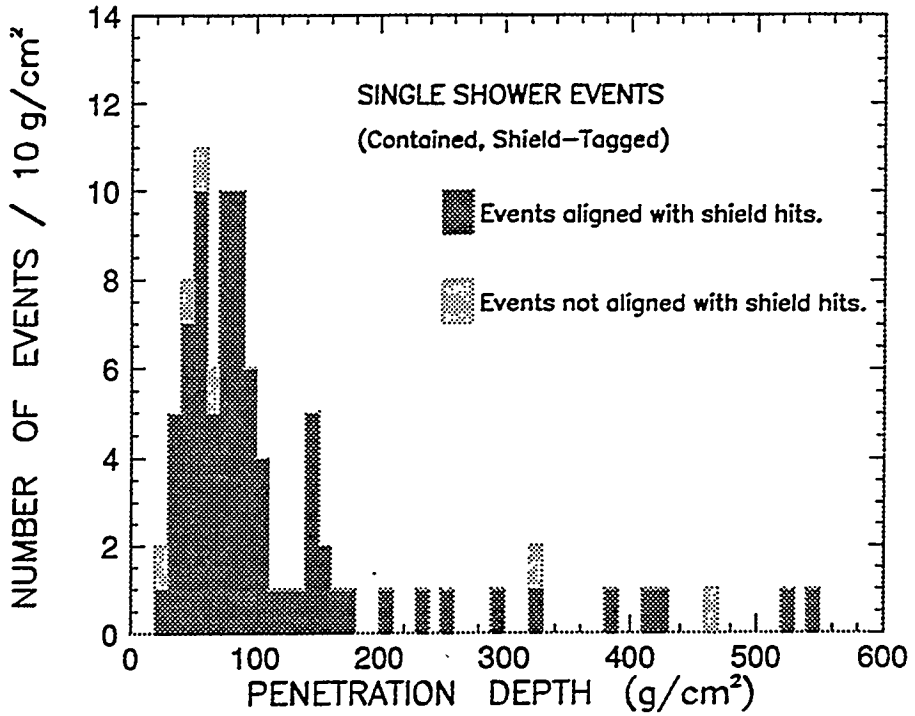

Figure 5.1: Rock single shower events.

Rock events is a reasonable estimator of the line–of–flight of the parent neutron or photon.

5.3 Penetration Depth of Shower and Track Neutrino Events

The penetration–depth distribution for the single–shower events with no associated shield hits is shown in Fig. 5.3 by the solid histogram. The detector geometrical acceptance (shown by the dashed line) was obtained from the line–of–flight information by a simple Monte Carlo calculation. Specifically, for each real event we randomly selected 100 "neutrino" penetration depths along the "neutrino" line of flight. Then, to each simulated path length we applied a cut requiring that the whole event lie within the fiducial volume. The ensemble of generated paths which pass these cuts is then used to estimate detector acceptance, shown by the dashed curve, normalized to the data above 250 g/cm^2. The lowest energy showers are considered suspect, since it is difficult to separate neutrino–induced showers of 6 – 10 hits from

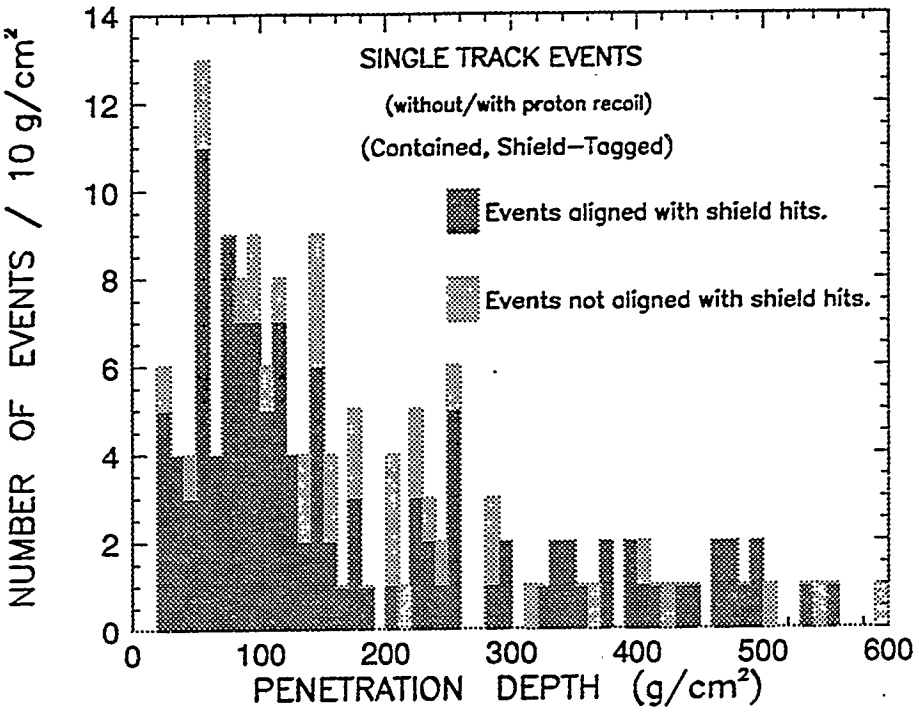

Figure 5.2: Rock single track events.

various kinds of electromagnetic discharges in the calorimeter. A cut on shower energy at 200 MeV eliminates this background. We therefore show the single–shower penetration–depth distribution in Fig. 5.4 for showers with energies exceeding 200 MeV.

A similar approach has been adopted for the single track (μ–like) event sample with no associated shield hits. As described in Section 6.4 below, the μ–like events can be usefully divided into three sub–samples based upon degree of knowledge of track directionality. The flight path for the two sub–samples having well–determined track direction, is based upon the direction of final–state visible momentum. For the third group, where the muon direction is ambiguous, we calculate the "neutrino" path using each of the two possible vertex points; each penetration depth is then entered into our histogram with a weight of 0.5. Fig. 5.5 shows the neutrino penetration depth for the single track events in terms of the amount of Soudan calorimeter material traversed (g/cm^2). The shaded areas depict events for which the muon direction is ambiguous; the dashed line shows the calculated acceptance curve, which

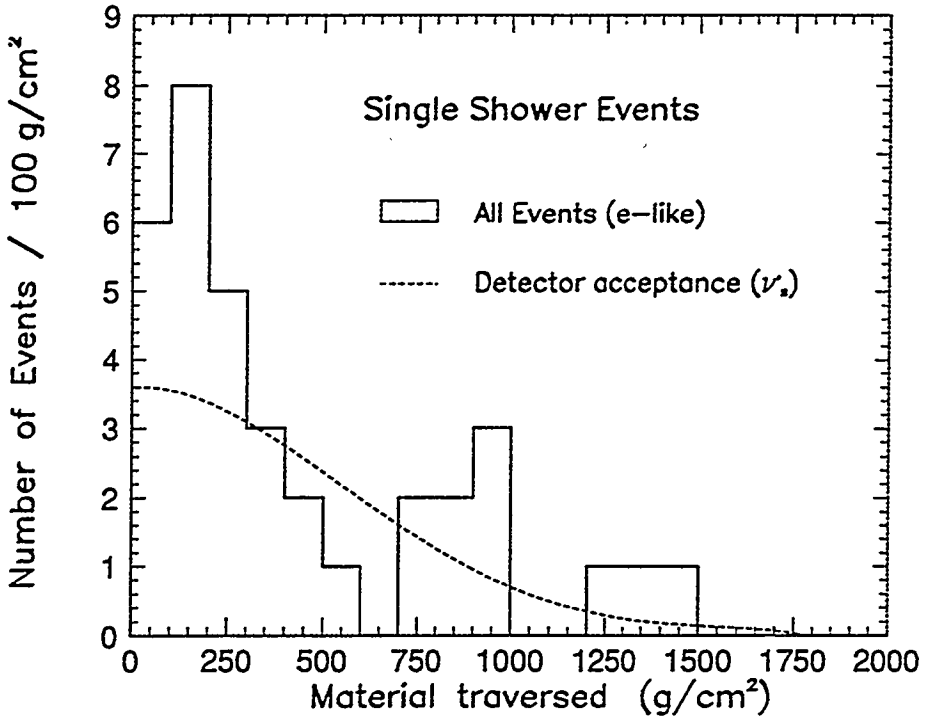

Figure 5.3: Penetration depth (in g/cm^2) from single shower events with no associated shield hits, all energies. The detector acceptance is shown by the curve superimposed (dashed line).

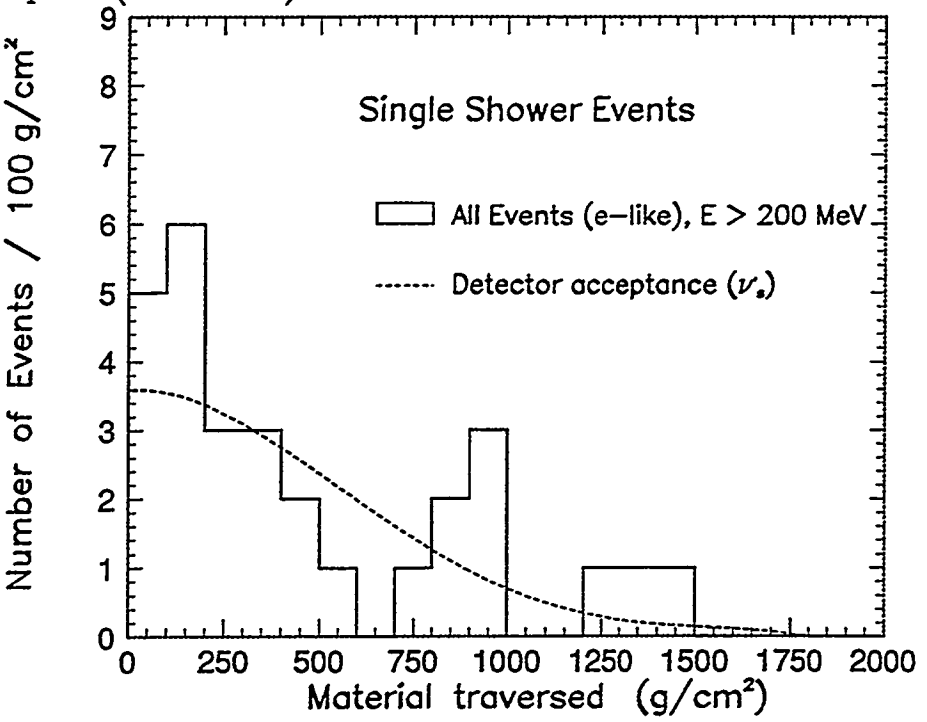

Figure 5.4: Penetration depth (in g/cm^2) from single shower events, with shower energy greater than 200 MeV. The detector acceptance is shown superimposed (dashed line).

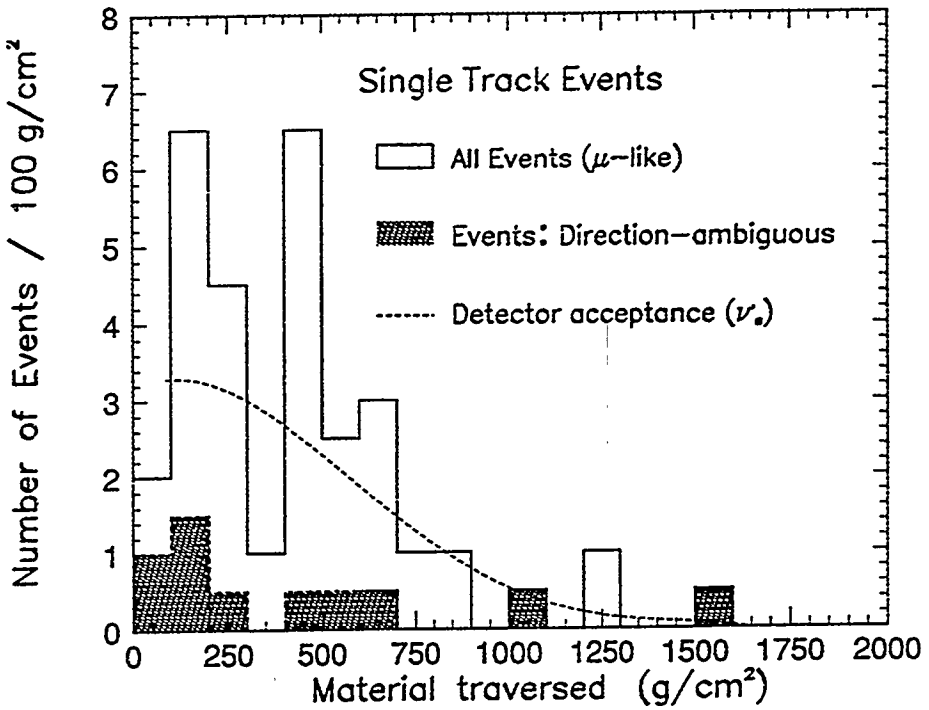

Figure 5.5: Penetration depth (in g/cm^2) from single track events with no associated shield hits; the detector acceptance is shown superimposed (dashed curve) normalized to the data above 250 g/cm^2.

has been normalized to the event distribution above 250 g/cm^2.

5.4 Rock Events as Neutrino Background

In both Figs. 5.4 and 5.5 one can discern the existence of an excess above the acceptance curve, suggesting there are some non–neutrino background events in these two contained event samples. In order to account for this background, we have utilized a recent study of Rock events carried out by D. Wall of Tufts. This study utilized the Silver and Bronze event samples (see Section 6.1), from the second 0.5 kiloton–year exposure of Soudan 2. From these samples, we extracted contained events with one or more Veto Shield hits in time with the Central Detector event time $T\emptyset$. D. Wall and Prof. Mann scanned these events using the STING Soudan–2 interactive graphics program and reduced the images to DST data, applying the same procedures as used for the "golden" contained event samples of this thesis (see Chapter 6).

The initial "raw" Rock sample for the second half kiloton–year exposure included 286 events. In a first scan pass, the events where checked in order to eliminate wire-plane noise events, cosmic ray muons which enter via cracks between calorimeter modules, and partially contained events. This initial scan eliminated 35 events; the final Rock sample for the second half kiloton–year exposure contains the 251 events summarized in Table 5.1. The Rock sample can be divided into two groups according to the particle reactions involved. The first group contains events which may originate with either gamma conversions or with neutron reactions involving π^0's; these are the single–shower events (56 events). The second group of 195 events contains topologies which must be neutron–induced (perhaps with a few K_L^0–induced). The latter topologies include multiple shower events, events which are either single pions or single protons, and multiprong events which contain tracks with or without accompanying showers.

5.5 Parametrization of the Rock Event Penetration Depth Distribution

For the purpose of obtaining representative curves, the distributions in Figs. 5.6 and 5.7 have been fitted to curves constructed from the sum of two exponentials:

$$f(x) \;=\; Ae^{-x/\lambda_1} + Be^{-x/\lambda_2} \;=\; e^{(P_1 - P_2 x)} + e^{(P_3 - P_4 x)} \,.$$

The fitted parameters are summarized in Table 5.2.

The Rock single track events are of hadronic origin, originating (almost) entirely with neutron interactions in the detector medium. Comparing Fig. 5.7 with Fig. 5.6, one observes that Rock single track events typically have deeper penetration depths, as expected. Thus it is sensible to fit the single track distribution using one exponential function of the penetration depth x:

$$f(x) \;=\; e^{P_1 - P_2 x}. \qquad (5.1)$$

Soudan–2 Rock Event Sample **2^{nd} 0.5 Kiloton–year Exposure**			
Event Topology	Particle Reaction(s)	Background to:	No. of Events
Single shower	$(\gamma\,(N) \rightarrow e^+e^-(N)$, or $n + N \rightarrow \pi^0 + X)$	ν_e quasi-elastic	56
Double shower	$n + N \rightarrow \pi^0 + X$	ν multiprong	12
> 2 showers	$n + N \rightarrow \pi^{0\prime}s + X$	ν multiprong	2
Single proton	$n + N \rightarrow p + X$	ν_μ quasi-elastic	72
Single pion	$n + N \rightarrow \pi^{\pm}$'s + X	ν_μ quasi-elastic	43
Multiprong tracks	$n + N \rightarrow (p's, \pi^{\pm}$'s, ...)	ν multiprong	52
Multiprong tracks with showers	$n + N \rightarrow (p's, \pi^{\pm}$'s, π^0's, ...)	ν multiprong	14
Total "Rock" Events:			251

Table 5.1: Contained "Rock" event sample.

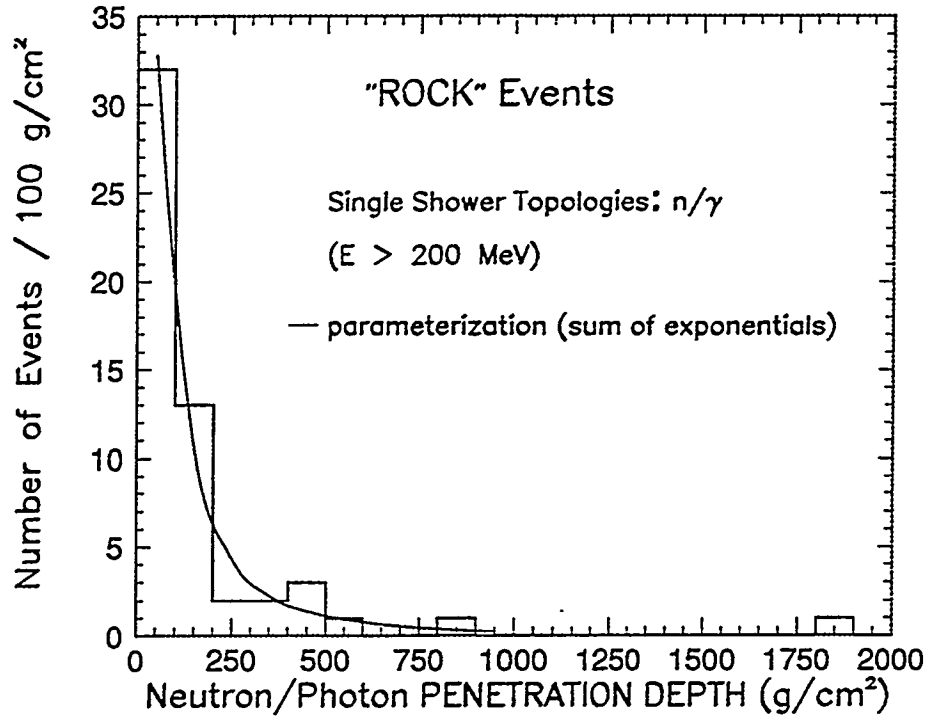

Figure 5.6: Penetration depth from gamma or neutron induced showers of energies > 200 MeV; superimposed is a parameterization based on the sum of two exponentials (solid curve).

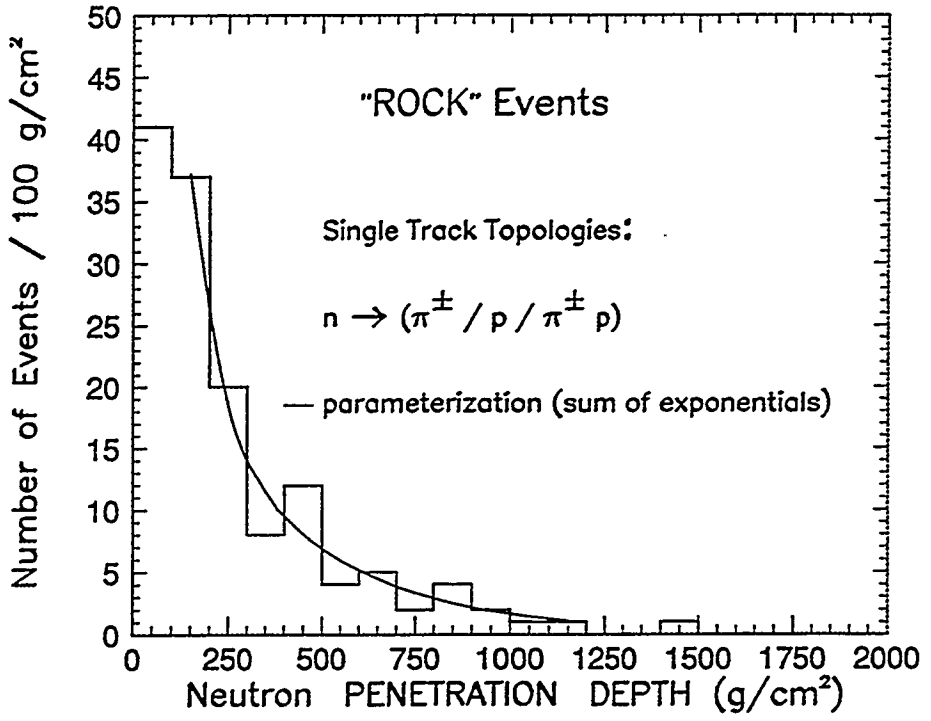

Figure 5.7: Penetration depth from neutron induced topologies, superimposed is a parameterization based on the sum of two exponentials.

Parameters	Showers (Fig. 5.6)	Tracks (Fig. 5.7)
Amplitude Constants		
P1	4.0 ± 0.8	5.0 ± 3.7
P3	1.8 ± 1.4	3.3 ± 1.4
Slopes		
P2	$0.014 \pm .010$	$0.014 \pm .002$
P4	$0.034 \pm .0003$	$0.003 \pm .0001$

Table 5.2: Fitted values for parameterizations of penetration depth distributions.

We find

$$P2 \;=\; 0.0072 \pm 0.0032,$$

consequently

$$\lambda \;\equiv\; (P_2)^{-1} \;=\; 138 \pm 21 \text{ g/cm}^2.$$

Since the mean density of Soudan calorimeter is 1.6 g/cm^3 [5], we conclude that the "effective" neutron penetration depth in the detector medium is

$$\lambda_n(eff) \;=\; 86 \pm 13 \text{ cm}.$$

The Rock single shower events on the other hand, are believed to have two components. The first bin in Fig. 5.6 contains showers initiated by photons emerging from the cavern walls. These "direct" photons have relatively small penetration depths. Events at deeper depths represent the neutron–induced shower component; the penetration depths are longer due to the fact that nuclear absorption lengths are distinctly longer than gamma conversion lengths for hundreds of MeV neutrals

in Soudan material. To separate the relative contributions from photon conversion versus neutron–induced π^0 production, a two–stage fitting procedure has been used. The single exponential form characterizing the neutron interaction falloff described above, has been normalized to the distribution of Fig. 5.6 for depths exceeding 150 g/cm^2. The fitted "neutron curve" is then extrapolated to lower depths. The data excess above the neutron curve is ascribed to the direct photon component. A fit to this excess using a single exponential form (Eq. (5.1)) yields

$$P2 \;=\; 0.024 \pm 0.018.$$

Equivalently,

$$\lambda \;\equiv\; (P_2)^{-1} \;=\; 42 \pm 32 \text{ g/cm}^2.$$

That is,

$$\lambda_\gamma(eff) \;=\; 26 \pm 20 \text{ cm}.$$

5.6 Residual Rock Events in the Quasi–Elastic Samples

With the above observations on Rock event characteristics in hand, we now estimate the amount of background in the golden contained single shower and track samples. Our approach is to fit the penetration–depth distribution of a golden sample to a sum of a Rock–event penetration–depth distribution and a neutrino acceptance curve. For this purpose we use the PAW package which is available in the CERN program libraries. Fig. 5.8 and Fig. 5.9 show the component contributions for the golden single shower (e–like) and single track (μ–like) events, respectively. In Fig. 5.8, the histogram shows the penetration depth in g/cm^2 for e–like events. Superimposed is the neutrino event acceptance curve (dashed line) and, more importantly, the combined parameterization which includes the neutrino acceptance with the n/γ induced background fit from the rock single shower sample (solid line). Using PAW one can integrate the areas under the solid line and the dashed line.

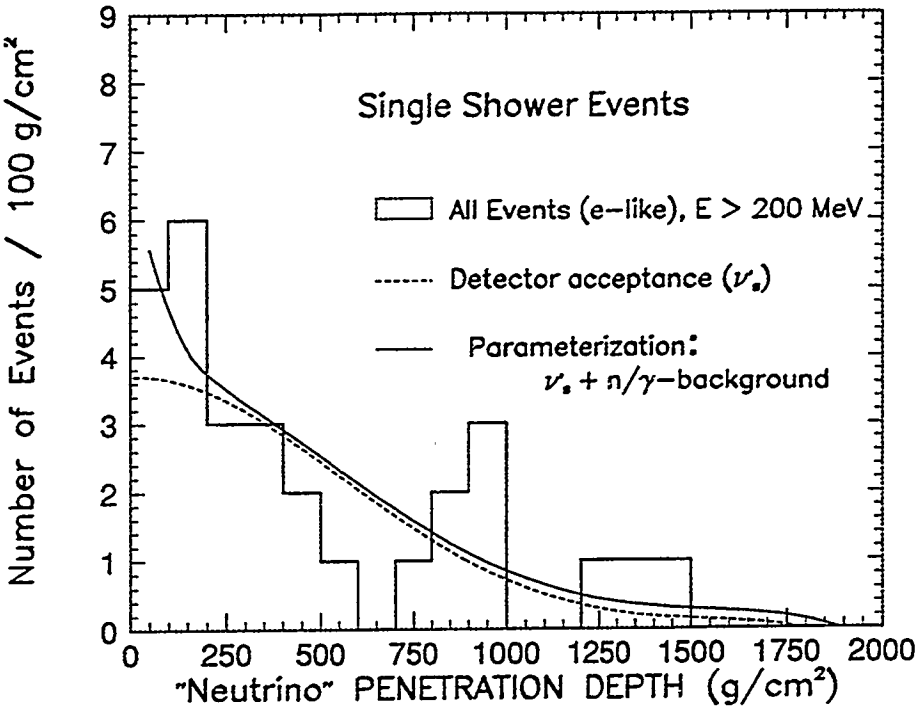

Figure 5.8: Neutrino penetration depth for single shower events.

The difference between the two areas divided by the bin width gives the rock event background count for the neutrino sample. In this way we estimate a background contamination of 2.0 ± 3.7 events for the single shower sample.

The histogram in Fig. 5.9 shows the neutrino penetration depth in g/cm^2 for the single track sample. The shaded areas depict events for which the direction is ambiguous. Superimposed is the detector acceptance (dashed line) and the overall fit, which includes the neutrino acceptance plus the neutron background parameterization of the rock single track topologies (solid line). After integrating to obtain the area under the curves (solid and dashed lines), one obtains (by subtracting the areas and dividing by the bin width) that the number of events due to neutron–induced background in the single track sample is 5.7 ± 3.5 events. In the fits to the gold track events (see Fig. 5.9), the first bin is omitted due to the presence of the Soudan fiducial volume cut (containment cut) on both the gold neutrino candidates and on the Rock events. The fiducial volume cut ($\sim$ 36 g/cm^2) and our binning edge do not coincide; therefore we thought it appropiate to leave out this transition region.

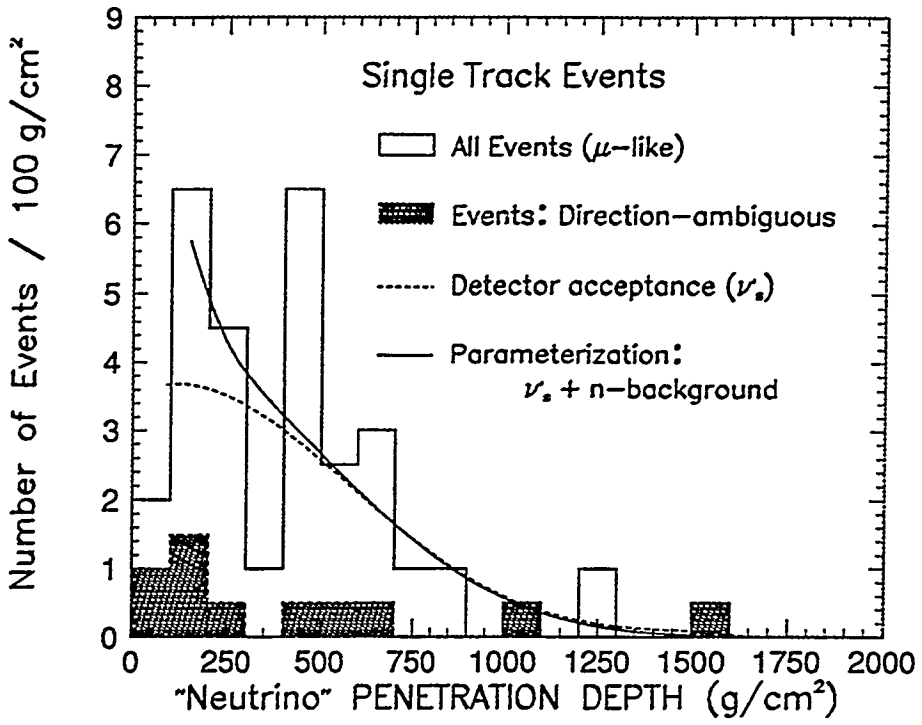

Figure 5.9: Neutrino penetration depth for single track events.

The background contamination in the μ–like sample is found to be slightly larger than in the e–like sample (with large statistical errors). However, both our neutrino e–like and μ–like samples appear reasonably clean. At present, our contamination estimation uses Rock event distributions obtained from the second half–kty exposure only. During 1995 it will be possible to enhance the statistics of the Rock samples by a factor of three to four and thereby strengthen the neutron and gamma background estimates.

5.7 Concluding Remarks

From the Rock event analysis we have obtained estimates of gamma/neutron induced background to our contained neutrino sample. No such detailed treatment of these backgrounds has been reported by other underground experiments. Our analysis shows that the Soudan contained atmospheric neutrino single track and single shower samples contain residual n/γ backgrounds at the level of 12%.

References

[1] O. G. Ryazhskaya, Preprint LNGS–94–110, Gran Sasso National Laboratory, November 1994.

[2] D. H. Perkins, *"Calculation of Neutron Background in Soudan 2"*, Soudan 2 Report PDK–445, August 1990.

[3] *Ibid*, see equation (12) and discussion on page 5.

[4] K. Daum *et al.*, *"Determination of the atmospheric neutrino spectra with the Frejus detector"*, Preprint WUB95–03, to be published in Zeitschrift für Physik C.

[5] D. Cockerill, *"The Soudan 2 Experiment"*, Soudan 2 Report PDK–409, Sept. 1989.

Chapter 6

"Quasi-Elastic" Samples: Properties and Physics Implications

6.1 Introduction

This chapter describes the general properties of the golden contained single track events and single shower events, either without or with proton recoils at the primary vertices, in the Soudan 2 detector.

6.2 Lepton Momentum Distributions

The momenta of event final–state leptons in the detector are calculated using the methods outlined in Sections 4.3 and 4.4. For shower (e–like) events, the number of matched pulses associated with the electron are corrected for polar angle θ_z, then used to calculate the kinetic energy (see Eq. (4.7)). For track (μ–like) events the range of the final state muon is calculated between end points and then corrected for traversal through intermodule gaps.

Figures 6.1 and 6.2 show the lepton momentum distributions for e–like and μ–like events respectively. The shaded regions depict events with visible recoil proton in the final state. The dashed histogram represents our Monte Carlo simulation normalized to the number of events in the data; here the lepton momentum was obtained from the truth table of our 3.45 kiloton–year simulation. Fig. 6.1 also shows e–like events with total momentum less than 200 MeV/c. In Fig. 6.1, the momentum scale is unlabelled above 2 GeV/c reflecting the uncertainty in energy

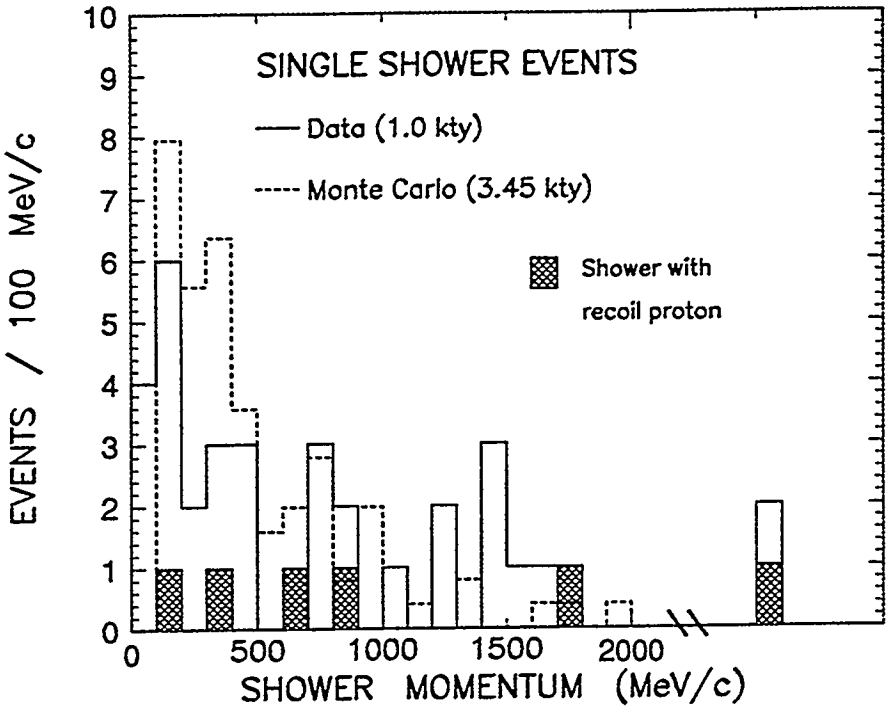

Figure 6.1: "Electron" momentum distribution, where the Monte Carlo has been normalize to the number of events in the data.

estimation for big showers. The agreement between the Monte Carlo simulation and our contained data samples is satisfactory, given the fact that the Monte Carlo is first–generation and the statistics of the data is low. The excess in the first bins in both Figs. 6.1 and 6.2 may be manifestation of the no–shield neutron/gamma background contamination in our contained single track and single shower samples.

6.3 Events with Recoil Protons

As described in Section 4.5, our contained event sample has 9 μ–like events and 6 e–like events with visible recoil protons. Fig. 6.3 shows the recoil proton momentum distribution from all contained single track and shower events (solid line); superimposed is the distribution from single shower events only (shown by the shaded area). As indicated by the distribution, we are unable to observe protons below 450 MeV/c, due to the granularity of the calorimeter. Fig. 6.4 shows the

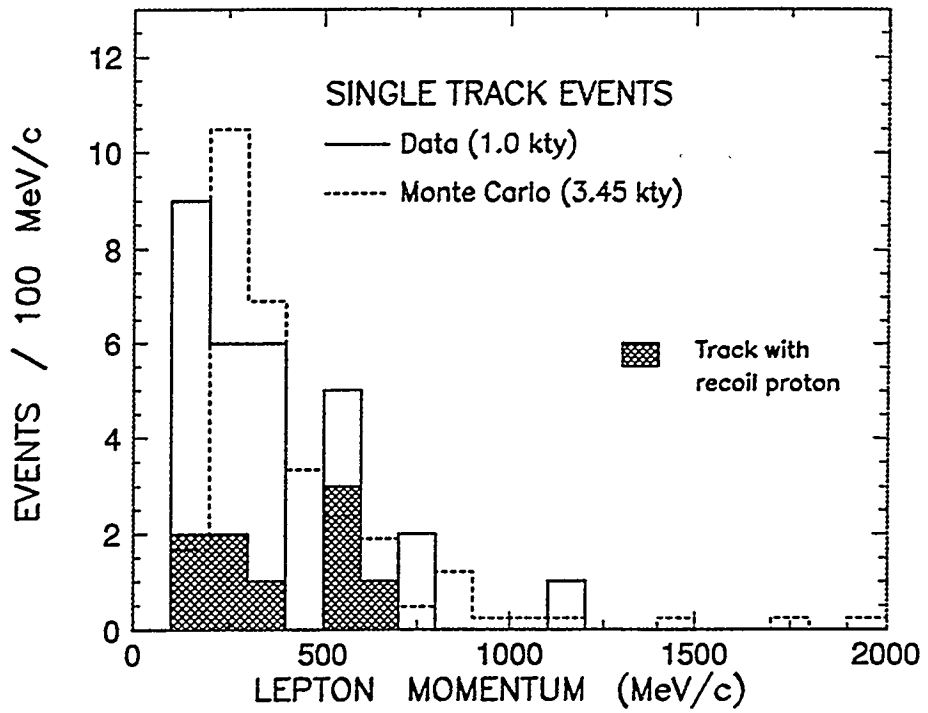

Figure 6.2: "Muon" momentum distribution,where the Monte Carlo has been normalize to the number of events in the data.

cosine of the separation angle between the electron and the proton (solid line). The dashed line represents Monte Carlo $e^- p$ final states, obtained from the Truth Table and normalized to the number of events in the data, where the electron has a momentum greater than 200 MeV/c and the recoil proton a momentum greater than 450 MeV/c. Both histograms are isotropically distributed. On the other hand, Fig. 6.5 shows cosine θ between the muon and the proton for the single track events (solid histogram) and the Monte Carlo simulation (dashed histogram, normalized to the data). Here the Monte Carlo contains only the $\mu^- p$ final state where the muon momentum is greater than 200 MeV/c and the recoil proton has a momentum greater than 450 MeV/c. Both distributions (in Fig. 6.5) are concentrated at negative cosine indicating that the angle between the muon and the recoil proton is usually larger than 78°.

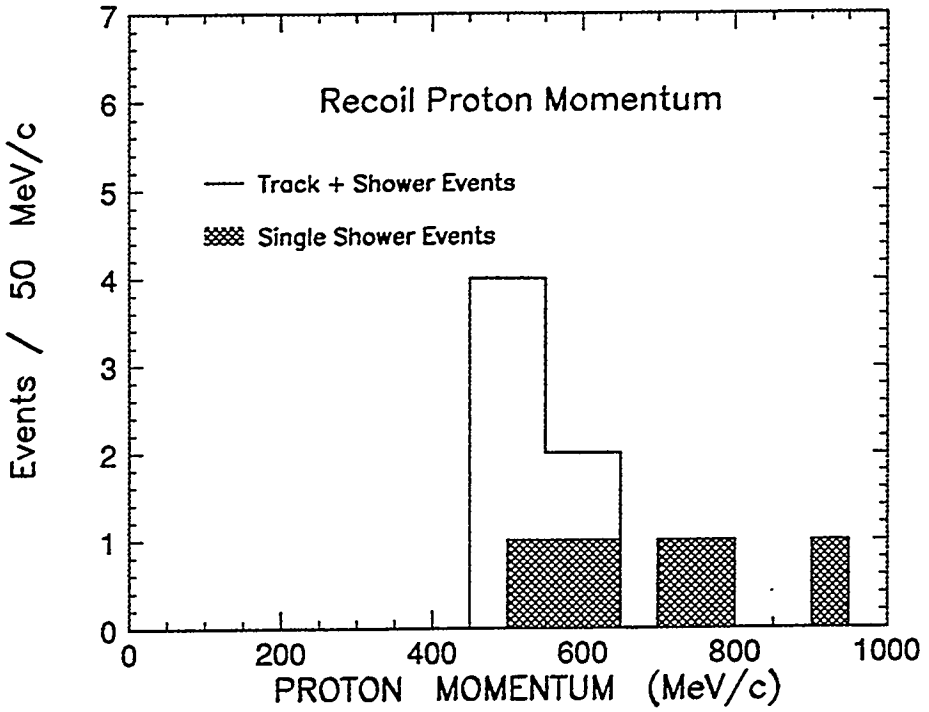

Figure 6.3: Distribution of recoil proton momenta in single track and single shower events.

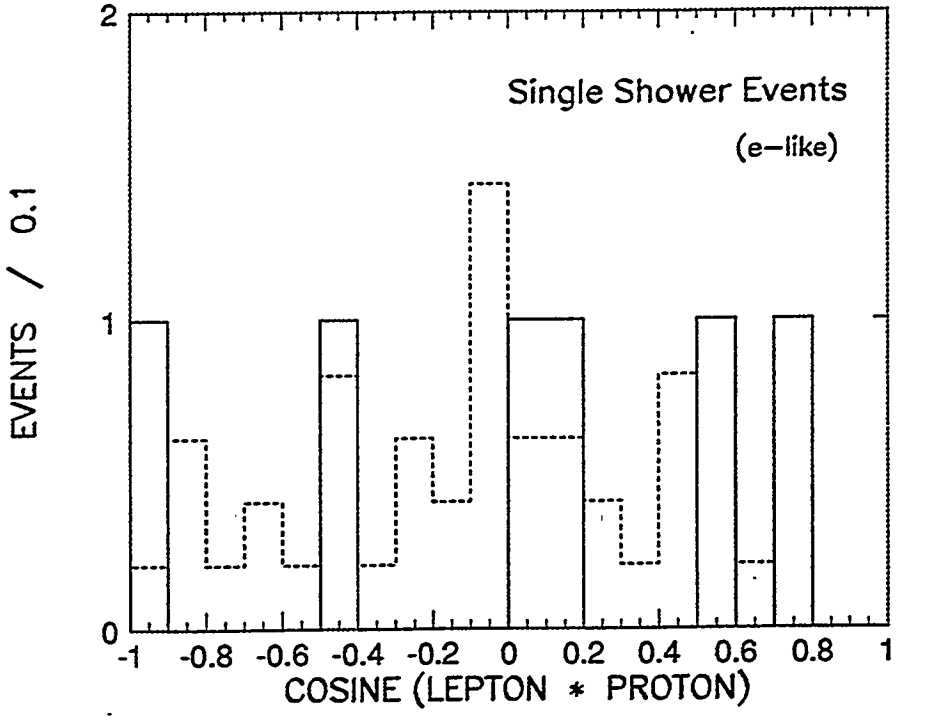

Figure 6.4: Cosine of opening angle between final state electron and proton; for the data (solid line) and for Monte Carlo $e^- p$ final state (dashed line, from the Truth Table) with $P_e \geq 200$ MeV/c and $P_p \geq 450$ MeV/c.

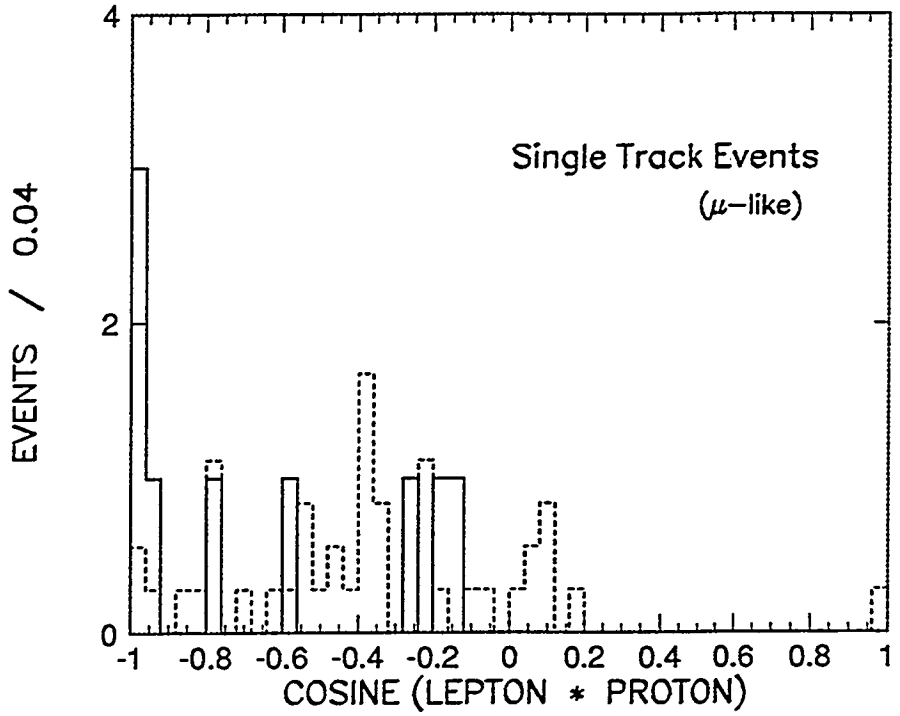

Figure 6.5: Cosine of opening angle between final state muon and proton; for the data (solid line) and for Monte Carlo $\mu^- p$ final state (dashed line, from the Truth Table) with $P_\mu \geq 200$ MeV/c and $P_p \geq 450$ MeV/c.

6.4 Event Directionality

Soudan samples of contained single track (μ–like) and single shower (e–like) events contain more information than is used for the neutrino flavor ratio. One realizable goal is the extraction of the neutrino quasi–elastic interactions (4.1) and (4.3) (see page 74); a fraction of each reaction sample can be expected to contain visible recoil protons. As described in Section 4.6, μ^- tracks almost always undergo nuclear absorption before they decay, whereas μ^+ tracks always decay via $\mu^+ \rightarrow e^+ \nu \bar{\nu}$. As a result, observation of track endpoint decay, in conjunction with observation of recoil protons, enables the net momentum of the final state to be well determined, because all the final state is visible. Additionally, these observations provide discrimination between quasi–elastic ν_μ and $\bar{\nu}_\mu$ reactions.

In the e–like sample, the determination of the final state net momentum is straightforward. As described previously, an electron or photon–induced shower tends to start at a point and then spreads laterally along the direction of shower

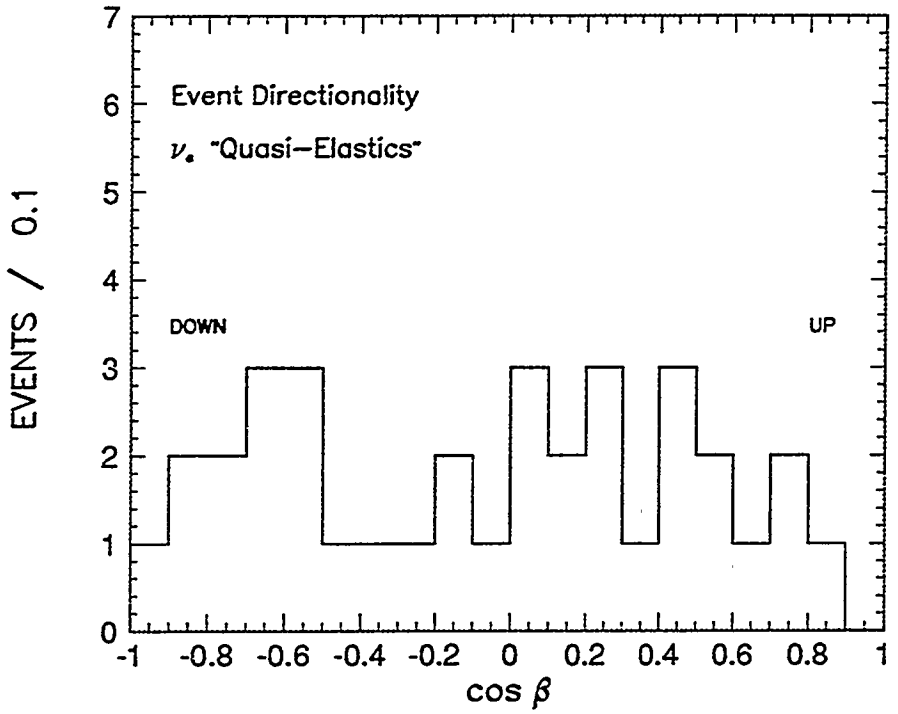

Figure 6.6: Event directionality for ν_e quasi–elastic candidates (e–like sample).

development. A four–momentum vector can be determined for each shower. If the e–like event has a visible recoil proton in the final state, then the corresponding four–momentum vector for the proton is also determined. The net visible final state four–momentum is then the sum of both four–vectors (shower plus recoil). Fig. 6.6 shows the cosine of the angle β between the visible final state three–momentum and the vertical (zenith direction, see Fig. 4.5) for the e–like sample. The distribution appears flat, hence the e–like events are oriented isotropically with respect to zenith. Since cosmic ray induced background events might be expected to point downward and inward to the tracking calorimeter, the apparent isotropy of the sample suggests that background contamination is low.

For the purpose of characterizing the final state net momentum directions for the ν_μ quasi–elastic candidates, we divide that sample into three different sub–samples. For the first group we take all events for which the direction of the muon track is well determined, either by the observation of a visible recoil proton at the vertex, and/or by observation of an endpoint decay shower. A second group contains events

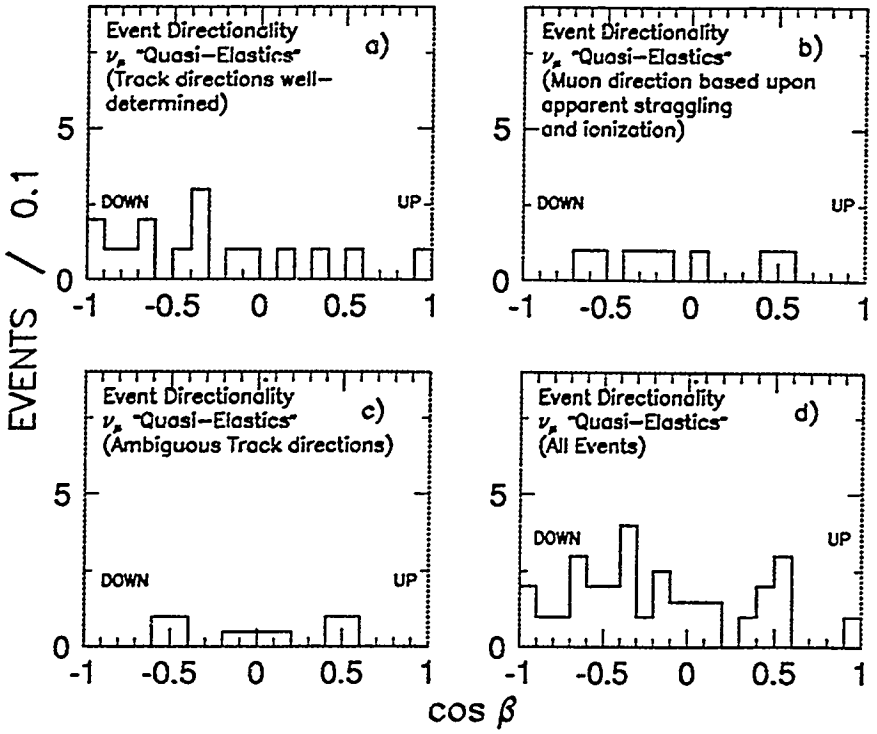

Figure 6.7: Event directionality of the single muon sample: a) well–determined, b) based upon ionization, c) ambiguous, and d) all single–track events.

for which the muon direction is based upon apparent ionization and/or straggling. Here the direction is assigned according to the judgement of the physicist scanner. Finally there is a third sub–sample for which the muon direction is ambiguous due to the fact that each event consists of a single, relatively short track.

Fig. 6.7a shows the cosine of the visible final state momentum relative to the zenith direction ($\cos\beta$), for the μ–like events which have well–determined track directions. Figs. 6.7b and 6.7c show respectively the cosine of the visible final state momenta with respect to zenith for the μ–like sub–sample with muon direction based upon apparent ionization and straggling, and for the sub–sample with ambiguous track directions. In Fig. 6.7c, the two possible track directions are both entered into the histogram, each with a weight of one–half. Fig. 6.7d shows all of the μ–like event sub–samples combined. Figs. 6.7b and 6.7c are flat distributions; consequently Fig. 6.7d reflects the up–down asymmetry of Fig. 6.7a.

Fig. 6.7a shows a mild excess of muon–neutrino events in the downward direction,

which could have two different interpretations. One could say that this mild excess in the downward direction, is evidence that our μ–like sample is contaminated by rock events, initiated by inelastic interactions of cosmic ray muons in the cavern walls. These background events would be predominantly neutron–induced and would preferentially point in the downward direction.

On the other hand, if our μ–like sample is free of background, then this mild effect is evidence for a dearth of muon–neutrino events in the upward direction. The latter effect would be evidence that neutrino oscillations deplete the muon–neutrino flux over distances of 10 to 10,000 kilometers. This latter interpretation is in accordance with the most recent observations of the Kamiokande collaboration with their multi–GeV sample (see Ref. [1]).

When event directionality is being analyzed, the Central Detector angular acceptance must be considered, in particular for the single track events. The triggering requirement (see Section 3.4) eliminates tracks that are nearly parallel to the drift direction or to the wire–plane. In addition, tracks with very few anode hits or with very few cathode hits are difficult to reconstruct. The extent of these acceptance holes is limited to 10°–15° from the horizontal and vertical direction (see Ref. [2]), corresponding to $|\cos\beta| \geq 0.97$ and $|\cos\beta| \leq 0.17$. What is important for our analysis, is the fact that the detector does not have any upward/downward bias for all directions within its acceptance.

6.5 Final State Energy for the Quasi-elastic Events

It is of interest to plot cosine θ of the final state net momentum relative to the zenith against the final state visible energy of the event. Figs. 6.8 and 6.9 show these diplots for the e–like and μ–like samples respectively. The dashed line indicates the Kamiokande separation of contained events for their sub–GeV and multi–GeV analyses. In Fig. 6.8 we show a break in the vertical axis scale at 2 GeV,

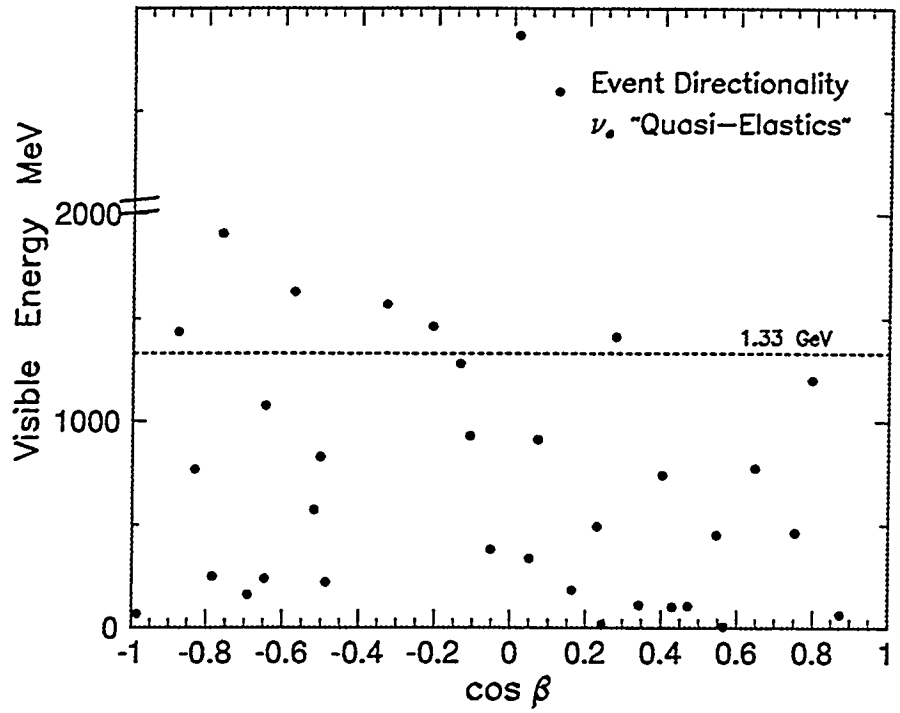

Figure 6.8: Total visible energy versus cosine θ of the visible final state momentum versus zenith angle for the e–like sample.

reflecting the large experimental uncertainty in the energy estimation of big showers. In these Figures the effect of reduced containment in Soudan 2 for energetic muon tracks relative to electron showers of similar energy, is apparent. Energetic muon tracks tend to exit the calorimeter, and so all visible energies in our contained μ–like sample are below 1300 MeV. The open squares in Fig. 6.9 depict those muon tracks for which the orientation of final state net momentum is ambiguous. It is clear that the majority of these direction–ambiguous tracks are low energy tracks (small track lengths).

If one scrutinizes these plots for hints of neutrino oscillations, then Fig. 6.8 may be taken to indicate that, in the multi–GeV region, there exists a mild dearth of electron–neutrinos in the upward direction (5 versus 3 events), but the difference is not statistically significant. We will show in Chapter 7 that our contained multiprong sample (also with limited statistics and containing interacting neutrinos of all flavors) exhibits the opposite trend.

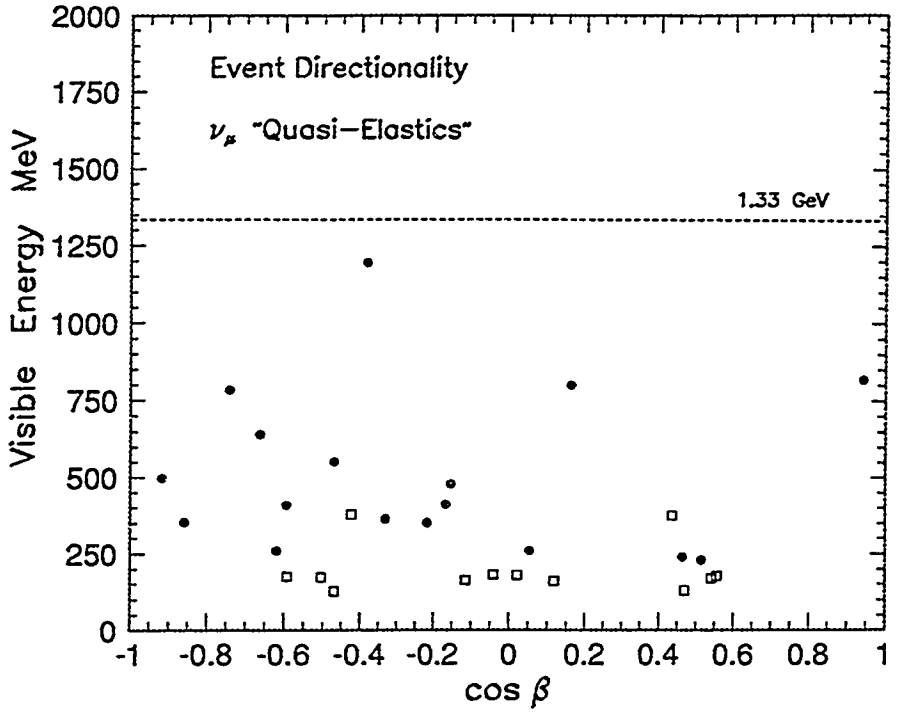

Figure 6.9: Total visible energy versus cosine of the angle between the visible final state momentum and the zenith direction, for the μ–like sample.

6.6 Neutrino ν_μ/ν_e Ratio: Sources of Error

A fiducial volume is defined as the volume containing the collection of nucleons considered for nucleon decay or neutrino interactions. The nucleons outside of this volume are not considered because interactions occurring near the outside of the calorimeter could be confused with detected particles originating outside the calorimeter. The fiducial volume definition allows detection efficiencies to be calculated in terms of fiducial volume exposure. For the Soudan 2 analysis, the fiducial volume contains those nucleons located more than 20 centimeters from the calorimeter steel stack edges in the anode and cathode directions and more than 50 centimeters from the calorimeter stack edges in the drift direction.

For determination of an atmospheric neutrino flavor ratio, sources of systematic errors must be accounted for. In the past, the largest systematic corrections to the atmospheric neutrino flavor ratio were those due to Veto Shield performance. Both the shield random ADJ rate and the shield efficiency can affect the flavor

ratio. Other systematic errors which need to be accounted for in measuring the atmospheric neutrino flavor ratio include the following:

i) Track versus shower misidentification: This error is accounted for implicitly by the scan of the simulated data because the expected neutrino flavor ratio is evaluated in terms of the scan decision and not by the true flavor. Based upon our scanning experience, approximately 14% of all single showers are difficult to distinguish from single tracks, and roughly 3% of single tracks are difficult to distinguish from single showers. If one applies the 200 MeV cut to shower energy, however, less than 7% of single showers are susceptible to possible misidentification.

ii) Low energy electromagnetic noise events: Much effort has been devoted to recognizing and rejecting in software and in scanning various kinds of detector noise events. It is possible that residual backgrounds of this type exist in the data which we are unable to identify. Detector electromagnetic noise events have the appearance – to a scanner – of low energy showers. The requirement that contained showers must have more than 200 MeV of visible energy effectively eliminates all residual noise events. At a future date the steady improvements made in calorimeter module hardware may allow the shower energy cut to be reduced.

6.7 The Atmospheric Neutrino Ratio

The atmospheric neutrino flavor can be estimated, based upon our identification of each event as an electron–neutrino or muon–neutrino interaction. We have isolated a quasi–elastic neutrino sample of 65 contained events, of which 35 events are classified as shower (e–like) and 30 as track (μ–like) events. To eliminate electromagnetic noise background in the low energy shower events, a shower energy cut of 200 MeV is applied to all single shower events. The number of shower (e–like) events is

Ratio–of–Ratios Soudan–2 Event Sample 1.0 Kiloton–year Exposure		
	No. Showers	No. Tracks
Monte Carlo (3.45 kty)	106	158
Total sample (single proton events removed)	35	30
With 200 MeV shower cut	29	30
Rock background subtraction	27	24.3
1^{st} Half Rescan	1	2
Final quasi–elastic samples	28.0	26.3

Table 6.1: Quasi–elastic event samples: Cuts and corrections.

then reduced to 29 (see Table 6.1). Residual "Rock" photon and neutron–induced backgrounds are estimated to be 2.0 ± 3.7 events in the shower (e–like) sample and 5.7 ± 3.5 in the track (μ–like) sample respectively. Additionally, we now include new events obtained in the rescan of the first half kiloton–year exposure; one event is to be added to the shower sample and two events to the track sample. Our final neutrino samples are then 28.0 ± 3.7 shower (e–like) and 26.3 ± 3.5 track (μ–like) events.

We estimate the atmospheric neutrino flavor ratio as follows:

$$R' = \frac{(track/shower)_{Obs}}{(track/shower)_{MC}} = \frac{(26.3/28.0)_{obs}}{(158/106)_{MC}} = 0.63 \pm 0.22 \quad (6.1)$$

where all errors are added in quadrature and are dominated by the uncertainty from neutron/gamma background subtraction.

As with previous determinations using Soudan data, this result is consistent at the 1σ level with the Kamiokande, IMB and Frejus results, but not with the NUSEX results. Our measurement does not show, by itself, a significant neutrino flavor anomaly. Nevertheless, it is interesting that our value of R' is below 1.0, as are the ratio values from the high statistics water Cherenkov detectors. Consequently we are in agreement with the claim that an anomaly is being seen in the atmospheric neutrinos. If this ratio–of–ratios is interpreted as being due to $\nu_\mu \rightarrow \nu_\tau$ oscillations, then the mixing angle would need to be large [3].

6.8 Concluding Remarks

With the detailed event images obtained with the Soudan tracking calorimeter, we can discriminate tracks from showers. The energy estimation of tracks from range is straightforward. However, better algorithms for determining shower energies, particularly energies of large showers (e.g. total number of matched hits bigger then fifty) are clearly needed. The experiment's capability to differentiate protons from charged muons and pions, and to partially distinguish μ^+ from μ^- final states, is providing information which has not been available previously in underground experiments.

The event directionality of the contained single track sample shows a modest deviation from isotropy in the zenith angle distribution, which could be interpreted as evidence for neutrino oscillations.

We have estimated the atmospheric neutrino flavor ratio for one kiloton–year of exposure from the Soudan 2 detector. The flavor ratio R' has been measured by the water Cherenkov experiments to be lower than expected (although lower statistics tracking calorimeter experiments have not previously observed the effect).

The atmospheric neutrino ratio deduced by the analysis of this thesis is 0.94 ± 0.19; the expected neutrino flavor ratio is 1.49 ± 0.10. Therefore the ratio of these ratios is 0.63 ± 0.22. This ratio–of–ratios should be 1.0 in the absence of new physics.

In addition to the flavor ratio, other aspects of atmospheric neutrino reactions can be measured with the Soudan 2 detector. The relative rates of recoil protons observed with e–like versus μ–like events provides one way in which an anomaly originating in nucleon decay could be distinguished from neutrino oscillation scenarios. That is, $p \rightarrow e^+\nu\nu$ proton decay (see Chapter 2) should be a process devoid of energetic protons in the final state. Consequently, one expects there to be a dearth of proton recoils observed to accompany single showers relative to the number observed with single tracks if $p \rightarrow e^+\nu\nu$ is to explain the atmospheric anomaly. In the 1.0 kiloton year data from Soudan 2, we observe $17 \pm 12\%$ of single shower events to have recoil protons whereas $30 \pm 12\%$ of single track events have protons. At present the difference is not statistically significant.

The Soudan 2 data, at the moment, does not exclude our proton decay scenario. On the other hand, the relatively low atmospheric neutrino fluxes proposed by us for our anomaly–as–proton–decay scenario, while still not excluded, are currently regarded as unlikely; the interpretation of the atmospheric neutrino anomaly as originating with neutrino oscillations is generally presumed to be more plausible. Whether or not a "new physics" interpretation for the atmospheric neutrino anomaly is eventually verified, we believe that our proton decay scenario has stimulated useful intellectual activity within the underground physics community. We remain hopeful that data from Soudan 2 will clarify the anomaly within the next few years.

References

[1] Y. Fukuda *et al.*, Phys. Lett. **B 335**, 237 (1994).

[2] N. Sundaralingam, Ph. D. Thesis, Tufts University, June 1993, (see Figs. 4.2, 4.3, and 4.4).

[3] J. Schneps, Nucl. Phys. **B** (Proc. Suppl.) **31**, 307 (1993); M. C. Goodman, Nucl. Phys. **B** (Proc. Suppl.) **38**, 337 (1995).

Chapter 7
Contained Multiprong Events in Soudan 2

7.1 Inelastic Neutrino Interaction Sample

We measure general properties of the contained inelastic (non–quasi–elastic or multiprong) events in the Soudan 2 detector. Pattern recognition techniques reminiscent of bubble chamber event reconstruction are utilized to extract and to analyze physical variables of interest. Inclusive distributions for final state particles are displayed; distributions from the data are compared to those obtained from a Monte Carlo. The Monte Carlo is Soudan's first–generation simulation of atmospheric neutrino interactions in the detector. We examine the ν_μ and ν_e interactions of the sample, and we search for inclusive production of the $\Delta(1238)$ resonance and of π^0's.

7.2 Physics Motivation

As described in Chapter 2, measurements of anomalously low values for the ratio of $(\nu_\mu + \bar{\nu}_\mu)$ to $(\nu_e + \bar{\nu}_e)$ events have emerged during the past seven years in the Kamiokande and IMB–3 water Cherenkov experiments [1, 2]. Here, the crucial observation involves relative rates among samples of contained events. The events composing these samples appear either as single, sharply–defined rings (muon–like), or as single, diffuse rings (electron–like). The majority of single ring events are supposedly quasi–elastic charged current interactions. However, there is a subset of contained underground events which have not been completely investigated in either

Kamiokande or IMB–3, namely the contained multiprong events ("multiprongs"). In a water Cherenkov detector such events appear as multiple ring events. In a tracking calorimeter such as Soudan 2, however, these contained neutrino interactions have two or more prongs (tracks or showers) in the final state from a vertex which is usually well–determined. We propose to investigate the flavor ratio in this event class. We will focus on the following question: *Is the ratio ν_μ/ν_e also anomalously low in the multiprongs?* If the answer is *Yes*, i.e. the *R'* anomaly is confirmed at the high E_ν regime characteristic of multiprongs, then the most plausible explanation is neutrino oscillations, possibly $\nu_\mu \rightarrow \nu_\tau$. On the other hand, if the answer is *No*, then one may infer that:

i) Neutrino oscillations of atmospheric neutrinos are unlikely, since an oscillation effect should exist in the higher energy multiprongs as well as in the lower energy single tracks and showers.

ii) Assuming that the anomaly remains in the E_ν regime below 1 GeV, a possible explanation is proton decay [3].

7.3 Event Topologies

In Section 6.4, the golden contained event sample was divided into three groups based upon topology, namely single track, single shower and multiprong events. Events which appeared to be inelastic (reaction (4.6)) were classified as multiprongs (or non–quasi–elastics). In 1 kiloton–year exposure of the Soudan 2 detector the collaboration has isolated 34 events which belong to the multiprong class (see Appendix D). A first–generation Monte Carlo event sample corresponding to an exposure of 3.45 kiloton–years was also analyzed, which contains 132 multiprong events. As described in Chapter 4, all the events were scanned and digitized with the online software STING, and reduced to a DST (see Appendix E).

In a first scan pass, an attempt to differentiate tracks from showers was made.

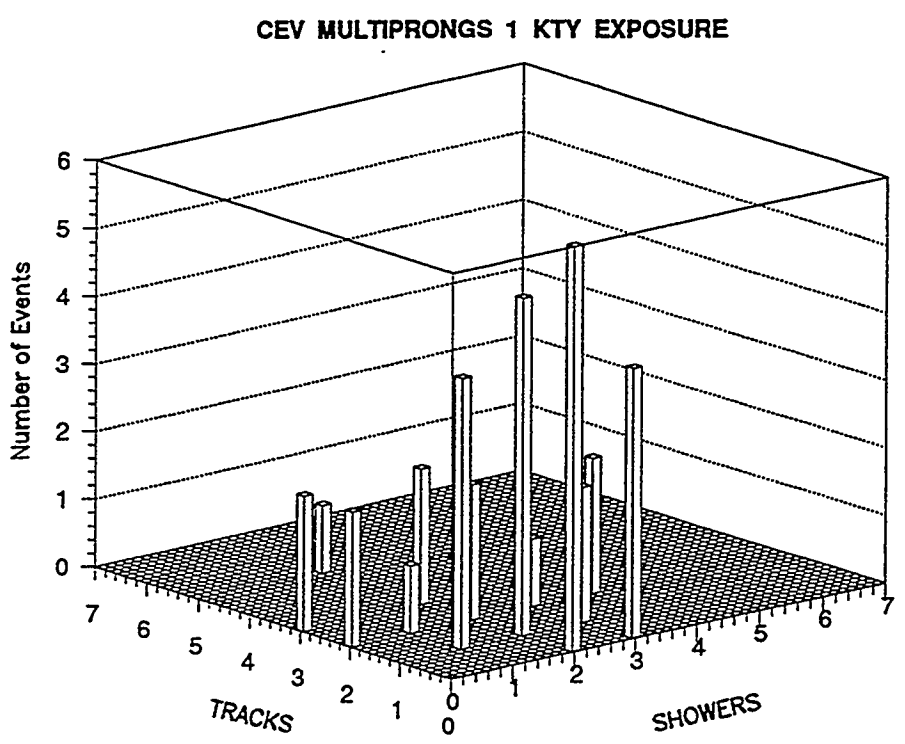

Figure 7.1: Number of tracks versus showers per event, for events in the contained multiprong sample.

This process was repeated several times by the author and by Prof. Mann at Tufts. Finally, with additional guidance from T. Fields of Argonne, agreement was reached on track and shower assignments for each of the multiprong events. Appendix D gives the number of tracks and showers for each event in the contained multiprong sample; the relative populations of the various topologies are shown in Fig. 7.1. The Figure shows a broad distribution over the track–shower combinations, with a mild peaking in the shower region; that is, the multiprong sample has a "tendency" towards showers. However, due to the detector's finite containment capability, we expect to observe more contained energetic showers than contained energetic tracks. The reason is, of course, that more energetic tracks have higher probability to exit the fiducial volume with the result that the parent event will be classified as not contained.

Fig 7.2 shows the topologies (in terms of track–shower combinations) from our 'reconstructed' Monte Carlo event sample. Here the topological distribution from this 3.45 kiloton–year simulation is rather different; the predominant feature is the

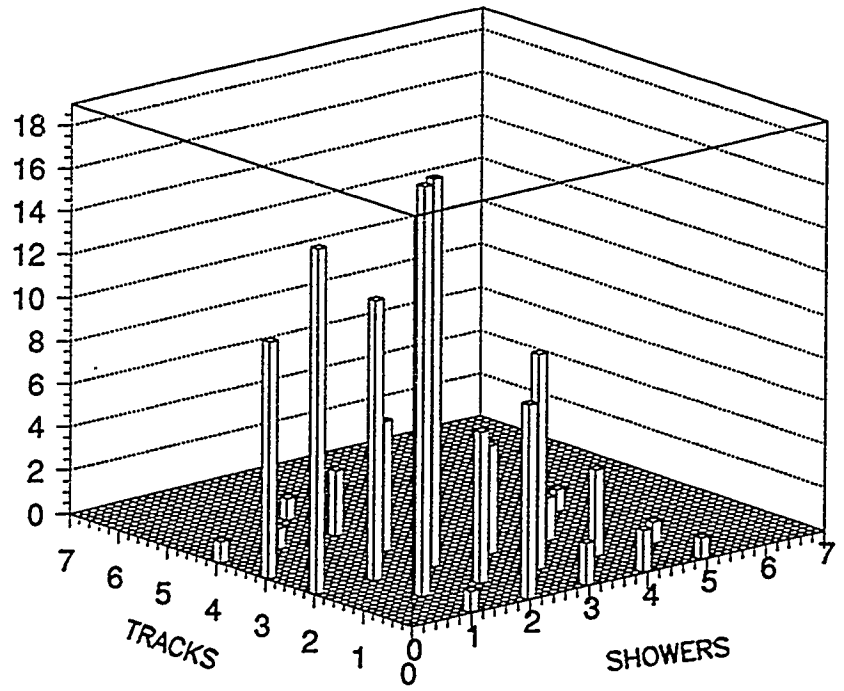

Figure 7.2: Tracks versus showers per event, for multiprong events in the Monte Carlo sample, where events were reconstructed using the same procedure as that applied to the data.

tracks, not the showers. Thus the first–generation Monte Carlo does not reproduce the overall distribution in topology very accurately. The data shows a preference for showers which is not reproduced in the Monte Carlo simulation. It is possible that this disagreement with the Monte Carlo is due to an anomalous ν_μ/ν_e ratio. The predominance of showers in the contained multiprong sample could be an oscillation effect, or a shortcoming of the Monte Carlo, or a background contamination effect. In the future, this disagreement will need to be reexamined with more data and with the second–generation Monte Carlo.

7.4 Visible Energy in Multiprong Events

In a typical multiprong event, the tracks and showers emerge from a common vertex, however in some events there appear track(s) and/or shower(s) which are not connected to the main vertex. These are the so–called "remote tracks" and "remote showers". A four–momentum vector can be determined for each track and

shower separately, and one can obtain the total event four–vector by summing the four–vectors for each track and shower. From the event four–vectors, the visible final state momenta and visible energies are readily extracted. Figure 7.3 shows the visible final state energy for the multiprong events. The solid line represents the 1.0 kiloton–year exposure of data; the dashed line shows the reconstructed 3.45 kiloton-year exposure of the Monte Carlo simulation normalized to the data. As shown by the solid histogram in Fig. 7.3, the multiprong sample contains energetic events, with visible energies extending up to 5 GeV. The Monte Carlo sample appears slightly more energetic, peaking around 875 MeV, whereas the data shows a lower peak around 625 MeV. For the purpose of visible energy estimation, the nucleon mass has not been included. The overall agreement between the multiprong sample and the first–generation Monte Carlo with respect to visible event energy is respectable but less than perfect. The Monte Carlo reproduces the energy spread of the multiprong sample, but it appears that our first–generation Monte Carlo needs to be adjusted to have less energy per event on average.

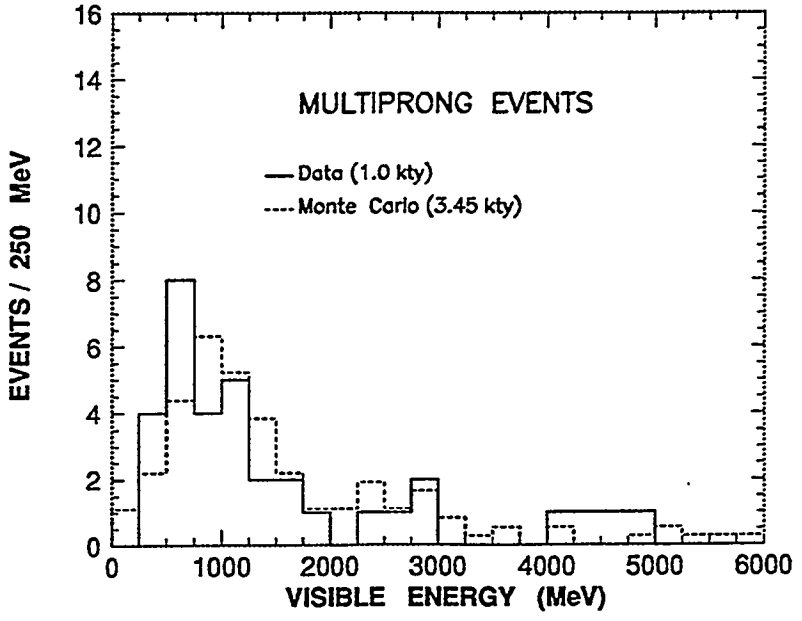

Figure 7.3: Event visible energy in the multiprong sample (Monte Carlo distribution is normalized to the number of events in the data).

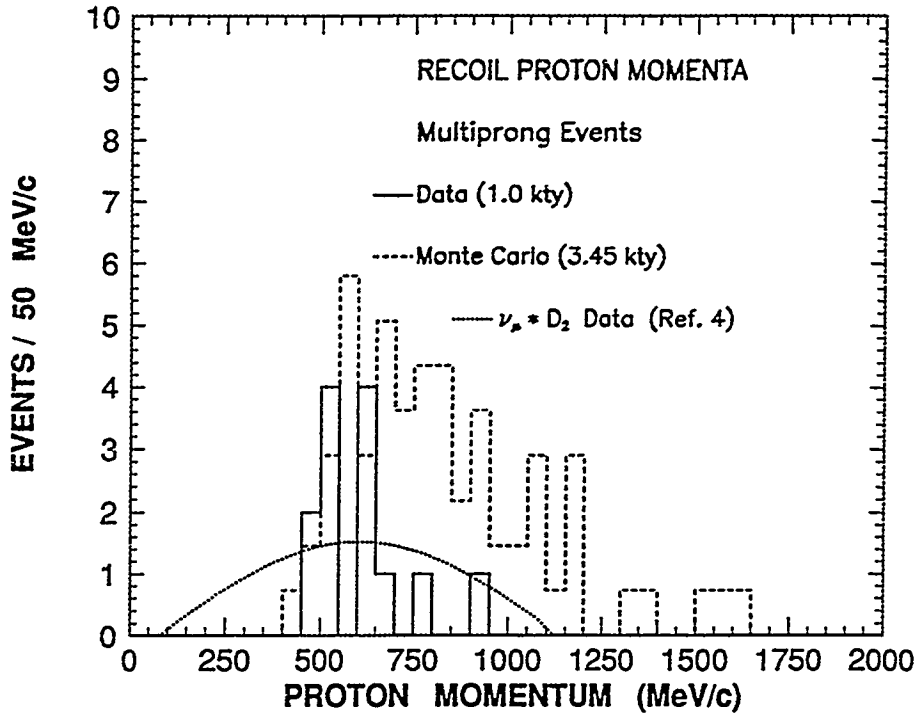

Figure 7.4: Momenta of protons in the multiprong event sample (Monte Carlo distribution is obtained from the truth table).

7.5 Inclusive Proton Momentum Distribution

As described in Section 4.5, we differentiate protons from muons and charged pions according to track ionization. We identify protons as having "heavy ionizing tracks" and "straight trajectories". Applying these criteria, we found 15 tracks in the multiprong sample and 69 tracks in the first–generation Monte Carlo, to be proton tracks. Among the 15 protons in the multiprong sample, two are lone remote proton tracks. The momentum for each recoil proton is based on track range; the range is calculated by digitizing the track endpoints and then correcting for traversal through intermodule gaps.

Fig. 7.4 shows the proton momentum distributions for the contained neutrino multiprongs (solid histogram) and for our Monte Carlo events (dashed histogram) respectively. The dotted line in Fig. 7.4 depicts the proton momentum distribution from ν_μ–deuterium bubble chamber data, where the neutrino energy was weighted

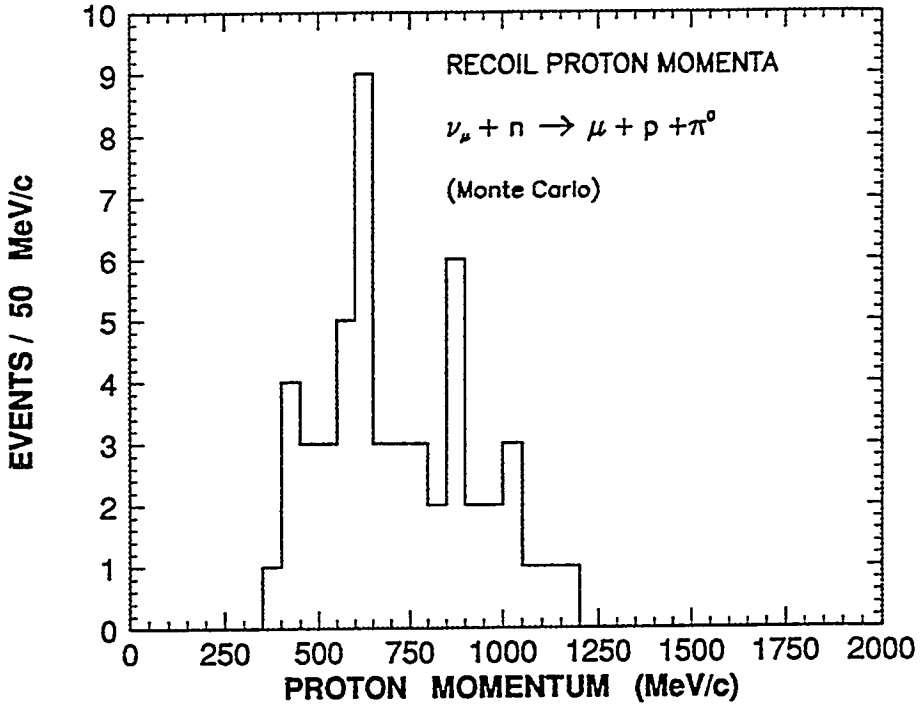

Figure 7.5: Distribution of final state proton momenta from a Monte Carlo sample of charged current single pion production reaction (3.2).

according to the E_ν fall–off of the atmospheric neutrino flux [4]. The proton distribution from Ref. [4], shows a peak at 600 MeV/c with a gradual fall–off beyond 1 GeV/c. In Fig. 7.4 we observe that the Soudan recoil proton momentum distribution may be consistent with the ν_μ D_2 data above 450 MeV/c, but the Monte Carlo clearly produces too many energetic protons.

We have also studied protons produced in exclusive charged current single pion production events. Figures 7.5 and 7.6 show the proton momentum distributions from the charged current single pion production reactions (3.2) and (3.3) respectively (see page 70). If one compares these distributions with the contained multiprong events or with the bubble chamber data, no major discrepancies are apparent. These exclusive channel proton momentum distributions from the Monte Carlo simulation roughly coincide with, but are slightly more energetic than, the inclusive proton momenta from Soudan multiprong events and also the flux–weighted inclusive proton momenta from the bubble chamber data.

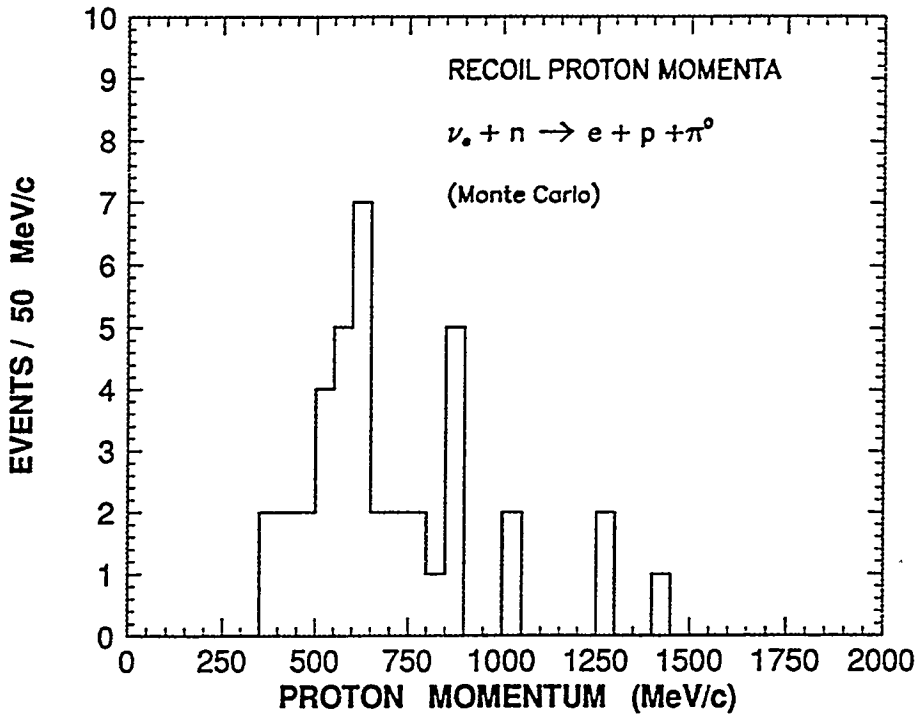

Figure 7.6: Proton momenta in Monte Carlo, from charged current single pion production reaction (3.3).

7.6 Pion and Muon Momentum Distributions

Our 34 multiprong event final states contain 44 tracks, of which we identify 15 to be proton tracks. The remaining 29 tracks include many which are ambiguous between charged pions and muons. Discrimination between muons and pions can be made using the fact that pions can scatter while muons cannot. An initial classification of tracks was carried out according to information available upon scanning. Specifically, we looked for hadronic behavior exhibited by the tracks. Based upon scan table observations we assign mass(es) to each track. A lightly ionizing, scattering track – any track which is visibly deflected from its original course – is assigned the pion mass. Lightly ionizing, long (e.g. > 100 cm), straggling tracks are assigned the muon mass. The remaining tracks are ambiguous between charged pions and muons, and are assigned both the pion and muon masses.

For each track, the path length is summed up to the end–point and then corrected for traversal through intermodule gaps. The total track length through Soudan

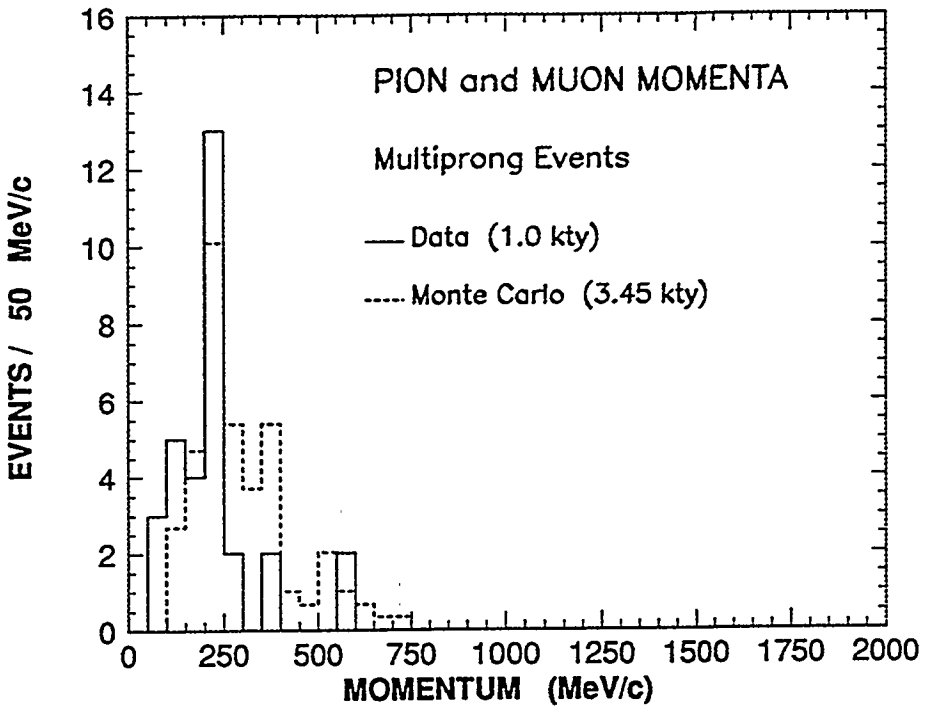

Figure 7.7: Pion and muon momenta from the multiprong event sample (Monte Carlo distribution is normalized to the number of events in the data).

material is taken to be the "range" of the track; the track momentum at the event vertex is then calculated using range–energy relations. Fig. 7.7 shows the pion and muon momentum distributions for the multiprong events; the solid line represents the 1.0 kiloton–year exposure of the data, the dashed line depicts our Monte Carlo simulation which is normalized to the number of events in the data. Fig. 7.7 indicates rough agreement between the multiprong and the Monte Carlo samples. Similar distributions can be found in reference [4], where the inclusive distribution of final state μ^- momenta from flux–weighted ν_μD events is observed to resemble the inclusive final state π^+ momentum distribution.

7.7 Shower Momentum Distribution

Using the methods described in Section 4.3, we have analyzed the 63 showers in the multiprong sample. For each shower, the number of matched pulses associated with the electron or photon was corrected for the polar angle θ_z, and then used to

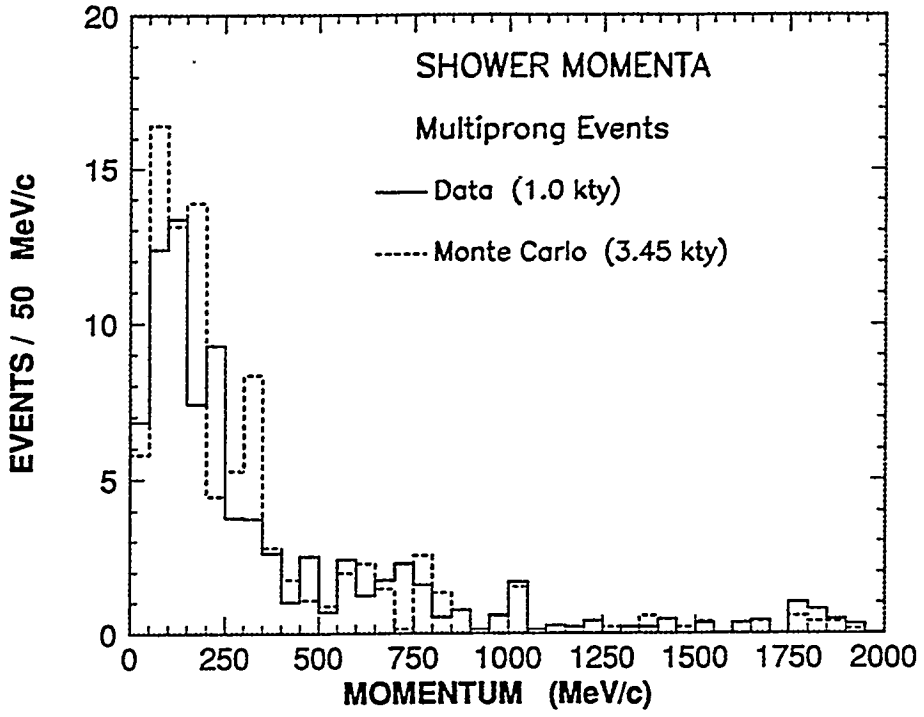

Figure 7.8: Momenta of showers in multiprong final states (Monte Carlo distribution is normalized to the number of events in the data).

determine the shower energy via Eq. (4.7).

Figure 7.8 shows the shower momentum distributions for the contained multiprong events. As with previous plots the solid line shows the data, while the dashed line depicts the Monte Carlo simulation normalized to the data. Comparing the distributions, one sees that the overall spread in momentum is reproduced by the Monte Carlo, but there is some difference in the shape of the distributions.

7.8 Search for π^0 in Multiprong Events

The π^0 decays electromagnetically into 2γ (98.8%) and $e^+e^-\gamma$ (1.2%) with a mean life $\sim 10^{-17}$ s. All possible pair combinations of showers in each event are examined for association with a parent π^0. Using the methods outlined in Section 4.3, a four–momentum vector for each shower is determined. For each shower, the number of matched pulses associated with the electron or photon were corrected for the θ_z angle and then used to determine the kinetic energy.

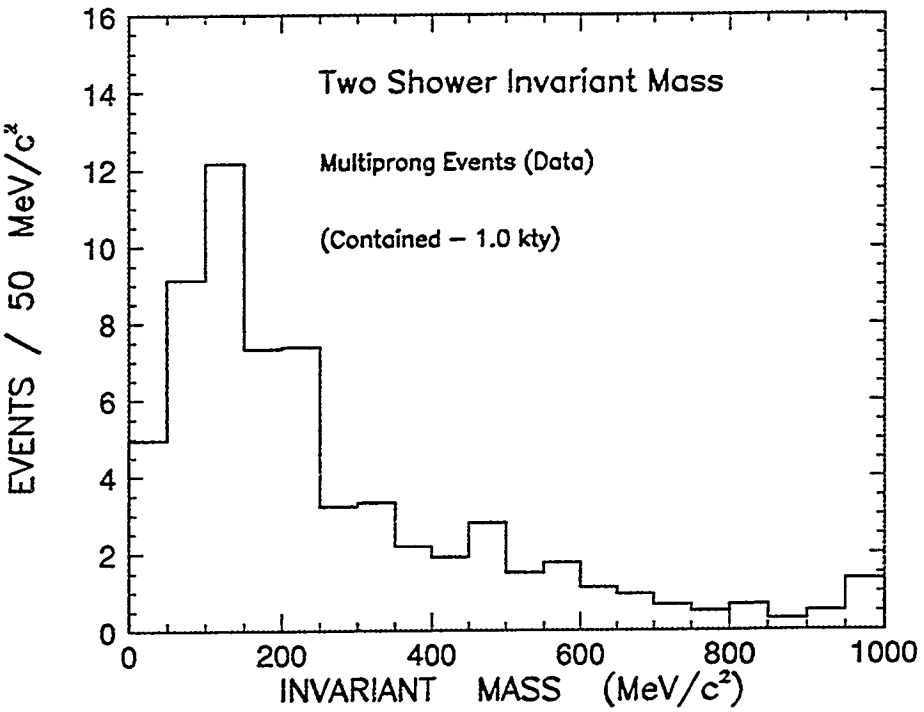

Figure 7.9: Inclusive two shower invariant masses from the multiprong event sample; plotted are all pair combinations weighted by the (inverse) number of measured vertices.

Fig. 7.9 shows the two shower invariant mass for all possible combinations weighted for all vertices (one over the number of vertices) and for all possible shower combinations (one over the number of combinations). Fig. 7.10 shows the two–shower invariant mass for all possible combinations with the "best" vertex selection. In general, a scanner assigns vertices interactively using the STING program from which he is allowed to designate "the best" according to his visual extrapolation of all tracks and showers to a converging point in space. Both Figs. 7.9 and 7.10 peak near the nominal position of the π^0 invariant mass. The bin size in both Figures is 50 MeV/c^2; candidate π^0 pairs lie in the range 80–200 MeV/c^2.

We have examined shower pairs in Monte Carlo multiprong events with the same procedure as above. Figs. 7.11 and 7.12 show the Monte Carlo two–shower invariant masses for all possible combinations weighted by the number of vertices and for the best vertex choice respectively. In both of the Monte Carlo distributions, we see peaks which are lower – by one bin – than the data. We do not have a ready

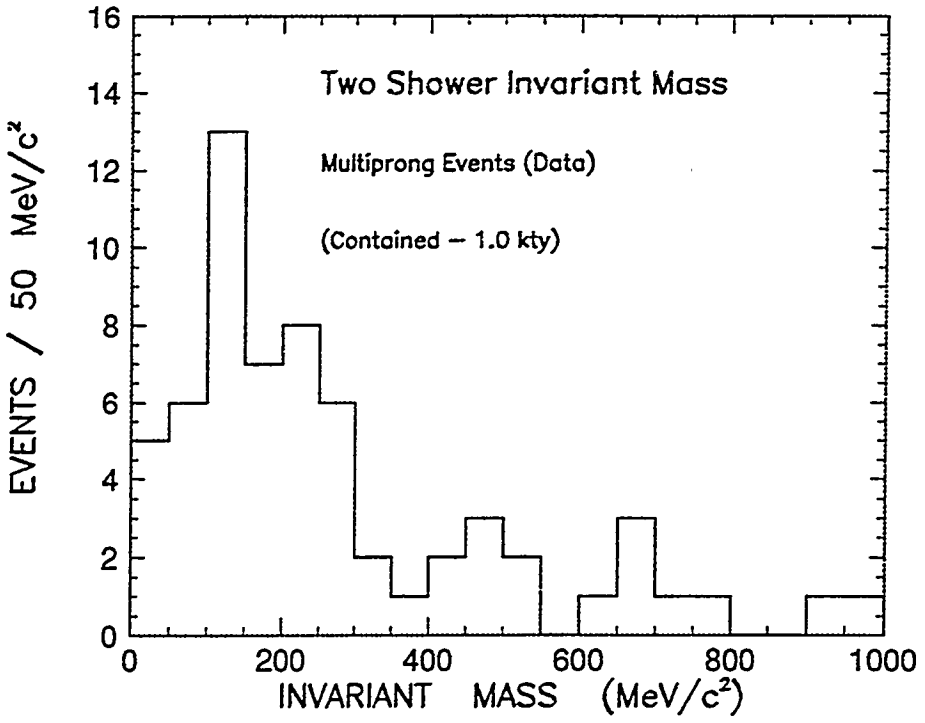

Figure 7.10: Inclusive two shower invariant masses from the multiprong data, where the "scanner's choice" vertex is used.

explanation for this effect.

We have further examined representative exclusive final states using Monte Carlo, for π^0 signatures. We analyzed the single pion production channels (3.2), (3.3) and (3.4) respectively (see page 70). The three reactions probe different aspects of π^0 signal reconstruction. For example, in the first neutrino reaction, (3.2), all the final state particles should be visible in the calorimeter. In particular, the spatial location of the vertex of the event is visually well–determined. Here one may have a straight, highly ionizing track (proton), plus a minimum–ionizing track emerging from a common vertex, with one or two showers from the π^0 decay. For a summary of the topologies encountered in this particular example, see Appendix C. A π^0 signal is observed, using 62 events of reaction (3.2). Fig. 7.13 shows the two–shower invariant mass for the interaction $\nu_\mu + n \rightarrow \mu^- + p + \pi^0$ using our best vertex selection; a clear peak in the π^0 region is seen.

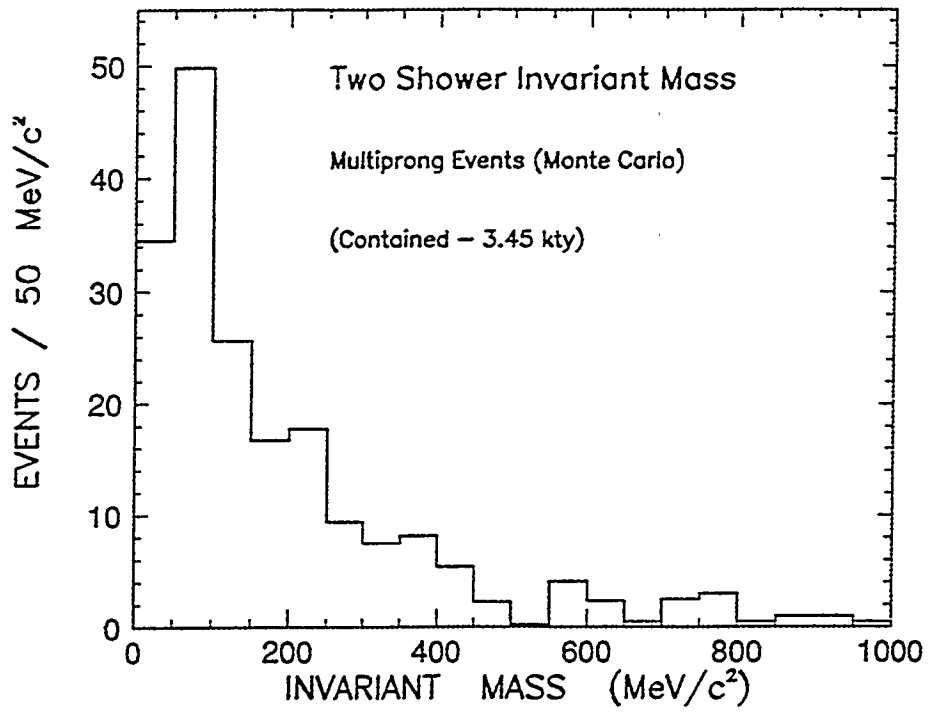

Figure 7.11: Inclusive two shower invariant masses for the Monte Carlo multiprong sample.

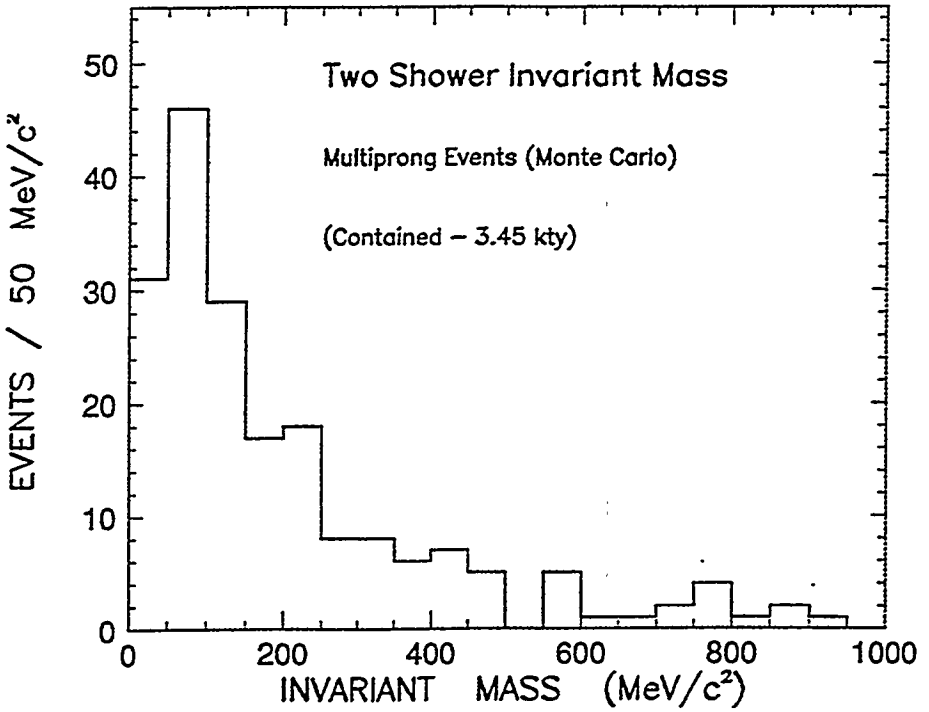

Figure 7.12: Inclusive two shower invariant masses for the Monte Carlo multiprong sample, using the scanner's choice vertex.

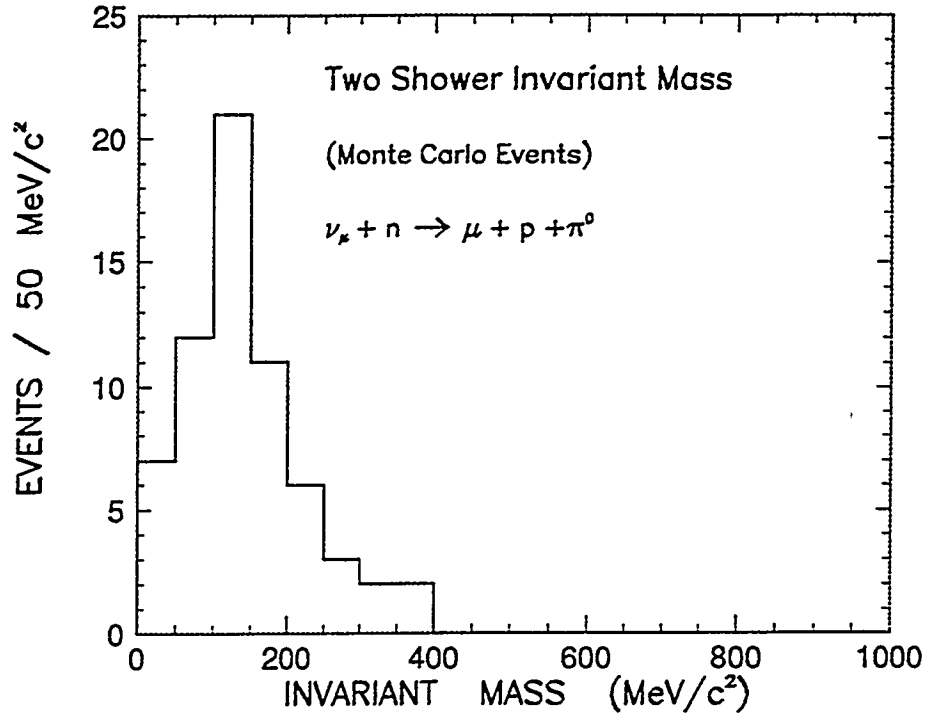

Figure 7.13: Two shower invariant masses from Monte Carlo simulation of reaction 3.2, using the scanner's choice vertex.

In our simulation of neutrino reaction (3.3), again all produced final state particles should be visible in the calorimeter. However the vertex position is less constrained than in our first example. Here we expect to see a straight, heavily–ionizing track plus several showers (one from the prompt electron and one or two showers for the π^0). In principle, at least one of the showers should connect with the proton track at a common vertex position. However one sometimes finds a track plus several remote showers, making the vertex position more ambiguous than for reaction (3.2). Appendix C summarizes the different topologies encountered with this final state. The π^0 signal obtained from reactions (3.3) is from 91 events. Fig 7.14 shows the two shower invariant masses for the e^- p π^0 events weighted for all possible combinations and using our best vertex selection. Here the invariant mass distribution is much broader than that of Fig. 7.13, arising from the uncertainty in the vertex determination and from the "gamma" shower combinatorics, as no attempt was made to distinguish prompt charged current $e^{\pm}$ from showers of gammas from π^0 decay. Nevertheless, a smaller peak is discernible in the π^0 region, indicating that among

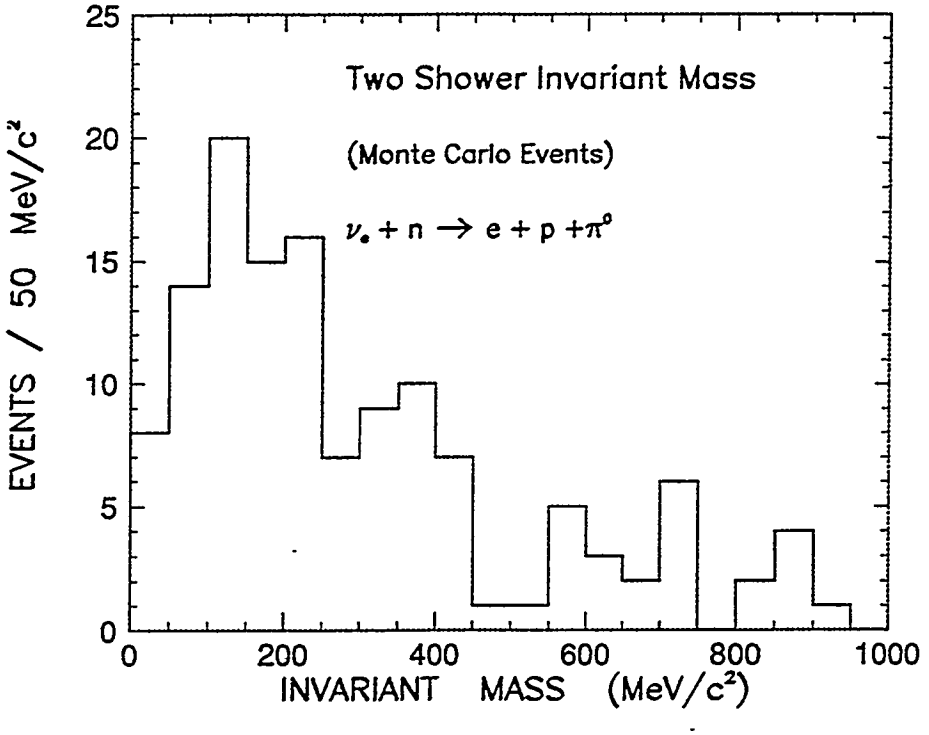

Figure 7.14: Two shower invariant mass for the Monte Carlo multiprong sample, using the scanner's choice for most plausible vertex location.

all the shower pair combinations there are some which originate with π^0 decay.

Our third Monte Carlo neutrino sample consists of examples of reaction (3.4). This is a neutral current final state for which the recoiling nucleon is a neutron, and so two out of the three final state particles are usually unobserved in the calorimeter. We are left with only the decay photons from the π^0 as evidence for the occurrence of the reaction. The vertex location is not well-determined; we depend upon extrapolation of the direction of the decay showers in order to estimate the location of the vertex. In fact, in some events the apparent topology is something other than two showers (see Appendix C). Fig. 7.15 shows the two shower invariant mass distribution from the ν n π^0 final states. In each event the pairs are weighted by the (inverse) number of combinations, and the scanner's choice vertex is used. The distribution in Fig. 7.15 is broad and no π^0 peak is discernible, indicating that our reconstruction is sensitive to the vertex determination. We believe that the ambiguity in the vertex location compromises the determination of shower directions, giving rise to "washout" of the π^0 peak.

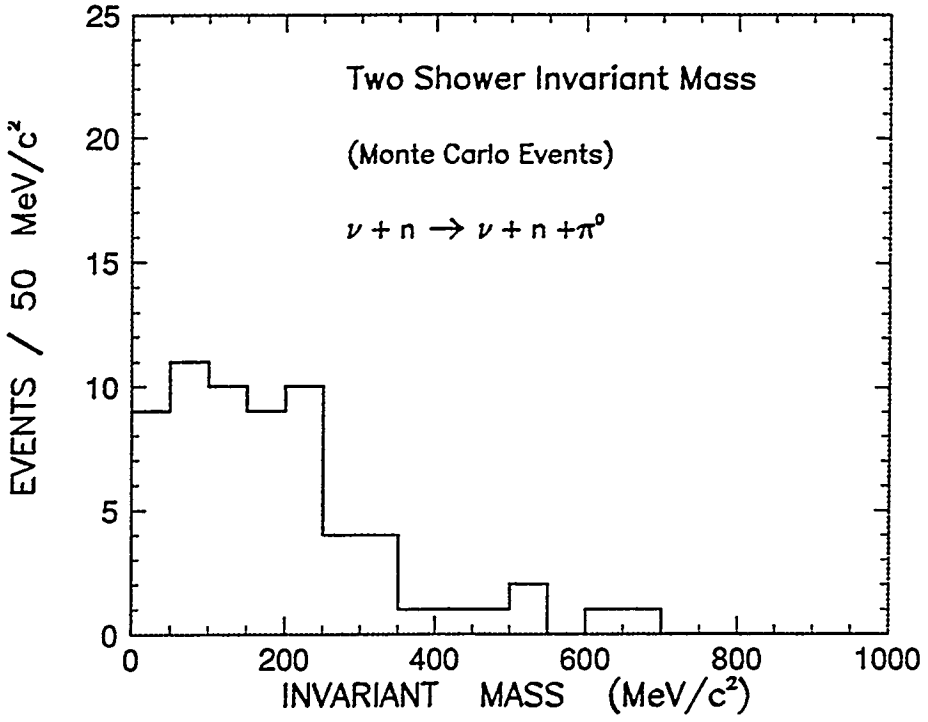

Figure 7.15: Two shower invariant mass for the Monte Carlo multiprong (ν n π^0) sample, using the scanner's choice for most plausible vertex.

Figs. 7.13, 7.14 and 7.15, show that our ability to reconstruct π^0's depends upon how much of the final state is imaged. This affects not only the initial recognition of the final state, but also the extrapolation in space of tracks and showers into the primary vertex region. The more tracks and showers which are imaged, the better the vertex determination is. A lesser problem arises with overlapping of tracks and showers; this situation can make the reconstruction of a final-state quite laborious, however with sufficient care taken, most final states can be untangled.

Based upon the distributions in Figs. 7.9 and 7.10, we conclude that we can and do observe inclusive π^0 production in the Soudan multiprong sample. In order to estimate our experimental resolution for extracting the π^0 signal using two-shower invariant mass, we have examined the optimal case represented by the Monte Carlo simulation for reaction (3.2) (see Fig. 7.13). We fit the invariant mass distribution using a gaussian function, as shown in Fig. 7.16. For the π^0 signal the fit yields a mean value of 124 ± 13 MeV/c^2, with a width (one sigma) of 84 ± 19 MeV/c^2. Our values are lower and broader than the π^0 invariant mass distribution obtained by

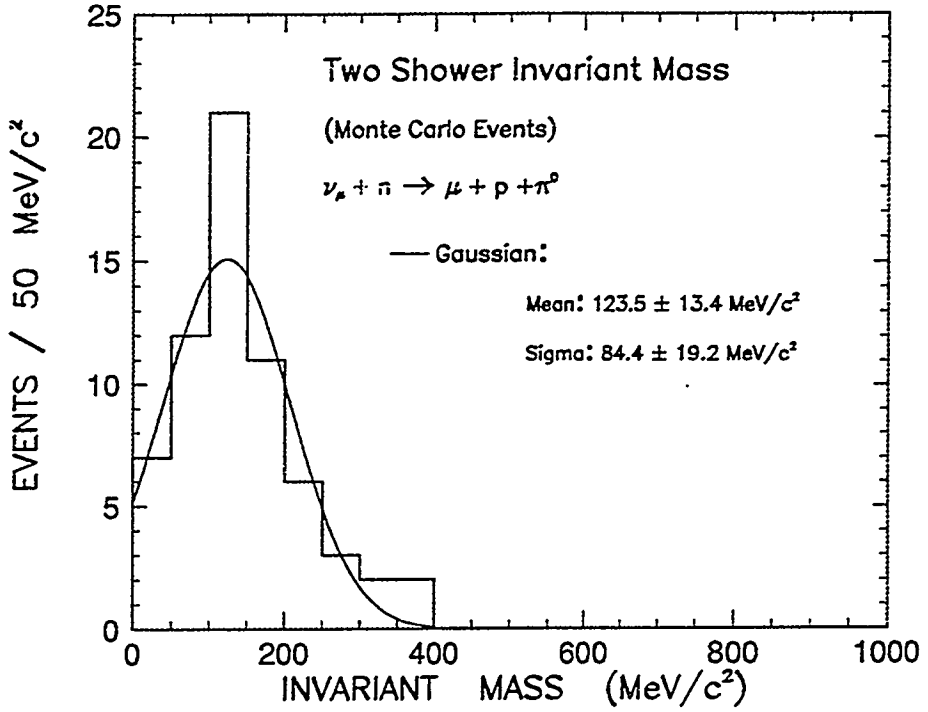

Figure 7.16: Two shower invariant mass for the Monte Carlo multiprong μ^- p π^0 sample, using the "scanner's choice" vertex.

Garcia–Garcia from charged pion charge exchange vertices in ISIS test beam data ($M_{\pi^0} = 136 \pm 3$ MeV/c^2, $\sigma = 40$ MeV/c^2 [5]).

It is possible in principle to distinguish charged current $e^{\pm}$, which occur "promptly" at the primary vertex, from photon–induced showers, on the basis of absorption length. This kind of separation would presumably improve the extraction of final state π^0's in charged current electron–neutrino reactions such as (3.3). A study of this separation is presented in the next chapter.

7.9 Search for $\Delta(1232)$ Resonance Production in Neutrino Final States

At low energies, pion–nucleon collisions produce a very prominent resonance, the $\Delta(1232)$. The Δ is an I=3/2 resonance and has four charge states Δ^{++}, Δ^{+}, Δ^{0} and Δ^{-} with corresponding quark content uuu, uud, udd, and ddd. The resonance appears just above the pion–nucleon threshold, and its width is about 180 MeV. In

neutrino interactions recorded in liquid hydrogen and deuterium bubble chambers, the Δ resonance is observed to be very prominent in single pion production reactions. This resonance may be expected to be prominant also in the neutrino–iron interactions recorded in Soudan 2, although final state rescattering and detector resolution limitations could conceivably wash out the resonance signal.

In multiprong events, one can have an assortment of tracks and/or showers originating from a primary vertex. Each track can then evolve, creating one or multiple secondary vertices. We have examined pion–nucleon combinations at the primary vertices. Using the methods outlined in Sections 4.3 and 4.4, a four–momentum vector is calculated for each track and shower; all possible proton–pion combinations are then formed for each event. Figs. 7.17 and 7.18 show the proton–pion ($p\pi^{\pm}$ and $p\pi^0$) invariant masses for contained multiprong events from the data (solid histogram) and from the Monte Carlo events (dashed histogram, which is normalized to the data) respectively. In both Figs. 7.17 and 7.18, the invariant mass distributions are relatively flat, with a tendency to pile up on the lower side of the nominal Δ resonance mass. On the other hand, the Monte Carlo samples exhibit weaks peaks on the low–mass side of the $\Delta(1232)$. Given that the width of the resonance is 200 MeV, the peaks in both Figs. 7.17 and 7.18 could be considered as a manifestations of Δ^{++} and Δ^{+}.

Fig. 7.19 shows the $p\pi^0$ invariant mass from 55 Monte Carlo events of the reaction $\nu_l\ n \rightarrow l^-\ p\ \pi^0$, where l^- is the lepton (e^- and μ^- respectively). The inclusive distribution (Fig. 7.19) shows a clear peak at the low–mass side of the Δ^0 resonance (even after allowing for a width of 200 MeV/c^2). Again, a possible explanation of this low Δ^0 resonance position may reside with limitations of the Garcia–Garcia algorithm.

Fig. 7.20 shows the proton–"pion" invariant mass for the contained neutrino single track events (solid histogram) and for the contained rock single track events (dashed histogram) respectively. The solid histogram depicts those 9 events in the

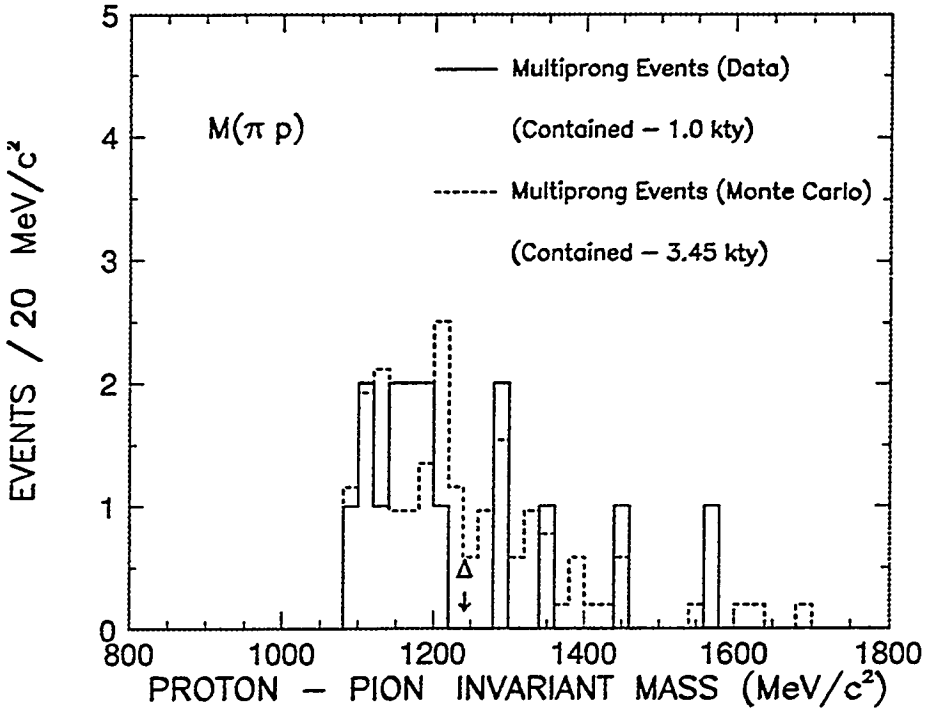

Figure 7.17: Proton–pion invariant mass; solid line shows data, dashed line is from Monte Carlo normalized to data.

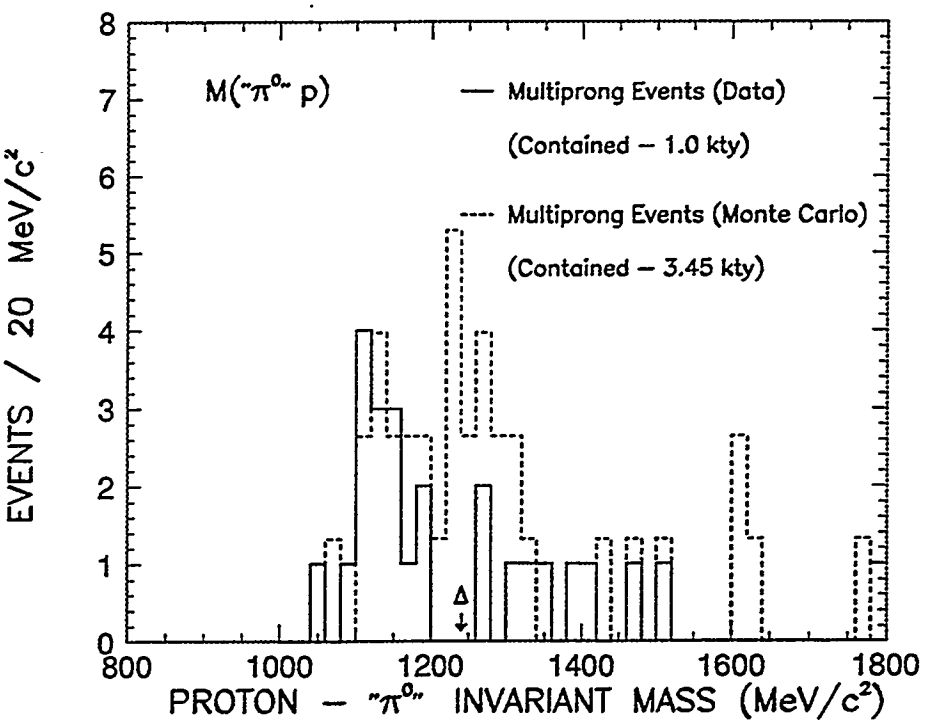

Figure 7.18: Proton–pizero invariant mass; solid line shows data, dashed line is from Monte Carlo normalized to data.

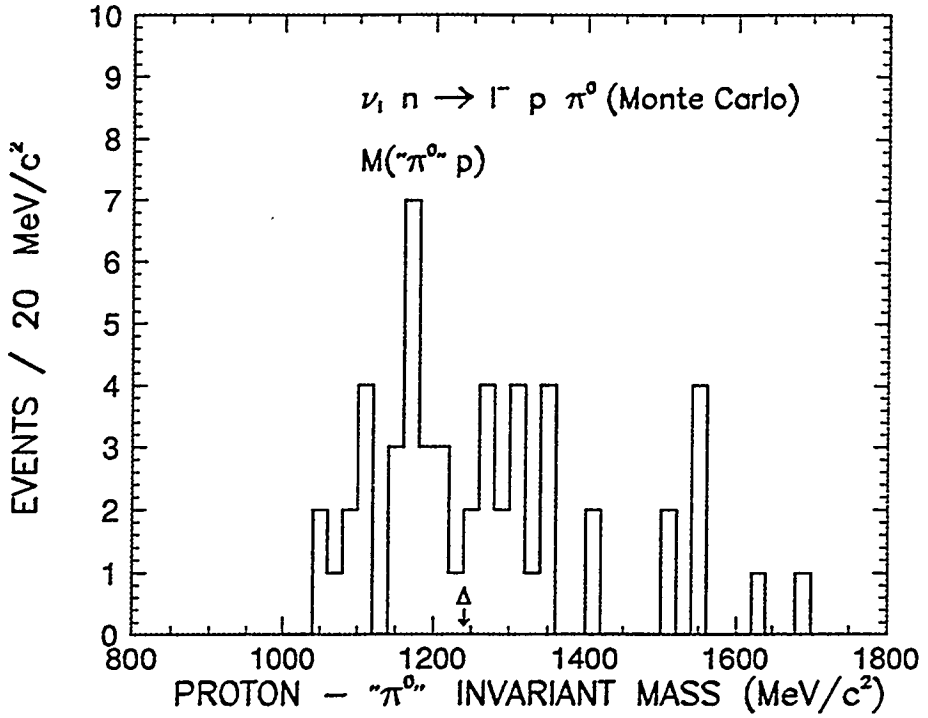

Figure 7.19: Invariant mass of p"π^0" from Monte Carlo events.

contained neutrino single track events which have a visible recoil proton in the final state. The events are believed to be neutrino–induced events, however the muon mass has been changed to the pion mass. Our purpose here is to examine whether the 9 events distribute differently from the neutron–induced rock events. The solid histogram of Fig. 7.20 shows that in the majority of the events the invariant mass is above 1400 MeV/c^2; only 3 events around the Δ^{++} resonance position. On the other hand, the dashed histogram of Fig. 7.20, which shows proton–pion combinations from the rock sample, has a peak on the low side of the Δ^{++} resonance mass. From Fig. 7.20 one sees that the contained single track (neutrino–induced) events have invariant masses which are rather different from those obtained with Rock events, supporting our view that Soudan contained single track events are free from gross contamination by neutron events which the shield failed to tag.

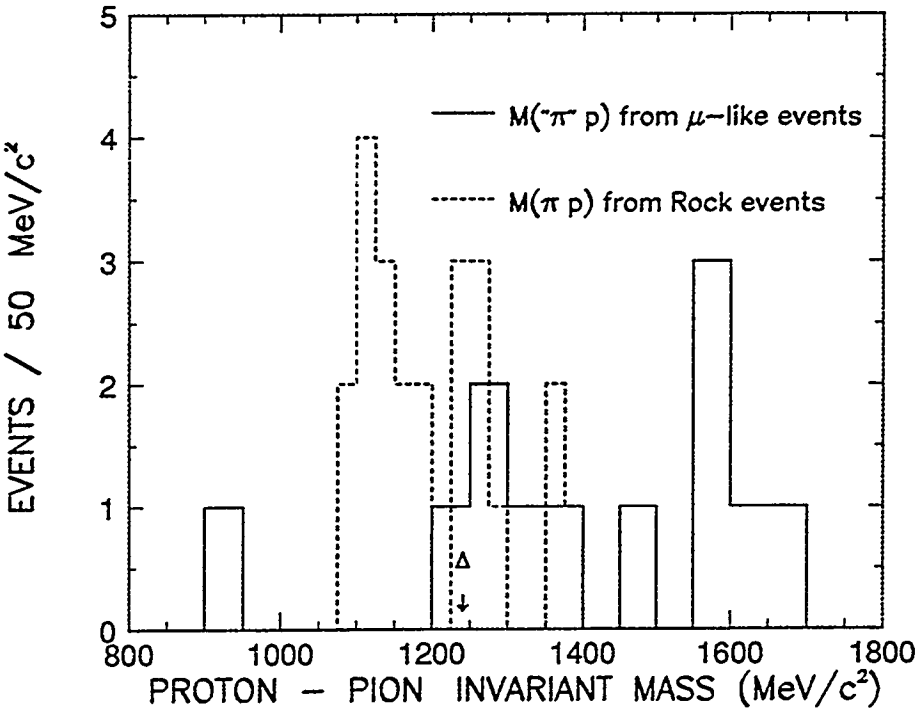

Figure 7.20: Proton–pion invariant mass: Solid histogram shows contained track plus recoil events with no activity in the Veto Shield; the dashed histogram depicts shield–tagged, neutron-induced events.

7.10 Directionality of Multiprong Events

For each event of the contained multiprong sample, a four–momentum vector can be determined for each track and shower separately, and one can obtain the event net momentum by adding each four–vector for each track and shower. Figs. 7.21 and 7.22 show the cosine of the angle between the visible final state three-momentum and the zenith direction for the multiprong data and for our Monte Carlo sample. Fig. 7.21 shows that more events are up–going than down–going, hence the multiprongs are not oriented completely isotropically with respect to zenith. The Monte Carlo distribution (Fig. 7.22) is however uniform with respect to the zenith direction. The trigger acceptance "holes" are not expected to affect the multiprong sample, as they do with the single track sample.

It is of interest to plot the cosine of final state net momentum relative to zenith ($\cos\beta$), against the final state visible energy of the event. Figs. 7.23 and 7.24 show these diplots for the multiprong data and Monte Carlo samples. The dashed

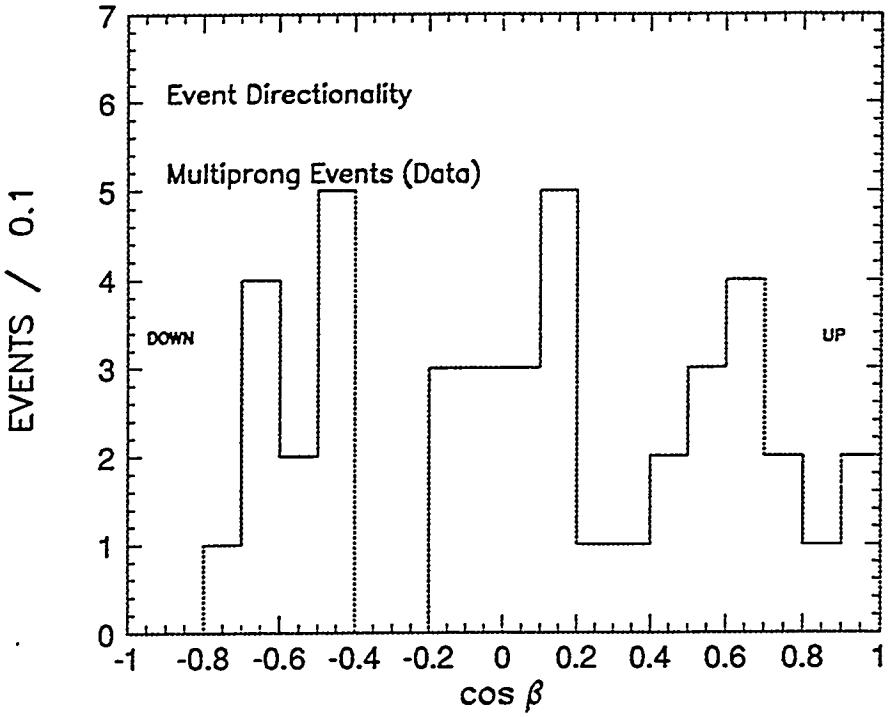

Figure 7.21: Event directionality for contained multiprong events (1.0 kty exposure).

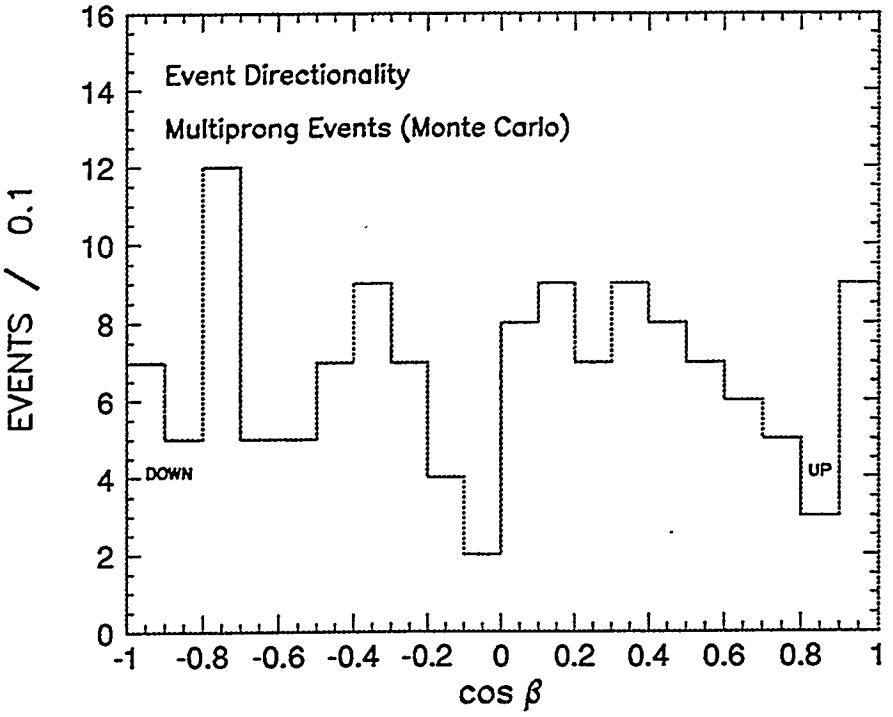

Figure 7.22: Event directionality for Monte Carlo multiprong candidates (3.45 kty exposure).

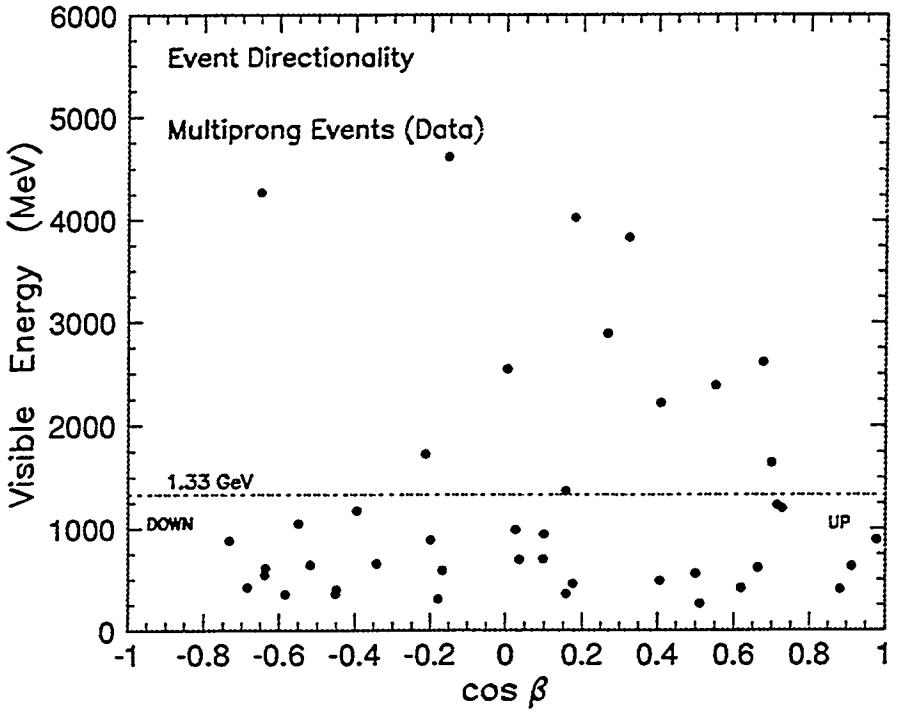

Figure 7.23: Total visible energy, versus cosine of the visible final state momentum versus zenith angle, for Soudan multiprong events.

line refers to the Kamiokande separation of contained events for their sub–GeV and multi–GeV analyses. Again we remark that there exist uncertainties in the energy estimation of large showers in Soudan data.

If one examines these plots for hints of neutrino oscillations, then Fig. 7.23 indicates that in the multi–GeV region there is a mild dearth of interacting neutrinos of all flavors in the downward direction (8 upward versus 4 downward events). This is to be compared with the Kamiokande oscillation scenario given by Fig. 3 of Ref. [?]. Here, Kamiokande consider fully–contained and partially–contained event samples in the multi–GeV region. In Ref. [6], Fig. 3a indicates a dearth of e–like events in the downward direction, whereas Fig. 3b shows a dearth of μ–like events in the upward direction. This muon–trend is consistent with an oscillation scenario where neutrinos produced on the other side of the Earth may oscillate while traversing the Earth, giving rise to a dearth of upward neutrinos, thus creating an asymmetry of the interacting neutrino flux between the downward versus upward directions.

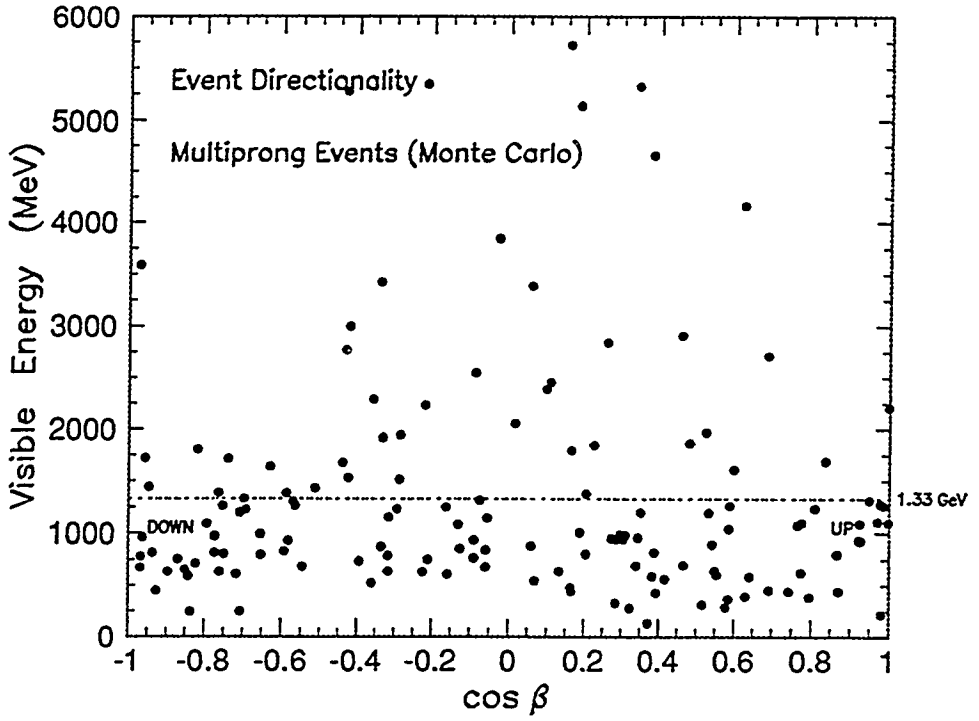

Figure 7.24: Total visible energy, versus cosine of the visible final state momentum versus zenith angle, for the multiprong Monte Carlo sample.

7.11 Concluding Remarks

The Soudan tracking calorimeter provides detailed event images from which one can discern the different topologies of the multiprong events. Its spatial resolution, approaching 1–3 cm in all three spatial coordinates, is the best ever achieved in underground experiments, providing new capability to discern the neutrino flavor composition of reaction samples.

From comparison of various inclusive distributions in this chapter, the Soudan first–generation Monte Carlo yields, on average, final states which are slightly too energetic.

We have searched for Δ (1232) resonance production in neutrino final states. A small signal may be present in the multiprong sample, however the peak is shifted below its nominal position observed in the Monte Carlo samples.

The event directionality of the contained multiprong sample shows a modest deviation from isotropy in the zenith angle distribution. This deviation, indicates

a mild dearth of interacting neutrinos of all flavors in the downward direction (8 upward versus 4 downward events).

We have investigated different aspects of π^0 signal reconstruction. Our reconstruction capability is sensitive to the vertex determination, to determination of shower directions, and to our ability to recognize the final state of the event. An inclusive π^0 signal is found in our Monte Carlo study. It has an invariant mass of 124 ± 13 MeV/c^2 with a width of 84 ± 19 MeV/c^2. Better algorithms for determining shower energies might yield improvement in the π^0 invariant mass signature.

Soudan's capability to reconstruct π^0 invariant masses together with its rough differentiation between γ showers and prompt electrons ($e^{\pm}$), is valuable for the study of nucleon decay modes having showers in the final state.

References

[1] K.S. Hirata *et al.*, Phys. Lett. **B 205**, 416 (1988); K.S. Hirata *et al.*, Phys. Lett. **B 280**, 146 (1992).

[2] D. Casper *et al.*, Phys. Rev. Lett. **66**, 2561 (1991); R. Becker–Szendy *et al.*, Phys. Rev. **D 46**, 3720 (1992).

[3] W.A. Mann, T. Kafka and W. Leeson, Phys. Lett. **B 291**, 200 (1992); W.A. Mann, T. Kafka and W. Leeson, *in*: Proceeding of DPF92 Meeting, Fermilab, 10–14 November 1992; p. 1330; W.A. Mann, T. Kafka and W. Leeson, DPF94, University of New Mexico, Alburquerque, NM, 2–6 August 1994; Soudan 2 Report PDK–590, July 1994.

[4] R. Merenyi *et al.*, Phys. Rev. **D 45**, 743 (1992); R. C. Merenyi, Ph. D. Thesis, Tufts University, May 1990, unpublished.

[5] C. Garcia–Garcia, Ph. D. Thesis, Universidad de Valencia, Sept. 1990, unpublished; C. Garcia–Garcia, "*Soudan 2 Response To Low Energy Particles*", Soudan 2 Report PDK–449, October 1990.

[6] Y. Fukuda *et al.*, Phys. Lett. **B 335**, 237 (1994).

Chapter 8

Neutrino Flavor Composition of the Multiprong Sample

8.1 Introduction

This chapter describes general properties of prompt electrons and gamma showers; these properties will be helpful for a π^0 signal reconstruction. A background study to the contained multiprong sample is also implemented. Inclusive distributions are examined using a variety of kinematic variables. The data sample is compared to a Monte Carlo simulation of inelastic atmospheric neutrino interactions in the Soudan detector. In particular, we try to determine the flavor (ν_μ, ν_e, or NC) composition of the contained multiprong sample.

8.2 Separation of Prompt Electrons from Gamma Showers

We present a study of the feasibility of differentiating between prompt electrons and gamma showers at primary event vertices. A separation of this kind can in principle improve our π^0 tagging. This capability will be utilized in Section 8.4 when we estimate the flavor composition of the contained multiprong sample.

The main difference between $e^{\pm}$ and γ showers in Soudan material is that an electron will produce hits in the detector in the immediate vicinity of where it is produced, while a photon may traverse many centimeters before the e^+e^- conversion occurs and the first shower hit is produced. The difference can be appreciated from an examination of distance–to–closest–hit distributions obtained from shower

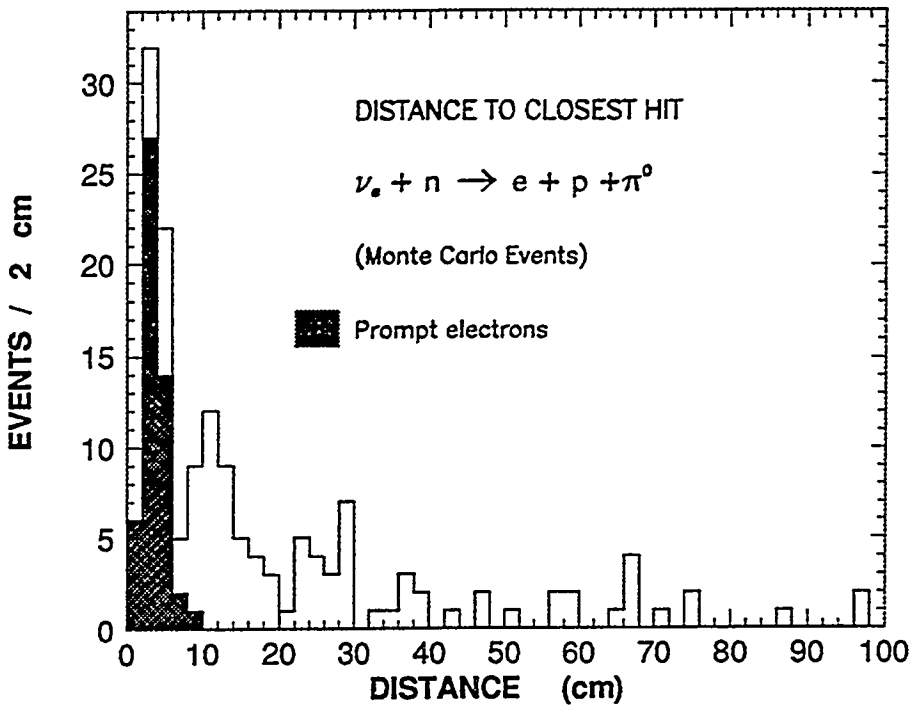

Figure 8.1: Distance to closest hit from showers in Monte Carlo reactions (3.3).

images of the Monte Carlo reaction samples $\nu n \rightarrow \mu^- p\pi^0$ (3.2), $e^- p\pi^0$ (3.3), and $\nu n\pi^0$ (3.4) (see page 70). Fig. 8.1 shows the distance to the closest hit from the primary vertex for all showers (prompt electrons and gamma showers) for the Monte Carlo simulations of reaction (3.3). The shaded area in Fig. 8.1 depicts the "true" prompt electrons, identified using the truth table of the Monte Carlo simulation. Considering the distance to the first hit from the vertex of electrons generated by the Monte Carlo, almost all electrons produce a hit within the first six centimeters. The distance–to–first–hit for electrons peaks at 4 centimeters, and extends up to 10 centimeters. The spread in initial hit distance reflects in part the uncertainty in the primary vertex location.

For comparison we show in Fig. 8.2, the distance to the closest hit in centimeters for simulated reaction (3.2) weighted for all possible vertex combinations. The events of reaction (3.2) have well–determined vertices (two visible tracks emerging from a common point; in addition the decay showers of the π^0 emerge from the same vertex). Fig. 8.2 shows the behavior characteristic of γ's from π^0 decay in Soudan material.

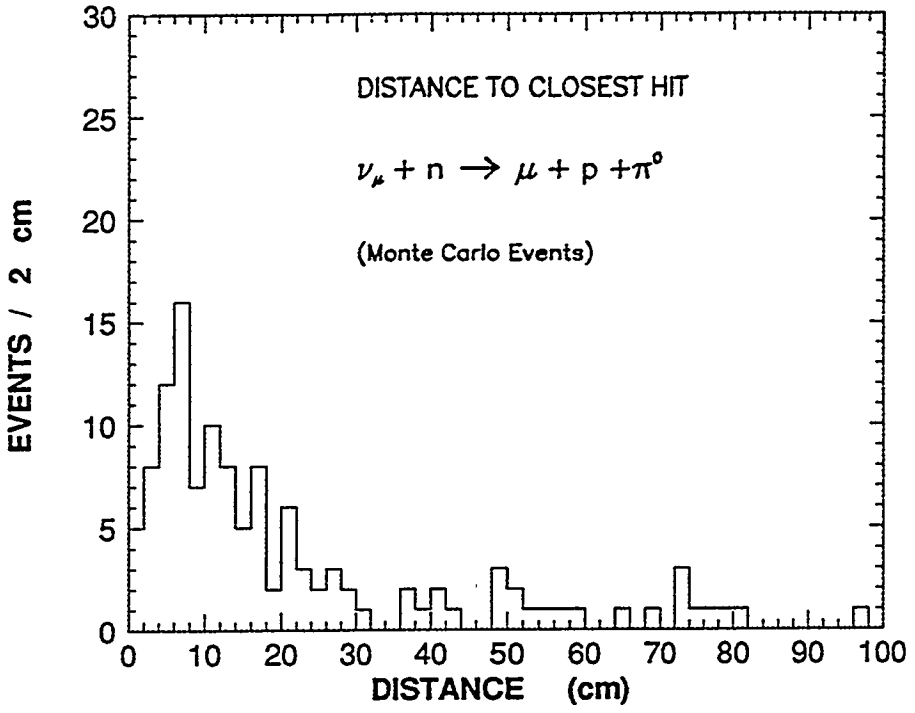

Figure 8.2: Distance to the shower hit closest to the vertex, from Monte Carlo reaction (3.2).

The inclusive distribution peaks at 8 centimeters, with distances extending up to a meter.

Fig. 8.3 shows the distance to the closest hit for reaction (3.4); the entries are weighted for all possible vertex combinations. In Fig. 8.3 we observe a peak at 12 centimeters, with distances extending up to 80 centimeters. Comparing Figs. 8.3 and 8.2, one sees evidence of the effect of vertex determination on γ conversion length. The shift of the peak outward in Fig. 8.3 versus Fig. 8.2 reflects the additional uncertainty in vertex location incurred in reactions (3.4) versus (3.2).

We conclude that γ showers can have a wide range of conversion lengths, whereas prompt electron ($e^{\pm}$) showers have relatively short distances to the first shower hit. Both depend on the verity of the vertex determination. Our plots are in rough agreement with Garcia–Garcia's observations [1] using ISIS test beam data. She recommended: *"If the conversion length is smaller than 4 cm the event is identified as an electron, whereas for a conversion length larger than 4 cm, the event is considered as a photon."* Based on our study here we prefer a discrimination length

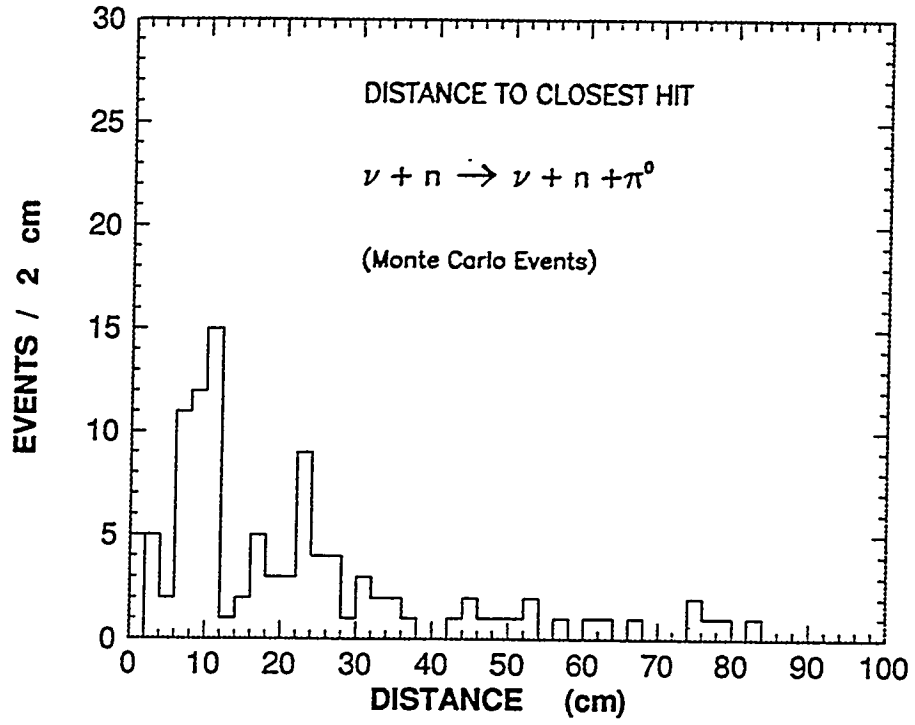

Figure 8.3: Distance to the first shower hit from the vertex, from Monte Carlo reactions (3.4).

which is slightly more conservative, one which allows for uncertainty arising from vertex determination. For well–defined vertices, showers which start at distances ≥ 7 centimeters are to be identified as photon–induced showers, whereas showers with conversion length <7 centimeters may be either prompt electron or photon showers. For poorly–defined vertices, prompt electrons and gamma showers are evaluated, in light of the above criteria, on an event–by–event basis.

It is of interest to consider the distribution of distance–to–first–hit in the contained multiprong sample. Figures 8.4 and 8.5 show distances to closest hits weighted for alternate vertex combinations, for the multiprong events and for the Monte Carlo simulation respectively. From the solid histogram in Fig. 8.4, we infer that the multiprong sample contains both prompt electrons and gamma showers. Using our criteria, one infers that the first four bins in Fig. 8.4 are populated by prompt electrons in the sample, whereas the more distant bins are populated entirely by gamma showers. Somewhat different conclusions are suggested by the closest hit distribution from Monte Carlo multiprongs shown in Fig. 8.5. The shaded area in

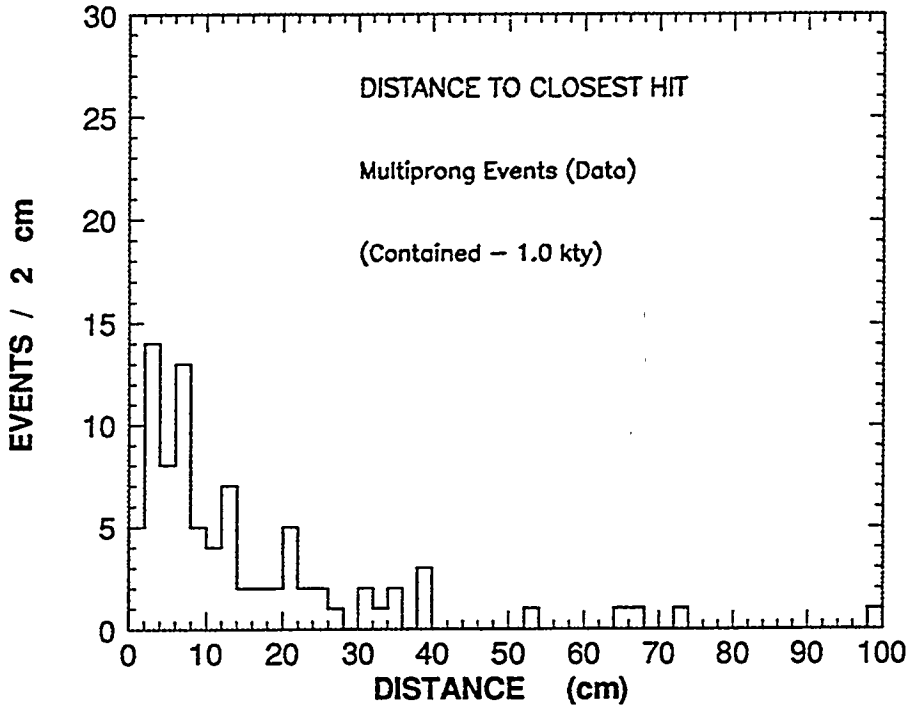

Figure 8.4: Distance to closest hit for showers in the multiprong sample.

Fig. 8.5 depicts the "true" prompt electrons, identified using the truth table of the Monte Carlo simulation. There the electron shower contribution clearly extends to 14 centimeters, which is double our criterion distance for events having well–defined vertices.

8.3 Estimate of Rock Event Background in the Multiprong Sample

There is a flux of energetic neutrons and photons within the Soudan cavern, originating from cosmic ray muon interactions within the rock surrounding the cavern walls. These particles can interact or convert inside the detector creating apparent contained neutrino events. The contained non–quasi–elastic (multiprong) neutrino events, which have several tracks and/or showers originating from a primary vertex, can only be imitated by energetic neutron interactions. Among the neutron–induced events which are tagged by the active shield (335 events in our initial one kiloton–year exposure), approximately 29% are judged to be Rock multiprong events. In the

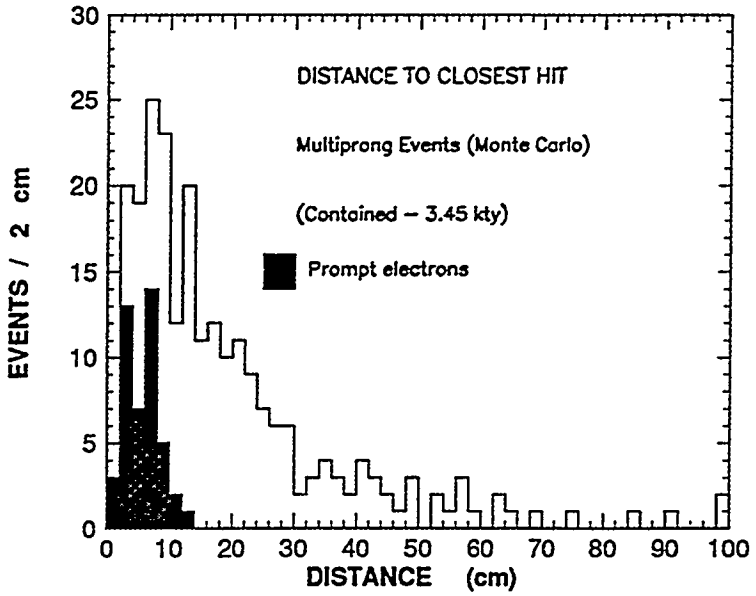

Figure 8.5: Distance to closest hit for showers in the Monte Carlo multiprong sample.

entire Rock sample, we find that 6% have the double shower topology, 18% appear as multiple tracks (without showers), and 5% appear as multiple tracks and showers. We now describe our study of neutron–induced background in the Soudan contained multiprong data.

Following our analysis of backgrounds to single shower and single track topologies (Section 5.4), we analyze the penetration depth associated with multiprong topologies in the Soudan detector. Neutrino interactions should be distributed uniformly with increasing penetration depth; interactions of neutral hadrons, however, should exhibit a fall–off in the number of events versus increasing penetration depth. From the line–of–flight information from each contained multiprong event, a simulation is used to obtain the detector geometrical acceptance. Here, an average event size is used to infer at what locations events will exit the fiducial volume. Fig. 8.6 shows the neutrino penetration depth distribution for the contained multiprong sample. The acceptance curve corresponding to the fiducial volume in the tracking calorimeter is shown superimposed (dashed curve). The curve has been normalized to the

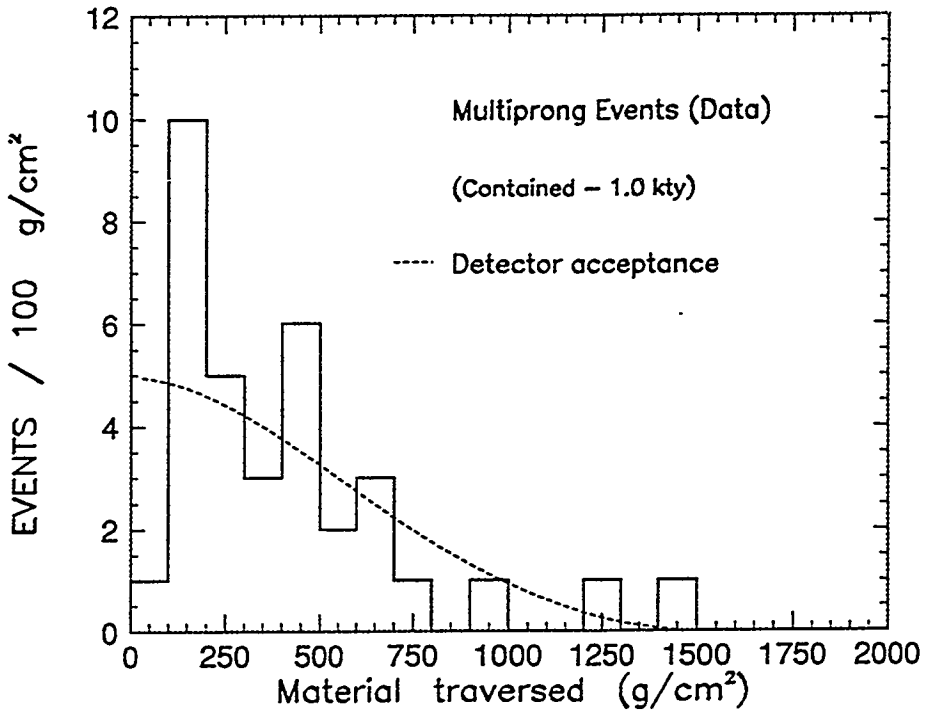

Figure 8.6: Penetration depth (in g/cm^2) from multiprong events; the detector acceptance (dashed curve) is shown superposed, normalized to the data above 250 g/cm^2.

contained multiprong sample above 250 g/cm^2.

From Fig. 8.6 one can discern the existence of a small excess above the acceptance curve, suggesting the presence of a few non–neutrino background events in the contained multiprong sample. To account for this background, we utilized a recent study of Rock events carried out by D. Wall of Tufts. There are 80 events in the multiprong Rock sample (see Table 5.1) which have topologies which must be neutron–induced. These topologies include multiple shower events and multiprong events which contain tracks with or without accompanying showers. Using the observations concerning neutron interactions of Section 5.4, we estimate the amount of background in the contained multiprong sample. We add, with variable amplitudes, a curve characterizing the neutron–induced event distribution in penetration depth, together with the neutrino vertex acceptance curve, so as to fit the penetration depth distribution of the contained multiprong sample. Fig. 8.7 shows the component contributions to the contained multiprong events. Here, the histogram shows

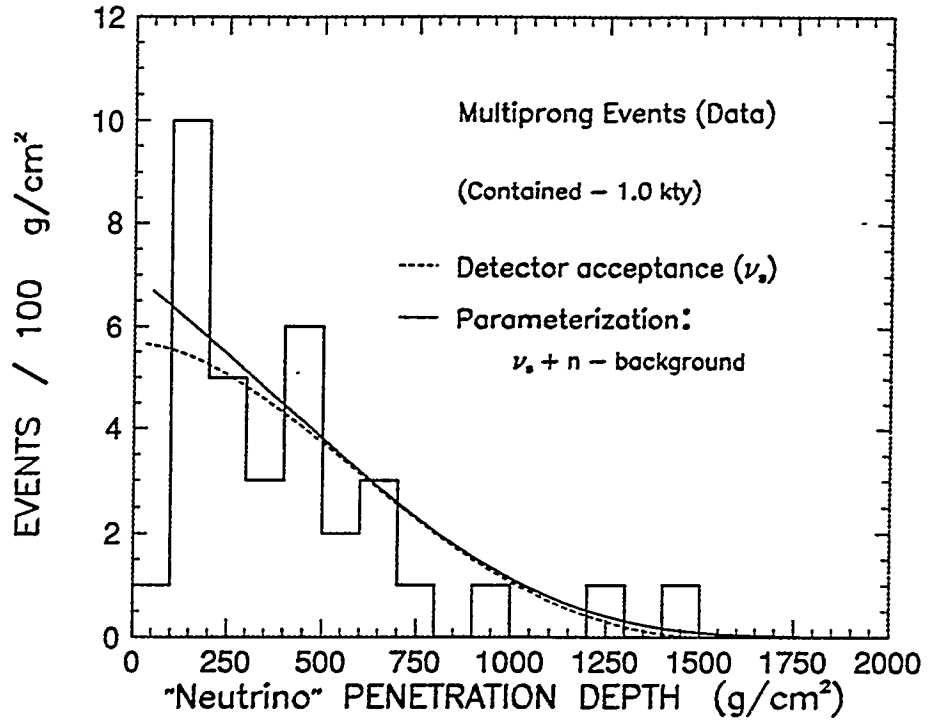

Figure 8.7: Neutrino penetration depth for contained multiprong events. The solid curve is normalized to the data above 100 g/cm^2.

the penetration depth in grams per square centimeter for the multiprong sample. Superimposed is the neutrino event acceptance curve (dashed line) and the solid line representing the combined parameterization which includes the neutrino acceptance with the neutron–induced background fit from the Rock single track sample (see Chapter 5, Fig. 5.7 and Table 5.2). Using PAW one can integrate the areas under the solid line and the dashed line. The difference between these two areas divided by the bin width gives the Rock event background count for the neutrino sample. In this way we estimate a background contamination of 1.1 ± 2.4 events for the contained multiprong events.

The background contamination in the multiprong sample is small (with large statistical errors). This contamination estimation is based upon a 0.5 kty Rock event sample. In the near future the statistics of the Rock sample will be increased, and the background estimation thereby improved.

8.4 On Determining the Neutrino Flavor Composition of the Multiprong Sample

In this Section we present two different approaches to the estimation of the neutrino flavor composition of the contained multiprong sample. The two methods give similar results, with large statistical errors. The first approach utilizes Soudan's capabilities for distinguishing the various elementary particles (p, $\pi^{\pm}$, $\mu^{\pm}$, $e^{\pm}$ and γ). In the second approach the sample is treated more globally; the number of tagged pion tracks is used to estimate the total number of inclusive charged pions and consequently the total number of produced muons.

8.4.1 Discrimination of Neutrino Flavor

In our first approach, we attempt to assign each event to one of three neutrino flavor classes, namely muon–neutrino charged current (ν_{μ}^{CC}), or electron–neutrino charged current (ν_{e}^{CC}) or neutral current (ν^{NC}). For this purpose we will define discriminators for particle identification and for flavor classification. The process of flavor tagging will be carried out in two stages on an event–by–event basis. We apply our previously developed techniques for identifying each particle in each event. We try to classify each track as being either a proton, charged pion or a charged muon. For showers, we try to distinguish whether they are gamma or prompt electron showers. The various track and shower criteria are as follows:

1.) For tracks:

Protons: we distinguish protons from $\mu^{\pm}$ and $\pi^{\pm}$ as being heavily ionizing tracks with straight trajectories.

$\pi^{\pm}$ versus $\mu^{\pm}$: i) if a non–proton charged track has a secondary kink or scatter, it is identified as being a charged pion.

ii) if a non–proton charged track is longer than 1 meter in the detector medium and does not scatter, we regard it to be a charged muon.

2.) For showers:

Prompt Electron: A candidate charged current electron $e^{\pm}$ must have a first hit within 7 centimeters of a well–determined vertex location.

Gamma shower: A shower whose first hit is beyond 7 centimeters from a well–determined vertex is a gamma shower; a shower whose first hit is within 7 centimeters can be either a prompt electron or a gamma shower.

π^0: Candidate π^0's are estimated on an event–by–event basis. We consider vertex determination as well as the number of showers in the event. The showers forming the π^0 are not subjected to conversion length cuts, however the shower pair must yield an invariant mass that falls in the range 80 MeV/c^2 $\leq$ M($\gamma\gamma$) $\leq$ 200 MeV/c^2.

Having assigned particle identifications to each track and shower in the contained multiprong sample, each event is evaluated for possible neutrino flavor assigment:

No ν_μ flavor: If there is no candidate muon track in the event, then the event is classified as being either ν_e^{CC} or ν^{NC}.

No ν_e flavor: If there are no showers in the event, then the event is classified as being ν_μ^{CC} or ν^{NC}.

The result of applying the above criteria to each multiprong event is summarized in Table 8.1. The above rules were applied straightforwardly, consequently the flavor assignment of many events is ambiguous. For this reason we call the approach "conservative". In Table 8.1 a star ($\star$) indicates that a flavor assignment is possible, whereas a solid circle ($\bullet$) signifies that the event flavor classification is definite. We are left with a sample, which has a large number of events being flavor–ambiguous

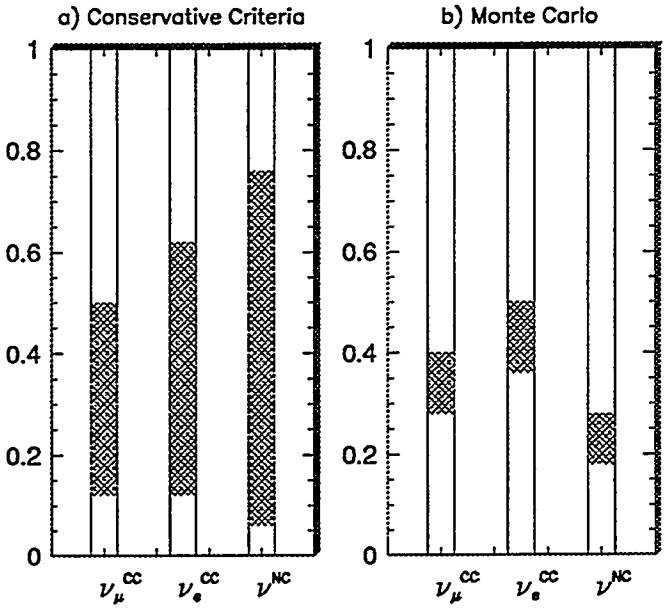

Figure 8.8: Flavor composition of the multiprong sample: Our "conservative" analysis (6.8a), compared to the Monte Carlo expectation (6.8b).

– events labelled with stars. Additionally in Table 8.1, the ranges for sample flavor are tallied with the corresponding percentages in parentheses (given by the quantities MAX and MIN respectively). Our first generation Monte Carlo sample, which is based upon the Bartol neutrino fluxes, predicts that $34 \pm 5\%$ [1] of multiprongs are muon–neutrino charged current reactions, while $43 \pm 6\%$ are electron–neutrino charged current events, and $23 \pm 5\%$ are neutral current events. From Table 8.1 we see that our contained multiprong sample contains a ν_μ^{CC} fraction in the range 12% to 50%. Similarly the range for ν_e^{CC} is between 12% and 62%, whereas the ν^{NC} varies from 6% to 76%. The results of Table 8.1 are displayed more graphically in Fig. 8.8. The shaded areas in Fig. 8.8 show the flavor component range for each of the three neutrino flavors. Fig. 8.8a shows the "conservative" results, to be compared to Fig. 8.8b showing the corresponding Monte Carlo simulation.

[1]The numbers were obtained from the truth table and the errors are statistically only.

I. CEV-MP Event Flavor
Conservative Criteria

	Event	ν_μ^{CC}	ν_e^{CC}	ν^{NC}
1	11940–1712		⋆	⋆
2	20307– 498		⋆	⋆
3	20366–1130	⋆	⋆	⋆
4	23354– 917	⋆	⋆	⋆
5	24283– 184	⋆	⋆	⋆
6	24290– 949			•
7	26439–1456		•	
8	26957–1891		⋆	⋆
9	27896– 766		•	
10	29136– 472		⋆	⋆
11	29750– 195		⋆	⋆
12	29834– 74		•	
13	31549–1040	⋆		⋆
14	31565–1041		⋆	⋆
15	31606– 633		⋆	⋆
16	31739–1567		⋆	⋆
17	31757– 249	⋆		⋆
18	33322– 55	⋆	⋆	⋆
19	34123–1064	⋆		⋆
20	34742–1579		⋆	⋆
21	35086–1441			•
22	35209– 670		⋆	⋆
23	35219– 766	•		
24	35314– 123	⋆	⋆	⋆
25	35998– 376		•	
26	36284–1523		⋆	⋆
27	36381–1189	•		
28	37148– 903	⋆		⋆
29	37722– 277	⋆		⋆
30	37731– 374	•		
31	38073– 886	•		
32	38345– 310	⋆	⋆	⋆
33	39280– 122	⋆		⋆
34	39432– 645	⋆		⋆
	MAX =	17 (0.50)	21 (0.62)	26 (0.76)
	MIN =	4 (0.12)	4 (0.12)	2 (0.06)
	MC =	0.34	0.43	0.23

Table 8.1: Flavor composiion of the contained multiprong sample; symbols ⋆ and • denote "flavor possible" and "flavor definite" respectively.

A more aggressive implementation of the above approach has also been tried. Here the event flavor is assigned according to 'Physicist Choice', using information (and impressions) obtained from scanning. Events which are ambiguous in light of the conservative criteria were carefully reexamined. We were able to resolve some of the ambiguities in flavor assignment using observation of an endpoint decay shower in the track, and observation of 'range–out' behavior based upon apparent ionization and/or straggling. Here the endpoint decay shower or 'range–out' decision is assigned according to the judgement of the physicist scanner. The terminology 'range–out' means that the track loses all of its kinetic energy by ionization and comes to rest. Results from the 'Physicist Choice' flavor estimation are summarized in Table 8.2. One notes that there still remains some events which have residual flavor ambiguity. From Table 8.2 we see that the 'Physicist Choice' analysis finds the ν_μ^{CC} component to be in the range 21% to 41% (versus 12%–47% in the previous analysis). Similarly we find the range in ν_e^{CC} to be between 29% and 53%, while the ν^{NC} range is 15% to 47%. In Section 8.3 we estimated that the background contamination of the contained multiprong events are 1.1 ± 2.4 events. This contamination, which is neutron–induced, should in principle affect only the Neutral Current events. If we implement this correction, then from Table 8.2 we infer that the quantity 'MAX' (in the ν^{NC} column) should be decreased by two units. This modification gives a new range for ν^{NC} which is between 15% and 41%.

Fig. 8.9 shows the 'Physicist Choice' (with background subtraction included) together with our first generation Monte Carlo expectation. The agreement in neutrino flavor to the Monte Carlo prediction now appears more definite. From Fig. 8.9 we conclude than any new physics process (neutrino oscillations, nucleon decay) would have to "hide" within the error bars of our flavor estimations. Unfortunately the errors are somewhat large from the first kiloton–year exposure analyzed here.

The primary source of flavor ambiguity arises from the π/μ uncertainty. The contained multiprong sample contains a number of short, lightly–ionizing tracks, for

II. CEV-MP Event Flavor
Physicist Choice

	Event	ν_μ^{CC}	ν_e^{CC}	ν^{NC}
1	11940–1712			•
2	20307– 498		•	
3	20366–1130			•
4	23354– 917	⋆	⋆	
5	24283– 184	⋆		⋆
6	24290– 949			•
7	26439–1456		•	
8	26957–1891		•	
9	27896– 766		•	
10	29136– 472		⋆	⋆
11	29750– 195		⋆	⋆
12	29834– 74		•	
13	31549–1040	⋆		⋆
14	31565–1041		•	
15	31606– 633		⋆	⋆
16	31739–1567		•	
17	31757– 249	•		
18	33322– 55	⋆	⋆	⋆
19	34123–1064	•		
20	34742–1579		⋆	⋆
21	35086–1441			•
22	35209– 670		•	
23	35219– 766	•		
24	35314– 123		•	
25	35998– 376		•	
26	36284–1523		⋆	⋆
27	36381–1189	•		
28	37148– 903	⋆		⋆
29	37722– 277	•		
30	37731– 374	•		
31	38073– 886	•		
32	38345– 310	⋆	⋆	⋆
33	39280– 122	⋆		⋆
34	39432– 645			•
	MAX =	14 (0.41)	18 (0.53)	16 (0.47)
	MIN =	7 (0.21)	10 (0.29)	5 (0.15)
	MC =	0.34	0.43	0.23

Table 8.2: Flavor composition of the contained multiprong sample based upon "physicist choice" criteria.

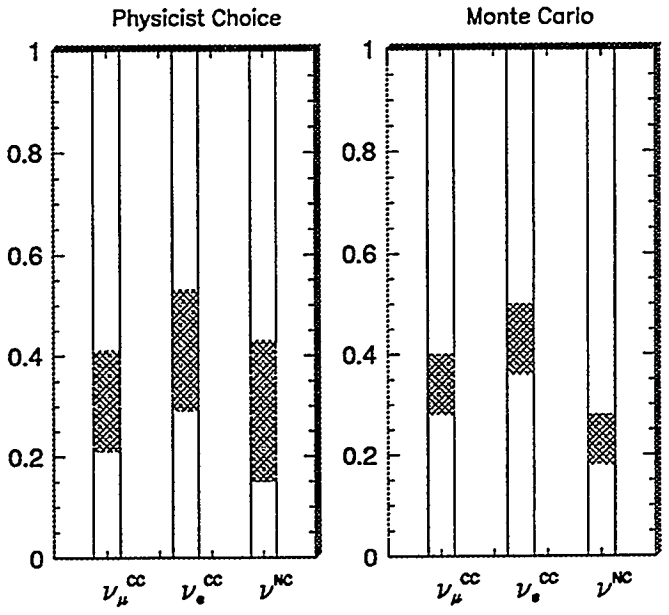

Figure 8.9: Flavor composition of the multiprong sample: "Physicist choice" flavor–tagging with background subtraction included, compared to the Monte Carlo expectation.

which we are unable to distinguish between pion and muon mass assignments.

8.4.2 Estimation of Sample Muon Population using Pions

We present a second approach to extracting the ν_μ flavor contribution to samples of contained multiprong events induced by atmospheric neutrinos interacting in the Soudan detector. Our strategy is to use the number of observed $\pi^\pm$ scatterings to estimate the number of non-scattered $\pi^\pm$ tracks. The remaining number of non-scattering tracks are then taken to be muons.

The sample of 34 contained multiprong events consists of a varied assortment of topologies. We observe 63 individual showers and 44 individual tracks in the sample. As described in Sections 7.5 and 7.6, classification of tracks can be made according to information which is available upon scanning each event. We have identified protons as heavily–ionizing, straight tracks. One can resolve (with certain precision) that lightly–ionizing tracks which scatter are charged pions. Here the

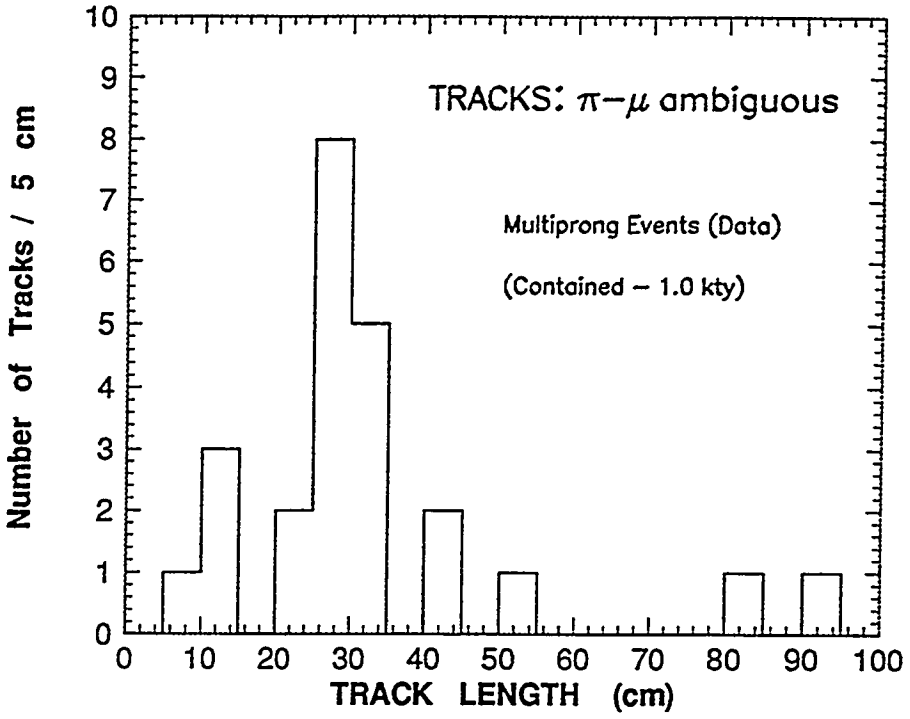

Figure 8.10: Track length for π–μ ambiguous tracks.

term "scattered track" (based upon scanning) refers to any non–proton track which is deflected from its original course by a visible angle, possibly producing a recoil proton at the deflection point.

From the 44 tracks observed in the contained multiprong sample, we identify 15 as being proton tracks and 5 tracks to be charged pions based upon visible scatters. Among the remaining 24 tracks, most are ambiguous between charged pions and muons. Upon plotting the track–length of this sample (see Fig. 8.10), we find that they are mostly short tracks.

The approach that we now take is to use the number of visibly–scattered (*"deflected"*) pion tracks to estimate the number of non–visibly–scattered (*"non-deflected"*) pions in the event sample. Information concerning the observed, deflected pions is given in Table 8.3. The pions all have a deflection angle (θ_d) bigger than 30°; the distance before scattering varies between 10 and 150 centimeters. For four of the five scattering pions, short recoil protons are observed at the scatter vertices.

The behavior of pions in matter at momenta of interest for this thesis is known

Deflected Tracks			
Event No.	dx_d (cm)	θ_d °	Recoil Proton
20366-1130	26	32	YES
27896-766	11	93	YES
31606-633	31	32	NO
35086-1441	29	50	YES
38073-886	145	62	YES

Table 8.3: dx_d is the pre-deflection distance and θ_d is the deflection angle.

[2, 3]. Fig. 8.11 shows the energy dependence of the pion-nucleus total cross section, while Fig. 8.12 shows the relative contributions of strong interaction processes based on experimental data [4]. This information is of course incorporated into the particle tracking software simulation package GEANT, and we can use this code to explore the behavior of an appropiate spectrum of pions moving through Soudan material. In comparing such a simulation to tracks from our contained multiprong sample, certain cuts need to be imposed on pions in the Monte Carlo simulation:

i) We need to specify a minimum scattered angle θ_{min}, for which a pion can be reliably detected as being deflected.

ii) We need to specify a minimum track length inside the detector l_{min}, for which the pion is reliably detected as a track prior to undergoing hadronic scattering.

iii) We need to specify a containment requirement, because the pions we are observing are contained in a detector of finite size.

iv) We need to specify a threshold momentum, to account for the fact that pion tracks at low momenta are not discernible.

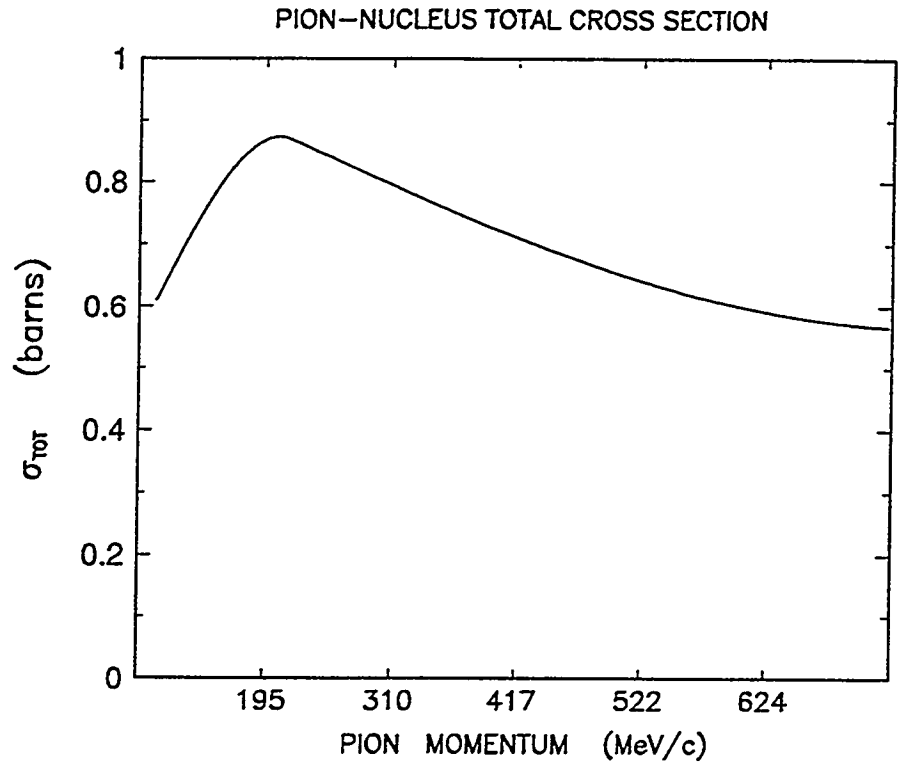

Figure 8.11: Energy dependence of the pion-nucleus total cross section.

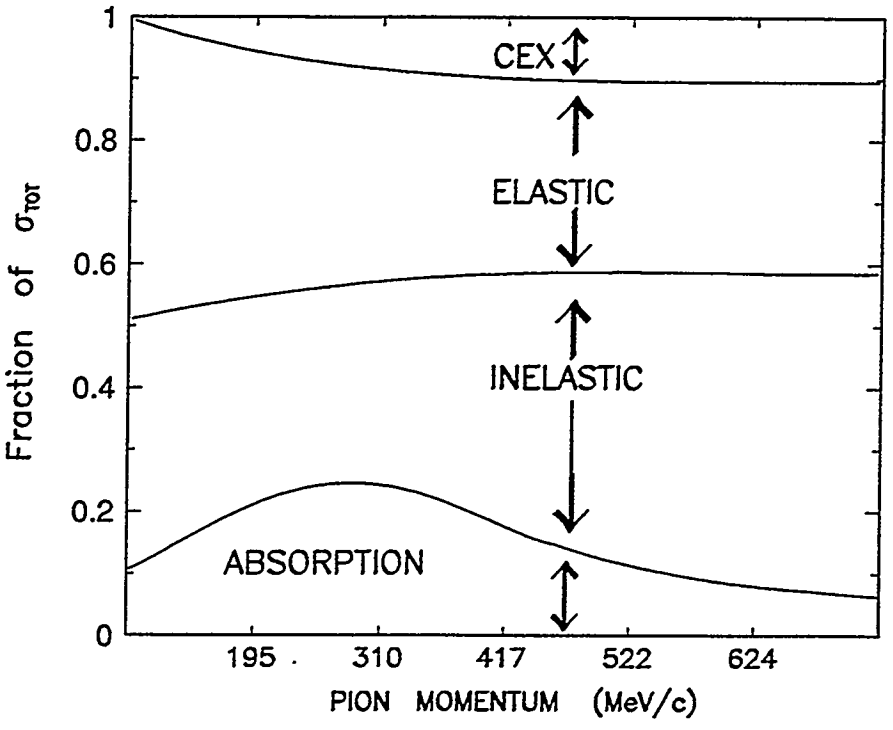

Figure 8.12: Relative rates among hadronic processes which constitute the pion–nucleus total cross section.

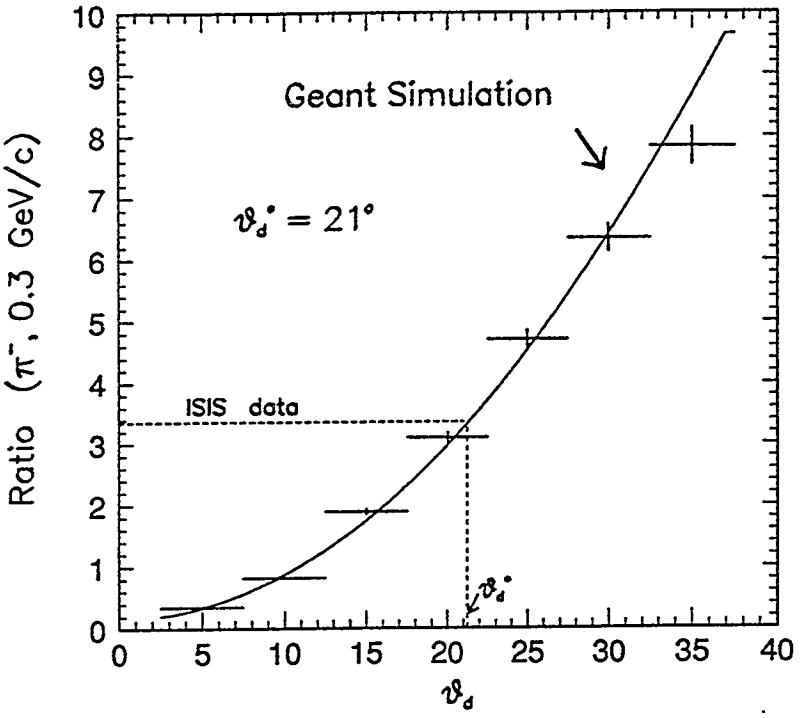

Figure 8.13: Deflection angle versus the ratio of non–deflected to deflected π^- tracks at 300 MeV/c.

We establish θ_{min} by comparing our GEANT simulation to the study of ISIS data by T. Fields [5], summarized in Table 8.4. From Table 8.4 we infer the ratio of non–deflected to deflected pions (at 0.3 GeV/c) is

$$R(\pi^-, 0.3\ GeV/c) \equiv \frac{\#\ non-deflected\ pion\ tracks}{\#\ deflected\ pion\ tracks} \tag{8.1}$$

$$R(\pi^-, 0.3) = 3.35 \pm 0.67$$

Using this result, an effective minimum deflection angle θ_d^* can be set on the basis of GEANT simulations. We use GEANT to simulate pions of 300 MeV/c momentum; the deflection angle is varied between 5°and 35°. Results from this exercise are shown in Table 8.5. The information in Table 8.5 is displayed in Fig. 8.13; from the $R(\pi^-, 0.3)$ value in Table 8.4, we infer that $\theta_d^* = 21°$. This θ_d^* value is in agreement with an early study using charged pions incident upon a Soudan planar prototype module (Ref. [6]).

From Fig. 8.10 we see that no tracks shorter than 4 centimeters are observed. Conservatively, we choose a minimum track-length l_{min} equal to 8 centimeters.

Scan of π^- at 300 MeV/c	
Track Topology	Number of Tracks
Range-out	24 ± 5
0-prong	53 ± 6
Non-Deflected =	77 ± 8
1-prong scatter	18 ± 4
Shower	5 ± 1.5
Deflected =	23 ± 4
$R(\pi^-, 0.3) = 3.35 \pm 0.67$	

Table 8.4: Ratio of "non–deflected" to "deflected" pions from ISIS data [Ref. 5].

A containment requirement can be inferred from the contained multiprong Monte Carlo sample. Fig. 8.14 shows the distribution of charged pion momenta in this sample. We observe in this Figure that there are no pions of momentum greater than 1 GeV/c. This is to be compared with Fig. 8.15, which depicts the atmospheric flux–weighted inclusive pion momentum distribution of Merenyi et al. [2]. From these figures we infer that containment leads to elimination of produced pions having momenta larger than 1 GeV/c in the initial 1.0 kty Soudan exposure. Finally, we need to impose a threshold momentum cut; this cut is set to the Soudan 2 threshold for charged pions, $P_{threshold} = 100$ MeV/c.

We apply these selections to the atmospheric–flux–weighted ν_μ· D_2 bubble chamber pions [2]; the momenta of pions which pass these cuts are used as input values

Geant Simulation of π^- at 300 MeV/c			
θ_d	Non-deflected	Deflected	Ratio
5	1658	4877	0.34 ± 0.01
10	2957	3628	0.82 ± 0.02
15	4332	2305	1.89 ± 0.05
20	5038	1627	3.10 ± 0.09
25	5509	1173	4.70 ± 0.15
30	5776	909	6.35 ± 0.23
35	5933	758	7.83 ± 0.30

Table 8.5: GEANT simulation corresponding to the ISIS test beam data of Table 8.4.

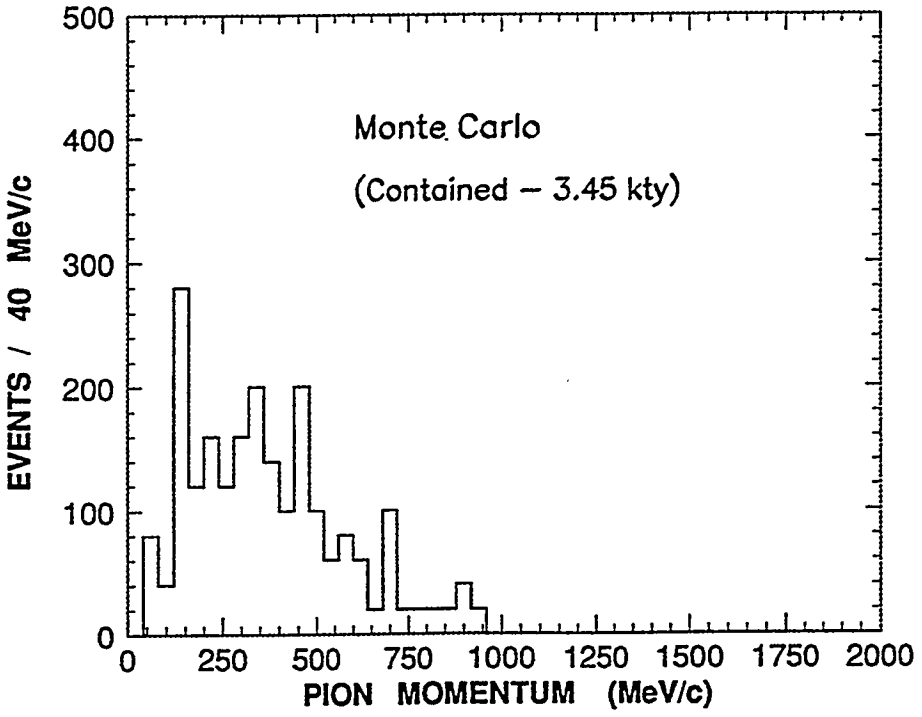

Figure 8.14: Distributions of charged pion momenta from the reconstructed Monte Carlo multiprong sample.

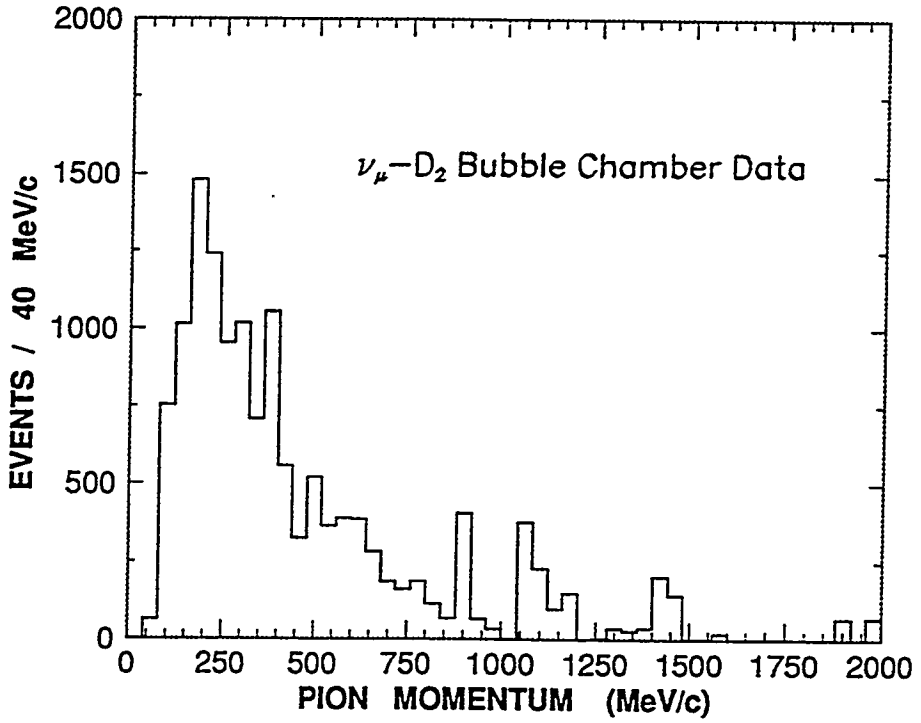

Figure 8.15: Distributions of charged pion momenta from ν_μ interactions in the deuterium filled ANL 12–ft bubble chamber [Ref. 3], weighted to atmospheric ν flux.

for GEANT simulations which track them through the Soudan medium. We obtain the results shown in Table 8.6. Then, using Table 8.3, we deduce that the number of non-deflected pions is 14.3 ± 6.3. We now subtract the number of non-deflected pions from the number of tracks in our π/μ sample to get the total number of muons in the multiprong sample. We conclude that there are 9.7 ± 6.3 muons in the sample. If we consider the background contamination of the contained multiprong sample, then the total number of multiprongs is 32 instead of 34 events. Hence the ${\nu_\mu}^{CC}$ fraction in the contained multiprong sample is 0.30 ± 0.19.

If we compare the ${\nu_\mu}^{CC}$ fraction value 0.30 ± 0.19 with the Monte Carlo expectation of 0.34 ± 0.05, we find no obvious dearth of muon–neutrinos. Unfortunately, our event sample has limited statistics, consequently this analysis is quite sensitive to the observed number of deflected pions. However, Soudan 2 is accumulating data steadily, and so the full potential of this approach may eventually be realized. Based upon our current statistically limited sample, we observe no evidence of an

Non–deflection Processes:	# π's	Deflection Processes:	# π's
Range-out	3070	Charge Exchange	1116
Absorption	3814	Inelastic	1350
Decay	206		
Total:	7090	Deflected	2466
$R(\pi^{\pm}, spectrum) = 2.86 \pm 0.02$			

Table 8.6: Pions from ν_μ·D_2 events, weighted to match atmospheric spectrum, propagated through Soudan medium using GEANT.

anomaly in the flavor composition of multiprong final states initiated by atmospheric neutrinos.

8.5 Concluding Remarks

Showers initiated by photons have been studied; their conversion lengths are typically longer than first hit distances for showers initiated by electrons. In events with well–determined vertices, if the distance (vertex to first hit) is smaller than 7 centimeters the shower can be either electron or photon–induced; at distances greater than 7 centimeters the shower is almost certainly photon–induced.

Soudan's capability to reconstruct π^0 invariant masses together with its rough differentiation between γ showers and prompt electrons ($e^{\pm}$), is valuable for the study of nucleon decay modes having showers in the final state.

From the Rock event analysis we obtained estimates of backgrounds to our contained multiprong sample. Our analysis shows that the Soudan contained atmospheric neutrino multiprong sample contain residual neutron backgrounds at the level of 3%.

We have developed two methods for estimating the atmospheric neutrino flavor component of the contained multiprong sample. Both methods indicate – with large statistical errors – that the flavor composition of the multiprong sample is in agreement with the flavor expectations of the Monte Carlo, for which no neutrino oscillation effects are included. Within the multiprong sample we detect no trend which would confirm the Kamiokande report [7] that the neutrino flavor ratio anomaly persists in contained event samples from neutrino interactions with E_ν above 1.33 GeV.

References

[1] C. Garcia–Garcia, Ph. D. Thesis, Universidad de Valencia, Sept. 1990, unpublished.

[2] R. Merenyi *et al.*, Phys. Rev. **D 45**, 743 (1992).

[3] R. C. Merenyi, Ph. D. Thesis, Tufts University, May 1990, unpublished.

[4] J. Bartelt *et al.*, *"Soudan 2 Proposal"*, Minnesota–Argonne–Oxford, Sept. 1981; see page 92.

[5] T. Fields, *"Proton and Negative Pion Interactions in Soudan2*, Soudan 2 Report PDK - 547, March 1993.

[6] W.A. Mann, L. Barret, U. Das Gupta, S. Werkema, *"Study of Charged pion Tracks with 350, 300, and 250 MeV/c Incident Momentum to the Planar Prototype Module"*, Soudan 2 Report PDK - 142, August 1984.

[7] Y. Fukuda *et al.*, Phys. Lett. **B 335**, 237 (1994).

Chapter 9
Partially Contained Events in Soudan 2

9.1 Introduction

We measure general properties of events which are partially contained in the Soudan 2 detector. Inclusive distributions for various final state particles are presented; distributions from the sample are compared to those obtained from a simulation of partially contained events. Following an examination of inclusive π^0 production, we consider the neutrino flavor content of this sample.

9.2 Motivation

The measurement of an anomalously low value for the ratio of atmospheric $(\nu_\mu + \bar{\nu}_\mu)$ and $(\nu_e + \bar{\nu}_e)$ events is in need of confirmation from an independent source. Events which are partially contained within the Soudan detector (hereafter referred to as PCE events) constitute a data sample which is independent of the contained neutrino event sample – the samples have no events in common. A PCE event has its interaction vertex within the Central Detector fiducial volume, but also has at least one visible track or shower which exits from the calorimeter. The exiting prong(s) may or may not be picked up by the active Veto Shield array surrounding the Central Detector.

There are several reasons why PCE events warrant investigation. Firstly, the ratio of the number of μ–like to e–like events, normalized by the corresponding ratio

in a Monte Carlo simulation, could, in principle, provide an independent measurement of neutrino flavor to be compared with our result from contained event data. Secondly, information on neutrino oscillations might conceivably be extracted by measuring the zenith–angle dependence. Thirdly, the sample represents neutrino interactions which are more energetic than those comprising the contained event samples. Now, for $E_\nu > 3$ GeV it is expected that the ν_e component will incur an additional suppression relative to the ν_μ component in the atmospheric ν flux which is not operative at low neutrino energies. The suppression arises from the fact that the ν_e's originate with cosmic ray muon decays, which typically occur at much lower altitude than do decays of cosmic ray pions, which give rise to ν_μ's and $\bar{\nu}_\mu$'s. At higher cosmic ray primary energies, muons resulting from cosmic–ray–induced particle cascades can have momenta sufficiently high to allow them to reach the Earth's surface before decaying. Consequently the ν_e flux is depleted relative to the ν_μ component [1]. Our PCE sample may allow us to probe the atmospheric neutrino flavor composition in this higher energy regime.

If the ratio ν_μ/ν_e is not anomalously low in the PCE sample, then neutrino oscillations would seem to be unlikely as the origin of the atmospheric ν flavor anomaly. If the anomaly is confined to the E_ν regime below 1 GeV, then a possible explanation for this anomaly in the sub–GeV region is nucleon decay [2]. It is for these reasons that we have undertaken an initial, exploratory examination of PCE events in Soudan 2, which we now summarize.

9.3 The PCE Event Sample

As described in Section 3.8, to isolate PCE events, our approach was based on the Veto Shield and upon track reconstruction within the Central Detector. In order to reduce the PCE file to a manageable level, a succession of computer cuts were

imposed on the data sample. We use the Veto Shield information to eliminated multiple muons, wall–to–wall muons, downward–going–stopping muons, and all events which have an in–time shield hit (ADJ hit) in the ceiling. The event sample which survived the computer cuts were then scanned by a "committee". To identify PCE events in data selected according to the criteria given in Section 3.8, the following rules were developed by physicists during scanning:

1. A PCE candidate must have its interaction vertex inside the fiducial volume, with one or more tracks or showers exiting the Central Detector.
2. The exiting track from a PCE must have no more than two ADJ hit groups associated.
3. The time of the shield hit should roughly correspond to the Central Detector trigger time.
4. The energy flow of the event must be consistent with the hypothesis that the primary interaction occurs within the Central Detector and that the final state track(s)/shower(s) extend to the outside, causing the observed coincident Veto Shield hit(s).
5. The PCE final state must have more than two visible prongs.

One–prong and two–prong events are eliminated, due to the fact that vertex location is ambiguous in these topologies. Events having numerous time–coincident shield hits are usually Rock events, consequently we have removed them. A PCE event sample is expected to contain both charged current and neutral current inelastic neutrino reactions. Our final one kiloton–year PCE sample contains 15 energetic neutrino interactions. Additionally we have isolated 70 upward, stopping track/shower candidates; the latter sample needs further study. Table 3.3 summarizes the selection rates for our partially contained and upward–stopping event samples. A list of the 15 neutrino interactions, with observational details for each, is given in Appendix F. A first–generation Monte Carlo event sample corresponding to an exposure of

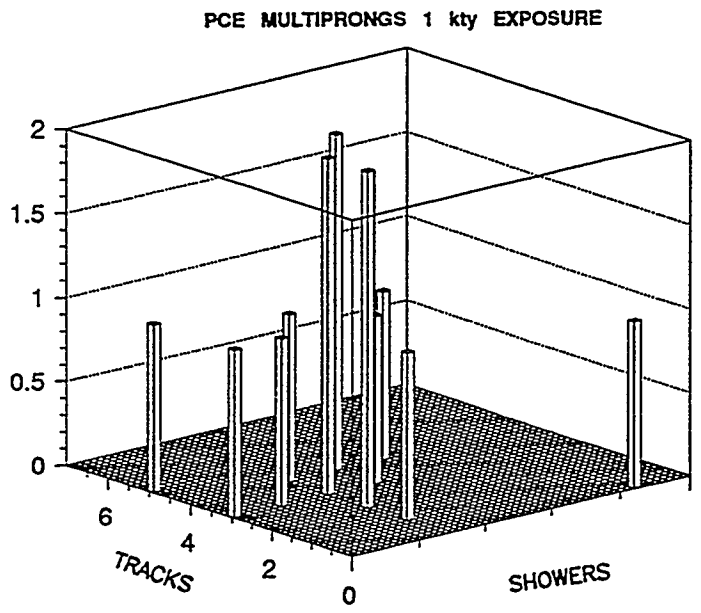

Figure 9.1: Number of tracks versus showers per event, for events in the partially contained multiprong sample.

17 kiloton–years was also analyzed, which contains 117 multiprong events which are partially contained neutrino interactions (see Section 3.9). All of the events included in the "golden PCE" sample were scanned by the author and by Prof. Mann using STING. Each event was digitized and the three–dimensional hit coordinates were stored on a DST.

9.4 PCE Topologies

PCE events generally have several energetic tracks and/or showers. Consequently they pose a formidable challenge to pattern recognition and to analysis. The level of topological complexity is indicated by their distribution in the track–versus–shower count–per–event diplot of Fig. 9.1. The sample exhibits a broad distribution over the track–shower combinations, with relatively more tracks than showers in most events. This is perhaps to be expected, since energetic tracks have higher probability to exit the fiducial volume, than do showers of similar energy.

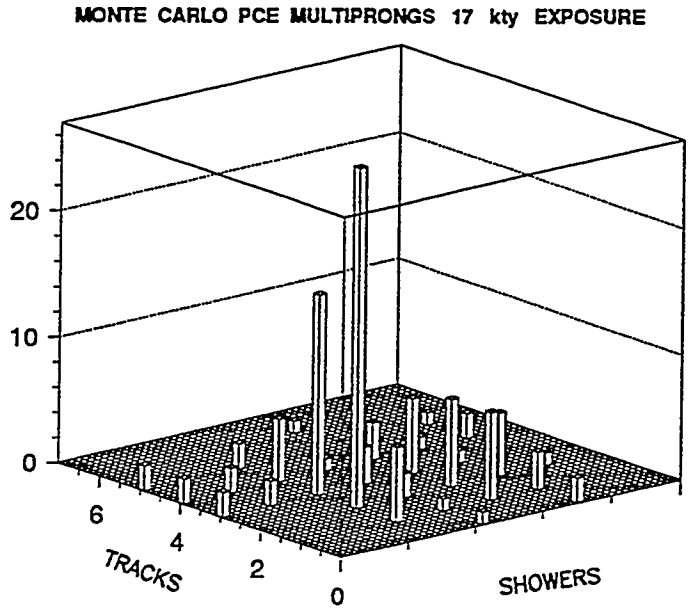

Figure 9.2: Number of tracks versus showers per event, for events in the Monte Carlo partially contained multiprong sample.

Fig. 9.2 shows the topologies – in term of track–shower combinations – from our scan of the Monte Carlo event sample. Here the topological distribution from our 17 kiloton–year simulation is rather different; two tracks with two showers appear to be the predominant topology. The PCE Monte Carlo also indicates the existence of shower–dominated events which do not appear in our statistically limited PCE sample. In the future, these differences will need to be reexamined with more data.

9.5 Locations of Primary Vertices

It is informative to plot the spatial locations of the PCE primary vertices. This distribution of vertices inside the calorimeter will be compared with the corresponding distribution for the CEV sample. Fig. 9.3 shows the event vertex distribution for the PCE sample from a 'top–view' of the Soudan 2 Central Detector, whereas Fig. 9.4 shows the same distribution from the 'side–view'. Modules non–existent

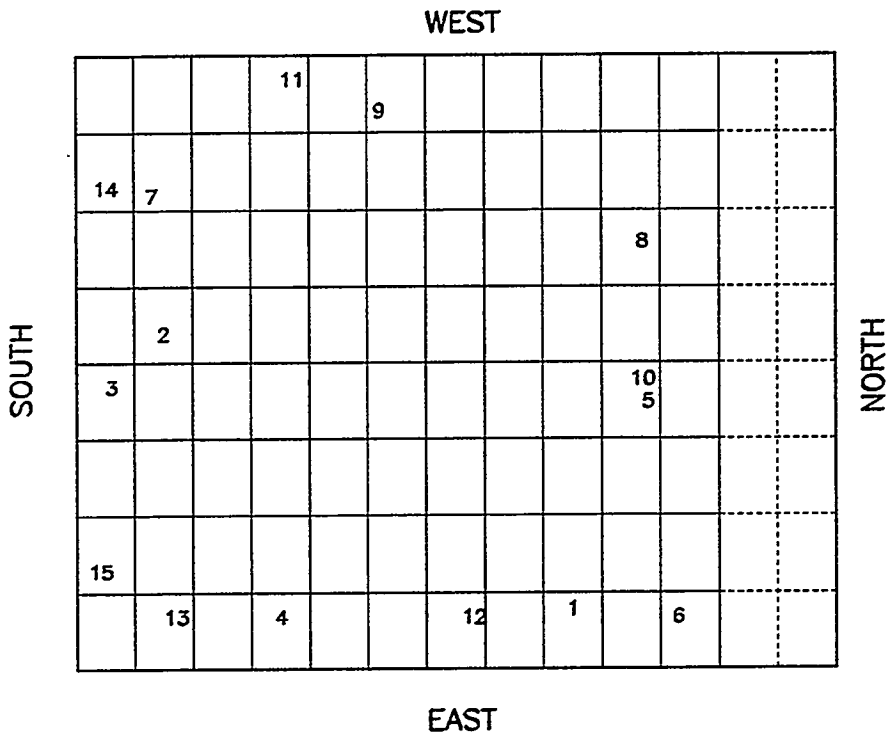

Figure 9.3: Top view of vertex locations of PCE events.

during our data running period are depicted in dashed lines, and individual events are identified according to their order of appearance in Appendix F.

In Figs. 9.3 and 9.4 we observe that PCE events distribute towards the outer surfaces of the Central Detector. In Fig. 9.4 we observe that the top modules of the calorimeter are relatively depleted in PCE events compared to the bottom modules. The latter trend is the manifestation of our selection cut 'Cut3' in the space distribution of the PCE sample, which eliminates events having shield hits on the ceiling.

Figs. 9.5 and 9.6 show the vertex locations of our contained multiprong sample, viewed from the top and the side of the Soudan 2 Central Detector respectively. Modules non–existent for data running are depicted in dashed lines; the events are designated according to the order in which they are listed in Table III of Appendix D. Here the distribution of vertex locations is more nearly isotropic than that observed with PCE events (see Fig. 9.5). This is as expected assuming the events are neutrino–induced. In Fig. 9.6 we observe that the contained multiprong sample

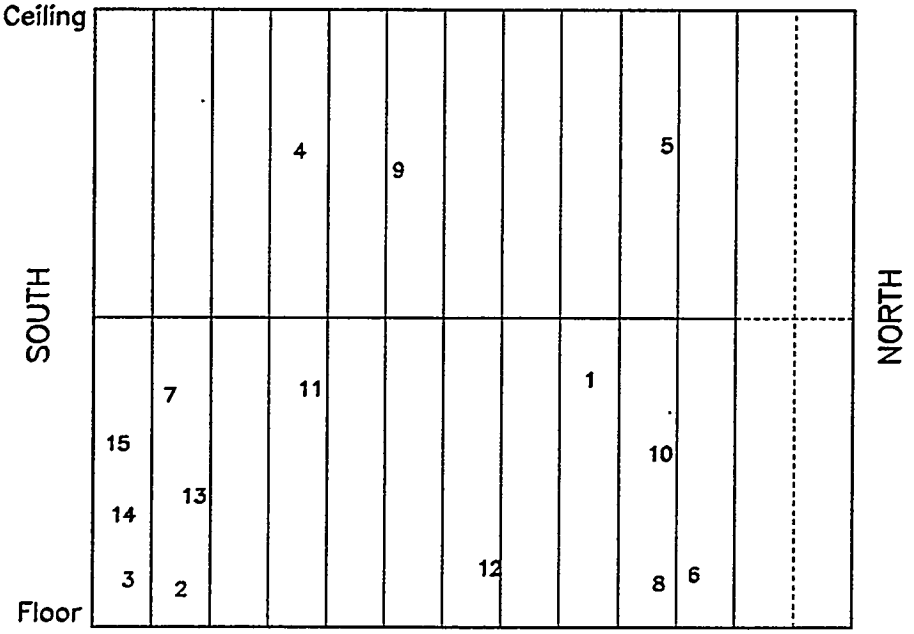

Figure 9.4: Side view of vertex locations of PCE events.

has more vertices near the top (23 out of 34) of the Central Detector than near the bottom (11 out of 34), however this trend (a 2σ effect) needs to be reexamined with more data.

Figs. 9.7 and 9.8 show the vertex locations of the contained single track (stars) and single shower (open circles) event samples, viewed from the top and from the side of the Soudan 2 Central Detector respectively. It is comforting that these distributions show no anisotropies which could be interpreted as evidence of contamination due to interactions of cosmic ray induced gammas or neutrons.

9.6 Visible Energy in PCE Events

Upon digitization of the PCE sample, a four–momentum vector is determined for each track and shower separately (see Chapter 4). For each event one can obtain a total event four–vector by summing the four–vectors for all tracks and showers. From the event four–vectors, the event visible energies can be calculated. Fig. 9.9 shows the visible final state energy for the partially contained multiprong events.

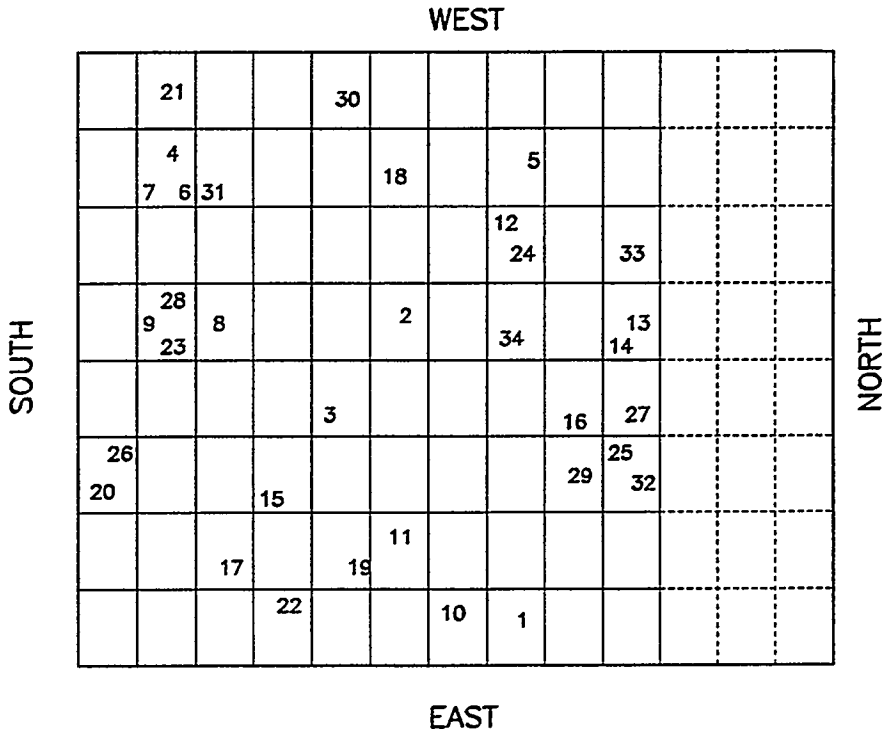

Figure 9.5: Top view of vertex locations of CEV multiprong events.

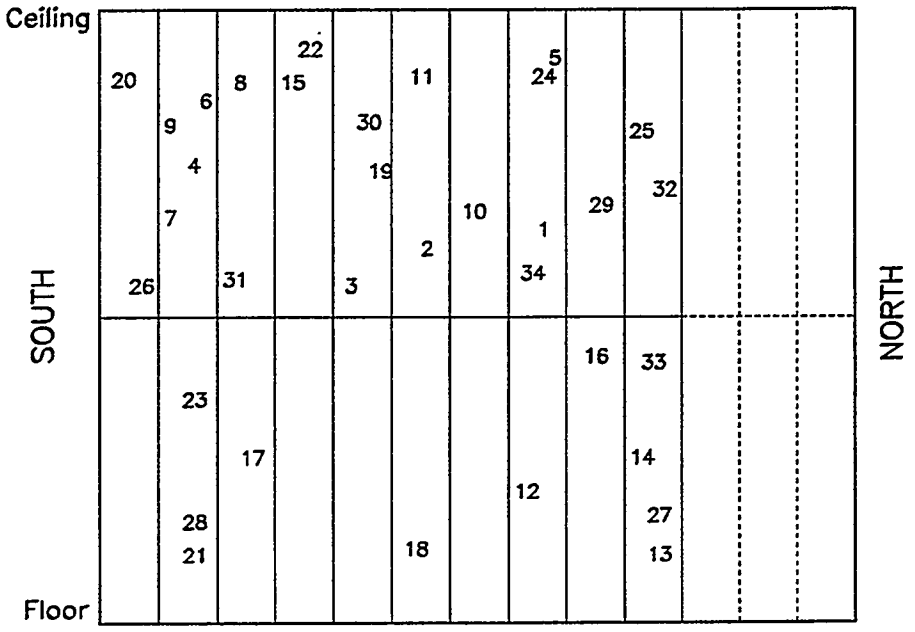

Figure 9.6: Side view of vertex locations of CEV multiprong events.

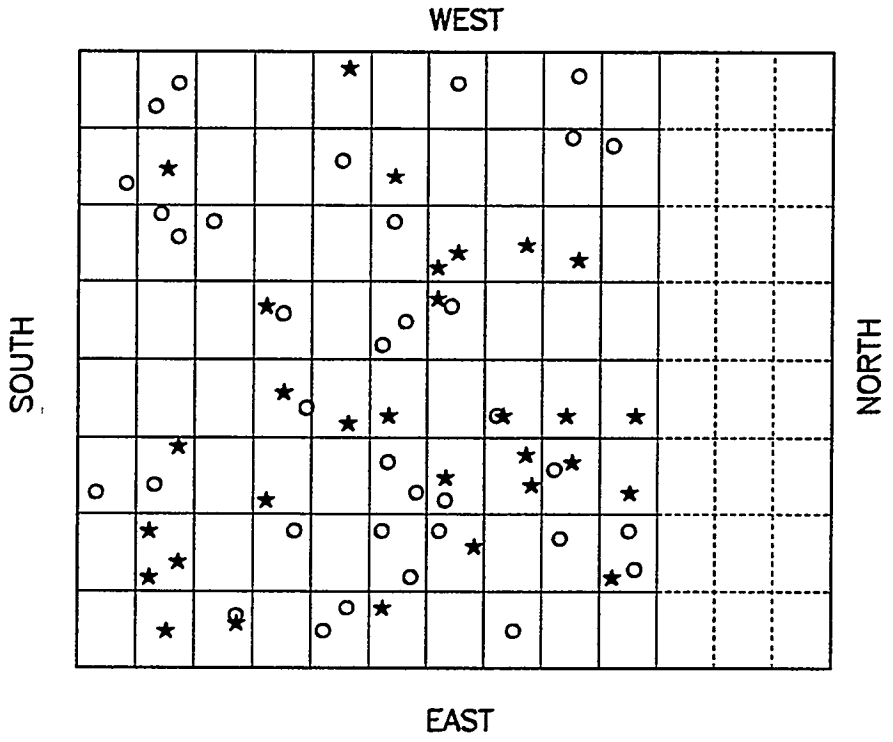

Figure 9.7: Top view of vertex locations of CEV single tracks (stars) and shower (open circles) events.

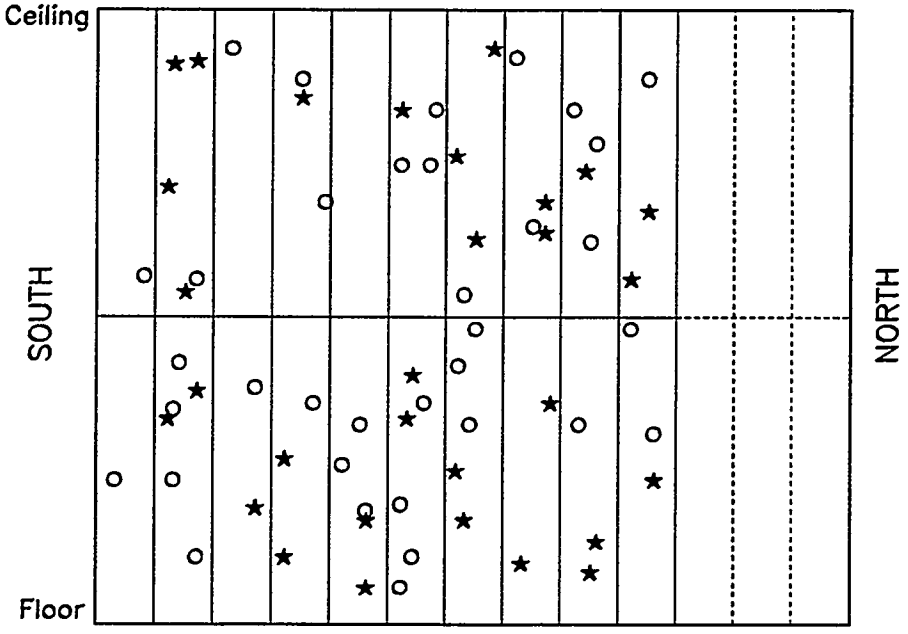

Figure 9.8: Side view of vertex locations of CEV single tracks (stars) and shower (open circles) events.

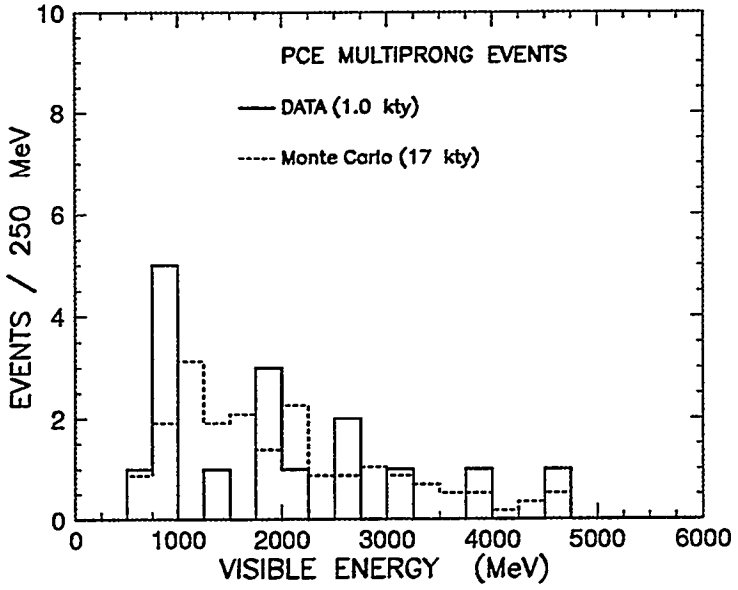

Figure 9.9: Event visible energy in partially contained multiprong event sample (Monte Carlo is normalized to the number of events in the data).

The solid line depicts our events from a 1.0 kiloton–year exposure; the dashed line shows reconstructed events of the 17 kiloton–year Monte Carlo simulation, with the area normalized to the data. As shown by the solid histogram in Fig. 9.9, the PCE sample contains energetic events, with visible energies extending up to 5 GeV. The Monte Carlo reproduces the energy spread of the PCE sample reasonably well.

9.7 Inclusive Particle Distributions

Classification of tracks was carried out according to information obtained in scanning. Specifically, we looked for heavy ionization and hadronic behavior exhibited by the tracks. Heavily ionizing tracks with straight trajectories were assigned the proton mass. A lightly ionizing, scattering track – any track which is visibly deflected from its original course – is assigned the pion mass. Lightly ionizing, long (e.g. $>$ 100 cm), straggling tracks are assigned the muon mass. The remaining tracks are ambiguous between charged pions and muons, and both the pion and

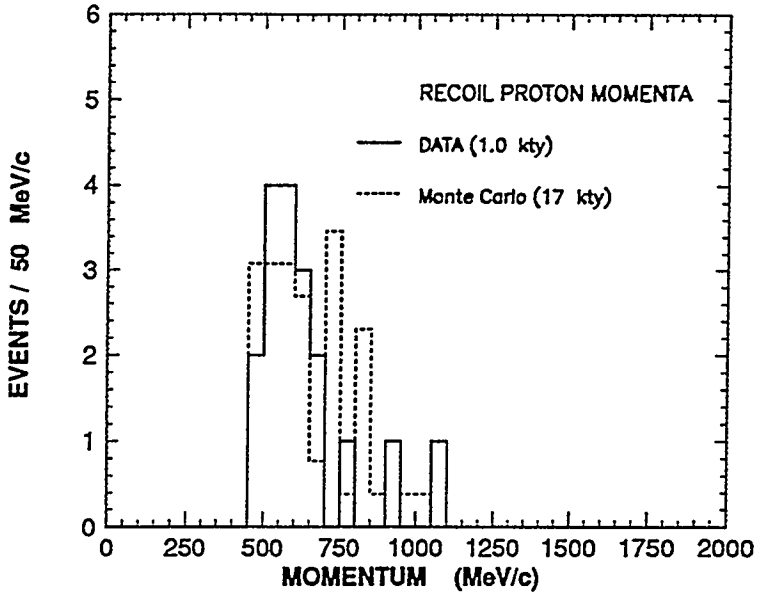

Figure 9.10: Momenta of protons in partially contained multiprong event sample (Monte Carlo is normalized to the number of events in the data).

muon masses are assigned to them.

Fig. 9.10 shows the proton momentum distribution for the PCE events; the solid histogram represents 1.0 kiloton–year exposure of the data, the dashed line depicts our reconstructed Monte Carlo simulation normalized to the data. The data (solid histogram) shows a peak at 600 MeV/c with a gradual fall–off beyond 1 GeV/c. The recoil proton momentum distribution from our PCE events follows the shape extracted from flux–weighted ν_μ D_2 events (see Fig. 7.4). Our Monte Carlo distribution (dashed histogram) is also in reasonable agreement.

Fig. 9.11 shows the pion/muon momentum distribution for the PCE events; the solid line represents the 1.0 kiloton–year exposure of the data, the dashed line depicts our reconstructed Monte Carlo simulation normalized to the data. Fig. 9.12 compares the momenta from identified pions with the corresponding reconstructed Monte Carlo distribution. Although the latter distributions indicate agreement between the data and the simulation, the former distributions (pion/muon momenta of Fig. 9.11) suggest that the Monte Carlo may be producing too many pions and

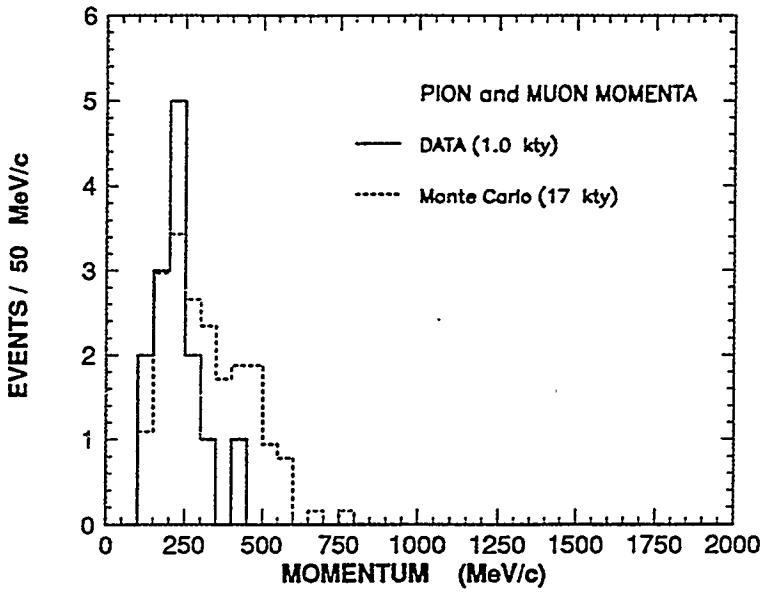

Figure 9.11: Pion/muon momenta in partially contained multiprong event sample (Monte Carlo is normalized to the number of events in the data).

muons with large momenta.

Using the methods discussed in Section 4.3, a four–momentum vector for each shower is determined. Fig. 9.13 shows the two shower invariant mass for all possible combinations – with the "best" vertex selection – weighted for all combinations (one over the number of combinations). The solid histogram shows the PCE data, whereas the dashed histogram depicts the reconstructed Monte Carlo simulation normalized to the data. In general, a scanner assigns vertices interactively using the STING program from which he is allowed to designate "the best" vertex according to his visual extrapolation of all tracks and showers to a converging point in space. The solid histogram in Fig. 9.13 peaks above the nominal position of the π^0 invariant mass. The bin size in the Figure is 50 MeV/c^2; candidate π^0 pairs lie in the range 80–200 MeV/c^2. In the Monte Carlo distribution (dashed histogram), we see a peak which is lower, by two bins, than the data. Nevertheless, a 'signal' is discernible around the π^0 region in both data and Monte Carlo, indicating that among all the shower pair combinations there are some which originate with π^0 decay.

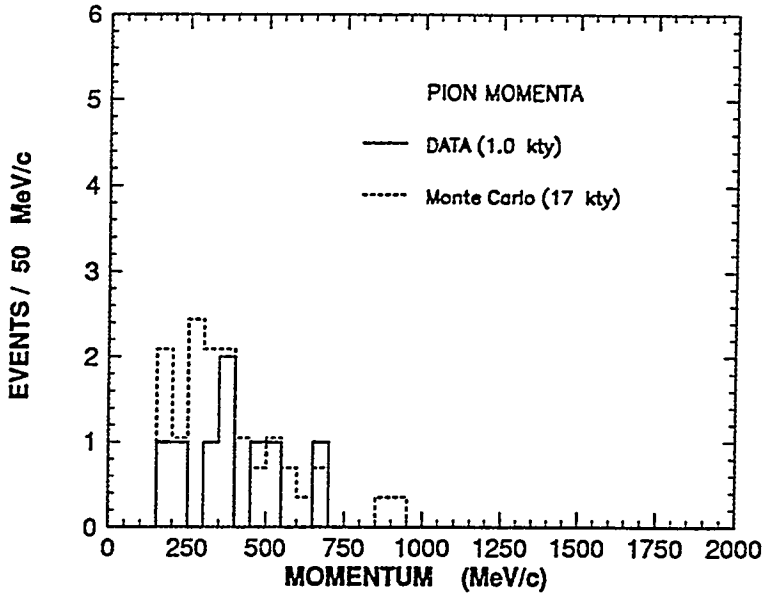

Figure 9.12: Pion momenta in partially contained multiprong event sample (Monte Carlo is normalized to the number of events in the data).

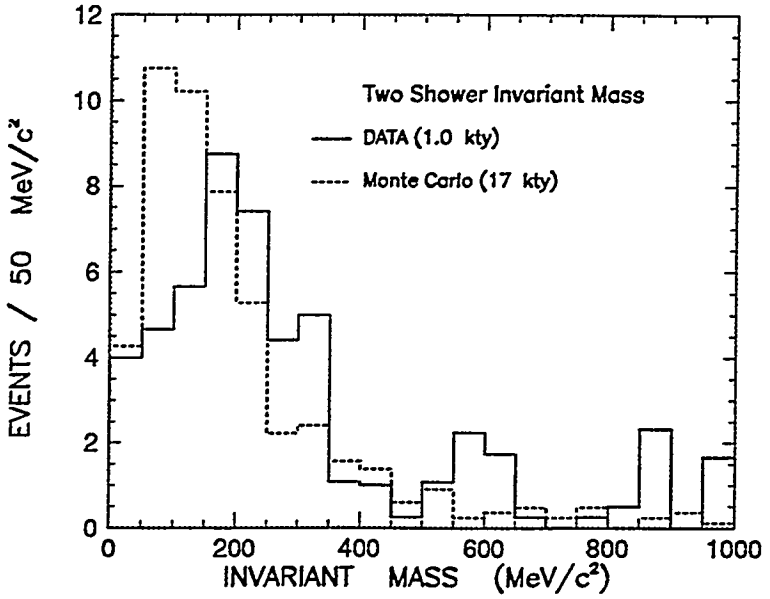

Figure 9.13: Inclusive two shower invariant masses from the PCE (solid line) sample and from our Monte Carlo sample (dashed line, normalized to the data); plotted are all pair combinations weighted by the (inverse) number of combinations, where the "scanner's choice" vertex has been used.

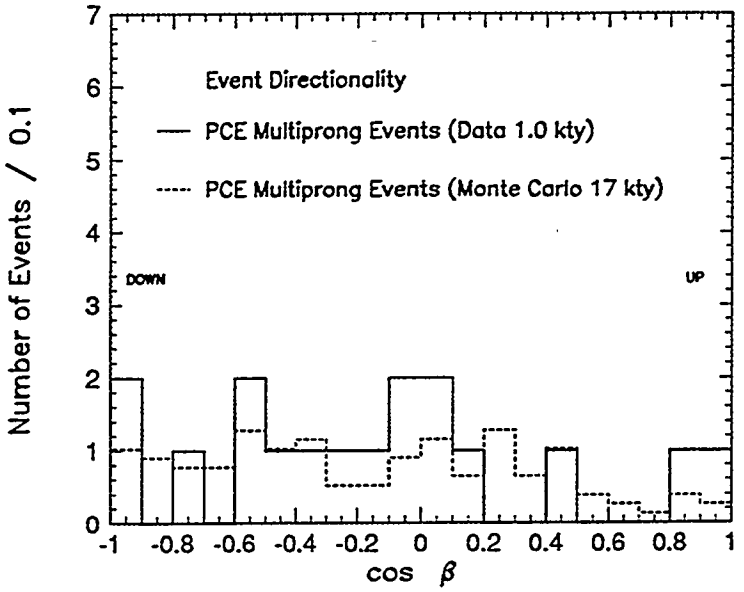

Figure 9.14: Event directionality in the partially contained multiprong event sample (Monte Carlo is normalized to the number of events in the data).

9.8 Event Directionality

For each event, one can obtain the event net momentum by adding each four–vector for each track and shower. Fig. 9.14 shows the cosine of the angle between the visible final state three–momentum and the zenith direction for the PCE events (solid line) and for our reconstructed Monte Carlo (dashed line, normalized to the data) sample. Fig. 9.14 contains more events that are down–going than up–going, which is to be expected since PCE's which exit the top of the Central Detector and hit the Veto Shield ceiling, are eliminated. The Monte Carlo distribution (dashed line) shows a similar mild depletion of upward–going events for this same reason.

It is of interest to plot the cosine of final state net momentum relative to zenith, against the final state visible energy of the event. Figs. 9.15 and 9.16 show these diplots for the PCE and Monte Carlo samples. The dashed line refers to the Kamiokande separation of contained events for their sub–GeV and multi–GeV analyses. Due to our cut which mitigates against energetic, upward–going PCE's,

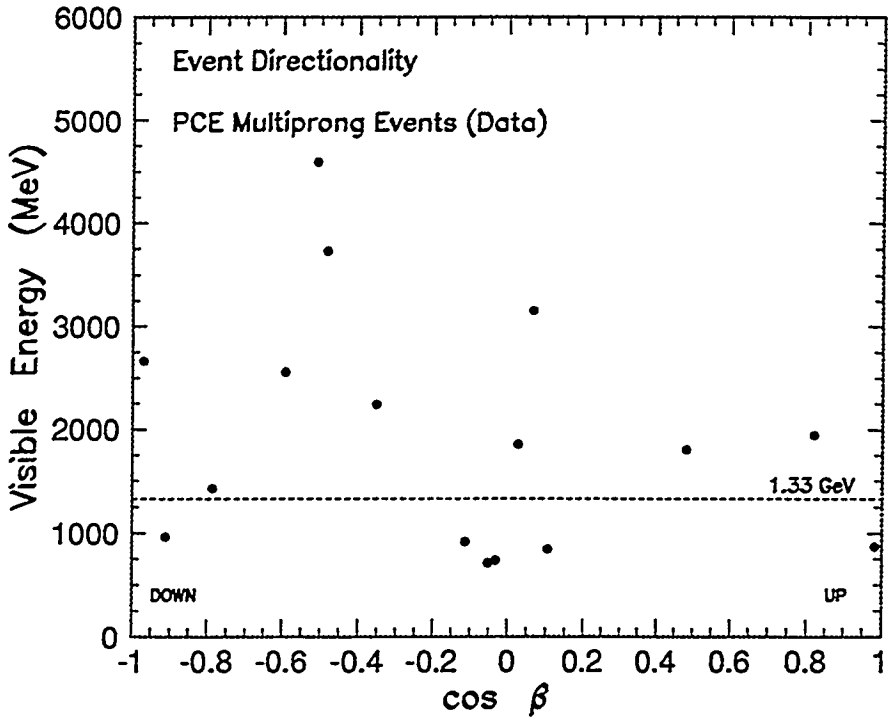

Figure 9.15: Total visible energy, versus cosine of the visible final state momentum versus zenith angle, for partially contained multiprong events.

which may leave 'through the top', we forego examination of these plots for hints of neutrino oscillations.

9.9 Neutrino Flavor Composition of the PCE Sample

In this Section we try to estimate the neutrino flavor composition of the PCE sample. Our approach utilizes the experiment's capabilities for distinguishing the various final state particles.

Upon applying the criteria described in Section 8.4.1, we obtain the results summarized in Table 9.1. The rules were applied straightforwardly; here, the event flavor is assigned according to 'Physicist Choice'. In Table 9.1 a star symbol ($\star$) indicates that a flavor assignment is possible, whereas a solid circle ($\bullet$) signifies that a flavor assignment is not possible. The sample is found to have several events which are flavor–ambiguous – events labelled with more than one star.

In Table 9.1, the ranges for sample flavor are tallied with the corresponding

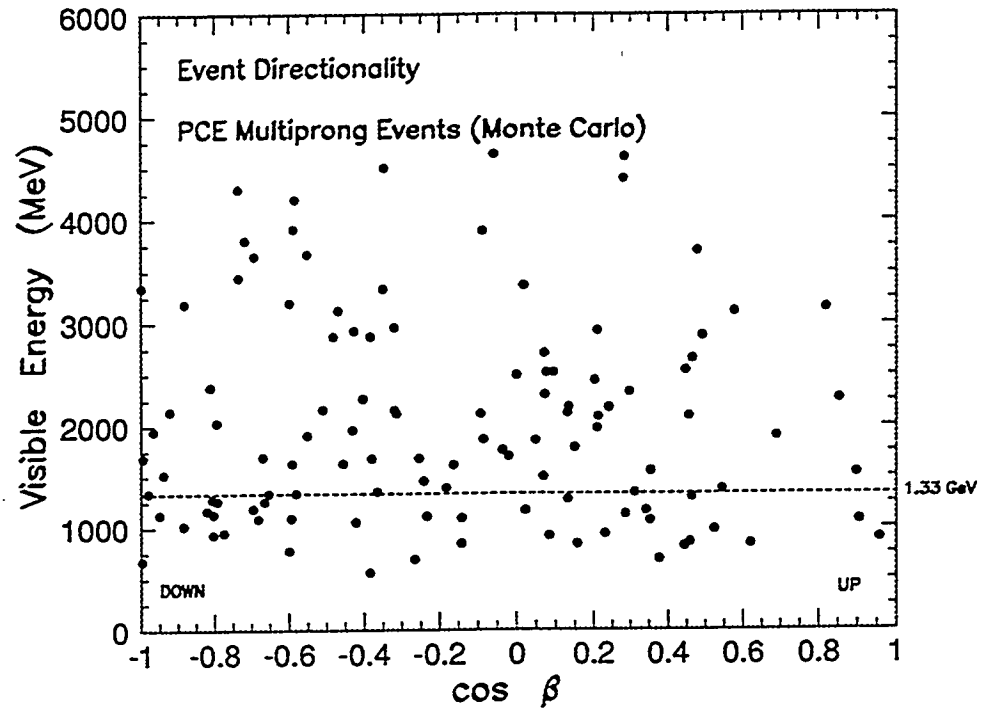

Figure 9.16: Total visible energy, versus cosine of the visible final state momentum versus zenith angle, for partially contained multiprong Monte Carlo events.

percentages in parentheses (rows labelled MAX and MIN). Our Monte Carlo simulation, which is based upon the Bartol neutrino fluxes, predicts that $0.83 \pm 0.09\%$ of events are muon–neutrino charged current reactions, while $0.15 \pm 0.04\%$ are electron–neutrino charged current events, and $0.03 \pm 0.02\%$ are neutral current [3]. As recorded in Table 9.1, physicists' scanning finds the Monte Carlo sample to contain a ν_μ^{CC} fraction in the range 65% to 83%. Similarly the range for ν_e^{CC} is found to be between 3% and 21%, whereas the ν^{NC} varies from 1% to 33%. The results of Table 9.1 are displayed graphically in Figs. 9.17 and 9.18. The shaded areas in Figs. 9.17 and 9.18 show the flavor component range for each of the three sub–samples.

In Fig. 9.17a we display the "physicist choice" of the Monte Carlo scanning results, to be compared to Fig. 9.17b showing the prediction from our Monte Carlo simulation. The agreement in neutrino flavor assignment, of scanning versus neutrino flavor content of the simulation, appears reasonable and is evidence that our flavor estimation method actually works. The comparison also suggests that this method will tend to overestimate the fraction of neutral current events.

I. PCE Event Flavor
"Physicist Choice"

	Event	ν_μ^{CC}	ν_e^{CC}	ν^{NC}
1	29891– 598	•		
2	32045– 982	•		
3	32107– 335		•	
4	35209– 670		⋆	⋆
5	37320– 691	•		
6	37797– 516			•
7	38390– 542	•		
8	39261–1428	⋆	⋆	⋆
9	40255– 987		⋆	⋆
10	41798– 737	•		
11	42124– 771	⋆		⋆
12	42189– 277	⋆		⋆
13	42223– 902		⋆	⋆
14	42550– 241	⋆		⋆
15	44553–1193	⋆		⋆
	MAX =	10 (0.66)	5 (0.33)	9 (0.60)
	MIN =	5 (0.33)	1 (0.06)	1 (0.06)
	Scanning MC_{max} =	0.83	0.21	0.33
	Scanning MC_{min} =	0.65	0.03	0.01
	Truth Table MC =	0.83 ± 0.09	0.15 ± 0.04	0.03 ± 0.02

Table 9.1: Flavor composition of the PCE multiprong sample; symbols ⋆ and • denote "flavor possible" and "flavor definite" respectively.

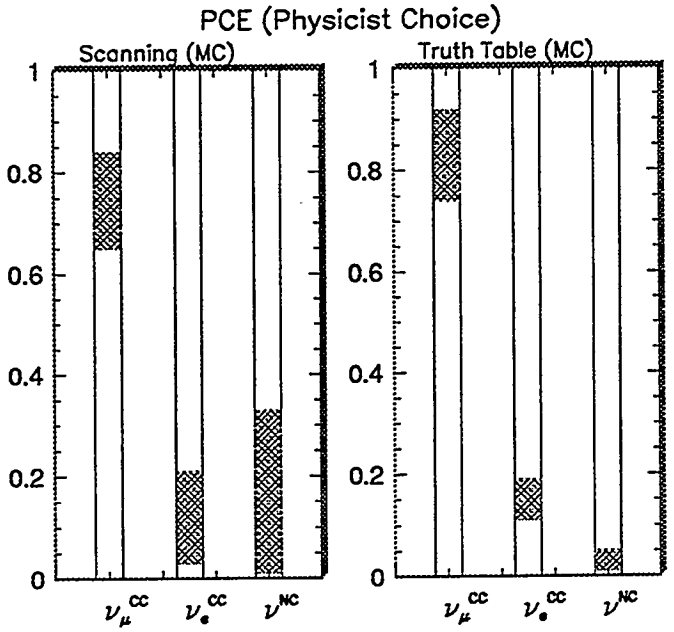

Figure 9.17: Flavor composition of the PCE sample based upon our "physicist choice" analysis.

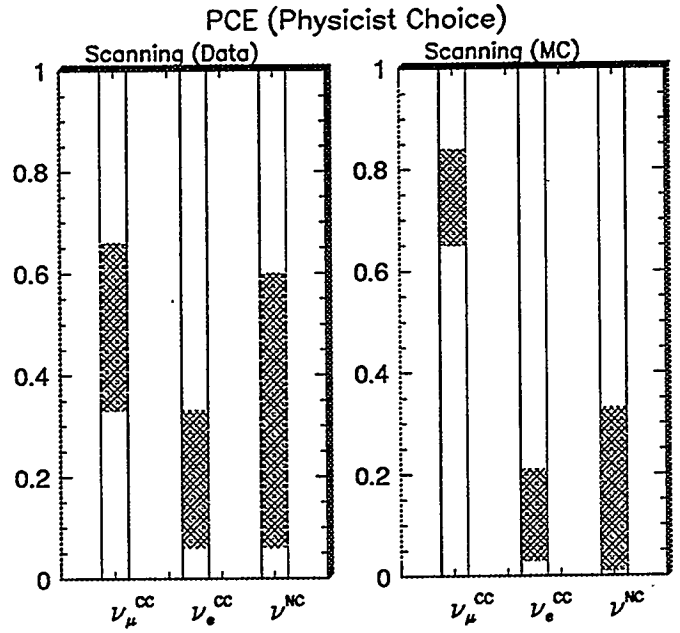

Figure 9.18: Flavor composition of the PCE sample based upon our "physicist choice" analysis.

Fig. 9.18a shows the "physicist choice" flavor estimations on the PCE sample; these are to be compared to Fig. 9.18b which shows corresponding estimations for the Monte Carlo simulation. Here we observe that the PCE flavor assignments are suggestive of a dearth of ν_μ events, and perhaps also of an excess of neutral current events. It would be of interest to review this method with a larger exposure of Soudan 2 data; unfortunately this initial PCE sample is statistically limited.

9.10 Concluding Remarks

In general our Monte Carlo simulation reproduced the energy spread of the PCE sample rather well (see Fig. 9.9). On the other hand it yields, on average, pions, muons and protons with large final state momenta (see Figs. 9.11, 9.10 and 9.12). From comparison of various inclusive distributions in this chapter we conclude that our first–generation Monte Carlo simulation produces final state events which are slightly too energetic.

Unfortunately, the event directionality of our PCE sample cannot be used to search for hints of neutrino oscillations due to our cuts, which reduce the number of upward–going energetic events.

An inclusive π^0 signal has been observed in the PCE sample, however the π^0 peak in two–shower invariant mass combinations appears at a lower mass in the simulation than in the observed data.

We have examined the atmospheric neutrino flavor component of the PCE sample. Our observations suggest – with large statistical errors – that the flavor composition of the PCE sample may contain a relative dearth of muon–neutrino events and also, perhaps, an excess of neutral current events, in comparison with predictions based upon the Bartol neutrino fluxes.

References

[1] T. K. Gaisser, *"Cosmic Rays and Particle Physics"*, Cambridge University Press, 1990 (see Fig. 7.1 on page 87).

[2] W.A. Mann, T. Kafka and W. Leeson, Phys. Lett. **B 291**, 200 (1992); W.A. Mann, T. Kafka and W. Leeson, *in*: Proceedings of DPF92 Meeting, Fermilab, 10–14 November 1992; p. 1330; Soudan 2 Report PDK–590, July 1994.

[3] This prediction is extracted from the Truth Table of the Monte Carlo simulation. The errors quoted here are statistical only.

[4] Y. Fukuda *et al.*, Phys. Lett. **B 335**, 237 (1994).

Chapter 10
Nucleon Decay in Soudan 2

10.1 Introduction

We review the present status of experimental searches for nucleon decay; we then utilize the capability of Soudan 2 for this search. Contained multiprong candidates for the different decay modes, with their kinematical properties, are presented. A background study has been implemented to enable calculation of nucleon decay lifetimes (τ/BR) as well as 90% confidence level lower limits. New measurements will be reported pertaining to event rates for single π^0 production in neutral current reactions initiated by atmospheric neutrinos.

10.2 Search for Nucleon Decay in Multiprong Events

For nucleon decay analysis it is necessary to account for the behavior of nucleons in matter at rest. Fig. 10.1 shows the Fermi momentum distribution for iron (solid histogram) and oxygen (dashed line) respectively [1]. From Fig. 10.1 we infer that the Fermi motion in iron peaks around 250 MeV/c and falls off dramatically above 260 MeV/c. Finite detector resolution can cause the reconstructed final state momentum to be smeared $\pm$100 MeV/c or more from the intrinsic Fermi motion values.

The collaboration has isolated 34 contained multiprong events in a 1.0 kiloton–year exposure. These are events which have two or more tracks and/or showers in the final state. Using methods described in Sections 4.3 and 4.4, a four–momentum

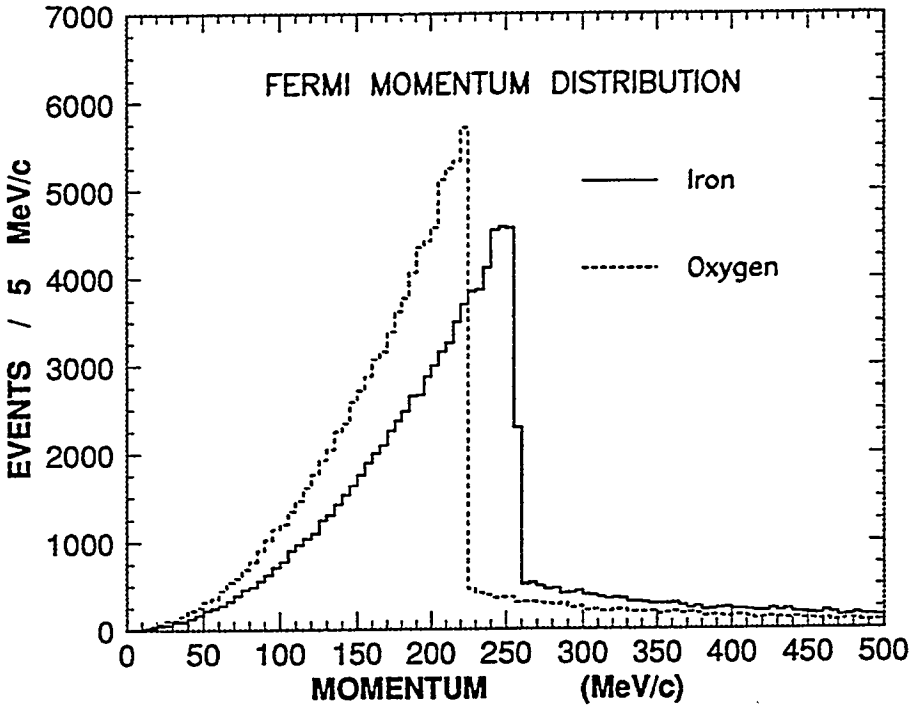

Figure 10.1: Fermi momentum distribution in iron (solid histogram) and oxygen (dashed line) respectively (Ref. 1).

vector can be determined for each track and shower in an event. From the four-vectors we can construct other variables – visible energy, invariant mass, etc. – in order to study our contained multiprong sample.

It is of interest to plot the final state visible energy against the final state net momentum of the event. Figs. 10.2 and 10.3 show these diplots for the multiprong events and for the ν Monte Carlo sample respectively. For events with a visible proton track, the proton mass is not included in the visible energy estimation. The dashed line indicates the nucleon decay region with allowance for Fermi motion and detector resolution. Note that 8 events have visible energy exceeding 2.0 GeV and do not appear in the plots. The solid circles depict events which have no visible proton in the final state, whereas the open circles depict events with a recoil proton. Fig. 10.2 shows that we have at least one candidate for nucleon decay. Fig. 10.3 shows that the amount of background to be expected from neutrino reactions in the nucleon decay sample is low. Our first-generation Monte Carlo indicates that we should have background of less than one neutrino event per kiloton-year. It can be

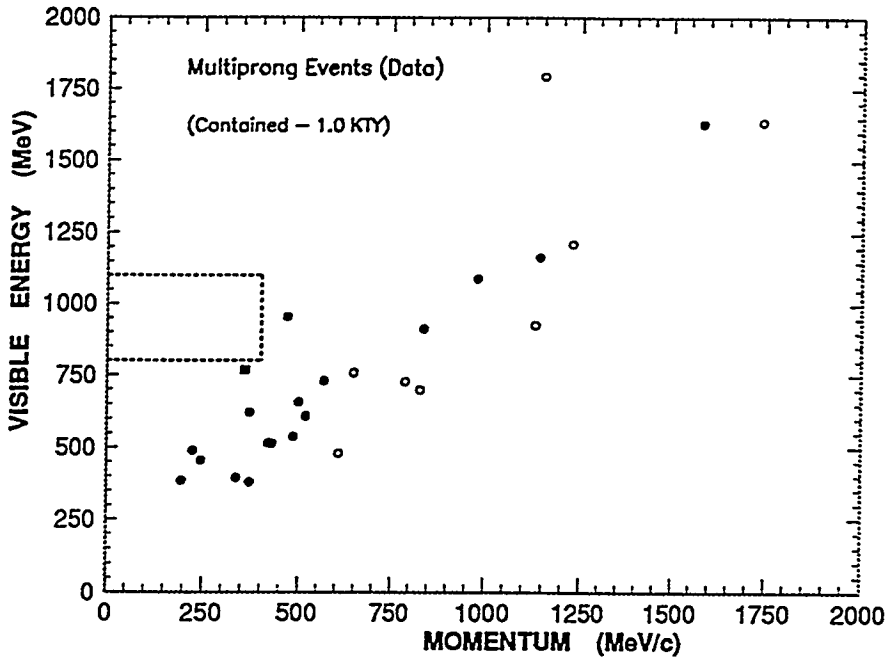

Figure 10.2: Total visible energy versus the visible final state momentum for the multiprong data sample; final state events with (without) recoil proton are depicted by open (closed) circles.

seen in Fig. 10.3 that events with recoil protons (open circles) are as common as those without (solid circles). The majority of protons in the Monte Carlo events come from Δ decay in neutrino reactions of energies exceeding 1 GeV.

We have also plotted the final state invariant mass against the net momentum for each event. Figs. 10.4 and 10.5 show corresponding diplots for the multiprong events and for the Monte Carlo sample respectively. Again, the dashed box encloses the nucleon decay region. In both Figures, events without or with a visible final state proton are distinguished via solid or open circle symbols. Fig. 10.4 confirms that we have one candidate for nucleon decay. Fig. 10.5 indicates that the neutrino background for nucleon decay, from 3.45 kiloton–years of exposure, is low, being of order $1/3.45 \sim 0.3$ events per kiloton–year.

The event which appears just below the nucleon decay region in both Figs 10.2 and 10.4 (depicted by solid square) is event 35219–766. This particular event has a

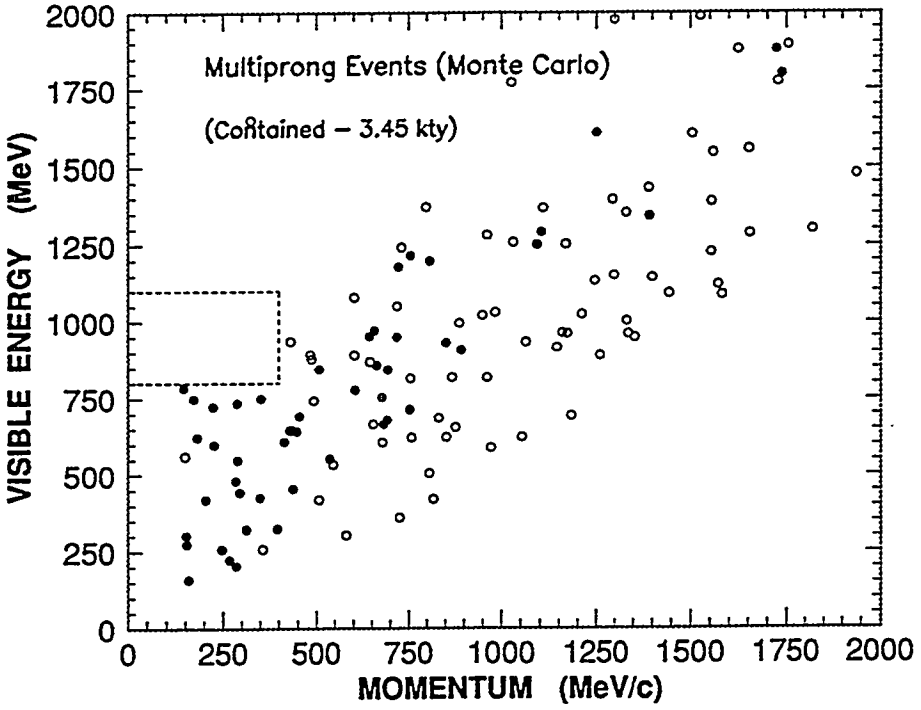

Figure 10.3: Total visible energy versus visible final state momentum for the Monte Carlo multiprong sample.

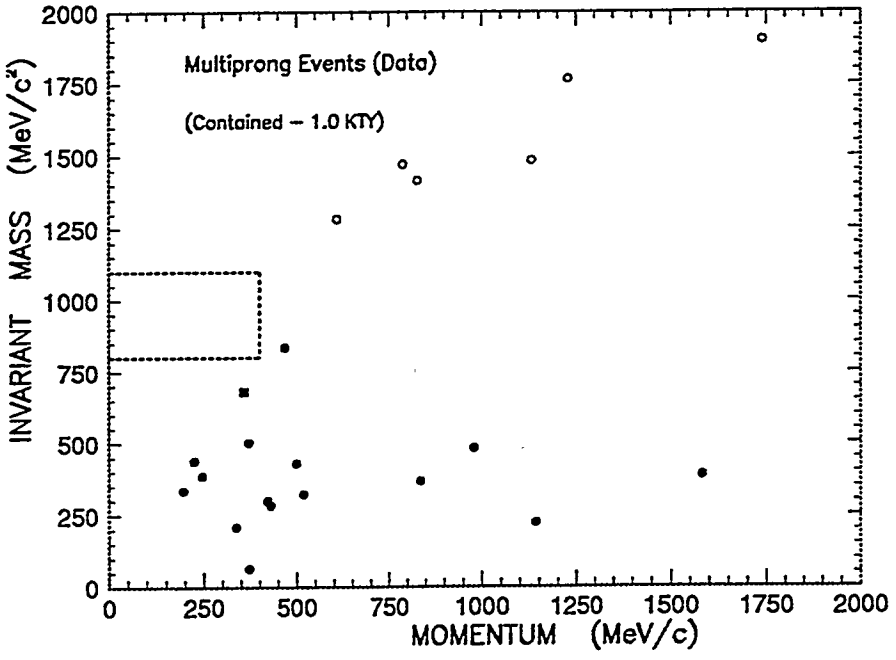

Figure 10.4: Invariant mass versus the visible final state momentum for the multiprong data.

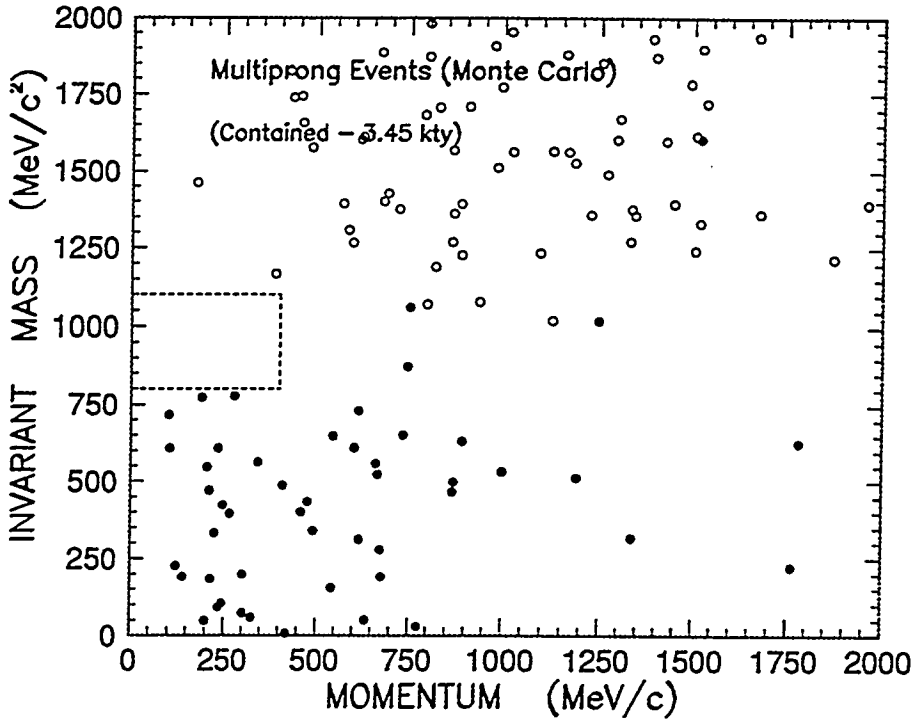

Figure 10.5: Invariant mass versus the visible final state momentum for the multiprong Monte Carlo sample.

three–prong topology. It contains a track 130 cm long which exhibits some straggling; an endpoint decay is possible. It also contains two small showers, one with 10 hits and the other with 8 hits. The two small showers have invariant mass in the range 160–320 MeV/c^2; the event is a possible $p \rightarrow \mu^+\pi^0$ candidate. Kinematic features of the event are summarized in Table 10.1.

10.3 Search for $n \rightarrow e^+e^-\nu$

We present here results from a search for two specific baryon–number–violating processes which we have undertaken with the Soudan 2 data. Our search makes use of the pattern recognition capability of our iron tracking calorimeter in multiprong events. Our investigation of the decay mode $p \rightarrow e^+\nu\nu$ [2] has motivated us to search for the mode

$$n \rightarrow e^+ + e^- + \nu. \tag{10.1}$$

Nucleon Decay Candidate Event 35219–766	
Visible energy = 754 MeV Net momentum = 349 MeV/c Invariant mass = 669 MeV/c^2	Muon momentum = 462 MeV/c γ_1 momentum = 169 MeV/c γ_2 momentum = 111 MeV/c
$\gamma_1\gamma_2$ momentum = 120–265 MeV/c d_{γ_1} = 10.6 cm	$M_{\gamma_1\gamma_2}$ = 165–318 MeV/c^2 d_{γ_2} = 9.3 cm

Table 10.1: Candidate nucleon decay event.

The only published limits on the lifetime over branching ratio τ/BR for this particular mode come from the Frejus [3] and IMB-3 [4] experiments, which are τ/BR $> 7.4 \times 10^{31}$ years and τ/BR $> 9.0 \times 10^{31}$ years respectively. Both quoted numbers are lower limits on the nucleon lifetime at 90% CL without background subtraction.

10.3.1 Kinematical Properties

We begin our study of decay mode (10.1) with a Monte Carlo examination of the final state kinematics, and then discuss signal extraction from our contained multiprong sample. It is helpful in formulating our approach to study the behavior of leptons ($e^{\pm}$ with Fermi motion) in matter. For this purpose we use a program called PPOP, a stand–alone program for simulation of proton and neutron decays written by T. Kafka [5]. We examine decay mode (10.1) in iron and oxygen, taking into account Fermi motion in both cases.

Fig. 10.6a shows the positron (or electron) momentum distribution. The solid histogram shows the Monte Carlo simulation in iron with Fermi motion, while the dashed line shows the simulation in oxygen. Fig. 10.6a shows that the momentum

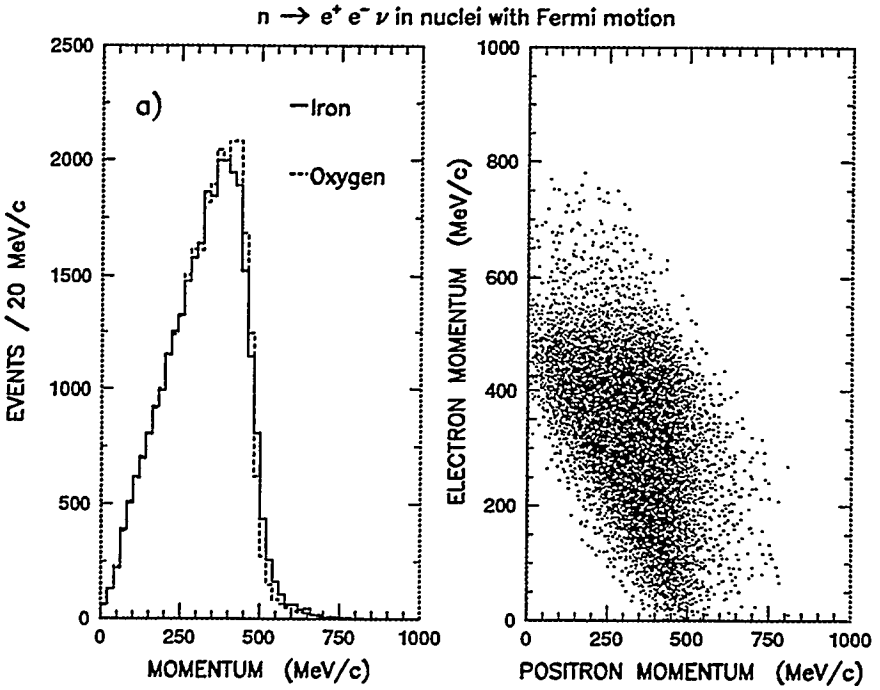

Figure 10.6: $n \rightarrow e^+e^-\nu$ decay mode: a) Positron momentum distribution; b) electron versus positron momenta. The solid line shows decays in an iron medium, whereas the dashed line shows decays in an oxygen medium.

of the positron peaks at 400 MeV/c with a sharp fall–off around 500 MeV/c. It is of interest to plot the positron momentum against the electron momentum and consider the phase space available to these particles. Fig. 10.6b show this diplot for an iron medium.

Fig. 10.7 shows the cosine of the angle between the positron and the electron (Fig. 10.7a), the total visible energy – the electron energy plus the positron energy – (Fig. 10.7b), and the invariant mass for the positron–electron pair (Fig. 10.7c). From Fig. 10.7a, we discern that the positron and electron tend to be produced back–to–back. Similarly, from Fig. 10.7b, we see that the visible energy peaks at 500 MeV with a gradual fall–off to the neutron mass. Finally, from Fig. 10.7c, we infer a broad distribution for the positron–electron invariant mass pair which ranges from 0 to 940 MeV/c^2. Fig. 10.8 displays the final state visible momentum of the positron–electron pair versus the invariant mass for the positron–electron pair.

Figs. 10.6, 10.7, and 10.8 display all of the kinematic observables that we require

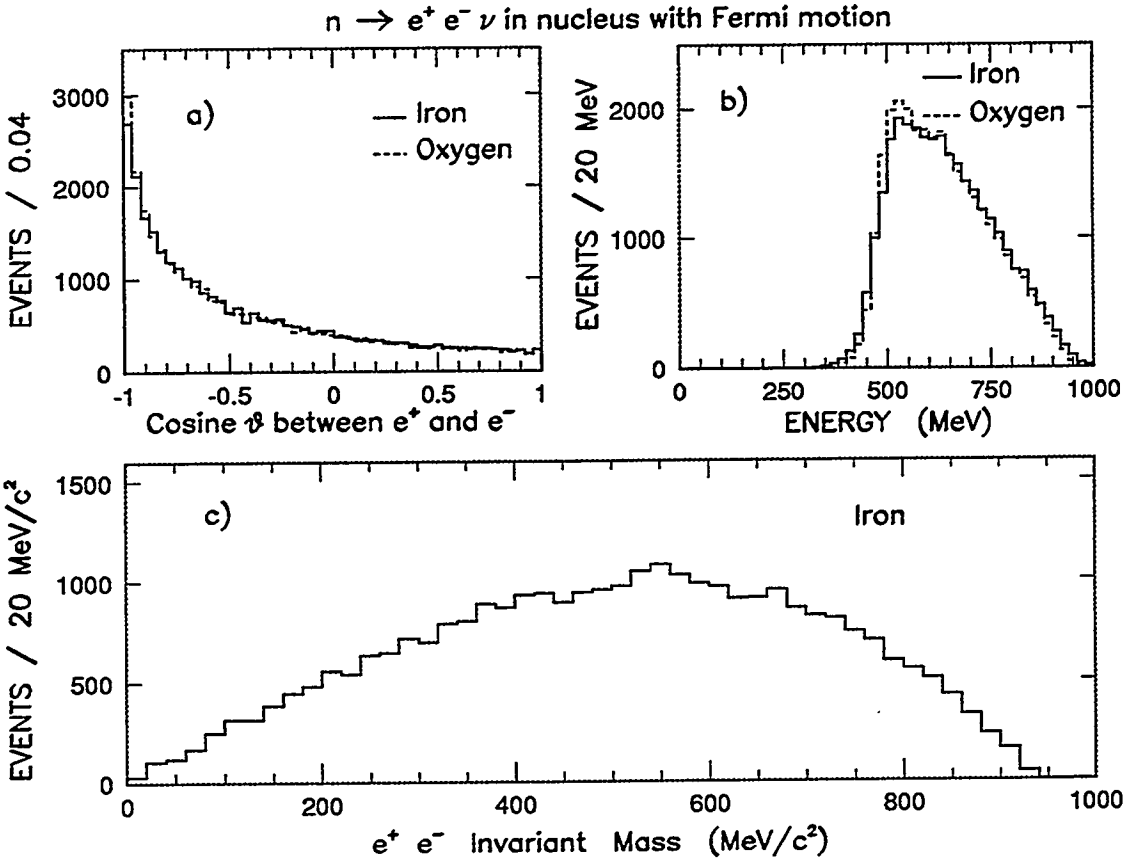

Figure 10.7: $n \to e^+e^-\nu$ decay mode: a) cosine of the angle between electron–positron pair; b) total visible energy distribution; c) electron–positron invariant mass distribution. The solid (dashed) line depicts visible energy in decays from iron (oxygen) nuclei.

for the study of decay mode (10.1). Using these observables one can choose kinematic selections which event candidates for mode (10.1) need to satisfy. From Fig. 10.6a, we infer that neither the positron or electron momentum should exceed 550 MeV/c. Fig. 10.7c illustrates the obvious constraint that the invariant mass of the positron–electron pair should not exceed 940 MeV/c^2. In the next section we will apply a set of suitable kinematical selections to the multiprong events and to the rock sample, in order to extract a signal for decay mode (10.1).

10.3.2 Extracting the Signal

In order to extract a signal for $n \to e^+e^-\nu$, we need to select events according to their topology, taking into account the influence of nuclear effects and of the

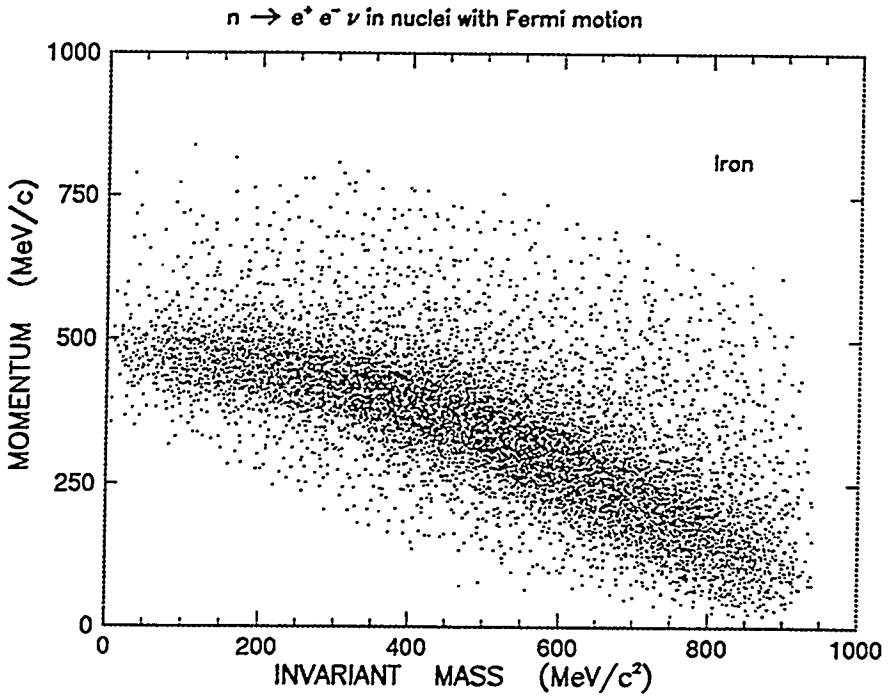

Figure 10.8: $n \rightarrow e^+e^-\nu$ decay mode: electron–positron net momentum versus invariant mass.

detector efficiencies. The decay mode $n \rightarrow e^+e^-\nu$ will have a distinctive topology in the Soudan 2 iron tracking calorimeter. In this mode, one out of three final state particles is always unobserved in the detector (the neutrino), and we are left with two prompt electron ($e^{\pm}$) showers as evidence for the occurrence of the decay. We now select events which have the two–shower topology and apply successively a number of cuts to impose the accepted momentum range on these events, according to expectation from nucleon decay kinematics.

Background for nucleon decay arises from atmospheric neutrino interactions and from neutron–induced events which can mimic the decay being studied. Our selections yield the extraction of the signal and of the background for decay mode (10.1) simultaneously. Specifically, we apply a two–shower topology selection to the 34 contained multiprong events, to the 98 Rock multiprong events, and to the 3.45 kiloton year ν Monte Carlo sample which contains 132 neutrino multiprong events. We are left with 7 contained multiprong events, 18 Rock multiprongs, and 11 simulated neutrino multiprong events (see Appendix G). We now impose additional

kinematical requirements.

Based upon Fig. 10.7c, we require that the invariant mass of the e^-e^+ pair lie in the range $200 \leq M_{e^-e^+} \leq 900$ MeV/c^2. We do not accept invariant masses below 200 MeV/c^2 because this region is populated by π^0 background. Fig. 10.9 shows the electron–positron invariant mass distribution. The solid and open squares depict multiprong events, solid and open stars are Rock events, and open circles depict Monte Carlo neutrino events. We have introduced the notation of an 'open symbol' to represent events being eliminated by a particular cut, whereas the 'solid symbol' depicts events that are not being eliminated. Fig. 10.9 shows that the majority of all Rock (open stars) and simulated neutrino two–shower events (open circles) fall below 200 MeV/c^2. The number of candidate multiprongs is then reduced to 4 events (illustrated by the four solid squares), while the number of Rock multiprongs is reduced to 6 (solid stars) and the simulated neutrino multiprongs reduced to 1 event (solid circle). The reason why simulated ν events have been eliminated as a potential background for decay mode (10.1), is because the majority of ν two–shower events originate with $\nu N \rightarrow \nu N \pi^0$ (see Appendix G). From Fig. 10.6a we discern that both the positron and the electron should have momenta less than 700 MeV/c. This requirement reduces the multiprong sample to 2 events; the Rock sample is reduced to 4 events (see Table 10.2).

We now examine correlations between different kinematical variables as illustrated in Figs. 10.6b and 10.8. Fig. 10.10 shows the electron versus positron momentum. Here we observe that the contamination due to Rock events (solid stars) can be reduced to 3 events and the simulated neutrino multiprongs reduced to zero. On the other hand, from the same Figure we see that the two contained multiprong candidates are inside the allowed phase–space (depict by the solid squares). Fig. 10.11 shows the visible momentum versus $e^{\pm}$ pair invariant mass. The solid and open squares depict the contained multiprong events, the solid and open stars depict the Rock multiprong events, and the open circles depict the simulated neutrino

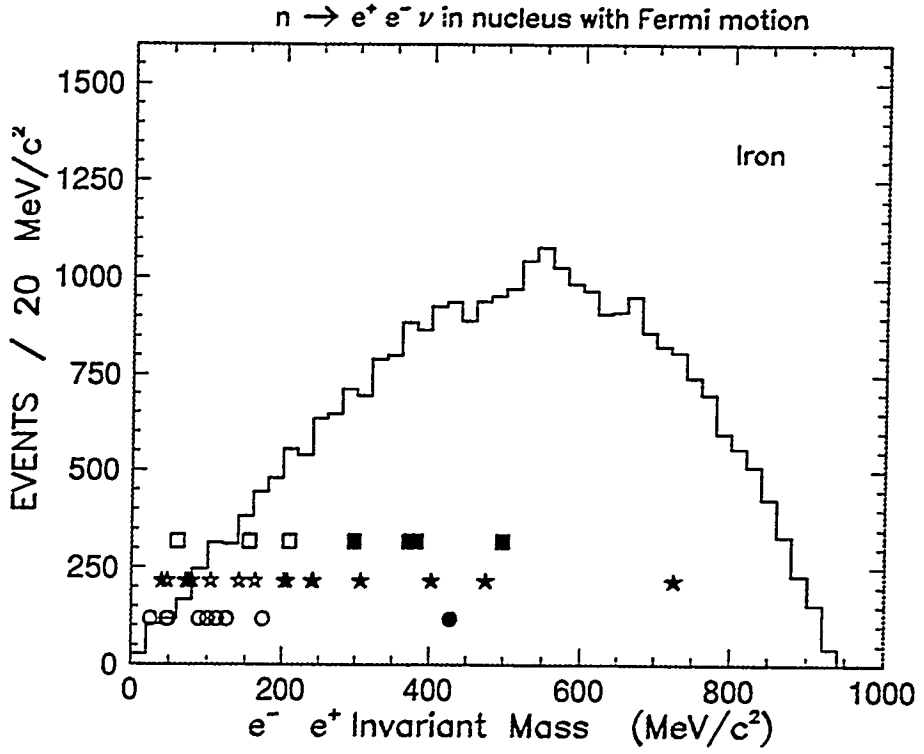

Figure 10.9: Invariant mass for e^-e^+ pairs: The solid and open squares are multiprong events, solid and open stars depict Rock events, and open (solid) circles depict Monte Carlo neutrino events.

Nucleon Decay Candidates

Mode $n \rightarrow e^+e^-\nu$

	Multiprong Sample	Rock Sample	Neutrino Sample (MC)
Exposure	1.0 kty	1.0 kty	3.45 kty
Number Events	34	98	132
Topology cut	7	18	11
Kinematical cuts:			
$200 \leq M_{e^-e^+} \leq 900$ MeV/c^2	4	6	1
P < 700 MeV/c	2	4	1
Correlation cuts:			
Fig. 10	2	3	0
Fig. 11	2	1	0

Table 10.2: Candidate events for $n \rightarrow e^+e^-\nu$.

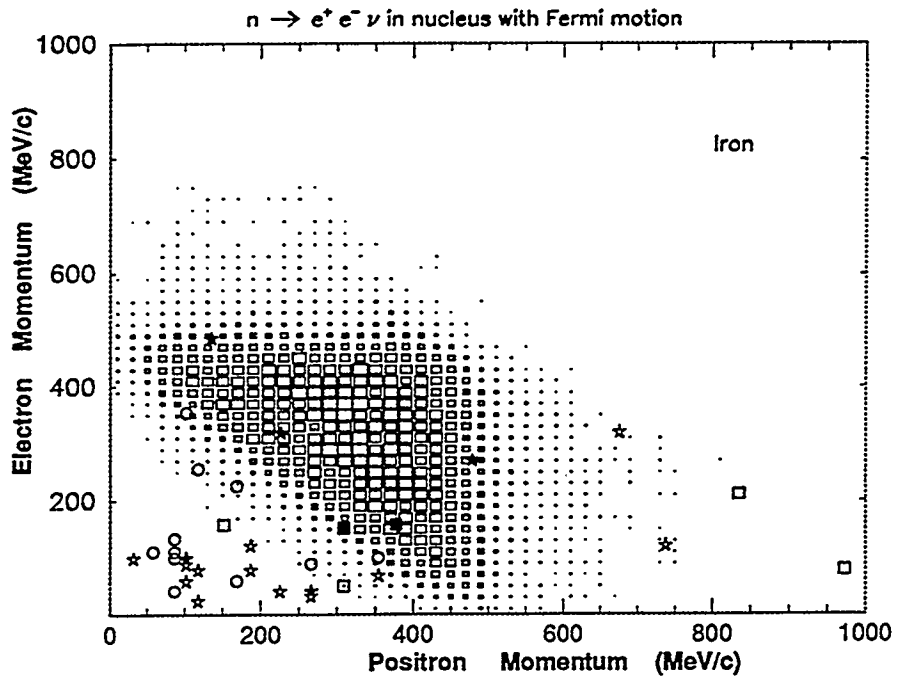

Figure 10.10: Electron versus positron momenta: solid and open squares show multiprong events, solid and open stars depict Rock events, and open circles depict Monte Carlo neutrino events.

multiprong events. From Fig. 10.11 we see that the Rock multiprong background can be reduced to 1 event (solid star). We also see that our two candidates are not excluded (solid squares); these remain viable as candidates for neutron decay mode (10.1).

We impose a final selection which distinguishes between prompt electrons and gamma showers. That is, we will require that the two candidates indeed contain two prompt electrons in their final states. Recall that in Section 8.2 we concluded that in events with well–determined vertices, a shower can be either electron or photon–induced if the vertex to first hit distance is smaller than 7 centimeters. However, if the distance is greater than 7 centimeters, the shower is almost certainly photon–induced. The key statement in this criterion is "well–determined vertex". Unfortunately for decay mode (10.1), the vertex determination is somewhat ambiguous due to the fact that the visible final state is incomplete. One concludes that this uncertainty in the primary vertex location will give rise to a spread in initial

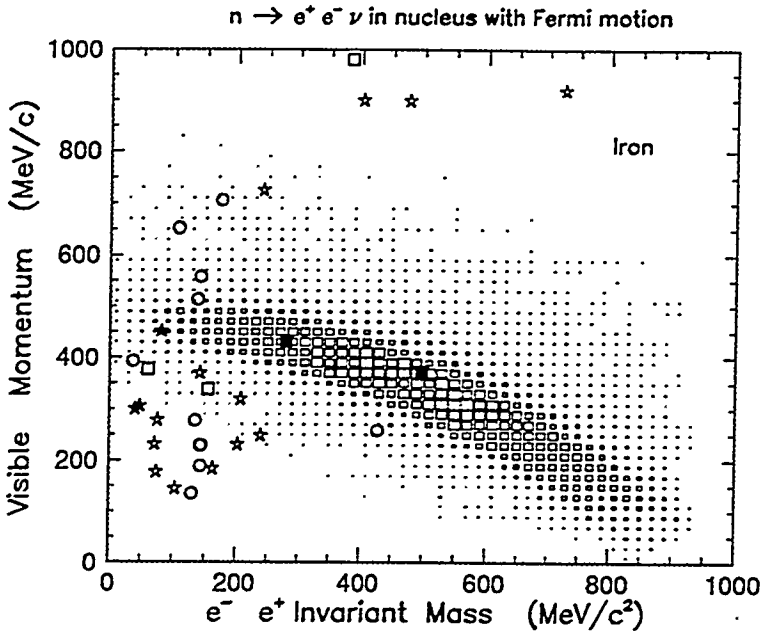

Figure 10.11: e^-e^+ pair momentum versus invariant mass: solid and squares show multiprong events, solid and open stars depict Rock events, and open circles depict Monte Carlo neutrino events.

hit distance as seen in Fig. 8.1. If we also allow for detector resolution, then we can consider that prompt electrons may have distance to first hit up to 10 centimeters. Table 10.3 shows the distance to closest hit from the best vertex determination for the candidates for decay mode (10.1). From Table 10.3 we see that event 20307–498 has both showers with distances to first hit from vertex location greater than 8 centimeters. The event 34742–1579 has two showers with distinctly different distances to first hit, one with a short distance and the other with distance comparable to the ones of event 20307–498. Thus event 20307–498 is less probable than event 34742–1579, to have two prompt electrons in its final state and therefore less probable to be a candidate for decay mode (10.1).

To first approximation, allowing for detector resolution and for uncertainty in the vertex determination, we conclude that in a 1.0 kiloton–year exposure of Soudan 2 we find two candidates for $n \to e^+e^-\nu$. For our best estimate, we assign weights for each event, based on the inverse number of equally possible vertices, selected

	Event 20307–498	Event 34742–1579
	Dist. to 1^{st} hit (cm)	Dist. to 1^{st} hit (cm)
Shower #1	9.7	1.9
Shower #2	8.6	8.7

Table 10.3: Distance to closest hit.

by a physicist during the event reconstruction. For each candidate vertex we check whether the showers are within 7 centimeters of the vertex. Using this method, we assign a weight of 0.14 to event 20307–498 and a weight of 0.43 to event 34742–1579. We conclude that the best estimate for the observed number of events for decay mode (10.1) is 0.57 in our 1.0 kiloton–year exposure.

10.3.3 Limits to $n \rightarrow e^+e^-\nu$

We summarize the considerations which need to be taken into account in calculation of the nucleon lifetime, both without and with background subtraction. The calculation of nucleon lifetimes or lifetime lower limits depends upon fiducial volume, exposure, trigger efficiency, detection efficiency, nuclear corrections, etc. In general, the ratio of the proton (neutron) lifetime over the unknown branching ratio into a particular decay mode is given by

$$\tau_B \equiv \tau/B = \frac{N_p \times N_{kty} \times \varepsilon_T \times I_t}{n_{obs}} \tag{10.2}$$

where

N_p = number of nucleons per kiloton = 6.02×10^{32}

N_{kty} = exposure (in kty)

ε_T = all efficiencies $\equiv \varepsilon_{trigger} \times \varepsilon_{scanning} \times \varepsilon_{pattern\ \ recognition}$

I_t = number of protons (neutrons) per nucleon (isoscalar target) ~ 0.5

n_{obs} = number of observed events.

The error on the lifetime τ_B depends predominantly on the Poisson statistics of n_{obs}. Obviously one cannot calculate a lifetime if no events are observed. However one can give a 90% confidence level lower limit (90% CL), which is the lifetime for which the probability that the experiment would see n_{obs} events or less is 90%. If we denote the 90% CL rate corresponding to n_{obs} events as $n_{90} \equiv n90(n_{obs})$, then Eq. (10.2) becomes

$$\tau_{90} \geq \frac{N_p \times N_{kty} \times \varepsilon_T \times I_t}{n_{90}}. \tag{10.3}$$

If we consider the number of background events (n_{bck}) for a given channel and if this background estimation is reasonably small, then Eq. (10.2) and Eq. (10.3) should be rewritten as

$$\tau_B^{'} = \frac{N_p \times N_{kty} \times \varepsilon_T \times I_t}{(n_{obs} - n_{bck})} \tag{10.4}$$

and

$$\tau_{90}^{'} \geq \frac{N_p \times N_{kty} \times \varepsilon_T \times I_t}{(n_{90} - n_{bck})} \tag{10.5}$$

The relevant efficiencies for the decay mode $n \rightarrow e^+e^-\nu$ are as follows:

$\varepsilon_{scanning} = 0.96$ [6]

$\varepsilon_{filter} = 0.90 \pm 0.11$ [7]

$\varepsilon_{pattern\ \ recognition} = 0.61 \pm 0.08$ [8]

the total efficiency is then

$$\varepsilon_T \equiv \varepsilon_{filter} \times \varepsilon_{scanning} \times \varepsilon_{pattern\ \ recognition} = 0.90 \times 0.96 \times 0.671 = 0.53 \pm 0.09.$$

In order to estimate the background, we reason as follows: In 1.0 kiloton–year of exposure, the contamination of the multiprong sample due to neutron–induced events with no associated shield hits was 2 events (for all topologies, see Section 8.3). The Rock multiprong sample contains 98 events. The fraction of Rock multiprong

events which have the same topology as decay mode (10.1) is 18/98, from which 1/18 have the correct kinematical properties. The estimated background is $2.0 \times (18/98) \times (1/18) = 2/98 < 0.1$ events.

We conclude that for $n \rightarrow e^+e^-\nu$ we found a signal of 0.57 events with a background estimation less than 0.1 events. From Eq. (10.4) we estimate that the lifetime is

$$\tau'_B \ (n \rightarrow e^+e^-\nu) = (2.90 \pm 1.70) \times 10^{32} \text{ years}$$

For a 90% CL estimation, if we assume that after background subtraction the number of observed events is 0.55, then according to Poisson statistics the number of unobserved events correspond to 3.18 events [9], and Eq. (10.5) yields

$$\tau'_{90} \ (n \rightarrow e^+e^-\nu) \geq 5.02 \times 10^{31} \text{ years}$$

10.4 Search for $n \rightarrow \bar{\nu}\eta^0$

A neutron decay mode which can have a two–shower topology similar to mode (10.1) is

$$n \rightarrow \bar{\nu}\ \eta^0. \tag{10.6}$$

Our search for this latter mode was conducted in parallel with the search for mode (10.1). The eta (η^0) meson decays electromagnetically into 2γ (38.8%), $3\pi^0$ (31.9%), and also into $\pi^+\pi^-\pi^0$ (23.6%). Its mass is 547 MeV. In decay mode (10.6), the (anti)–neutrino will be unobserved in the detector and so the only evidence for occurence of the process will be the decay daughters of the η^0. Among the decay modes of the η^0, the predominant two–photon decay provides the cleanest signature, and this is the one we have searched for.

We begin by considering all seven contained two–shower events found in Section 10.3 to be candidates for $n \rightarrow \bar{\nu}\eta^0$. As our first kinematical selection, we require

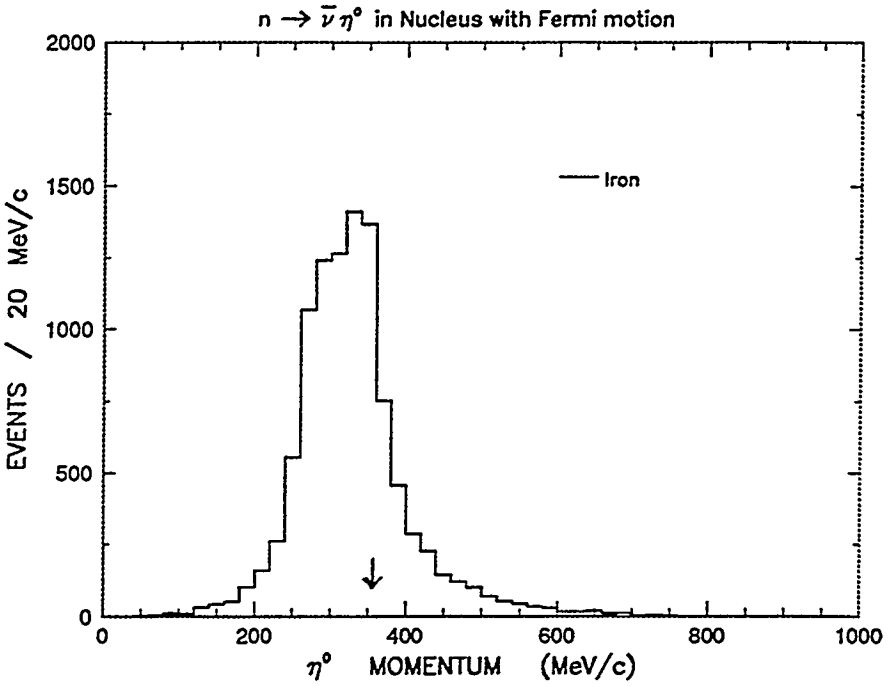

Figure 10.12: Eta momentum distribution from decays of neutrons in iron nuclei.

that the shower pair invariant mass approximate 547 MeV/c^2 to within $\pm$60 MeV/c^2, allowing for detector resolution. Secondly, we require the two showers forming the η^0 not to be prompt electron showers, by requiring that the distance from the vertex location to the first hit of each shower be greater than 7 centimeters.

The only candidate which survives all the kinematical cuts is event 20307–498. Properties of this particular event are:

Invariant mass (γ pair) = 509 (MeV/c^2,

Visible energy (γ pair) = 609 (MeV),

Net momentum (γ pair) = 362 (MeV/c).

Fig. 10.12 shows the expected eta momentum distribution from decays (10.6) in iron with Fermi motion. The arrow indicates the momentum of the γ pair of event 20307–498. Similarly, Fig. 10.13 shows the total visible energy distribution from decays (10.6) in iron; the arrow depicts the visible energy of the γ pair of our selected event.

In order to estimate the background for decay mode (10.6), we need to account for two independent background sources. First, we have the contamination of the

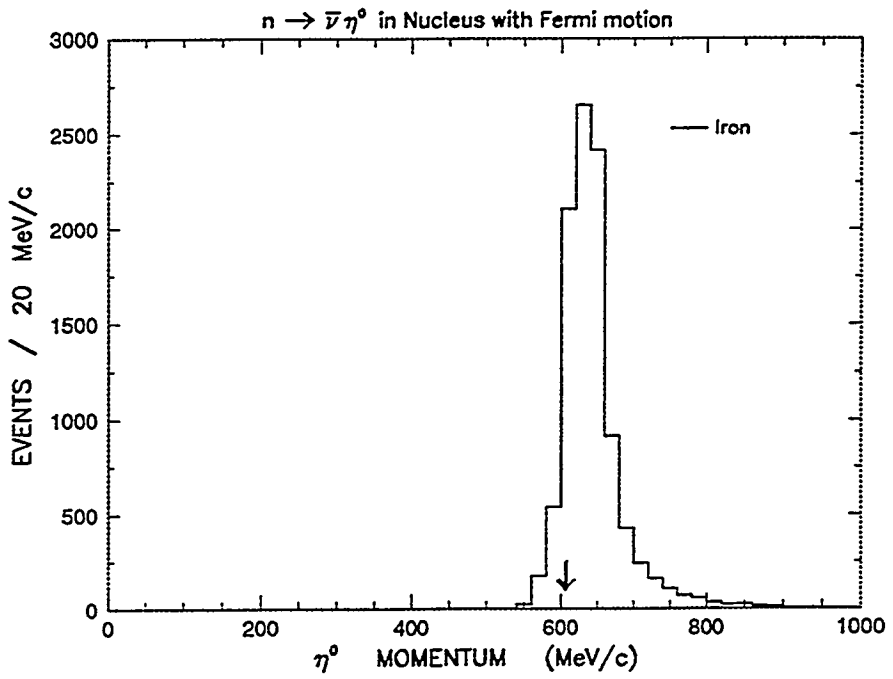

Figure 10.13: Eta visible energy from decays of neutrons in iron nuclei.

multiprong sample due to neutron–induced events with no associated shield hits. In this case, due to the similarity (in topology) between decay mode (10.1) and (10.6), the estimated background from neutron induced events is estimated similarly to that in mode (10.1) as follows: The overall contamination of the 1.0 kty multiprong sample is 2 events. From the 98 Rock multiprong events only 18 have two–shower topology, from which 2 events have the correct kinematics. Thus we obtain a background of $2.0 \times (18/98) \times (2/18) = 4/98 = 0.04$ events. Secondly, we consider the background from ν interactions. From Table III of Appendix G we infer that the ν background for decay mode (10.6) is zero.

We conclude that for $n \rightarrow \bar{\nu}\eta^0$ we found a signal of 1 event with a background of 0.04 events. Using Eq. (10.4) – and taking into account the branching ratio of the η^0 into 2γ – we estimate that the lifetime is

$$\tau'_B \ (n \rightarrow \bar{\nu}\eta^0) = (6.45 \pm 2.54) \times 10^{31} \text{ years}$$

For a 90% CL estimation, if we consider that after background subtraction the number of observed events is 0.96, then the number of unobserved events is 3.83 [9].

Using Eq. (10.5), we obtain

$$\tau'_{90} \ (n \rightarrow \bar{\nu}\eta^0) \geq 1.62 \times 10^{31} \text{ years}$$

10.5 Search for $n \rightarrow \bar{\nu}\pi^0$

Another interesting mode is

$$n \rightarrow \bar{\nu} \ \pi^0. \tag{10.7}$$

The π^0 has a mass of 135 MeV and decays electromagnetically into 2γ (98.8%). The topology produced by this decay mode will be similar to $n \rightarrow e^+e^-\nu$ in the Soudan 2 tracking calorimeter. Because the antineutrino is unobserved in the detector, we are left with only the photon showers from the π^0 as evidence for the occurence of process (10.7). In order to obtain a signal we consider all seven contained two–shower events found in Section 10.3 to be candidates for $n \rightarrow \bar{\nu}\pi^0$. The kinematical property required for this mode is for the shower pair invariant mass to be less than 350 MeV/c^2. This invariant mass cut is based upon Fig. 7.15. We require that the net momentum for the gamma pair be smaller than 1.0 GeV/c, the latter cut being based upon Fig. 7.7. From Table I of Appendix G, which summarizes kinematical properties of the contained multiprong events, we observe that three candidates survive this cut.

But decay mode (10.7) imposes a strong constraint on the π^0. Due to the fact that the antineutrino is massless and that in a stationary two–body decay the daughters will be emitted back–to–back, the π^0 momentum should have a value in the vicinity of 461 MeV/c to within $\pm$80 MeV/c, allowing for Fermi motion. Fig. 10.14 shows the π^0 momentum distribution of all seven contained two–shower topology events of Table I (two events are out of the range being plotted, see Appendix G). As Fig. 10.14 indicates, there is only one event candidate whose momentum is within 80 MeV/c of the nominal value.

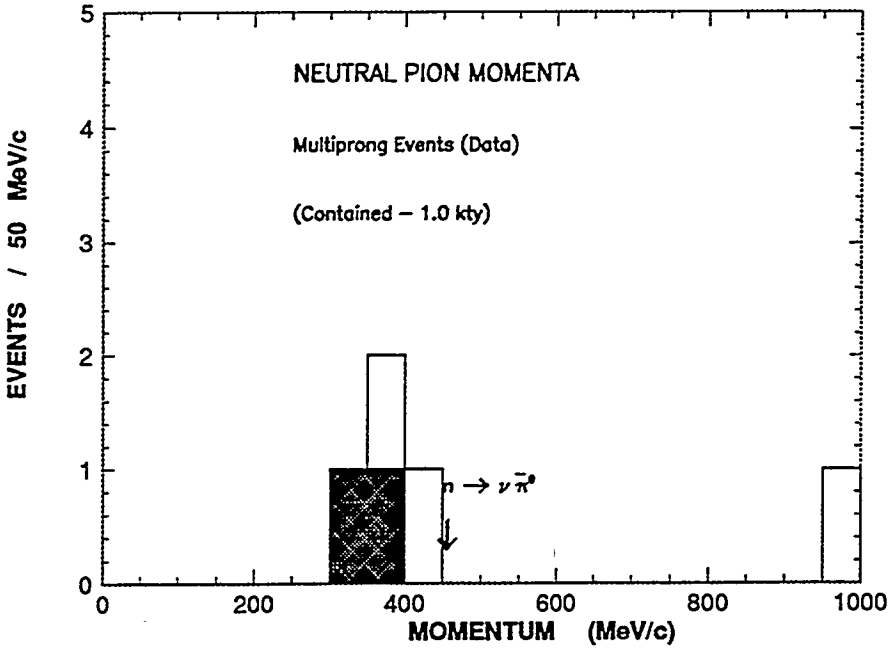

Figure 10.14: Net momentum distribution for two–shower events listed in Table I of Appendix G. Shower pairs with invariant mass below 350 MeV are shown shaded.

To determine the background for decay mode (10.7) we reason as follows: First, in 1.0 kiloton year of exposure, the neutron–induced contamination of the multiprong sample for all topologies is 2 events. From the 98 Rock multiprong events, only 18 events possess the two–shower topology, from which 1 event passes the invariant mass and momentum requirement (see Table III of Appendix G). The estimated background from neutron–induced events is $2.0 \times (18/98) \times (1/18) = 2/98 = 0.02$ events. Secondly, we need to consider the background from neutrino interactions. Table III of Appendix G summarizes the kinematical properties of all (contained) two–shower topology events generated with our first–generation Monte Carlo, corresponding to an exposure of 3.45 kiloton-years. From Table III we infer that 10 ν events have the correct invariant mass, from which only three events are within the allowed π^0 momentum range. Fig. 10.15 shows the π^0 momentum distribution for the 10 simulated ν events (solid histogram) and for the 18 Rock events (dashed histogram) respectively. The arrow in Fig. 10.15 indicates the allowed π^0 momentum for decay mode (10.7). The relevant kinematical properties of the Rock two–shower

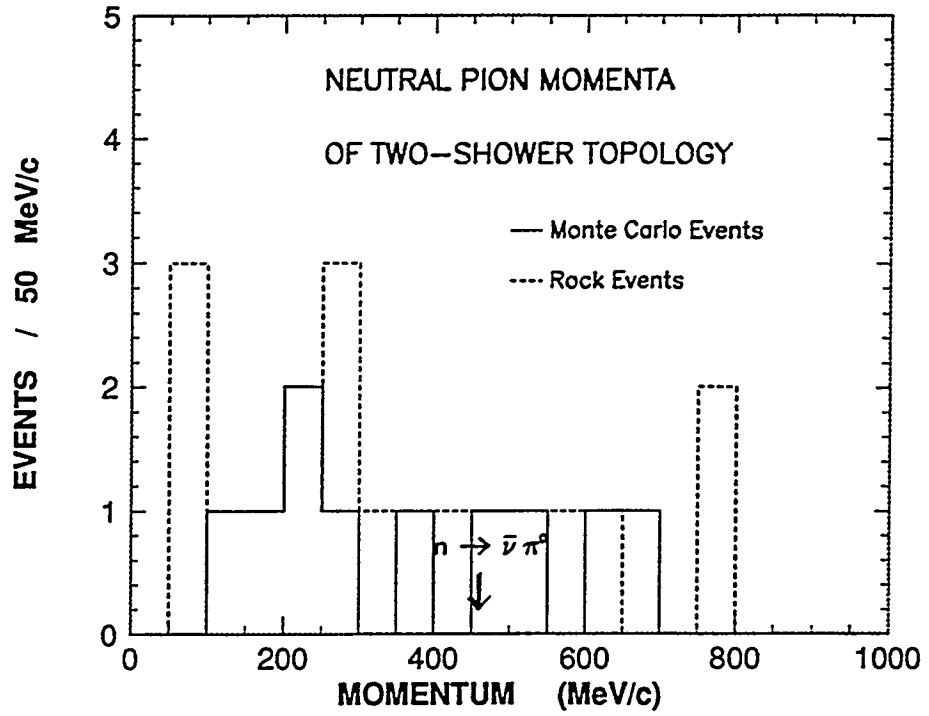

Figure 10.15: Pizero momentum distribution for two–shower topology event; solid line depicts simulated ν events, whereas dashed line depicts Rock events.

events are summarized in Table II of Appendix G. Fig. 10.15 shows the expected background from neutron–induced events and neutrino interactions for decay mode (10.7). Assuming 3 background events in 3.45 kty one estimates a neutrino background of $3/3.45 \sim 0.87$ events per kiloton year of exposure.

We conclude that for $n \to \bar{\nu}\pi^0$ we found a signal of 1 event with a background estimation of 0.89 events. From Eq. (10.4), using an overall efficiency of $\varepsilon_T = 0.27 \pm 0.15$ (see Section 10.6), we estimate a lifetime of

$$\tau'_B \ (n \to \bar{\nu}\pi^0) = (7.30 \pm 2.70) \times 10^{32} \text{ years.}$$

For a 90% CL estimation, if we consider that after background subtraction the number of observed events is 0.11, then the number of unobserved events is 2.48 [9]. Using Eq. (10.5) we obtain

$$\tau'_{90} \ (n \to \bar{\nu}\pi^0) \geq 3.24 \times 10^{31} \text{ years.}$$

10.6 Single π^0 Production by Neutral Currents

An investigation of the rate of single π^0 production by neutral currents is presented. We distinguish between two processes (which are not necessarily independent reactions) on the basis of visible topology:

$$\nu\,(N) \;\rightarrow\; \nu\,(N)\,\pi^0, \tag{10.8}$$

$$\nu\,(N) \;\rightarrow\; \nu\,p\,\pi^0. \tag{10.9}$$

These two processes yield different signatures. For process (10.8), the recoil nucleus is unobserved in the detector, and we have only the decay of the π^0 as evidence for its occurrence; the visible final state will contain one or two gamma showers. For process (10.9), the recoil proton momentum is above the Soudan 2 threshold; we expect to see a straight, heavily–ionizing track (the proton) plus one or two showers from the π^0 decay. For process (10.8) we consider final states composed of two showers only; for process (10.9), the final state will have one proton track plus two photon–showers emerging from a common vertex.

The analysis done in Section 10.3 for our $n \rightarrow e^+e^-\nu$ search carries over to our study of neutrino process (10.8). The extraction of a signal and the background estimation are similar. As summarized in Appendix G, we have 7 contained multiprong candidates and 18 Rock multiprong events. Also, from our first–generation Monte Carlo we have 11 neutrino events with the correct topology in the final state.

In Section 7.8 we showed our simulation of the inclusive π^0 signal; it has a peak at an invariant mass of 124 MeV/c^2 with a width of 84 MeV/c^2. In order to isolate events from reactions (10.8) and (10.9) we use an invariant mass cut, based upon Fig. 7.15, at 350 MeV/c^2. We require the net momentum for the gamma pair to be smaller than 1.0 GeV/c, the latter cut is based upon Fig. 7.7. Then from Appendix G we identify 3 contained multiprong candidates, 13 Rock multiprongs, and 10 simulated ν events to have the two–shower topology and to satisfy both selections. For the neutrino process (10.9) we find 1 candidate in the contained multiprong

sample, 1 event in the Rock sample, and zero events in our first–generation Monte Carlo multiprongs.

To estimate no–shield neutron–induced backgroud we reason as follows: For process (10.8) in 1.0 kiloton year of exposure, the neutron–induced contamination of the multiprong sample for all topologies is 2 events. The Rock multiprong sample contains 98 events, from which 18 events possess the two–shower topology of mode (10.8), from which 13 events have the correct kinematical properties. Therefore the estimated neutron induced background is $2.0 \times (18/98) \times (13/18) = 26/98 = 0.27$ events. For process (10.9) we find only 1 event out of 98 Rock multiprongs to have the appropiate topology. Thus the estimated background is $2.0 \times (1/98) = 2/98 = 0.02$ events.

To estimate background from other neutrino reactions which can mimic our final state topology, we reason as follows: From Table III of Appendix G, we observe that, among two–shower topologies 2 events out of 10 are reactions other than (10.8). The background from other neutrino events is roughly 20%. Similarly, for process (10.9) we find a background of 50%.

Our estimates for the numbers of events from the neutral current processes (10.8) and (10.9) are shown in Table 10.4. For each process, the number of observed candidates 'N_{obs}', the estimated nucleon–induced background 'Rock', the estimated neutrino background 'ν', the total background 'Total', and the number of observed events minus the total estimated background 'N_{signal}' is shown. We estimate a signal of 2.67 ± 1.97 events in 1.0 kiloton year of exposure. Before comparing this to predicted rates, we need to estimate the experimental efficiency for detecting processes (10.8) and (10.9) in the Soudan 2 experiment.

The relevant efficiencies for both modes are:

$$\varepsilon_T \equiv \varepsilon_{Total} = 0.27 \pm 0.15 \Longrightarrow \begin{cases} \varepsilon_{scanning} & = & 0.96\ [6] \\ \varepsilon_{filter} & = & 0.73 \pm 0.09\ [10] \\ \varepsilon_{pattern\ \ recognition} & = & 0.61 \pm 0.08\ [11] \\ \varepsilon_{inv.\ mass\ cut} & = & 0.89 \pm 0.09\ [12] \\ \varepsilon_{intranuclear\ \ rescattering} & = & 0.70 \pm 0.16\ [13] \end{cases}$$

Predicted rates for processes (10.8) and (10.9) are shown in Table 10.5. For each process, the Table gives the predicted absolute rate per kiloton–year neglecting intranuclear rescattering GB [14], at solar maximum $W_{sol.max.}$ [15] and solar minimum $W_{sol.min.}$ [15]. These are followed by the detected rates per kiloton–year GB [14], at solar maximum $W_{sol.max.}$ [15] and solar minimum $W_{sol.min.}$ [15]. The latter rates are calculated taking into account losses due to intranuclear absorption and charge exchange.

Comparing Tables 10.4 and 10.5, we observe 2.67 ± 1.97 events per kiloton–year of exposure for single π^0 production by neutral current processes (10.8) and (10.9). This is to be compared with predicted rates of 2.49 events/kty, or with 2.51 events/kty at solar maximum, or with 2.74 events at solar minimum. This exercise demonstrates Soudan 2 capability to measure rates for selected NC processes from atmospheric neutrinos. In the near future it will be possible to increase the statistics for these neutral current event samples.

10.7 Search for Two–Body Nucleon Decay Modes

Experimental and phenomenological discussions of nucleon decay have devoted much attention to two–body modes. In fact, the water Cherenkov experiments were motivated in part by the possibility for detection of $p \rightarrow e^+\pi^0$, the decay favored by minimal SU(5) GUTs. In this particular decay mode, all the daughter particles are above Cherenkov threshold. However, for SUSY–favored modes such as $p \rightarrow \nu K^+$,

Neutral Current Single-π^0 Production: Observations					
		Background			
Process	N_{obs}	Rock	ν	Total	N_{signal}
$(\bar{\nu})N \rightarrow (\bar{\nu})$"$N$"$\pi^0$ "N" = n, p_{slow}	3	0.27	0.55	0.82	2.18 ± 1.70
$(\bar{\nu})N \rightarrow (\bar{\nu})p_{fast}\pi^0$	1	0.02	0.49	0.51	0.49 ± 1.00
Total $\nu N\pi^0$	4	0.29	1.04	1.33	2.67 ± 1.97

Table 10.4: Rates for single π^0 neutral current process in Soudan 2.

Neutral Current Single-π^0 Production: Predictions						
Process	Abs. Rate per kty			"Detected" Rate per kty ($\varepsilon_T = 0.27 \pm 0.15$)		
	GB	$W_{sol.max.}$	$W_{sol.min.}$	GB	$W_{sol.max.}$	$W_{sol.min.}$
$(\bar{\nu})n \rightarrow (\bar{\nu})n\pi^0$	4.72	5.03	5.52	1.27	1.36	1.49
$(\bar{\nu})p \rightarrow (\bar{\nu})p\pi^0$	4.50	4.26	4.62	1.22	1.15	1.25
Total $\nu N\pi^0$	9.22	9.29	10.14	2.49	2.51	2.74

Table 10.5: Predictions for single π^0 neutral current processes in Soudan 2.

the kaon is below the Cherenkov threshold, and so tracking calorimeter detectors offer advantages in such modes. It is of interest to search for two–body nucleon decay modes in Soudan 2, especially in decay modes such as $p \rightarrow \mu^+\pi^0$ or $n \rightarrow \mu^+\pi^-$. For this purpose, we examine our contained multiprong sample, which contains 34 events from our 1.0 kiloton–year of exposure. We plot the event final state invariant mass against the net momentum for multiprong events with two or three prong topologies. These are events for which the final state is completely identified. Table 10.6 summarizes the kinematical properties of the selected events. It shows the run–event number, the final state topology, the net momentum of the final state P_{Net} (in MeV/c), the final state invariant mass M (in MeV/c^2), the total visible energy E_{vis} (in MeV/c), and the invariant mass of the π^0, M_{π^0}, when appropriate.

Fig. 10.16 shows the M versus P_{Net} scatter plot. The dashed line shows the nucleon decay region with allowance for Fermi motion and detector resolution. Events depicted by an asterik ($*$) in Fig. 10.16 have a recoil proton in the final state; these can only be neutrino interactions and not nucleon decay events. The majority of the neutrino events in Fig. 10.16 have invariant mass below 500 MeV/c^2. Events which are in the lower left corner of Fig. 10.16 would constitute background for nucleon decay into neutrino modes if the final state lepton had not been identified. This background is in agreement with Fig. 2 of Ref. [16] which shows that the background from neutrino events tends to populate the area below the nucleon decay region. We observe that there is only one event (35219–766), depicted by a triangle ($\triangle$) in Fig. 10.16, with kinematics roughly compatible with nucleon decay. The most plausible interpretation however seems to us that the event represents $\bar{\nu}p \rightarrow \mu^+\pi^0 n$.

Multiprong Events with "Identified" Final State						
Event No.	Topology	P_{Net} (MeV/c)	M (MeV/c^2)	E_{vis} (MeV)	M_{π^0} (MeV/c^2)	Symbol in Fig. 10.16
11940–1712	$\nu\pi^0$	367	132	372	132	□
20307–498	$e\pi^0/e\pi^0\pi^0$	362	509	609		○
24290–949	$\nu p\pi^0$	567	1265	448	135	*
26439–1456	$e\pi^{\pm}$	208	415	464		•
26957–1891	$e\pi^0/e\pi^0\pi^0$	1132	210	1151	210	○
27896–766	$e\pi^{\pm}$	398	283	489		•
29750–195	$\nu\pi^0$	328	136	382	136	□
31757–249	$\mu\pi^{\pm}$	737	373	811		•
34123–1064	$\mu\pi^0$	152	305	341	134	•
34742–1579	$\nu\pi^0$	421	261	484	261	○
35219–766	$\mu\pi^0$	349	669	754	252	△
35998–376	$e\pi^{\pm}$	2412	935	2587		•
36284–1523	$e\pi^0$	509	309	595	151	•
36381–1189	$\mu p\pi^{\pm}$	1467	1765	1357		*
37148–903	$\mu\pi^0$	205	352	407	136	•
37722–277	$e\pi^0/e\pi^0\pi^0$	1573	373	1616	373	○
39280–122	$e\pi^0/e\pi^0\pi^0$	970	466	1076	466	○

Table 10.6: Contained multiprong events with identified final states.

10.8 Concluding Remarks

The detailed event images provided by the Soudan 2 iron tracking calorimeter provide excellent discrimination among topologies of contained multiprong events. This capability has enabled us to distinguish among different neutrino reactions, including single π^0 production by neutral current reactions.

We have searched for nucleon decay in contained multiprong events. We find no compelling candidates for decay modes which have charged lepton(s) plus hadron(s) in the final state; such modes would be completely imaged in the Soudan 2 detector.

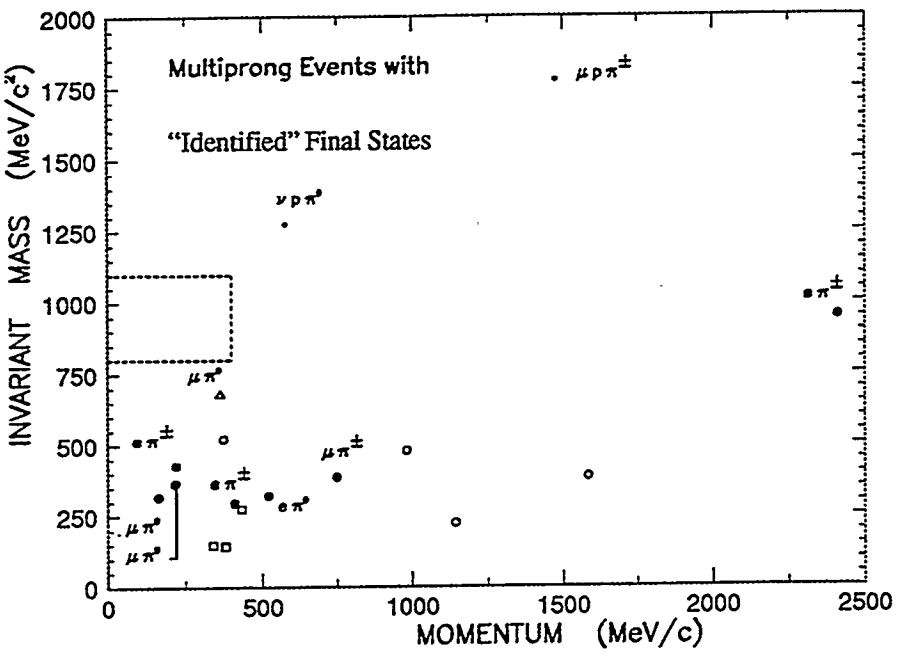

Figure 10.16: Final state invariant mass versus momentum for multiprong events with "identified" final states.

We have investigated decay modes yielding two showers in the final state. Lifetime limits for the relevant modes are as follow:

$$\tau'_{90}\ n \to e^+e^-\nu \ \geq\ 5.02 \times 10^{31} \text{ years}$$

$$\tau'_{90}\ n \to \bar{\nu}\eta^0 \ \geq\ 1.62 \times 10^{31} \text{ years}$$

$$\tau'_{90}\ n \to \bar{\nu}\pi^0 \ \geq\ 3.24 \times 10^{31} \text{ years}$$

If one chooses to interpret the excess above our background estimates to represent signals (the author does not claim there to be justification for doing this), then one obtains the following lifetimes:

$$\tau'_B\ n \to e^+e^-\nu \ =\ (2.90 \pm 1.70) \times 10^{32} \text{ years}$$

$$\tau'_B\ n \to \bar{\nu}\eta^0 \ =\ (6.45 \pm 2.54) \times 10^{31} \text{ years}$$

$$\tau'_B\ n \to \bar{\nu}\pi^0 \ =\ (7.30 \pm 2.70) \times 10^{32} \text{ years}$$

We have used the capability of the tracking calorimeter to differentiate between γ showers and prompt electrons ($e^{\pm}$) in order to study single π^0 production by

neutral current reactions. After background subtraction we observe 2.67 ± 1.97 neutral current candidates per kiloton–year. This value is to be compared with a rate expectation of 2.49 events/kty, or with 2.51 events/kty at solar maximum, or with 2.74 events/kty at solar minimum (predicted rates are from Ref. [14] and [15] respectively).

Among our contained multiprong events, $\sim 50\%$ have final states with all particles identified. This provides information useful for the study of ν interactions as a background to nucleon decay.

References

[1] A. Bodek and J.L. Ritchie, Phys. Rev. **D 23**, 1070 (1981).

[2] W.A. Mann, T. Kafka and W. Leeson, Phys. Lett. **B 291**, 200 (1992); W.A. Mann, T. Kafka and W. Leeson, *in:* Proceedings of DPF92 Meeting, Fermilab, 10–14 November 1992; p. 1330; W.A. Mann, T. Kafka and W. Leeson, Soudan 2 Report PDK–590, July 1994.

[3] C. Berger *et al.*, Phys. Lett. **B 269**, 227 (1991).

[4] The decay limits quoted here appear in an early preprint of Becker-Szendy *et al.*; the paper quoted here is the same but with Table 1 omitted. R. Becker-Szendy *et al.*, *in:* Proceedings of DPF92 Meeting, Fermilab, 10–14 November 1992; p. 1334.

[5] T. Kafka, *"PPOP-A Proton Decay Generator"*, TUFTS Report PDK–28, July 21, 1983; T. Kafka, *"Running PPOP"*, TUFTS Report PDK–29, July 23, 1983; T. Kafka, *"Inside PPOP"*, TUFTS Report PDK–30, July 24, 1983.

[6] Efficiency for two scans to find and record an event. The double–scan efficiency from Soudan FILTER scanninng is not yet available; we use here a value typical of double–scanning in bubble chamber experiments.

[7] Filter efficiency with statistical error only. It was obtained by T. Kafka by generating 182 $n \rightarrow e^+e^-\nu$ events using our first–generation Monte Carlo simulation. From the 182 events, 3 were Monte Carlo failures, 33 events had the vertex outside fiducial volume, 15 events had track endpoint outside fiducial volume, and 2 events were recovered by one of the two filters.

[8] The error shown is only statistical. This efficiency was obtained from 140 Monte Carlo events passing the filter requirements, from which 60.7% were accepted as two shower events, 15.7% were rejected due to vertex location within or very close to an inter–module gap, 6.4% were rejected due to other topological features then two–showers, and 17.1% were rejected because they look like one single shower.

[9] Particle Data Group, *"Review of Particle Properties"*, Phys. Rev. **D 50**, 1279–1280 (1994).

[10] Based upon the simulation by T. Kafka in which 80 $\nu N\pi^0$ events were generated using the first–generation Monte Carlo. From the 80 events, 1 was without hits, 12 events failed the software trigger, 11 events were outside the fiducial volume, and 2 events were recoverd by the Filter.

[11] The error shown is statistical. This efficiency was obtained from 140 good trigger events inside the fiducial volume, from which 60.7% were accepted as two shower events, 15.7% were rejected due to vertex location within or very close to an inter–module gap, 6.4% were rejected due to other topological features then two–showers, and 17.1% were rejected because they look like one single shower.

[12] This efficiency was obtained from Fig. 7.15, by using an invariant mass cut at 350 MeV/c^2. The number of events below 350 MeV/c^2 is 57, whereas the number of events above that is 7 events. The error shown here is statistical.

[13] Obtained from the thesis of R. Merenyi; see Chapter 10.

[14] G. Barr, Ph. D. Thesis, Keble College, Oxford, May 1987, unpublished; (see Table 7.4 on page 148).

[15] S. Werkema, Ph. D. Thesis, University of Minnesota, May 1989, unpublished; (see Appendix B).

[16] M. Derrick, B. Musgrave, R. Ammar, D. Day, T. Kafka and W.A. Mann, Phy. Rev. **D 30**, 1605 (1984).

Chapter 11
Summary and Discussion

11.1 Issues Pertaining to the Atmospheric Anomaly

The anomaly reported in the atmospheric neutrino flavor ratio ν_μ/ν_e has motivated the research of this Thesis. The research is intended to obtain new information having relevance to three general issues:

1) Does the low R' ratio, Eq. (1.8), originally observed by Kamiokande and IMB–3 in interactions of (mostly) sub–GeV neutrinos, represent a valid measurement, or are there instrumental effects and/or backgrounds not accounted for which give rise to the effect?

2) Kamiokande has reported that the R' ratio remains anomalously low in interactions of neutrinos of multi–GeV energies. To what extent can this result be checked using Soudan 2 data?

3) If the low R' ratio is a valid result for either or both sub–GeV and multi–GeV neutrino data, then what is the physical origin of the effect? What alternative explanations are viable, and what are their implications? To what extent can these implications be examined using Soudan 2 data?

11.2 Reality of Low R'

Relative rates reported for contained single track versus single shower neutrino events indicate an anomalous ratio of neutrino flavors ν_μ/ν_e. Is this effect real or

instrumental? Since the most statistically significant observations are from the two large water Cherenkov detectors, confirmation from measurements using tracking calorimeter techniques, is highly desirable.

Preliminary to our studies using Soudan 2 data, we compared Kamiokande and IMB–3 data for observational consistency. The Kamiokande and IMB–3 event samples were recorded at different latitudes, and so some differences are to be expected, particularly for low energy incident neutrinos. Our comparison of single lepton momentum distributions (Chapter 2) suggests a modest level of disagreement. From Fig. 2.14 we find that, relative to Kamiokande, the IMB–3 data contains an excess of e–like events with lepton energy between 500 and 900 MeV, and a less–pronounced dearth of μ–like events in the 700 to 1200 MeV regime. These differences suggest to us that track versus shower separation differs somewhat in the two experiments. Since Kamiokande is slightly better than IMB–3 in imaging resolution, and since its pattern recognition algorithms have recently been confirmed with test beam exposures of an instrumented water tank at KEK, the Kamiokande data appears to us to be the better established of the two Cherenkov data sets.

We have also considered the consistency of the sub–GeV atmospheric neutrino sample populations with time. Table 11.1 shows the evolution of the two water Cherenkov data samples. We find that the Kamiokande data exhibits consistency between data and extrapolation based on an earlier exposure. However, IMB–3 event samples show a 2.8σ (0.5σ) difference in the μ–like (e–like) event populations when the final data set is compared to an extrapolation based upon the earlier exposure. For these reasons we favor Kamiokande data over IMB–3 data when searching for hints of new physics.

In this Thesis we examined background processes which have not been explicitly treated by the water Cherenkov detectors. There is an underground flux of energetic neutrons and of energetic photons within the Soudan cavern, originating from cosmic ray muon interactions within the rock surrounding the cavern walls. These particles

Data Evolution History						
IMB–3 and Kamiokande						
Event Type	**KAM**			**IMB–3**		
Ref.	Data (4.92 kty) [1]	*Extrp.* (7.7 kty)	Data [2]	Data (3.4 kty) [3]	*Extrp.* (7.7 kty)	Data [4]
μ–like	151	*236*	**234**	97	*220*	**182**
e–like	159	*249*	**248**	139	*315*	**325**
Total	310	*485*	**482**	236	*535*	**507**

Table 11.1: Data evolution in time for Kamiokande from 4.92 to 7.7 kty and for IMB–3 from 3.4 to 7.7 kty of exposure. The KAM data has lepton momentum $0.1 < p_e < 1.33$ GeV/c and $0.2 < p_\mu < 1.5$ GeV/c, whereas the IMB–3 data are single ring with lepton momentum $p < 1.5$ GeV/c.

can interact or convert inside the detector, creating contained events, which are not induced by neutrino interactions or by nucleon decay. In Chapter 5 we have fitted distributions of penetration depth to determine background in our data samples. We estimate a background contamination of 2.0 ± 3.7 events out of 35 events for the single shower sample. The number of neutron–induced background events in the single track sample is 5.7 ± 3.5 events in a sample of 30 events, and 1.1 ± 2.4 events among 34 events in the contained multiprong sample.

These background estimates are compatible with corrections assigned to the Soudan 2 data arising from shield inefficiencies, and so the reported values of R' from Soudan 2 have allowed for neutron and photon–induced backgrounds at these levels.

We have reexamined the atmospheric neutrino flavor ratio obtained from Soudan 2 data, using track ionization more aggressively than was used in the "official" analysis (see Chapter 6). As a result, some events have been classified by us differently than was done by the collaboration. We view the result obtained in this Thesis to be a consistency check on the collaboration determination. The R' we obtained is 0.63 ± 0.22. It is identical to the nominal collaboration value 0.64 ± 0.17, however our method of estimating background gives rise to a larger error assignment.

We note that new (preliminary) measurements of R' using Soudan's third 0.5 kty data, from two independent analyses within the collaboration, are consistent with earlier Soudan 2 results described above. These new measurements add to our confidence that the low R' values reported are valid, at least for events initiated by sub–GeV neutrinos.

At present (November 1995), the Soudan 2 experiment has 2.46 kiloton years of exposure, which will be fully analyzed in perhaps one year's time. By 1999, the expected lifetime of the experiment, we will have accumulated more than 5.0 kiloton–years of data. Thus the Soudan 2 experiment appears to us well–poised to verify conclusively the apparent atmospheric neutrino anomaly and its interpretation, using a different technique and with good understanding of systematic errors.

We have examined whether the anomaly persists in the so–called multi–GeV neutrino events, as claimed by Kamiokande. For this purpose, we developed two methods for estimating the atmospheric neutrino flavor components in the Soudan 2 contained multiprong sample, as described in Chapter 8. Both methods indicate – with large statistical errors – that the flavor composition of the multiprong sample is in agreement with the flavor expectations of a Monte Carlo with no neutrino oscillation effects included. Within the multiprong sample, we find no obvious trend which would confirm the Kamiokande report that the neutrino flavor ratio anomaly persists in contained event samples from neutrino interactions with E_ν above 1.33 GeV.

We have also examined the atmospheric neutrino flavor components in a sample of 15 partially contained events, obtained from our 1.0 kty exposure (see Chapter 9). Our observations suggest – with large statistical errors – that the flavor composition of the PCE sample may contain a relative dearth of muon–neutrino events and also perhaps an excess of neutral current events, in comparison with predictions based upon the Bartol neutrino fluxes. These trends are in agreement with the Kamiokande oscillation scenario in the multi–GeV region.

In summary, the evidence for anomalous R appears to us to be reasonably strong in the sub–GeV data, but less compelling in the multi–GeV data.

A remaining question is whether our understanding of contained μ–like and e–like event samples is being confused by neutrino–nucleus threshold or form factor effects which are not accounted for. The quasi–elastic scattering cross section for $\nu_\mu n \rightarrow \mu^- p$ is reported to be consistent with standard phenomenology for $E_\nu \geq 300$ MeV, based upon interactions in a deuterium–filled bubble chamber (see Fig. 22 of Barish *et al.*, Ref. [5]). A detailed calculation of nuclear effects for quasi–elastic neutrino scattering in oxygen has been carried out by Engel *et al.* [6]. For neutrinos in the energy range 0.1–3.0 GeV they find no significant shift in the final state momentum spectra of electrons relative to final state muons, that would distort the atmospheric neutrino ν_μ/ν_e ratio. Thus, while it is still possible, it seems to us unlikely that nuclear effects in oxygen or iron target nuclei are distorting the atmospheric neutrino data in a unknown way.

11.3 Anomaly as New Physics

We have considered in this Thesis several alternative explanations for the atmospheric flavor ratio anomaly which propose "new physics". Assuming the anomaly is real, one needs to distinguish whether it is due to a predominant shortage of "μ" events (e.g. due to oscillations $\nu_\mu \rightarrow \nu_\tau$), or to a mild dearth of μ–like and a mild

Kamiokande					
Events	Data	Monte Carlo predictions			
		BGS [8]	HK [9]	LK [10]	BN [11]
μ–like	234	369	356	321	280
e–like	248	257	238	200	172

Table 11.2: Contained event rate for Kamiokande: 7.7 kty exposure.

excess of e–like events (e.g. due to $\nu_\mu \rightarrow \nu_e$ oscillations), or to an excess of "e" events (e.g. due to $p \rightarrow e^+\nu\nu$). To decide among these possibilities, one requires knowledge of the absolute neutrino fluxes rather than their ratios. Table 11.2 shows a comparison of the Kamiokande results with Monte Carlo event rate calculations based upon four different neutrino fluxes [7]. Note that with the exception of the Bugaev–Naumov flux, the calculations indicate that the anomaly is due to a deficit of μ events.

In this Thesis, the possibility that the Bugaev–Naumov flux is the best approximation to the true atmospheric flux has been examined in detail in Chapter 2. An analysis consistent with this scenario has been carried out. We argue that the rate of single–ring e–like events with lepton momenta of 100 - 600 MeV/c appears to be enhanced; the spectral excess follows three–body $p \rightarrow e^+\nu\nu$ phase space. The e–like event excess from 7.7 kiloton–years exposure of the Kamiokande detector yields $\tau/B \sim 3.0 \times 10^{31}$ years.

In the proton decay interpretation, one expects the e–like sample to contain a contribution from a process which does not contain final state protons. It is therefore of interest to compare the relative rates for protons accompanying single showers versus single tracks in Soudan 2 data. In the 1.0 kiloton year data from Soudan 2,

we observe $17 \pm 12\%$ (6 out of 35) of single shower events to have recoil protons whereas $30 \pm 12\%$ (9 out of 30) of single track events have protons. Although the trend shown by the Soudan 2 sub–GeV data sample is compatible with the proton decay scenario, the limited statistics do not allow a strong supporting statement to be made at this time.

A question which naturally arises with the proton decay interpretation is 'Where are the other nucleon decay modes?' In Chapter 10 we presented results from searches using contained, two–shower topologies. Our results for three baryon–number–violating processes having the two–shower topology are summarized in Table 11.3. For comparison we show published limits on the lifetime over branching ratio τ/BR for these same modes from the Frejus experiment. The numbers quoted in Table 11.3 for the Frejus experiment are lower limits on the nucleon lifetime at 90% CL without background subtraction [12]. In the near future, with more Soudan 2 data, these limits can be pushed upward.

To consider effects possibly originating with neutrino oscillations, we examined our contained multiprong sample for evidence of directional anisotropy. For this sample, Fig. 7.23 indicates that in the multi–GeV region there is a mild dearth of interacting neutrinos of all flavors in the downward direction (8 upward versus 4 downward events). This is to be compared with the Kamiokande oscillation scenario given by Fig. 3 of Ref. [2]. Here, Kamiokande consider fully–contained and partially–contained event samples in the multi–GeV region. In Ref. [2], Fig. 3a indicates a dearth of e–like events in the downward direction, whereas Fig. 3b shows a dearth of μ–like events in the upward direction. This muon–trend is consistent with an oscillation scenario where neutrinos produced on the opposite side of the Earth may oscillate while traversing the Earth giving rise to a dearth of upward neutrinos, thus creating an asymmetry of the interacting neutrino flux between the downward versus upward directions.

In summary, measurements based upon various published atmospheric neutrino

Soudan 2			
Nucleon Decay Limits			
Decay Mode	Lifetime (years)	Poisson Limit 90% CL (years)	Frejus 90% CL (years) Ref. [12]
$n \to e^+e^-\nu$	$(2.90 \pm 1.70) \times 10^{32}$	$\geq 5.02 \times 10^{31}$	$\geq 7.34 \times 10^{31}$
$n \to \bar{\nu}\eta^0$	$(6.45 \pm 2.54) \times 10^{31}$	$\geq 1.62 \times 10^{31}$	$\geq 2.91 \times 10^{31}$
$n \to \bar{\nu}\pi^0$	$(7.30 \pm 2.70) \times 10^{32}$	$\geq 3.24 \times 10^{31}$	$\geq 1.29 \times 10^{31}$

Table 11.3: Soudan 2 nucleon decay limits

flux calculations are not in agreement as to the extent to which the reported anomaly represents a deficit of muons and/or an excess of electrons. Currently most researchers view the anomaly to be due to a deficit of μ–like events, with the most likely new physics explanation to be neutrino oscillations. But one must keep in mind that there may be other explanations for the anomalous value of R'.

11.4 Other Measurements in 1.0 kty Data

A number of other useful measurements have emerged from our examination of anomaly issues:

The detailed event images provided by the Soudan 2 iron tracking calorimeter provide excellent discrimination among topologies of contained multiprong events. Among Soudan 2 contained multiprong events, we have identified all final state particles in nearly 50% of the sample (see Table 10.6 and Fig 10.16). This information

is extremely useful for the study of ν interactions as a background to nucleon decay.

We have investigated various aspects of π^0 signal reconstruction. We find Soudan's reconstruction capability to be sensitive to vertex determination, to determination of shower directions, and to our ability to recognize the final state of the event. Our capability to reconstruct an inclusive π^0 signal in our Monte Carlo study has been demonstrated yielding a peak at an invariant mass of 124 ± 13 MeV/c^2 with a width of 84 ± 19 MeV/c^2. Better algorithms for determining shower energies might yield improvement in the π^0 invariant mass signature.

We have used the capability of the tracking calorimeter to differentiate between γ showers and prompt electrons ($e^{\pm}$), examined in Section 8.2, to study single π^0 production by neutral current reactions in Chapter 10. After background subtraction, we observe 2.67 ± 1.97 neutral current candidates per kiloton–year for the $\nu N \rightarrow \nu N \pi^0$ channel (see Table 10.5 in Section 10.6).

Observation of track endpoint decays allows discrimination between quasi–elastic ν_μ versus $\bar{\nu}_\mu$ reactions. In the near future, a measurement of the atmospheric neutrino to antineutrino ratio $\nu_\mu/\bar{\nu}_\mu$ should be feasible. Among 30 single track events, we observe 9 to have endpoint decay showers ($\mu^+ \rightarrow e^+ \nu \bar{\nu}$, see Section 4.6).

We compare various inclusive distributions from the multiprong and partially contained event samples, with simulations using Soudan's first–generation Monte Carlo code. For these comparisons, the simulated events are reconstructed using the same procedures and codes as with the data (see Chapters 7 and 9). We find the simulation to reproduce inclusive shower distributions rather well (see Fig. 7.8); however momentum distributions of tracks in the simulations, e.g. separate distributions for muons plus pions (see Figs. 7.7 and 9.11) and for protons (see Figs. 7.4 and 9.10), tend to be more energetic than corresponding distributions from the data. A modest level of disagreement is observed for distributions of event topology (number of tracks versus number of showers per event) in the contained multiprong (as indicated by Figs. 7.1 and 7.2) and also partially contained samples (see Figs.

9.1 and 9.2). For multiprong samples, a larger number of showers than tracks per event is observed in the data (Fig. 7.1), whereas the simulated sample (Fig. 7.2) indicates the opposite trend. In the near future, this disagreement will need to be reexamined with more data and with the second–generation Monte Carlo which is now available.

The analyses of this Thesis use data from both the Central Detector and the active Veto Shield. Improvements to the honeycomb iron tracking calorimeter and to the shield array have been made continually since the data used here was taken. Future investigations will benefit from these detector enhancements as well as from ever–increasing experiment run–time, and so should be able to reduce systematic uncertainties. The work of this Thesis, then, provides a first foundation for more extensive studies, using contained and partially contained events in Soudan 2.

References

[1] K. S. Hirata *et al.*, Phys. Lett. **B 280**, 146 (1992).

[2] Y. Fukuda *et al.*, Phys. Lett. **B 335**, 237 (1994).

[3] D. Casper *et al.*, Phys. Rev. Lett. **66**, 2561 (1991).

[4] R. Becker–Szendy *et al.*, Phys. Rev. **D 46**, 3720 (1992).

[5] S. J. Barish *et al.*, Phys. Rev. **D 16**, 3103 (1977).

[6] J. Engel *et al.*, Phys. Rev. **D 48**, 3048 (1993).

[7] D. H. Perkins, Astropart. Phys. **2**, 249 (1994).

[8] G. Barr, T.K. Gaisser and T. Stanev, Phys. Rev. **D 39**, 3532 (1989).

[9] M. Honda *et al.*, Phys. Lett. **B 248**, 193 (1990).

[10] H. Lee and Y.S. Koh, Nuovo Cim. **105 B**, 883 (1990).

[11] E.V. Bugaev and V.A. Naumov, Phys. Lett. **B 232**, 391 (1993).

[12] C. Berger *et al.*, Phys. Lett. **B 269**, 227 (1991).

Appendix A
The Soudan 2 Collaboration

W. W. M. Allison[3], G. J. Alner[4], I. Ambats[1], D. S. Ayres[1], L. J. Balka[1], G. D. Barr[3],[a], W. L. Barret[8],[1], D. Benjamin[5], C. Bode[2], P. M. Border[2], C. B. Brooks[3], J. H. Cobb[3], D. J. A. Cockerill[4], R. Cotton[4], H. Courant[2], J. W. Dawson[1], D. M. Demuth[2], V. W. Edwards[4], B. Ewen[5], T. H. Fields[1], H. M. Gallagher[2], C. Garcia–Garcia[4],[b], R. H. Giles[3], G. L. Giller[3], M. C. Goodman[1], R. N. Gray[2], S. J. Heilig[6],[1], N. Hill[1], J. H. Hoftiezer[1], D. J. Jankowski[1], K. Johns[2],[d], T. Kafka[5], S. M. S. Kasahara[2], J. Kochocki[5],[f], W. Leeson[5], P. J. Litchfield[4], N. P. Longley[2],[l], F. V. Lopez[1], M. J. Lowe[2],[g], W. A. Mann[5], M. L. Marshak[2], E. N. May[1], D. Maxam[2], L. McMaster[5], R. H. Milburn[5], W. H. Miller[2], C. P. Minor[2], A. Napier[5], W. P. Oliver[5], G. F. Pearce[4], D. H. Perkins[3], E. A. Peterson[2], L. E. Price[1], D. M. Roback[2], D. B. Rosen[2],[h], K. Ruddick[2], B. Saitta[5],[i], D. J. Schmid[2], J. Schlereth[1], J. Schneps[5], R. Seidlein[1], P. D. Shield[3], M. A. Shupe[2],[d], A. Stassinakis[3], N. Sundaralingam[5], M. A. Thomson[3],[k], J. L. Thron[1], H. J. Trost[1],[m], L. M. Tupper[3],[e], G. Villaume[2], D. Wall[5], S. J. Werkema[2],[j], N. West[3], U. Wielgosz[3] and C. A. Woods[4],[a]

(1) Argonne National Laboratory, Argonne, IL 60439, USA

(2) University of Minnesota, Minneapolis, MN 55455, USA

(3) University of Oxford, Oxford OX1 3RH, UK

(4) Rutherford Appleton Laboratory, Chilton, Didcot, Oxfordshire, OX11 0QX, UK

(5) Tufts University, Medford, MA 02155, USA

(6) Grinnel College, Grinnel, IA 50112, USA

(7) Carleton College, Northfield, MN 55057, USA

(8) Western Washington University, Bellingham, WA 98225, USA

(a) Now at CERN, CH-1211, Geneva 23, Switzerland

(b) Now at IFIC, E-46100 Burjassot, Valencia, Spain

(c) Now at LeCroy Corporation, Chestnut Ridge, NY 10977, USA

(d) Now at University of Arizona, Physics Department, Tucson, AZ 85721, USA

(e) Now at University of Oxford, Department of Physiology, Oxford, UK

(f) Now at Virginia Polytechnic Institute, Blacksburg, VA 24061, USA

(g) Now at Rice University, Houston, TX 77251, USA

(h) Now at Boston University, Boston, MA 02215, USA

(i) Now at Univ. di Ferrara, Dipartimento di Fisica, 44100 Ferrara, Italy

(j) Now at FNAL, Batavia, Il 60510, USA

(k) Now at Department of Physics and Astronomy, University College London, London WC1E 6BT, UK

(l) Now at California Institute of Technology, Pasadena, California, CA 91125

(m) Now at Texas A&M University, Department of Physics, College Station, Texas, TX 77843

Appendix B
Binary Data Summary Tape Format

The format below was used to summarize partially contained events on an event–by–event basis. The data summary tape (DST) record is a linear vector written in binary format. For each event, the DST is organized into six different blocks, namely the Header Block, the Hitbox Block, the ADJ Block, the Single Hit Block, the All Hit Block, and the Main Detector Track Block. The format for each block is as follows:

I. HEADER BLOCK

1) Number of words in entire event record, counting this word.
2) Number of words in the header block, including word 1) and this word. The value of this word is 14.
3) Exabyte number where the DST binary files are saved. The Value of this word is 2. The Tape number is DST002.
4) Run number.
5) Event number.
6) Date.
7) Time-(HHMMSSCC). This word is positive if the time is from WWVB, negative if it is taken from the VAX.
8) Time-(Millisecond×10000).
9) Trigger Word (Packed).
10) Event Type (0 or 1 or 2 or 3).

Note: Event Type 0 = Unknown.

Event Type 1 = Candidate partially contained event.

Event Type 2 = Candidate horizontal muon event.

Event Type 3 = Candidate multiple muon event.

11) DST_ V4.FOR program version number (4).

12) The date when the DST was created.

13) T_0 from the central detector.

14) The error in T_0.

II. HITBOX BLOCK

1) Number of words in the Hitbox Block, including this word.

2) Number of tracks passing through the Central Detector.

3) T_0 from the Central Detector.

The following coordinates are for the Veto Shield Box:

4 - 9) Hitbox coordinates (6).

10 -12) Direction cosine (α, β, γ).

The following coordinates are for the Central Detector Box:

13 -18) Hitbox coordinates (6).

19) Calculated Time Slot (TS) using the Central Detector T_0.

20) Slope (a) in line parameterisation $z = ax + b$ for Anode vs Time.

21) Intercept (b) for the above line.

22) Slope (c) in line parameterisation $z = cy + d$ for Cathode vs Time.

23) Intercept (d) for the above line.

24) T_0 for Anode time.

25) T_0 for Cathode time.

26) Error on slope (a) in line parameterisation $z = ax + b$ (Anode vs Time).

27) Error on constant (b) in line parameterisation $z = ax + b$.

28) Error on slope (c) in line parameterisation $z = cy + d$ (For Cathode vs Time).

29) Error on constant (d) in line parameterisation $z = cy + d$.

30) Error on T_0 (Anode vs Time).

31) Error on T_0 (For Cathode vs Time).

32) Packed word for face number:

Face (1)× 1000+Face (2)

33 etc.) For second, third, ... tracks the format is repeated, starting from "hitbox coordinate (for the shield box)" above.

III. ADJ BLOCK(Summarizes the Adjacent Group hits in the veto shield)

1) Number of words in the ADJ Block, including this word.

2) Number of Groups of adjacent hits.

For the first group:

3) Time span (TSPAN).

4) Number of hits in this group.

5 - 16) XYZ–coordinates for all four corners (12).

17) Leading–edge TS, Panel, First Tube, INOUT packed word.

(TS×10000000+Panel×10000+Tube×10+1 or 0)

18) Trailing–edge TS, Panel, Last Tube, INOUT packed word.

19 etc.) For the second, third ..... groups, the format repeats beginning with "Time span" above.

IV. SINGLE HIT BLOCK

1) Number of words in this block, including this word.

2) Number of single hits.

3) Packed word for TS, Panel, Tube, In–Out for this hit.

TS× 10000000+PANEL× 10000+TUBE× 10+INOUT

4 - 9) XYZ–coordinates for both ends of the tube (6).

10 etc.) This sequence repeats for the other single hits, starting from "packed word" above.

V. ALL HITS BLOCK (Summarizes all hits in a time slot)

1) Total number of words in this block, including this word.

2) Total number of single hits.

3) Packed word for TS, Panel, First Tube, INOUT packed word.

(TS×10000000+Panel×10000+Tube×10+1 or 0)

4 - 9) XYZ–coordinates for both ends of the tube (6).

10 etc.) This sequence repeats for the other single hits, starting from "packed word" 3) above.

VI. CENTRAL DETECTOR TRACK BLOCK

1) Total number of words in this block, including this word.

2) Total number of track entries.

3) Total number of Anode vs Time lines.

4) Total number of Cathode vs Time lines.

5) Total number of unassociated anode hits in the event.

6) Total number of unassociated cathode hits in the event.

For each track:

7) The Status packed word:

1st bit (hits outside fuducial volume, start),

2nd bit (hits outside fuducial volume, end).

8) The Track classification packed word:

1st bit (Track contained at neither end),

2nd bit (Track contained at one end),

3rd bit (Track contained at both ends),

7th bit (Good contained event),

8th bit (Downward going stopping muon),

9th bit (Upward going stopping muon),

12th bit (Track part of a parallel muon bundle).

9 etc.) This sequence repeats for the other tracks, starting from "Status packed word" 7) above.

Appendix C

Monte Carlo Samples of Charged Current Single Pion Production Reactions

In order to explore systematic effects with multiprong neutrino event reconstruction, we generated three exclusive event samples involving single pion production. The reactions are

$$\nu_\mu + n \rightarrow \mu^- + p + \pi^0,$$
$$\nu_e + n \rightarrow e^- + p + \pi^0,$$

and

$$\nu + n \rightarrow \nu + n + \pi^0.$$

Using the Soudan first generation Monte Carlo, 100 events of each reaction were generated. To reconstruct these samples we used the same procedures which were applied to the contained neutrino data sample (described in Chapter 4). That is, we utilized the online software STING, to scan, digitize, and reduce to a DST format all 300 events. The topologies observed for these simulated samples are as follows:

Table I: Topologies of Monte Carlo Single Pion Production Channels.

Topology (ranked by decreasing complexity)		Number of Events/Topology		
		$\mu^- p \pi^0$	$e^- p \pi^0$	$\nu n \pi^0$
No. Tracks	No. Showers			
4	2	1	0	0
2	2	55	0	2
1	3	1	45	3
2	1	19	0	0
1	2	5	23	9
0	3	0	8	9
1	1	12	5	0
2	0	2	0	0
0	2	0	15	58
1	0	2	0	0
0	1	2	4	18
Reconstruction Failure		1	0	1
Total		100	100	100

Table II: Shower Size in Monte Carlo Single Pion Production Channels.

No. of Showers		Final States		
(> 10 hits)	(< 10 hits)	$\mu^- p \pi^0$	$e^- p \pi^0$	$\nu n \pi^0$
3	0	–	–	–
0	3	–	–	–
2	1	–	36	3
1	2	–	17	8
2	0	20	28	30
0	2	42	9	39

Appendix D

Soudan 2 Contained Neutrino Sample

The Soudan 2 collaboration has analyzed an exposure of 1.0 kiloton-years. A total of 101 events have been identified as contained events. For the purpose of this thesis, each contained event was classified as being either a single track topology, a single shower topology, or being a multiprong topology (that is, not due to a quasi-elastic neutrino interaction). In this separation, an observed recoil nucleon or muon decay is allowed, in addition to the single lepton, for quasi-elastic track and shower events. Events which appear to be neutrino neutral current or inelastic interactions are classified as multiprongs. A summary of these 101 events are as follows:

I. Contained Single Shower Events:

Event No.	Run-Event	No. matched Hits	No. unmatched Hits	Candidate Recoil Proton
1	11719–1796	28	5	No
2	21479–2044	10	3	No
3	23083–1449	20	8	No
4	23179– 524	35	16	No
5	23752– 234	28	8	Yes
6	23819–1140	53	15	Yes
7	24881– 842	9	4	No
8	25667– 610	10	3	No
9	25997– 556	22	8	Yes

I. Contained Single Shower Events; *continued:*

Event No.	Run-Event	No. matched Hits	No. unmatched Hits	Candidate Recoil Proton
10	26034– 674	5	3	No
11	26500–1734	33	9	No
12	26653–1898	19	16	No
13	28011–1100	68	19	Yes
14	28416–1703	47	15	No
15	28537–1281	6	2	No
16	30415– 255	15	2	Yes
17	31200– 61	43	1	No
18	32172– 506	13	0	No
19	33027– 877	6	1	No
20	33331– 655	27	2	No
21	33418– 543	10	1	No
22	33516–1088	34	6	No
23	34485–1310	30	2	No
24	34520–1637	18	5	No
25	34703–1778	6	2	No
26	35460– 373	8	5	Yes
27	35701–1227	45	10	No
28	37216– 128	53	7	No
29	37790–1477	13	1	No
30	38019–1335	20	2	No
31	38029– 309	12	0	No
32	38793– 722	28	4	No
33	38929– 639	44	9	No
34	39766– 889	11	1	No
35	39821– 655	48	16	No

II. Contained Single Track Events:

Event No.	Run-Event	Muon length (cm)	Candidate Recoil Proton	Proposed End Point Decay No. Hits
1	18362– 966	128.3	Yes	
2	19117–1647	42.9	Yes	
3	22950–1034	13.7	No	
4	23364–1639	22.4	Yes	
5	23950– 172	71.6	No	2
6	24896–1924	219.1	No	3
7	26063–1218	18.0	No	4
8	26132– 569	138.2	No	2
9	26190–1511	72.4	No	3
10	26317– 57	18.5	No	
11	26329–1525	30.5	No	
12	28277– 392	186.2	Yes	
13	32001–1322	37.9	No	
14	33947–1501	160.5	Yes	3
15	34374– 236	28.7	No	
16	34676–1314	84.3	No	3
17	36155– 117	158.8	Yes	
18	36543–1277	22.9	Yes	
19	36722–1411	56.5	No	
20	36804– 511	34.3	No	
21	36828– 205	76.4	No	
22	37381–1855	129.3	No	
23	37712– 92	16.4	No	
24	37934– 433	346.2	No	
25	38136– 91	47.4	Yes	
26	38583– 528	202.8	No	4
27	39266–1544	75.1	No	
28	39626– 452	25.6	No	
29	39746–1334	27.3	No	
30	39762–1439	80.3	Yes	4

III. Contained Multiprong Events:

Event No.	Run-Event	Proposed Primary Vertex	Proposed Number of Showers	Proposed Number of Tracks
1	11940–1712	2	2 (3)	0 (0)
2	20307– 498	2	3 (2)	0 (0)
3	20366–1130	1	2	3
4	23354– 917	1	4	2
5	24283– 184	1	2	3
6	24290– 949	1	2	1
7	26439–1456	1	1	1
8	26957–1891	1	2	0
9	27896– 766	1	1	1
10	29136– 472	1	3	1
11	29750– 195	1	2	0
12	29834– 74	1	1	2
13	31549–1040	1	2 (1)	1 (1)
14	31565–1041	1	3	2
15	31606– 633	2	4 (4)	2 (2)
16	31739–1567	1	3	0
17	31757– 249	1	0	2
18	33322– 55	1	2	2
19	34123–1064	1	2	1
20	34742–1579	1	2	0
21	35086–1441	1	0	3
22	35209– 670	1	3	0
23	35219– 766	1	2	1
24	35314– 123	1	3	1
25	35998– 376	1	1	1
26	36284–1523	1	3	0
27	36381–1189	1	0	3
28	37148– 903	2	2 (3)	1 (0)

III. Contained Multiprong Events; *continued:*

Event No.	Run-Event	Proposed Primary Vertex	Proposed Number of Showers	Proposed Number of Tracks
29	37722– 277	2	2 (2)	0 (1)
30	37731– 374	1	0	2
31	38073– 886	1	2	5
32	38345– 310	1	2	2
33	39280– 122	2	2 (1)	0 (1)
34	39432– 645	2	1 (2)	1 (1)

IV. Isolated Recoil Proton Events:

Two of the original "single track" events have been identified by us as being recoil proton tracks rather than being single muon (or pion) tracks:

Event No.	Run-Event	Recoil Proton length (cm)
1	22031– 151	18.9 (13.9)
2	37735– 682	17.8

Event (22031-151) actually contains two separate, short recoil protons and lies close to the edge of the fiducial volume. Event (37735-682) contains one lone recoil proton. These events could either be neutrino induced neutral current events

$$\nu\, N \rightarrow p\, +\, \nu\, +\, (N^*), \tag{D.1}$$

or, neutron-induced "ROCK" events:

$$n\, N \rightarrow n\, +\, p\, +\, (N^*). \tag{D.2}$$

V. Rescan of first 0.5 kty:

They are ten new events from the rescan of the first half kiloton year exposure of Soudan 2 data (carried out by Craig Bode of Minnesota). The new contained events thus obtained include five single shower events, four single track events, and one multiprong event;

Event	Run-Event	Classification
1	12190–1656	Shower
2	13074–1060	Shower
3	14046–510	Track
4	16287–1103	Track
5	18141–1369	Track
6	20491–147	Shower
7	22031–151	Track
8	23929–337	Shower
9	25100–723	Shower
10	27107–1482	Multiprong

Appendix E

ASCII Card-Image Data Summary Format

We summarize events which are contained or partially-contained within the Soudan 2 tracking calorimeter, using the data format below. Information is recorded event-by-event on ASCII card images. Included along with each event ID are topological, geometric, and kinematic information obtained by scanning and measuring of STING images. The information is stored on "cards" of various types, including a Header, a Shield Hits card, Vertex cards, a Topology card per vertex, Track and/or Shower Geometry and Kinematics cards for each vertex, and - when appropriate - Pi-Zero, Track end-point-decay shower, and Proton-Pion cards for each vertex. The format for each block is as follows:

For each and every card, columns 1 through 4 contain

Card Type (1X, I3)

Formats for the various card types are given below, beginning with column 5. The order of the card types within each event is also indicated.

1. HEADER Card: Card Type = 001

Run number (I6)

Event number (I5)

Event type (I5)

Event type = yx,

where x = 1 ... CEV = contained event; no shield coincident two-layer hits (CTL hits or ADJ groups)

2 ... REV = "Rock event", i.e. contained event with shield CTL hits

3 ... PCE = partially contained event with tracks leaving the central detector fiducial volume.

4 ... up-going stopping track or shower.

5 ... stopping cosmic ray muon (not up-going).

9 ... other

y = 1 ... single track (possible with recoil).

2 ... single shower (possible with recoil).

3 ... multiprong

Event T0, Best estimate (I5)

Event T0, Allowed range (2I3)

Total number of candidate primary vertices in this event (I4)

Lab/Institution-ID (I3)

Person-ID (I3)

Date (I9)

2. SHIELD HITS Card: Card Type = 002

Shield fully operational ? (1=Yes, 2=No) (I3)

Total number of coincident shield hits (ADJ groups) in the event, in all shield timeslots (I4)

Number of shield ADJ groups within a narrow window around T0 (I4)

Number of shield ADJ groups between T0LO and T0HI (I4)

STING times for the shield ADJ groups compatible with the event time (maximum of 10 times can be listed) (10I5)

3. VERTEX Card: Card Type = 003

Vertex number (I3)

Total number of vertex measurements, for this vertex (I4)

Number of the "Best" measurement of this vertex (I4)

x, y, z of this candidate vertex, in cm (3F8.2)

Repeat, one VERTEX card for each measurement of this vertex.

4. EVENT TOPOLOGY Card: Card Type = 004

Vertex number (I3)

Topology information for the above candidate primary vertex:

Total number of tracks (I3)

Number of tracks connected to the vertex (I3)

Number of tracks remote from the vertex (I3)

Number of recoil protons from the vertex (I3)

Number of tracks with scatters (I3)

Number of non-proton tracks from the vertex (I3)

Total number of showers (I3)

Number of showers connected to the vertex (I3)

Number of showers remote from the vertex (I3)

Number of candidate π^0's (I3)

Number of proton-pion combinations (I3)

Number of tracks with end-point showers/decays (I3)

5. TRACK GEOMETRY Card: Type = 005

Vertex number (I3)

Track number, this vertex (I3)

Total points on this track, excluding vertex (I3)

Point number (I3)

x, y, z of this point, in cm (3F8.2)

Cumulative track length in centimeters (F8.2)

End-point shower/decay on this track? YES=1, NO=2 (I2)

Repeat, one Track Geometry card for each point measured on this track.

Repeat, Track Geometry cards for each track at the vertex.

6. TRACK KINEMATICS Card: Type = 006

Vertex number (I3)

Track number, this vertex (I3)

Number of mass assignments this track/this vertex (I3)

Mass number, this track/this vertex (I3)

Track mass assignment in MeV/c^2 (F8.1)

Track momentum Px, Py, Pz in MeV/c (3F8.2)

Track energy in MeV (F8.2)

Repeat, one Track Kinematics card for each mass assignment for this track.

Repeat, Track Kinematics cards for each track associated with this vertex.

7. SHOWER GEOMETRY Card: Type = 007

Vertex number (I3)

Shower number, this vertex (I3)

Total matched (3D) hits, this shower (I3)

Estimated number of unmatched (2D) hits, this shower (I3)

x, y, z of "Direction Point", in cm (3F8.2)

x, y, z of 1st matched hit, in cm (3F8.2)

Repeat Shower Geometry card for each shower associated with this vertex.

8. SHOWER KINEMATICS Card: Type = 008

Vertex number (I3)

Shower number, this vertex (I3)

Shower momentum Px, Py, Pz in MeV/c (3F8.2)

Shower energy in MeV (F8.2)

Repeat Shower Kinematics card for each shower associated with this vertex.

9. Pi-Zero Card: Type = 009

Vertex number	(I3)
Pi-zero number, this vertex	(I3)
Number of 1st shower	(I3)
Number of 2nd shower	(I3)
Invariant mass in MeV/c^2	(F8.2)
Pi-zero Px, Py, Pz in MeV/c	(3F8.3)
Pi-zero energy in MeV	(F8.3)

Repeat Pi-Zero card for each π^0 associated with this vertex.

10. PROTON-PION Combination Card: Type = 010

Vertex number	(I3)
Proton-pion combination number	(I3)
Track number of proton from this vertex	(I4)
Charge (= 0 or 1) of pion	(I3)
Pi-zero number (if Charge=0), or	
Track number (if Charge=1)	(I3)
Invariant mass in MeV/c^2	(F8.2)
Proton-Pion combination Px, Py, Pz in MeV/c	(3F8.2)
Proton-Pion combination energy in MeV	(F8.2)

Repeat Proton-Pion cards for each Proton-Pion combination at this vertex.

11. TRACK ENDPOINT SHOWER/DECAY card - Type 011

Vertex number	(I3)
Endpoint shower number, this vertex	(I3)
Track number, this vertex	(I3)

Total hits in end-point shower (I3)

xyz of closest shower hit, in cm (3F8.2)

xyz of shower "direction point", in cm (3F8.2)

Shower energy in MeV (F8.2)

Repeat the card sequence below for each candidate primary vertex for this event:

VERTEX Card(s)

TOPOLOGY Card

TRACK GEOMETRY Card(s)

TRACK KINEMATICS Card(s)

SHOWER GEOMETRY Card(s)

SHOWER KINEMATICS Card(s)

PI-ZERO Card(s)

PROTON-PION COMBINATION Card(s)

TRACK END-POINT-DECAY Card(s)

DST ANNEX CARD(S)

Additional cards can be created which reside in an independent data file. For example, we summarize the flight path of the incident neutral particle through Soudan material using event cards which contain the following information:

12. NEUTRINO FLIGHT PATH Card: Card type 012

Card number (I2)

Run number (I5)

Event number (I4)

Event type (I2)

x, y, z of this Vertex, in cm (3F8.2)

x, y, z of the Net Momentum vector, in cm (3F8.2)

x, y, z of the neutral beam particle's entrance Point, in cm (3F8.2)

Geometrical distance between Entrance point and Vertex (F8.2)

Material traversed within calorimeter modules (F8.2)

13. NEUTRINO PENETRATION DEPTH Card: Card type 013

Card number (I2)

Run number (I5)

Event number (I4)

Event type (I2)

Backward direction: from vertex to exiting the main detector

x, y, z of the exiting point, in cm (3F8.2)

Geometrical distance, in cm (F8.2)

Length in gas, in cm (F8.2)

Material traversed, in g/cm^2 (F8.2)

Forward direction: from vertex to exiting the main detector

x, y, z of the exiting point, in cm (3F8.2)

Geometrical distance, in cm (F8.2)

Length in gas, in cm (F8.2)

Material traversed, in g/cm^2 (F8.2)

Appendix F

Soudan 2 Partially Contained Neutrino Sample

We analyzed an exposure of 1.0 kiloton-years. A total of 15 events have been identified as partially contained events. A summary of these 15 multiprong events is as follows:

I. Partially Contained Multiprong Events:

Event No.	Run-Event	Proposed Primary Vertex	Proposed Number of Showers	Proposed Number of Tracks
1	29891–598	1	2	4
2	32045–982	1	3	4
3	32107–335	1	6	0
4	35209–670	2	2 (3)	1 (0)
5	37320–691	1	0	5
6	37797–516	1	3	3
7	38390–542	1	3	4
8	39261–1428	1	2	2
9	40255–987	1	2	3
10	41798–737	1	0	3
11	42124–771	2	1 (0)	3 (2)
12	42189–277	1	4	4
13	42223–902	1	7	0
14	42550–241	1	2	2
15	44553–1193	1	2	3

II. Events from first 0.5 kty:

Four PCE events were found in the first–half kiloton year exposure of Soudan 2 data (scanning by Don Roback and Craig Bode of Minnesota). These partially contained events correspond to an earlier data–taking period than was processed for this thesis. Our understanding is that event 16753–239 is a contained multiprong, whereas event 16970–1644 is a contained single shower.
These four events are summarized below:

Event	Run-Event	Topology
1	16753–239	2S–1T
2	16970–116	1S
3	22870–1644	2S–2T
4	25079–456	1S–2T

Appendix G

Kinematical Properties of Two–Shower Events

The Tables below summarize kinematical properties of samples of events which have only two visible showers in the final state. For each event, The Tables give the momentum for each shower, the invariant mass of the shower pair, the net momentum of the shower pair, the visible energy of the shower pair, and the distance from the physicist's choice vertex to the first hit for each shower.

Table I: Contained Multiprong Events

Event–No.	$\lvert\vec{P}\rvert$ γ_1/γ_2 (MeV/c)	Invariant Mass γ pair (MeV/c^2)	Net Momentum γ pair (MeV/c)	Visible Energy γ pair (MeV)	distance to 1^{st} Hit γ_1/γ_2 (cm)
11940–1712	302/64	132	367	372	6/25
20307–498	370/239	509	362	609	10/9
26957–1891	827/324	210	1132	1151	7/3
29750–195	144/238	136	328	382	7/4
34742–1579	301/229	261	421	484	2/9
37722–277	1436/180	373	1573	1616	32/11
39280–122	965/110	466	970	1076	18/19

Table II: Rock Multiprong Events

Event–No.	$\lvert\vec{P}\rvert$ γ_1/γ_2 (MeV/c)	Invariant Mass γ pair (MeV/c^2)	Net Momentum γ pair (MeV/c)	Visible Energy γ pair (MeV)	distance to 1^{st} Hit γ_1/γ_2 (cm)
13195–854	638/2633	1461	2927	3271	10/12
13610–177	110/110	194	107	220	4/5
18094–761	110/25	95	96	135	2/3
24382–1104	258/51	198	238	309	6/6
27316–1911	218/51	67	261	269	9/4
27651–649	258/37	39	293	296	18/16
30275–774	95/127	63	213	222	34/2
30882–1332	347/95	71	436	442	2/30
31587–951	127/762	467	757	889	6/51
33588–1072	180/180	135	335	360	8/16
33845–1	470/419	393	798	889	1/16
34359–1514	180/110	32	289	290	2/23
35738–403	730/180	716	562	910	2/2
37923–1001	218/497	232	676	715	20/8
38020–1180	95/80	154	82	175	4/3
38205–1086	95/144	230	63	239	1/5
39499–512	668/497	298	1127	1165	21/30
39868–900	25/144	66	155	169	7/8

Table III: Monte Carlo Multiprong Events

Event–No.	Truth Table	$\lvert\vec{P}\rvert$ γ_1/γ_2 (MeV/c)	Invariant Mass γ pair (MeV/c^2)	Net Momentum γ pair (MeV/c)	Visible Energy γ pair (MeV)	distance to 1^{st} Hit γ_1/γ_2 (cm)
10013–56	$\nu n\pi^0$	111/395	132	546	506	24/64
10013–339	$\nu n\pi^0$	162/80	135	218	241	12/14
10013–354	en	161/346	419	288	508	28/9
10013–619	$\nu n\pi^0$	347/144	128	482	491	33/16
10013–803	$\nu n\pi^0$	51/162	134	178	213	17/18
10014–355	$\nu n\pi^0$	95/552	98	641	647	28/7
10014–555	$\nu n\pi^0$	80/51	121	124	131	8/35
10014–615	$\nu n\pi^0$	80/162	133	218	242	44/49
10015–242	$\nu n\pi^0\pi^0$	218/497	165	695	715	52/86
10015–532	$\nu n\pi^0$	80/199	125	266	279	13/8
10015–831	ep	127/259	27	382	386	9/20